Collider Phenomenology of Dark Matter Models

Memoria de Tesis Doctoral realizada por

Víctor Martín Lozano

presentada ante el Departamento de Física Teórica
de la Universidad Autónoma de Madrid
para optar al Título de Doctor en Física Teórica

Tesis Doctoral dirigida por el
Dr. David G. Cerdeño,
Lecturer en la Universidad de Durham
y por el
Dr. Jesús Moreno,
Científico Titular del Instituto de Física Teórica, IFT-UAM/CSIC

Departamento de Física Teórica
Universidad Autónoma de Madrid

Instituto de Física Teórica
UAM-CSIC

Madrid, noviembre de 2016

Departamento de Física Teórica
Universidad Autónoma de Madrid

Instituto de Física Teórica
UAM-CSIC

Collider Phenomenology of Dark Matter Models

Víctor Martín Lozano

Madrid, noviembre de 2016

「勝負あった安心だうきけっ、きにててたにあ、、だあり負勝、ててけち一り、にに筋、油屈傲の恐断する道れすることをるること、こことな踏ととなくんもなく、でなく、ゆく、け、。」

「嘉納治五郎師範」

“Pasea por un único camino.
No te vuelvas engreído por la victoria, o roto por la derrota.
No te olvides de ser precavido cuando todo esté en calma,
y no tengas miedo cuando el peligro aceche”

- Maestro Jigoro Kano

Agradecimientos

Es muy difícil llegar a este punto del camino y poder decir que todo este trabajo es obra de una sola persona. En mi caso una gran cantidad de gente ha estado construyendo este proyecto conmigo, aunque lo mismo esas personas ni siquiera se han dado cuenta.

En primero lugar quiero agradecer mis dos directores de tesis, David y Jesús, el haberme dado la oportunidad de poder realizar el doctorado y acercarme al terreno de la investigación. Gracias también David por darme la oportunidad de conocer esa parte de la ciencia que es la divulgación. He de decir que gracias a ti me ha apasionado el hecho de divulgar el conocimiento de la física. Gracias a ti Jesús, por todas las tardes de física en tu despacho y sobre todo por confiar en mí cuando me dejaste volar solo en el proyecto de los tripletes. Gracias a eso le cogí más el gusto si cabe a investigar.

En segundo lugar, aunque casi debería ocupar el primer puesto, quiero agradecer a Luis Ibáñez todo lo que he aprendido de él. Gracias por confiar en mí cuando pedí aquella beca de colaboración contigo y me contagiaste el gusto por investigar. Gracias también por ser un ejemplo constante de pasión por la física y sobre todo por transmitirnos parte de ella. Puedo decir que las navidades del 2015 fueron las más divertidas y emocionantes que he pasado por culpa del Megaxión. De mayor quiero ser un cientefico masemo como tú.

En el tema científico le debo todo a Miguel Peiró. Por haberme enseñado a ser riguroso, a hacer ciencia, a investigar, por las charlas en tu despacho o en la entrada del IFT mientras fumabas, por las risas en los MultiDark... pero sobre todo por tu paciencia infinita. Gracias.

Quiero agradecer a Germano y Chiara el haberme dado la oportunidad de poder realizar mi primer proyecto de investigación sin jefazos. Gracias por confiar en mí. También quiero agradecer a Miki su amistad de muchos años.

Mil gracias al "Gang of Five" 「五人幫」. Irene, me siento agradecido de haber podido forjar nuestra amistad a la vez que íbamos aprendiendo cada vez más de física. Por las aventuras en las que sabes que la única salida está en tirar hacia adelante. Gracias por apoyarme en los momentos más duros. Miguel, qué puedo decir de ti que no sepas. Gracias por todo, por apoyarme constantemente, por las risas, por los coffees, por el dumb, por la física, por los cotilleos y el ser las marujas del IFT, por las conversaciones de historia, de política, de feminismo, por los viajes y por todo lo que nos queda vivir juntos. Ander, gracias por las risas mañaneras y por desparpajo euskoandaluz, gracias por tu amistad. Gianluca, grazie mille per tutto, per la tua amicizia. Gracias por aguantar conmigo a Miguel, gracias por escucharme cuando lo he necesitado. El "Gang of Five" se hará famoso.

A Disco Chino. Mario y Miguel, habéis hecho de un lugar de trabajo un sitio magnífico para procrastinar, reír, tomar café, mirar vainas, twittear y un largo etcétera maravilloso. Os echaré de menos.

También quiero agradecer a toda la demás gente del IFT. Ana, muchas gracias por todo. Gracias por escucharme cuando lo he necesitado y por contarme cuando lo has necesitado tú. Gracias por los abrazos y las sonrisas espontáneas. Xabi, gracias por todo. Por las risas, por la física aprendida, por tu capacidad para razonar, por tu paciencia, por aguantarme tanto. Gracias por compartir tanto conmigo. Espero que sigamos haciéndolo. Josu, mi hermano, muchas gracias por los momentos divertidos y por confiar en mí. Gracias Ginevra por todas las conversaciones que hemos tenido. Por las noches en Lavapiés en las que literalmente nos lavaron los pies. Gracias a Rocío, que aunque has sido un descubrimiento tardío he disfrutado mucho de tu compañía en este tiempo en el IFT. Ilaria, muchas gracias por aguantar mi verborrea y por compartir los nervios y tensión del final del doctorado y de la fatídica hora de echar postdocs. Gracias Juanmi por toda la historia que hemos aprendido juntos y la que nos queda por aprender. Gracias a Carlos Pena por confiar en mí y dejarme currar en todas las actividades de divulgación habidas y por haber, y por dejar que fuera a Tánger a divulgar la física. A Javier Martín por pasarme el Age of Empires en pleno periodo de escritura de tesis. Gracias también a los Masterchef, aquellos que conocimos cuando eran estudiantes de grado y ahora están con el doctorado. Sobre todo quiero agradecer especialmente a Uga y a Claudia todas las risas que nos hemos podido echar juntos. No me quiero olvidar de todas las personas que nos han hecho más fácil nuestra estancia aquí, gracias Isabel, Chabe, Mónica Vergel y Mónica Encinas, María y Susana. Gracias a todos los postdocs que llegaron al final de mi doctorado y con los que me lo he pasado tan bien, Jong, Marco, Pedro... y sobre todo a Valentina. Gracias por aguantarme, por nuestras risas cuando no entendemos a Osamu en Skype, por aguantarme tantas conversaciones y charlas, por darme ánimos. Gracias a María José, nuestras charlas en la hora de la comida han hecho que me plantee cosas que nunca había pensado y sobre todo a contruir un espíritu crítico. Gracias también por darme la oportunidad de dar las clases de Física de Altas Energías con las que he disfrutado y aprendido tanto. Gracias también a toda la gente que pasó por el IFT y que marcharon, Diego, Amadeo, Robaina, Bryan, Fran, etc. Sobre todo quiero agradecer a Mateo García todo lo que hemos vivido juntos, nuestro paso por el doctorado, las discusiones de física, las conferencias, etc. Gracias también a Aitor, Doris, Santi (y los días de escalada), Wieland y todos los que me olvido.

Gracias a todos y a cada uno de mis estudiantes (incluido el de las antiprácticas), porque aún siendo yo el que intentaba enseñar, al final acababa aprendiendo de vosotros. Gracias Uga por ser un crack, contigo he aprendido y he disfrutado mucho, espero que sigamos haciéndolo. A Gabriela y Teseo por el año tan divertido que pasamos con vuestro TFG. A Dani y su lentitud extrema que le permitía hacer las cosas de una manera perfecta. A Berta por todo. Gracias por quitarme la venda que tenía en los ojos y enseñarme tanto. Desde que empezamos a charlar y discutir sobre el mundo nada ha sido igual. Gracias también a Catuxa y a Julia por ser mis primeras alumnas y que con más cariño recuerdo.

No me quiero olvidar de todos aquellos que aunque no se dedican a la física han estado presentes en nuestro trabajo diario siempre con una sonrisa y ayudándonos. Gracias en primer lugar a Pili, por tu simpatía infinita a pesar de todo. Gracias por ser un ejemplo a seguir y de fortaleza. Gracias por darme los buenos días todos los días desde que estaba en la carrera alegrándome las mañanas. A Loli, por las conversaciones que teníamos en DiscoChino cuando venías a limpiar. Al chino kundeiro, Alberto, por la alegría que nos das cada mañana al entrar al trabajo. Gracias a todas aquellas personas que con sus trabajos y gestos voluntariosos permiten que personas como

yo podamos estar trabajando en lo que nos gusta.

Gracias a la Morada de la Liche. Gracias a todos por la cantidad de veces que me ha dolido el estómago y he llorado de tanto reírme. Gracias Santi por tu amistad, los viajes y las risas. Juanma, amigo de muchos años y muchas batallas, gracias por todo, sabes que nos unen muchas cosas, hermano. Javi, no puedo agradecer aquí todo lo que me gustaría hacer. Amigo con mayúsculas, gracias por querer compartir este último año de doctorado piso conmigo. Gracias por escucharme y apoyarme cuando más lo he necesitado. Gracias por los pushing to the limit mañaneros y los ¡No, Lute! Gracias por tu amistad. Aday, gracias por todas las risas que nos echamos hace ya muchos años en tu casa. Julia, creo que ya está todo dicho, gracias por tu amistad incondicional y por tu confianza en mí. Ha sido una constante en mi vida desde que nos conocimos hace ya demasiados años. Gracias también a todas aquellas personas que pasaron por la carrera y dejaron huella en mí. Gracias Raquelandas por tu amistad a pesar de la distancia. Siempre nos quedará Planck.

A mis amigos de Leganés, Julia, Maite, Ale, Rober, Tamara, Santi, José, Yisus y Sandra. Sin vosotros no podría haber hecho esto. Gracias por todos los momentos únicos que hemos vivido y que nos quedarán por vivir. Os quiero amigos. Gracias también al trío calavera, a Pako, al Quini y al Monte. Porque Leganés no hubiera sido lo mismo.

A Víctor Moreno, por compartir nuestra pasión y por todas las cosas que me has enseñado. Por toda la música que hemos escuchado juntos. A Marta, mi eterna amiga, gracias por los martes locos que pueden acabar a las seis de la mañana y tu sonrisa infinita. A Mar, por los momentos de risas y vinos que nos hemos echado.

A mis amigas Sara y Violeta. Gracias por dar siempre lo mejor de vosotras.

A mi amiga Cristina por todo. Por tu amistad infinita, por tu bondad extrema, por tu inteligencia artística, por las charlas nocturnas, por la cantidad de horas habladas y por tu gran conexión conmigo. Gracias.

A toda la gente del Judo. Gracias José y Óscar por haberme enseñado este noble camino y todos sus valores. Mi vida sería muy diferente sin todo ello. Gracias a mis compañeros de Judo, Paco e Iván y su amistad duradera a pesar de los años. A toda la gente del JiuJitsu, a mis profes Javi y María por darme la oportunidad de conocer dicho deporte y a todos mis compañeros. Gracias en especial a Thaer, Almansa, Óscar, José, Yisus y Esther. Gracias por todo, sois unos líderes.

Gracias a mi familia. Primeramente a mis abuelos, gente humilde que sacó a sus hijos adelante en tiempos muy difíciles. Gracias a mis padres, ejemplo de lucha, sacrificio, amor, apoyo, etc. Si hoy estoy aquí es gracias a vosotros y a todo lo que me habéis enseñado. Gracias a mi hermano Alejandro. Por su amor infinito y su cariño siempre leal. Gracias por todo lo que hemos compartido y que me ha hecho llegar a ser mejor persona. Te quiero. Gracias también a toda mi familia, mis tíos, tías, primos, primas, etc. Con todos vosotros he aprendido a querer, respetar, jugar, reír, etc.

Gracias Bea por todo. Gracias por estar ahí siempre. Por todos los momentos de risas, de bailes, de dibujos, de viajes, de querernos, de chino petula, de paseos por Madrid, de terraceo, de solecito Siciliano o Amalfitano, de viajes infinitos, de cafelitos trabajando, y un largo etcétera. Gracias por querer compartir todo esto conmigo. Te quiero.

List of Publications

This Thesis is based on the following scientific articles:

[1] **Displaced vertices and long-lived charged particles in the NMSSM with right-handed sneutrinos**
David G. Cerdeño, Víctor Martín-Lozano, Osamu Seto
JHEP **1405** (2014) 035 (arXiv: 1311.7260)

[2] **Dark Matter versus $h \to \gamma\gamma$ and $h \to \gamma Z$ with supersymmetric triplets**
Chiara Arina, Víctor Martín-Lozano, Germano Nardini
JHEP **1408** (2014) 015 (arXiv: 1403.6434)

[3] **Resonant Higgs boson pair production in the $hh \to b\bar{b}WW \to b\bar{b}\ell^+\nu\ell^-\bar{\nu}$ decay channel**
Víctor Martín-Lozano, Jesus M. Moreno, Chan Beom Park
JHEP **1508** (2015) 004 (arXiv: 1501.03799)

[4] **Isospin violating dark matter in Stückelberg portal scenarios**
Víctor Martín-Lozano, Miguel Peiró, Pablo Soler
JHEP **1504** (2015) 175 (arXiv: 1503.01780)

During the development of this thesis the candidate has also published the following papers although they are not in the manuscript:

[5] **A Megaxion at 750 GeV as a First Hint of Low Scale String Theory**
Luis E. Ibáñez, Víctor Martín-Lozano
JHEP **1607** (2016) 021 (arXiv: 1512.08777)

[6] **Confronting dark matter with the diphoton excess from a parent resonance decay**
Valentina De Romeri, Jong Soo Kim, Víctor Martín-Lozano, Krzysztof Rolbiecki, Roberto Ruiz de Austri
Eur.Phys.J. **C76** (2016) no.5, 262 (arXiv: 1603.04479)

[7] **Confronting SUSY models with LHC data via electroweakino production**
Chiara Arina, Mikael Chala, Víctor Martín-Lozano, Germano Nardini
arXiv: 1610.03822

Resumen

La Materia Oscura (MO) constituye el 27% del contenido del Universo y compone el 85% de la materia total. Dentro del Modelo Estándar (ME) de las interacciones fundamentales no hay ninguna manera de poder explicar este tipo de materia invisible, por ello es necesario extenderlo. Además el Gran Colisionador de Hadrones (LHC) ha empezado su segunda puesta en marcha después de haber sido mejorado hasta tener una energía en el centro de masas de 13 TeV. Debido a que en el anterior funcionamiento a 8 TeV fue muy exitoso, donde se encontró el bosón de Higgs y se pusieron muchos límites a nuevos modelos, se espera encontrar señales nos indiquen Nueva Física en esta nueva configuración.

Esta Tesis está dedicada a estudiar la fenomenología en colisionadores de cuatro modelos de MO. Dos de ellos entran dentro de los llamados portales de MO, donde una partícula mediadora es la responsable de las interacciones entre el sector oculto y la materia ordinaria. El primero de dichos modelos es una extensión escalar singlete del ME donde se estudian los límites experimentales a la masa y el ángulo de mezcla del nuevo bosón de Higgs. También estudiamos la producción de este bosón escalar en el LHC analizando la desintegración a dos Higgses del ME que se desintegran en el canal $H \to hh \to b\bar{b}WW \to b\bar{b}\ell^+\nu\ell^-\bar{\nu}$. El segundo modelo de portal de MO está basado en extensiones $U(1)$ del grupo del ME, motivados por modelos fenomenológicos de teoría de cuerdas. El bosón Z' que aparece en las simetrías $U(1)$, se convierte en el mediador entre el sector de MO y la materia visible. Debido a la naturaleza de los acoplos del mediador, aparece un patrón de violación de isospín en las interacciones entre ambos sectores. Este hecho tiene un fuerte impacto en los experimentos de detección directa de MO dado que este tipo de interacciones se acopla a neutrones y a protones de manera diferente, en contraste con la mayoría de modelos que hay en la literatura donde ambos acoplos son iguales.

Los otros dos modelos tratados en esta Tesis son extensiones del modelo estándar supersimétrico mínimo. El primero de ellos está basado en una extensión con un singlete del modelo estándar supersimétrico mínimo con sneutrinos dextrógiros. En esta construcción el sneutrino dextrógiro es buen candidato a MO mientras que el neutrino dextrógiro tiene un tiempo de desintegración muy largo debido a que su anchura de desintegración es proporcional al acoplo Yukawa del neutrino predicho muy pequeño por la teoría. La desintegración tardía de los neutrinos dextrógiros deja señales claras en el LHC en forma de vértices desplazados. Otra señal exótica de esta construcción es la producción de staus con vida media larga que podrían escapar del detector dejando una traza cargada. El segundo modelo supersimétrico es la extensión del modelo mínimo de supersimetría con un triplete que hace que aumente el sector electrodébil fermiónico y como consecuencia las desintegraciones del Higgs, $h \to \gamma\gamma$ y $h \to Z\gamma$, inducidas por *loops*, se ven aumentadas hasta un 40–60% comparadas con aquellas del ME. Además estos nuevos estados son relevantes para la fenomenología de MO. De hecho, se encuentra que el más ligero de los neutralinos es un buen candidato a MO. Si se imponen sobre éste todos los límites experimentales de MO, encontramos que esto afecta directamente al sector de Higgs reduciendo el aumento de las desintegraciones inducidas por *loops* del Higgs, $h \to \gamma\gamma$ y $h \to Z\gamma$, hasta un 20% como máximo.

Abstract

Dark Matter (DM) is the 27% of the content of the Universe and make the 85% of the total matter. There is no possibility to explain this kind of invisible matter within the Standard Model (SM) of fundamental interactions so extensions of it are necessary. Furthermore the Large Hadron Collider (LHC) has started its second run after being upgraded up to a centre-of-mass energy of 13 TeV. Due to its great past run at a centre-of-mass energy of 8 TeV, where the Higgs boson was discovered and several limits to new models where imposed, we expect that new Physics could be found with the new configuration.

This thesis is devoted to the study of collider phenomenology of four DM models. Two of them are embedded in the so-called DM portals, where a mediator particle is the responsible of the interactions between the hidden sector and the ordinary matter. The first of these models is a scalar singlet extension of the SM where the latest constraints on the mass and the mixing of the new Higgs boson are studied. We also study the production of this scalar boson at the LHC analysing the decay channel into two SM Higgses with final products $H \to hh \to b\bar{b}WW \to b\bar{b}\ell^+\nu\ell^-\bar{\nu}$. The second model of the DM portals is based on $U(1)$ extensions of the SM, motivated by String Theory phenomenological models. Here, the massive Z' that arises from the $U(1)$ symmetries becomes the mediator between the DM sector and the visible matter. An important pattern of isospin-violating interactions is found between both sectors due to the nature of the couplings with the mediator. This has a strong impact on direct detection experiments of dark matter, since this kind of interactions couples differently to neutrons and protons, in contrast to the majority of models in the literature where both couplings are equal.

The other two models described in this Thesis are both supersymmetric extensions of the Minimal Supersymmetric Standard Model. The first of these models is based on the Next-to-Minimal Supersymmetric Standard Model with Right-Handed (RH) sneutrinos. In this construction the RH sneutrino is a good candidate for DM while the RH neutrino is long-lived since its decay width is proportional to the neutrino Yukawa coupling that is predicted to be small. The late decay of the RH neutrinos leads to very specific signatures in the LHC that are displaced vertices. Another exotic signature of this construction is the production of a long-lived stau that could escape the detector leaving a characteristic trail. The second supersymmetric model is the Triplet extension of the Minimal Supersymmetric Standard Model that enlarges the electroweakino sector. As a consequence the loop induced decays of the Higgs $h \to \gamma\gamma$ and $h \to Z\gamma$ could enhance up to a 40–60% compared with the ones of the SM. Furthermore, those new states are also relevant for DM phenomenology. We found that the lightest neutralino is a good candidate for DM and fulfils all the experimental constraints. Those requirements strongly affects the Higgs sector reducing the loop-induced decays, $h \to \gamma\gamma$ and $h \to Z\gamma$, to a 20% at most.

Contents

1

Introduction

In the last decades the Standard Model (SM) has been exhaustively tested in different experiments. Particle colliders such as LEP, Tevatron and now the LHC have been the principal tool to study the SM. With them all the particles and interactions provided by SM have been confirmed. Furthermore electroweak (EW) precision tests agree with the SM prediction with exceptional accuracy. Moreover the new state discovered at the Large Hadron Collider (LHC) can be compatible with the SM Higgs boson [8, 9], the only missing link in this construction.

The SM of fundamental interactions is a quantum field theory defined in 4 dimensions that is based on the gauge group $SU(3)_c \times SU(2)_L \times U(1)_Y$ and it is renormalizable and invariant under Poincaré group. In that construction all the different particles found so far are embedded as different representations of the gauge group. The SM content can be found in Figure 1.1, and it is make up of fermions and bosons. Fermions are divided in quarks and leptons, each with three families and two components. On the other hand, bosons can be separated between vector bosons and scalar bosons. The former ones are the force carriers such as the photon, γ, the W and Z bosons and the gluon, g. There is only one scalar boson in the SM, that is the Higgs boson, h. Such boson is the responsible for the Electroweak EW symmetry breaking (EWSB).

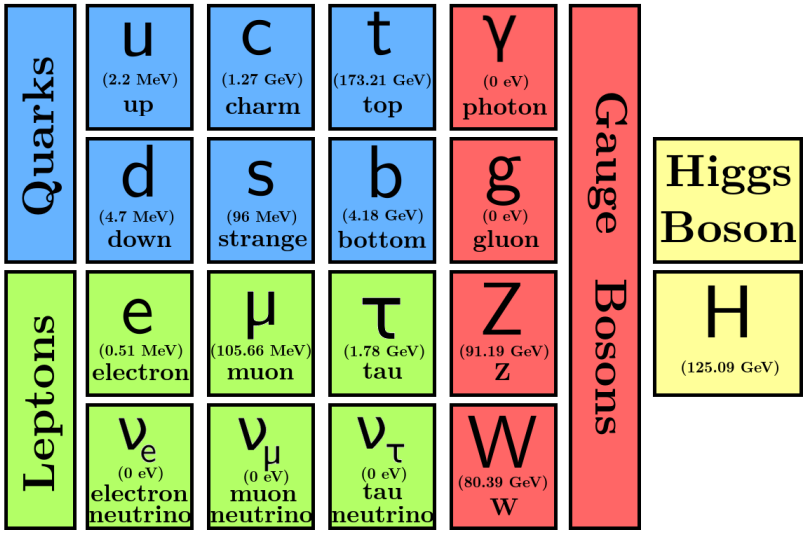

Figure 1.1: Particle content of the SM.

Electroweak symmetry breaking is a phenomenon appearing when the Higgs field acquires a vacuum expectation value (vev), v. When this occurs, the SM gauge group is no longer a good

symmetry for the ground state, shrinking it to $SU(3)_c \times SU(2)_L \times U(1)_Y \rightarrow SU(3)_c \times U(1)_{em}$. As a consequence, the W and Z bosons acquire masses proportional to the value of the vev, v. Moreover leptons (excluding the neutrinos) and quarks also get masses due to its Yukawa couplings to the Higgs field. After EWSB takes place, there is an extra degree of freedom in the theory that is interpreted as a spin 0, neutral particle, the Higgs boson, h. The scalar potential of the SM can be written as

$$V_H = \mu^2 H^\dagger H + \frac{\lambda}{2}(H^\dagger H)^2. \tag{1.1}$$

The two Lagrangian parameters μ and λ can be replaced by the physical magnitudes v and the mass of the Higgs, m_h. The Higgs vev is inferred by the EW processes and it is found to be $v = 174$ GeV. However, due to the fact that the scalar potential of Eq. (1.1) has two parameters and only one physical parameter was known, the mass of the Higgs boson, m_h, cannot be predicted by the SM. On the other hand, one can look at the EW processes where the Higgs boson plays a role to infer its imprint. Those are called EW precision observables (EWPO) and they are a set of experimental processes where one can actually fit the Higgs mass. According to those, the Higgs boson mass is found to be $m_h = 93^{+25}_{-21}$ GeV [10].

Nonetheless, the ATLAS and CMS collaborations reported the discovery of a scalar particle compatible with the SM Higgs boson [8, 9]. The mass of this particle is [11]

$$m_h = 125.09 \pm 0.21\,(\text{stat.}) \pm 0.11\,(\text{syst.})\,\text{GeV}. \tag{1.2}$$

One can then ask whether this boson is the SM Higgs boson. There exist one variable called signal strength, that can measure the difference between the production and decay of the measured boson compared with the one predicted by the SM. This variable is defined as

$$\mu_i = \frac{(\sigma \times \text{BR}_i)_{\text{exp.}}}{(\sigma \times \text{BR}_i)_{\text{SM.}}}, \tag{1.3}$$

where σ stands for the production cross section, BR for the branching ratio [1] and i represents the different decay channels. In the Run 1 of the LHC, with a centre-of-mass energy of 7 and 8 TeV, both ATLAS [12] and CMS [13] measured the signal strength of the Higgs boson and the combined measurement was found to be [3],

$$\hat{\mu}_{\text{ATLAS+CMS}} = 1.10 \pm 0.10. \tag{1.4}$$

For the 13 TeV configuration, one can also use the recent data given by the ATLAS [14] and CMS [15, 16] collaborations and combine them to obtain,

$$\hat{\mu}_{\text{ATLAS+CMS}} = 1.02 \pm 0.12. \tag{1.5}$$

And finally combining both 7, 8 and 13 TeV data,

$$\hat{\mu}_{\text{ATLAS+CMS}} = 1.07 \pm 0.08. \tag{1.6}$$

[1] In Eq. (1.3) the Narrow Width Approximation (NWA) is applied. This is possible since for a SM Higgs boson mass of order $\mathcal{O}(10^2)$ GeV the width is of order $\mathcal{O}(10^{-3})$ GeV.

These results are in agreement with the expected predictions from the SM Higgs boson. As the mass of the Higgs boson and the EW vev are the two physical parameters present in the theory, we can translate them into the Lagrangian parameters to obtain $\lambda = 0.26$ and $\mu = 88.4$ GeV. One important feature is that a detailed study of the stability of the vacuum of the Higgs potential for amass of $m_h = 125$ GeV, reveals that it is valid up to energies below the Planck scale, $m_P = 10^{19}$ GeV [17–19], that is the scale energy in which quantum effects of gravity are important. So it seems that the SM lives in a long-lived metastable vacuum.

With the Higgs boson discovery all the SM parameters are known. Far from being a pleasant situation in the understanding of Nature, there are several problems that arise both from the theoretically and the experimental point of view. Some of these problems could be found in the next list:

- ▷ **Dark Matter:** Astrophysical and cosmological observations provide conclusive evidence supporting the existence of a new kind of matter that would make the 27% of the Universe. This new matter does not emitt or absorb light and so it is called DM. None of the SM particles can account for the properties of the DM particle. It seems that the solution for this problem could be found in models that go beyond the SM (BSM). Different candidates have been proposed within particle physics (see for a review Ref. [20]). It is the aim of this thesis to address the DM problem and for that reason in Chapter 2 we review the current status.

- ▷ **Neutrinos Masses:** The observation of the fact that neutrinos oscillate into different flavours is a clear indication that they present non-vanishing masses. There are no renormalizable terms within the SM that can accommodate such mass terms for the neutrinos. Considering higher dimensional operators, the lowest one is the $d = 5$ Weinberg operator [21], $\mathcal{O}_5 = (\tilde{\bar{L}}\phi)(\tilde{\phi}^\dagger L)/\Lambda$. One of the realizations of the Weinberg operator is the well-known see-saw mechanism [22–25], where Majorana masses for the neutrinos are generated. In this case, in order to obtain the correct neutrino masses the scale of new physics goes up to energies of the order of the unification scale, *i.e.* $\Lambda \sim 10^{15}$ GeV.

- ▷ **Hierarchy Problem:** If the Standard Model is an effective theory, the Higgs boson mass would receive quantum corrections proportional to the cut-off scale of the theory. Apart from the EW scale the other scale in Nature is the Planck mass, $M_P \simeq 10^{19}$ GeV, so the loop corrections to the scalar Higgs mass are proportional to this cut-off scale. Given that the Higgs mass is m_h=125 GeV there must be a cancellation among the different mass terms of the Higgs to achieve this mass, so the fine tuning is certainly huge. This uncomfortable fact is alleviated if a new Physics scale appears around the TeV region.

- ▷ **Hierarchy in the Fermionic Sector:** Although the Higgs mechanism is able to explain how the fermionic sector of the SM acquires mass the hierarchy among them is still puzzling. There is no explanation in the SM to why the ratio between the Yukawa couplings of the top quark and the electron is $m_t/m_e \sim 10^6$ or any reason explaining the difference in masses among the different families in the quark and leptonic sector.

- ▷ **Strong CP Problem:** Although the QCD gauge sector of the SM allows for a CP-violating term of the form $\mathcal{L} \subset \frac{\theta}{32\pi^2} F_{\mu\nu}\tilde{F}^{\mu\nu}$, the experiments provides strinct bounds for the CP phase,

θ. Within the SM there is no reason for this term to be zero since it is not protected by any symmetry. The Peccei-Quinn mechanism could solve this problem invoking a spontaneous symmetry breaking driving this CP-violating term to small values.

- ▷ **Gravity:** Although it was completely successful explaining the origin of the strong and electroweak forces, the SM is not able to embrace a quantum description of gravity. This fact points into the direction that the SM is not the ultimate theory but an effective description of an ultraviolet one. Albeit, this problem arises only when reaching energy scales similar to the Planck scale. In this context, String Theory is presented as the best candidate to define a quantum description of gravity containing also the SM.

This Thesis focuses on the first problem in the list: Dark Matter. Nonetheless some of the other listed items are also addressed. Two different approaches are used in order to solve the DM problem: Simplified models, in which the DM sector is connected by a portal with the SM, and Supersymmetric models.

Dark Matter Portals

A common theoretical framework for DM studies is the hidden sector scenario. In its minimal form, visible matter resides in a sector of the theory that hosts the SM gauge and matter content (or simple extensions thereof), while DM resides in a hidden sector, with, maybe, its own gauge and matter content, but is otherwise neutral under the SM gauge group.

Within such a framework, several mechanisms have been proposed to mediate non-gravitational interactions between the different sectors, usually referred to as portals [26–41]. Among them, perhaps the most popular is the Higgs portal [26] in which the SM Higgs boson has renormalizable couplings to scalar fields of the hidden sector. This kind of construction could lead to important phenomenological consequences such as the contribution to the Higgs invisible width [42, 43]. However the present status of different experiments rule out the majority of the parameter region while the forthcoming ones are expected to explore the current allowed areas [44]. This pushes to extend the Higgs sector of the theory adding a new scalar state that is used as the portal to DM [45–48]. Another popular kind of portal is the one mediated by a Z'. In this scenario, a hidden sector communicates with the SM via a gauge boson, provided that the SM is enlarged with an extra abelian gauge group [49]. The phenomenology of these constructions is very rich, and ranges from colliders to direct and indirect searches of DM [50–56]. Both portals are within the most simple strategies to follow in order to connect the SM and the DM sectors. In Figure 1.2 the diagrams that drive this connection are illustrated.

If the mediator is a new scalar particle, for example a real singlet field, the way to connect the dark sector with the one of the SM is through the mixing with the SM Higgs boson. Such a mixing implies that all the couplings of the Higgs particle are rescaled according to the mixing angle between both scalar states. This angle is constrained by Higgs coupling measurements at the LHC, but also the electroweak precision observables (EWPO) could impose bounds since the Higgs contributions at loop level have an important role. Different works showed that this mixing angle is constrained to be less than $\sin^2\alpha < 0.1$ [3, 57–59]. However, this bound is very dependent

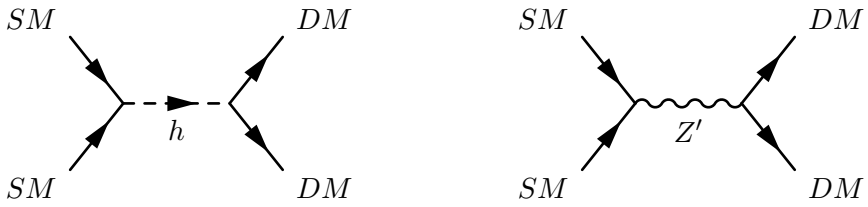

Figure 1.2: Schematic diagrams for a scalar, h, and a vector, Z', portals.

on the mass of the heavy state, that is the one considered as DM mediator. Using this limit it is possible to obtain regions in which the correct relic abundance for the DM particle is achieved and the constraints on DM searches are fulfilled for a large range of the heavy scalar state. One particular feature of this kind of models is the production of the mediator in the LHC and its subsequent decay. One interesting decay of the singlet state is the one into two SM Higgses. So, in order to study this process one must focus on the decay products of the di-Higgs system. There are several final states that are studied in the literature such as $b\bar{b}b\bar{b}$ [60,61], $b\bar{b}\gamma\gamma$ [62–64], $b\bar{b}\tau^+\tau^-$ [65] or $b\bar{b}W^+W^-$ [3].

If, on the contrary, the mediator is a vector boson, a new extended symmetry, usually a $U(1)$ is required. In principle, one can parametrise this model as the product of the SM gauge group times $U(1)_V^n$ of the visible sector, times $U(1)_h^m$ of the hidden sector, $SU(3)_c \times SU(2)_L \times U(1)_V^n \times U(1)_h^m$ [2], where n and m are the number of $U(1)$s in the visible and in the hidden sector respectively. All the vector bosons corresponding to the $U(1)$ will mix. However, here we consider only the two lightest states, one that is massless and it accounts for the massless vector boson of the hypercharge symmetry and the lightest massive Z' that plays the role of mediator between both SM and DM sectors. The rest of states are considered heavy enough to have a contribution in the DM or LHC phenomenology. This kind of constructions can be embedded into String Theory Type IIA models, where different gauge groups are formed by stack of branes that intersect [3]. The most important feature of this kind of construction is the fact that in a general model the DM interactions are isospin violating. That means that the Z' couplings to SM particles are different for both states within a fermionic doublet. That is the case for the up and down quarks that would present different couplings to the DM mediator. This property has a deep impact in Direct Detection experiments of DM. Those experiments study the elastic scattering of DM off nuclei, so experiments with different nuclei would obtain results that will not be the same. These properties can be contrasted against the recent results of DM direct detection experiments. This Z' can also be produced in the LHC and detected through its decay channels, in particular experimental searches are focused on jets, electrons and muons as final states. Using these data it is easy to constraint the allowed parameter space for this kind of construction. It is possible then to compare both kind of experimental bounds and study their complementarity.

[2] The hidden sector could also have a larger group multiplying the m $U(1)_h$, $U(1)_h^m \times G_h$

[3] String Theory is one of the best candidates to describe quantum gravity (for a review see Ref. [66]). In that sense the SM is an effective theory embedded into String Theory that acts as a ultraviolet complete theory.

Supersymmetric Dark Matter

Another theoretical reason to go beyond the SM is the hierarchy problem. There are two fundamental scales in Nature, the EW scale and the Planck scale. The SM is expected to be valid in scales of energy up to the Planck scale. However, if one studies the quantum corrections to the Higgs mass, it is found that these are proportional to a certain cut-off, Λ_{UV}, in the following way $\delta m_h^2 \propto \frac{y_t}{16\pi^2}\Lambda_{UV}^2$, where y_t is the top Yukawa coupling since it presents the larger corrections. This cut-off scale is the scale up to which the SM is valid, *i.e.* the Planck scale. Nevertheless, we observe that the Higgs mass is of the order of the EW scale that is by far, lower than the Planck mass, $v/m_{Pl} \sim 10^{-17}$. Thus, there should be some cancellations of the parameters to obtain the correct Higgs mass, which induces a high grade of fine-tuning. This is the so-called hierarchy problem. Furthermore, if the Higgs potential is studied for a Higgs mass of 125 GeV, it is found that the stability of this potential is excluded at the Planck scale [17–19]. Supersymmetry (SUSY) is a theory that introduces new particles that cancel the quantum corrections of the Higgs mass produced by the SM particles and provides a scale in between where the Higgs potential is still valid.

SUSY introduces a symmetry in which every SM particle has a partner with the same mass and quantum numbers but differing in the spin by one-half. This makes the quantum corrections on the Higgs mass cancel. However, these new particles have not been found, so this symmetry must be broken at some scale. When breaking that symmetry, the superpartners acquire masses greater than the SM ones and related with the breaking scale. So, in order to have finite quantum corrections to the Higgs mass and solve the hierarchy problem the SUSY scale must be of the order of 1 TeV.

Usually, in the construction of SUSY models a discrete symmetry, called R-parity, is imposed. The reason for it, is to avoid processes that have not been observed so far, such as the decay of the proton [67]. A consequence of this, is the fact that SUSY particles must be produced or annihilated in pairs, so the lightest SUSY particle (LSP) is stable. This particle could be a WIMP candidate for DM if it is neutral and has only EW interactions. In the minimal realization of a supersymmetric model, the well-known minimal supersymmetric standard model (MSSM), there are two candidates that fulfill these requirements: the lightest neutralino [68–71] and the sneutrino [72, 73]. The neutralino is a mixing between the neutral parts of the superpartners of the Higgses, the Higgsinos, and the superpartners of the neutral gauge bosons, Bino and Wino. The neutralino has been widely studied in the literature both in the MSSM (see for example Ref. [74]) and extensions of it [75–78]. The sneutrino is the superpartner of the neutrino. Although the left-handed sneutrino fulfils the conditions to be a WIMP candidate, due to the strength of the coupling with the Z boson, it generally has a large annihilation cross section (and therefore a too small relic density) or it would have been detected in direct detection experiments [79]. Such left-handed sneutrino is therefore not a viable candidate for DM.

Nonetheless, there are different motivations to consider extensions of the MSSM. One of the most important ones is the fact that the actual value for the Higgs mass, $m_h = 125$, GeV is larger than the tree-level value expected for the SM-like Higgs boson in the MSSM, that is $m_h < m_Z|\cos(2\beta)|$ [80, 81]. Thus, large quantum correction to the Higgs mass are expected requiring a heavy third generation of squarks and large stop mixing [82–85]. In that sense, it seems that

the MSSM does not *naturally* predict this mass. This problem could be alleviated if we add a new chiral superfield to the Higgs sector in the superpotential. If we do not require an extension of the gauge symmetry group only singlets and $SU(2)_L$ triplets with hypercharges $Y = 0, \pm 1$ are allowed. Those new states lead to a tree-level extra term for the Higgs mass of the form $m_h^2 = m_z^2 \cos^2 2\beta + \lambda^2 v^2 \sin^2 2\beta/2$.

The Next-to Minimal Supersymmetric Standard Model (NMSSM) is an extension of the MSSM where a $SU(2)_L$ singlet superfield, S, is introduced [86–88]. In this model a trilinear term of the form $\lambda S H_1 H_2$ is added to the superpotential so after radiative EW symmetry breaking takes place, the singlet field, S, acquires a vacuum expectation value, v_s, generating an effective μ parameter, $\mu = \lambda v_s$. This term alleviates the μ problem [89]. The introduction of S enlarges the spectrum and the parameter space and leads to a rich and attractive phenomenology (see e.g. Refs. [78, 90–92]), besides the fact of adding an extra tree-level term to the Higgs mass as pointed out before. The NMSSM can be also extended with a new superfield [93–96], N, enlarging the spectrum with two states, the RH-neutrinos and the RH-sneutrinos. The former ones induce a low-scale see-saw mechanism for the left-handed neutrinos providing them masses, whereas the latter ones could play the role of DM candidate [94, 96–100]. The presence of this two new states could lead to interesting signals at the LHC, such as displaced vertices and long-live charged particles due to the late decay of the RH-neutrino as it was hinted in Ref. [96].

Another possibility to enhance the tree-level mass of the Higgs boson is to enlarge the MSSM by including a $Y = 0$ triplet of $SU(2)_L$, known as the Triplet extended MSSM (TMSSM) [101, 102]. This extension extends the particle spectrum, in particular, a new extra state in both neutralino and chargino sectors appears. These new particles could influence significantly the phenomenology of the model, one example is the contribution at loop-level to Higgs observables such as the decay channels $h \to \gamma\gamma$ and $h \to Z\gamma$ [103, 104]. In this kind of models the lightest neutralino is a good and viable candidate to be the DM particle. In that sense, the lightest neutralino in the TMSSM could play this role. As a new component not present before in the MSSM is now in the game the DM phenomenology could be affected to this. The contribution of the triplino component mixes up with the other components to form the well known *well-tempered* [105] neutralino opening up a new viable DM parameter space.

Structure of the Thesis

This thesis is structured as follows. In Chapter 2, we review the Dark Matter problem in the Universe. First of all, DM evidence at different scales of the Universe is summarised showing that DM is ubiquitously present. Then, the characteristics for a particle to be a DM candidate are listed followed by the thermal history of the Universe and how the DM decoupled from the original plasma to give the relic density measured nowadays.

Part I is devoted to the idea of Dark Matter portals. Two examples of portals regarding the nature of the mediator are studied: the scalar and the vector portals. The former one is based on a singlet extension of the SM sector where the possibility of mixing with the Higgs particle is studied. This analysis is addressed in Chapter 3. Electroweak precision observables as well as LHC data are used to set constraints on the mixing angle between both scalar states. Then a new

possible decay channel for the heavy singlet into two SM Higgses is analysed, $H \to hh \to b\bar{b}WW$ where the W bosons decay leptonically, finding that it could be relevant for LHC Run II. Also the DM phenomenology using a scalar mediator is studied giving proofs that it is possible to fulfill all the relevant constraints in the interesting regions for the LHC. The latter portal, the vector one is then presented in Chapter 4. A general study is carried out within the framework of Type IIA String Theory models where a Z' is found to be the vector mediator. An isospin violating pattern in DM interactions is found and the consequences of that are studied. The DM phenomenology is contrasted with recent DM searches by direct detection experiments and also compared with LHC searches of Z' where a complementarity between both experimental results is found.

Part II focuses on the phenomenology of two SUSY models that are simple extensions of the MSSM. In Chapter 5, the NMSSM in which RH-neutrinos are added is studied. In this context the RH-sneutrino is a good candidate for DM and this possibility provides an interesting LHC phenomenology. In particular this fact induces to have long-lived particles that lead to displaced vertices and long-lived charged particles that could be traced in the LHC. We analyse these signals for Run I LHC and also we give prospects for Run II. In Chapter 6, we study another MSSM extension called TMSSM. We focus on the phenomenological implication of the new fermionic states introduced in the model. These affect directly to the DM sector since now we add a new component to the neutralino sector. Another feature of the new states is related to the Higgs phenomenology through the loop-induced decays $h \to \gamma\gamma$ and $h \to Z\gamma$. We study how imposing DM constraints could affect to the Higgs decay channels by constraining the neutralino and chargino sectors.

Finally, in Chapter 7 general conclusions from the work presented in this Thesis are derived.

2

Dark Matter

In the 19th century the observations of Uranus position presented slight differences with respect to those calculated using Newton's law. Two astronomers, Urbain Le Verrier and John Couch Adams computed independently the modifications of the Uranus orbit given the possibility that another planet remaining hidden was in our planetary system. That planet was Neptune and it was discovered in 1846, one year after it was predicted. A similar story occured with the binary system of Syrius. Friedrich Bessel pointed out that a hidden partner of Sirius A star was the responsible for its anomalous behaviour. In 1862 Sirius B was discovered solving that mystery. It seems that apparently when looking at the Universe one finds *hidden forces* that afterwards, turned out to be a planet, a star or any kind of matter that at that time was impossible to be observed.

Nowadays, we are facing a similar problem. In 1933 Fritz Zwicky found a special behaviour of the peculiar velocities in the Coma cluster [106]. In order to understand that situation, he assumed that a hidden kind of matter that was invisible to our observations. This topic was ignored until 1970's when Vera Rubin showed that the observed velocity of the rotation curve of a disc galaxy does not coincide with the one provided by Newton's laws [107]. To explain this discrepancy the presence of this hidden matter should be necessary. After Rubin's discovery, different observations in the Universe that needed to be explained in terms of hidden matter appeared. This kind of matter that it is present in the whole Universe, as it is not seen in any range of the electromagnetic spectrum it was called Dark Matter (DM).

The nature of the DM is not known, however some of its aspects could be inferred by observations. If DM was made of baryons it would be in strong disagreement with Big-Bang Nucleosynthesis and also with the small anisotropies present in the Cosmic Microwave Background (CMB). This could be a hint of the possibility of a non-baryonic particle as DM candidate. Several proposals have been introduced to become the DM. The most popular kind of particle is the well-known Weakly Interacting Massive Particle (WIMP) that is present in the majority of BSM models. The WIMP has the property that they easily reproduce the correct relic abundance of DM in the Universe for a wide range of their parameter space.

As the WIMPs have other interactions apart from the gravitational one they could eventually be detected through its interaction with ordinary matter. Direct detection searches are based on the DM scattering off nuclei [108]. Deep underground laboratories host low temperature detectors containing different elements sensitive to small perturbations caused by the interactions with DM

particles. Other way to search for DM is to observe its annihilation products as cosmic rays. Those cosmic rays could be detected with telescopes on the ground of the Earth or even in the outer space in satellites. This kind of search is named indirect detection. The last kind of search is the production of DM particles in colliders. As they have non-vanishing couplings with ordinary matter, DM particles could be produced in the collisions that take place in the accelerators. However, if produced, they will not leave any trace in the detectors of the experiment so one can only infer its presence through the missing transverse energy at the collisions.

In this chapter we will discuss fist the main evidences of DM in the Universe at different scales. Secondly we analyse the special case where the DM is made of particles and to be more precise it is also a WIMP.

2.1. Evidence

Starting with Zwicky's discover and following by Rubin's observations several evidences of the existence of DM have been found up to now. These evidences are found in astrophysical and cosmological contexts and they are related with its gravitational properties. In this section different evidences are shown for different scales in our Universe, starting with galactic observations, going through clusters of galaxies and ending with the large scale structure of the Universe.

Rotation Curves of Spiral Galaxies

Spiral galaxies are characterised by arms that conform its spiral shape. These arms have their origin in the bulk of the galaxy and they form a narrow disc[1], so the spiral galaxy lies on a plane. Other property of the spiral galaxies is the fact that they have a rotation movement. In principle the velocity rotation curve of a spiral galaxy depends on its radius. If we assume Newton's laws, the velocity of a point of the galaxy situated at a radius r can be written as

$$v(r) = \left(\frac{GM(r)}{r}\right)^{1/2}, \tag{2.1}$$

where $M(r)$ is the mass enclosed in a radius r. If one assumes that the majority of the luminous mass is situated in the bulk of the galaxy and when one gets out of the centre the luminous mass is constant with the radius, then the velocity of the objects have a dependency $v(r) \propto r^{1/2}$. That means that the velocity decreases when the radius r grows.

However it was first observed by Vera Rubin [107] that the measured value for the velocity of the rotation curve for large radius is constant. This measurement was made for the Andromeda galaxy but observations of other galaxies gave the same result (see e.g. [109, 110]). In order to explain this one can suppose that there is extra mass that is not visible that compose the most part of the galaxies. If this mass has a mass profile that grows linearly with the radius, $M(r) \propto r$, then for large radius the sum of the luminous and not-luminous matter contributions make the velocity rotation curve to be constant. One of the most famous examples is the barred spiral galaxy in

[1]The disc is narrow compared to the radius of the galaxy.

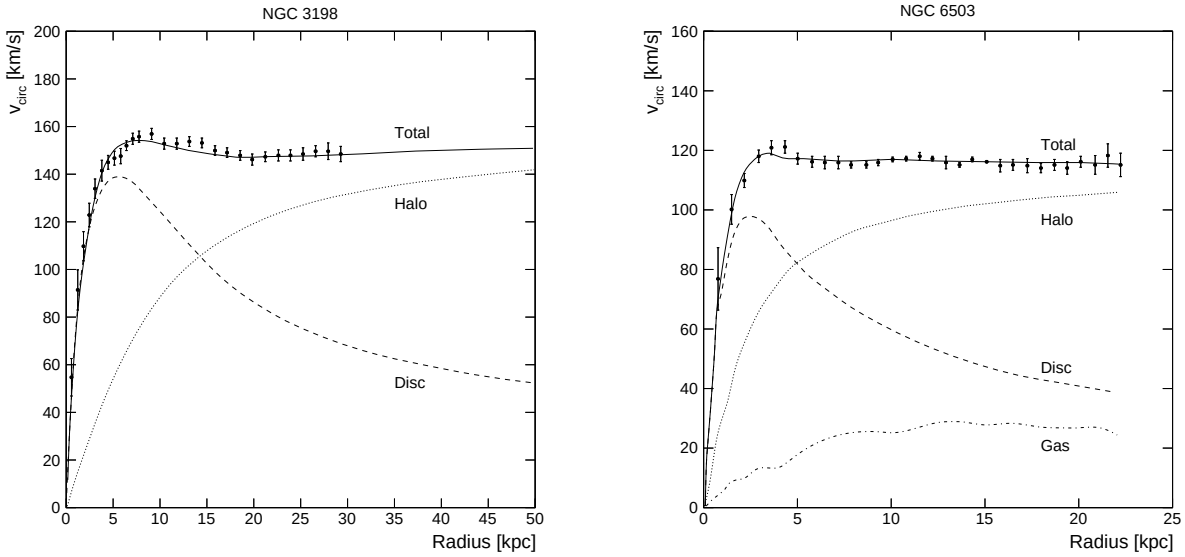

Figure 2.1: Results from the measurement of the velocity rotation curve of the galaxies NGC3198 [109] and NGC6503 [110]. In dotted points the measured data is shown with errors bars that take into account the uncertainties in the observation. Different contributions to the total rotation velocity are depicted. The halo contribution is shown as a dotted line, the disc one as a dashed line and the gas component as a dot-dashed curve, while the sum of all of them is drawn as a black solid curve.

the constellation Ursa Major. In the left panel of Figure 2.1 the results of the measurement of the velocity rotation curve for the NGC3198 [109] are shown. By means of black dot points the experimental results are shown with vertical error bars that account for the uncertainties in the measurement of the velocity. The disc contribution, i.e. the luminous matter, is depicted as a dashed line. It can be shown that it follows the gravitational laws of Newton and the velocity decreases as a function of $v \sim 1/\sqrt{r}$. If we add the DM contribution as an spherical halo with a mass density that grows linearly with the radius we obtain the dotted curve of Figure 2.1. If we add both contributions the result is the solid black line that fits the data with a very good precision. In the right panel of Figure 2.1 the measurements of the curve rotation for the galaxy NGC 6503 [110] are depicted, where despite being a different galaxy from NGC 3198 a similar behaviour is present. We can see the data points that fit the total curve that takes into account all the contributions from the galaxy including visible matter, gas and DM. This is a result that is inherent in every spiral galaxy supporting the idea of having a spherical halo of DM that in fact composes the majority of the mass of the galaxy.

Clusters of Galaxies

Galaxy clusters are gravitationally bound objects of approximately 2-10 Mpc diameter that could content from 50 to 1000 galaxies. They are the biggest structures that are bound gravitationally in the Universe and usually they have typical masses in the range of $10^{14} - 10^{15} M_{\odot}$, where $M_{\odot}$

means solar mass. They are characterised by large amounts of hot gas in the intracluster medium with temperatures oscillating between $2 - 15$ keV ($\sim 10^8 - 10^9$ K) depending on the total mass of the cluster. The hot gas emits X-rays that can be measured so astronomers are able to measure properties of the cluster. Within the DM history they are a key point since in the 1930s the astronomer Fritz Zwicky postulated firstly the possible presence of DM ("*Dichte dunkler Materie*" as he wrote [106]) in the Coma cluster.

▷ Bullet cluster

One of the most important evidence for DM at the cluster level is the Bullet cluster. The Bullet cluster (1E 0657-558) consists of two colliding cluster of galaxies composed of hot gas, dark matter and galaxies. These two cluster collided [111] modifying their structure. The galaxies resulted almost unaffected by the collision and were distributed in two groups. However, the hot gas that is the main component of baryonic matter in a cluster where found using X-ray techniques in the region in between of the two groups of galaxies. That could be interpret as if the hot gas from the two clusters underwent to a violent collision modifying their trajectory and reaching heavy temperatures so they emitted X-rays. In Figure 2.2 the different temperatures of the hot gas measured in X-rays are shown as a map of colours where the darker the colour is the colder the X-ray emission is. Furthermore using weak lensing techniques one can trace where the majority of the mass of the cluster is placed. The gravitational density contours are depicted in Figure 2.2 as green lines. Those contours coincide with the two groups formed by the galaxies. This behaviour is easily explained if one assumed that DM is composed by weak coupled particles that evaded the collision with the baryonic matter when the two clusters collided.

In order to solve the problem of the DM there exist attempts trying to modify the Newton's law of gravity to take into account all the astrophysical discrepancies. These theories, commonly known as Modified Newton Dynamics (MOND) were first proposed to find a solution to the galactic rotation curves [112]. The Bullet cluster plays a main role here since MOND theories cannot explain it. The observational fact of the Bullet cluster discard MOND theories supporting the hypothesis of the DM being a particle or a set of particles.

There are theories of modified gravity that claim to solve the anomalies in astrophysical observations usually attributed to the DM. However they failed when explaining the Bullet cluster while DM does. This is the reason why the Bullet cluster is one of the most important evidence of DM.

▷ Virial Theorem

Fritz Zwicky was the first scientist proposing the necessity of DM in order to explain the observational data of the Coma cluster. He made use of the virial theorem to compute the total mass of the cluster [106, 113]. If we assume that the cluster is in statistical equilibrium and we consider that the only important force is due to gravitational interactions we can use the virial theorem to relate the total kinetic energy of the system with its virial,

$$\overline{VIR} = -2\overline{T}, \tag{2.2}$$

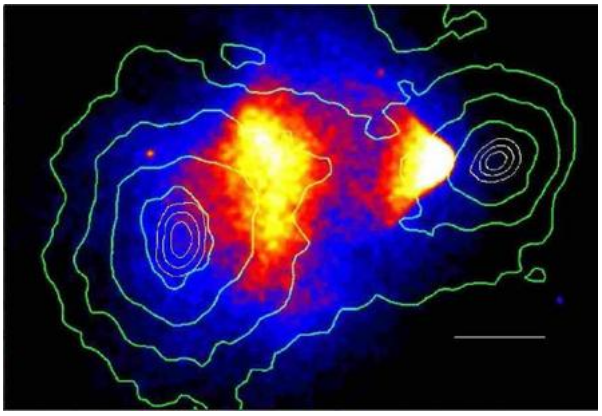

Figure 2.2: Gravitational contours (green) and different temperatures of the hot gas (colours) of the Bullet cluster. Figure taken from Ref. [111].

where VIR is the virial of the system and T is the sum of all the kinetic energies and the bar over the operators means averaged in time. The kinetic energy can be written as $2\overline{T} = M\overline{v^2}$ while the virial is $\overline{VIR} = -\frac{GM^2}{2}\overline{(1/r)}$ under the assumption that Newton's law is the one that describes the interactions in the cluster. So now the virial theorem provides the next relation for the mass of the cluster,

$$-\frac{GM^2}{2}\overline{(1/r)} = -M\overline{v^2} \rightarrow M = \frac{2\overline{v^2}}{G\overline{(1/r)}}. \tag{2.3}$$

Both $\overline{v^2}$ and $\overline{(1/r)}$ are quantities that are able to be measured by astronomers. Using this technique Zwicky found that the Coma cluster has approximately a mass of $M \simeq 4.5 \times 10^{10} M_{odot}$. The luminosity of the cluster was known to be approximately $L \simeq 8.5 \times 10^7 L_\odot$, where $L_\odot$ is the luminosity of the Sun, and given the fact that galaxies has a mass to light ration of order one this gives a prediction for the mass of the cluster $M \simeq 8.5 \times 10^7 M_\odot$. Zwicky was the first to point out this difference in mass of two orders of magnitude and to propose the possibility that some kind of non-visible matter was present in the cluster and take into account the difference in mass that was observed.

▷ Gravitational Lensing

The trajectory of the light emitted by a distant source can be modified if a mass distribution is placed between the source and the observer. This phenomenon is known as gravitational lensing. As galaxy clusters are massive objects they can bend the trajectories of the light produced by galaxies situated behind them. It is then possible to estimate the mass of the clusters by observing the geometrical distortions. If one compare those measurements with the ones done using the Virial Theorem or X-Rays an agreement between different methods. However if one computes the light to mass ratio they disagree in different orders of magnitude indicating the existence of a non-luminous kind of matter [114]. Gravitational lensing can be used also to find coherent distortions when

studying different sources of light. These measurements are used to find distributions of DM in clusters of galaxies as it is the case of the Bullet Cluster [115].

▷ X-Rays

The hot gas in the intracluster medium is characterised by very high temperatures that allow it to radiate X-rays. That emission can be measured so the baryonic matter can be traced within a cluster. It is usually assumed that the cluster is in hydrostatic equilibrium so the gravitational force and the pressure are balanced. Under this assumption one can use the X-ray spectral data to obtain the temperature and the density of the gas that together with the velocity distribution of the galaxies one can compute the binding mass of the cluster. Once the total mass of the cluster is known and given the density profiles of the baryonic matter (gas and galaxies) it is easy to extract the density profile of the DM. This was done for the case of the galaxy cluster Abell 665 placed in the constellation Ursa Major [116]. The authors extracted the different density profiles using X-ray spectral data and optical data that are,

$$\frac{\rho_{gal}(r)}{\rho_0} = \frac{750}{1 + (r/530\,\mathrm{kpc})^2}, \tag{2.4}$$

for the galaxy content,

$$\frac{\rho_{gas}(r)}{\rho_0} = \frac{1500}{1 + (r/380\,\mathrm{kpc})^2}, \tag{2.5}$$

for the gas content and finally,

$$\frac{\rho_{tot}(r)}{\rho_0} = \frac{19700}{1 + (r/298\,\mathrm{kpc})^2}, \tag{2.6}$$

for the total cluster. Here r is the radius of the galaxy cluster and ρ is the critical density that is used for normalization. The density profile of DM can be found substracting the visible matter to the total mass density,

$$\rho_{DM} = \rho_{tot} - \rho_{gal} - \rho_{gas}. \tag{2.7}$$

It was found that the DM density was very important since the majority of the mass in the cluster comes from it. It was also shown that the DM density profile peaks at the centre while it decreases when the radius growns even coming to the point where the visible matter is greater than the DM. This is shown in Figure 2.3 where the ratios of the DM density profile with all the different combinations of visible density profiles from the galaxy cluster Abell 665 are plotted. The solid black line depicts the ratio between the DM density profile and the whole visible sector, where the contributions of galaxies and hot gas are included, by means of a dotted line the ration between the DM and the galaxies density profiles are shown. The dashed line represents the ration between the density profiles of the DM and the hot gas of the cluster. It is clear from Figure 2.3 that the DM is mostly placed in the centre of the galaxy cluster and it decreases rapidly so when it reaches the horizontal blue line that corresponds to ratio 1, the visible matter content exceeds the DM one. From this kind of measurements it was clear that only about the 10% of the mass of the clusters was composed of galaxies, and the greatest contribution comes from the DM sector.

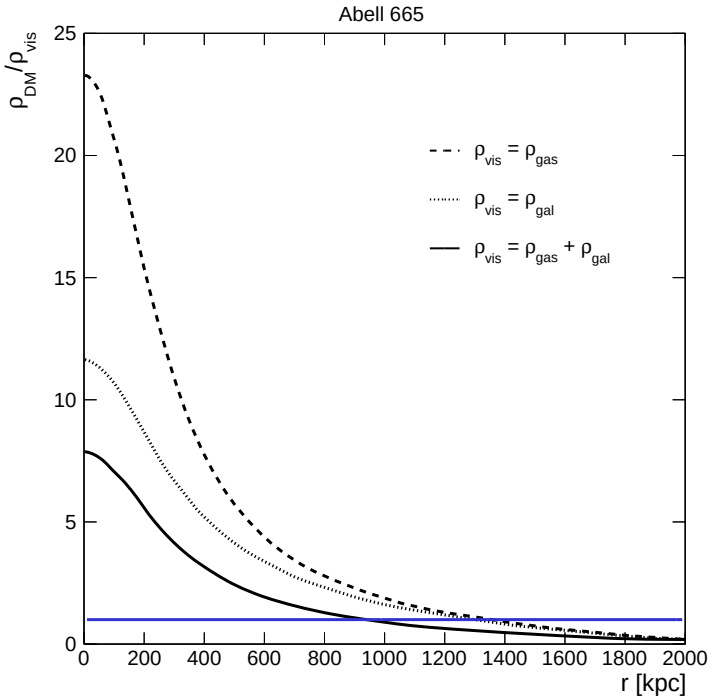

Figure 2.3: Ratios between the DM and the visible matter density mass profiles of the galaxy cluster Abell 665 [116]. The ration between the DM and the hot gas (galaxies) density profiles is shown as a dashed (dotted) line, while the ratio between the DM and the whole visible sector is depicted as a solid black line. The horizontal blue line is set to 1 in such a way that if one of the other line cross it the ratios between density profiles are 1, so the densities of DM and the visible sector are the same.

CMB

In the Early Universe, matter and radiation formed a plasma in thermal equilibrium due to the collisions were efficient enough. When the Universe was cooling down the photons lose energy so they started not to interact with matter. At that point, ($\sim$ 380000 years after the Big Bang) photons expanded across the Universe unaffected by the matter. However as DM was also present in the primordial plasma the differences in the density of DM in the Universe when everything was in thermal equilibrium left an imprint in the density of photons that later propagated. The reason is that differences in the DM density profile made the ordinary matter by gravitation to group around the peaks where more DM population were present. As the photons were in thermal equilibrium with matter when the photons decoupled from the primordial plasma and expanded across the Universe they followed the density profiles that the DM had at that point. The image of these photons that we can measure nowadays it is named the Cosmic Microwave Background (CMB). This peculiar phenomenon has been measured several times by different telescopes every time with more precision. The last image we have from the CMB is shown in Figure 2.4 and it was taken by the Planck satellite. Figure 2.4 shows the CMB measured temperature. The mean

temperature is approximately of $T = 2.7$ K, however there have been found anisotropies in the temperature depending on the direction of the Universe they measure. Those anisotropies are shown in Figure 2.4 as different colours, points with colour that goes to the red are hotter than those that have colour going to the blue. It is important to note that the difference in temperature from the hottest point to the coldest one is of the order of $\mathcal{O}(10^{-5})$ K. These anisotropies are a consequence of the distribution of DM in the Early Universe, it is important to know that those points with a high concentration of DM were the seeds of the large scale structures of the Universe. Another important point of the CMB is the high and impressive agreement with the well-known

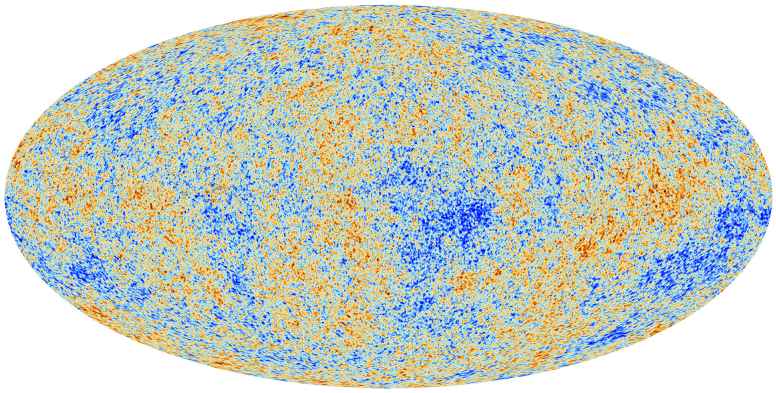

Figure 2.4: Map of the temperature anisotropies of the CMB. The blue (red) points accounts for those regions where the temperature is 500 μK lower (higher) than the average temperature of the CMB, $T = 2.7$K. Figure taken from Ref. [117].

ΛCDM paradigm. The ΛCDM model is a consistent model of the content of the Universe considering that it is dominated by dark energy and it has a large component of DM that is the predominant component in the matter sector. Those anisotropies can be parametrized as a function of spherical harmonics ($Y_{l,m}(\theta, \phi)$)

$$\frac{\delta T}{T} = \sum_{l=2}^{\infty} \sum_{m=-l}^{+l} a_{lm} Y_{lm}(\theta, \phi), \tag{2.8}$$

where a_{lm} are coefficients related with the power spectrum that is,

$$\frac{l(l+1)}{2\pi} C_l. \tag{2.9}$$

The relation between the power spectrum and the coefficient is that C_l is the variance of a_{lm}, $C_l = \langle |a_{lm}|^2 \rangle$. This is possible because all the measurements have shown that the anisotropies are Gaussian-like located. In Figure 2.5 the temperature anisotropies are shown as a function of the multipole moment, l, directly related with the measured angle by $l \simeq 180°/\theta$. The points are the data obtained by the Planck satellite with error bars that take into account the uncertainties in the measurement. The continuous line is the best fit assuming a ΛCDM scenario. The first point to note is the good agreement between the observation data and the prediction of the model that could reproduce all the peaks that appear in the plot. The worst agreement is found in the region

with low multipole moment, l, however the observational uncertainties are important in this case and taken them into account the prediction is still valid. The relevant physical information that can be extracted from Figure 2.5 are the position of the peaks. They reveals the position where in the photon decoupling era the large amounts of DM were. From these peaks it is possible to obtain the different amounts of constituents of the Universe. The last results obtained by the Planck satellite [118] determined the densities of the DM, the baryonic matter and the dark energy,

$$\Omega_c h^2 = 0.1187 \pm 0.0017, \quad \Omega_b h^2 = 0.02214 \pm 0.00024, \quad \Omega_\Lambda = 0.692 \pm 0.010. \tag{2.10}$$

Here Ω_i means the density of each of the components of the Universe, ρ_i, divided by the critical density ρ_c. From the data we can extract that the matter content of the Universe is dominated by the DM (84%) as it was suggested by the different astrophysical evidences. Furthermore the matter content of the Universe is small if we compare it with the dark energy content that is 68%.

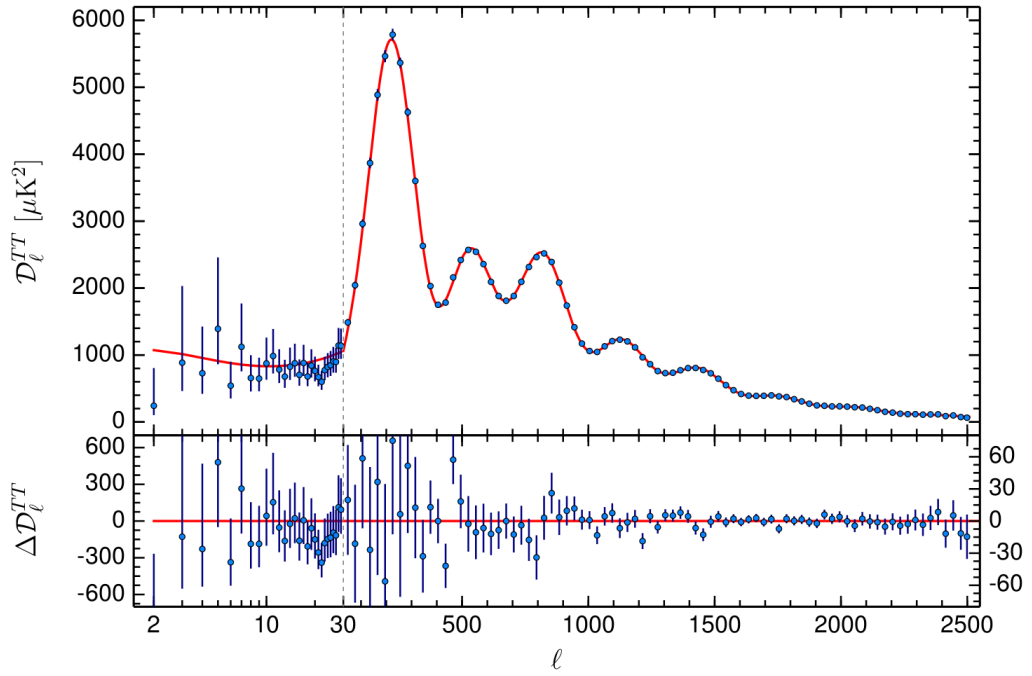

Figure 2.5: Temperature power spectrum, $\mathcal{D}_l = l(l+1)C_l/2\pi$, as a function of the multipole, l. Blue points accounts for the data obtained by Planck satellite [118] with error bars while the red line is the best fit of the temperature angular power spectrum of the ΛCDM model.

2.2. Particle Dark Matter: WIMPs

In Section 2.1 it was shown that there is an important amount of evidence situating DM as the principal component of the matter of the Universe. However the nature of the DM is still

unknown. One of the first proposals to solve this problem was the possibility that baryonic matter in terms of massive objects like black holes or neutron stars could be the DM. Those objects were called MAssive Compact Halo Objects (MACHOs) and in principle they would not have been detected because of light suppression travelling through intergalactic medium. However MACHOs are totally in disagreement with the total baryonic production in the Big Bang Nucleosynthesis [119]. Furthermore there is evidence such as the Bullet cluster [111] that, as we said above, points to the direction of a particle-like DM candidate instead of a sizeable object. If such a particle exists and plays the role for the DM candidate then it should fulfil a list of requirements:

- ▷ It must not interact with photons. Otherwise we could have seen it in astrophysical observations. Nevertheless it could have other kind of interactions. Furthermore colour charge for the DM particle is also disfavoured since coloured objects hadronise and they could be observed.

- ▷ It must be cold. This means that at the moment of decoupling and the DM particles behave as non-relativistic particles. Cold DM is favoured by the large scale structure of the Universe since the large structures are formed from smaller structure that were conceived first. Numeric simulations of cold DM in the Universe are in agreement with a wide range of observations. On the contrary hot DM, relativistic particles such as the neutrinos, predict formation of large structures before the smaller ones that is in contradiction with the data. There is also the possibility to the DM particle to be warm. Cold DM suffers from different problems, one of this is the missing satellites problem [120] that is related with the fact that N-body simulations predict a higher number of cold DM subhaloes than the number of satellites known in the Local Group. Warm DM could evade this problem since N-body simulations suggest that the number of satellites for galaxies like the Milky Way is comparable as the one observed imposing also a bound on the mass of the warm DM less than 1.5 keV [121].

- ▷ It must be stable. DM particle must be stable, otherwise we would not have observed it relic density nowadays. This requirement can be also interpreted as if the DM particle could have a lifetime of the age of the Universe or greater, that is $\tau \sim 13 \times 10^9$ years.

- ▷ It must agree with experimental constraints and observations. There are different experimental constraints that set bounds on the phenomenological properties of the DM particle. One of the most important is that it must fulfil the correct relic density or at least have less than the one observed by Planck [118]. It must also agree with other experiments such as the direct detection experiments, indirect detection experiments or collider searches.

Those properties suggest that one has to enlarge the SM content in order to find a particle that fulfils all the requirements. Within the SM only the neutrinos have the majority of the requirements, however they are hot particles so they are in contradiction with observations of the large scale structure of the Universe and they are so light that they cannot account for the relic density of the DM. A large plethora of models containing DM candidates that go beyond the SM are present in the literature.

Cosmological Context

At large scales we know by different observational experiments that our Universe follows the Cosmological Principle, i.e. the Universe is isotropic and homogeneous. These considerations are in principle valid for the space components while for the temporal coordinate may be not the case. Thus the geometry of our Universe may be thought to be $\mathbb{R} \times \Sigma$, where $\mathbb{R}$ represents the temporal coordinate and Σ are 3-dimensional hypersurfaces at constant time that take into account the isotropic and homogeneous spatial sections of the Universe. Those 3-dimensional hypersurfaces have 6 generators, 3 for translations and 3 for rotations, that is the maximum of Killing vectors for a 3-dimensional space, so Σ must be maximally symmetric. One kind of metric that fulfils these considerations is the following,

$$ds^2 = dt^2 - a^2(t)\left(\frac{dr^2}{1-kr^2} + r^2 d\theta^2 + r^2 \sin^2\theta d\phi^2\right), \tag{2.11}$$

where r, θ, ϕ are the spherical coordinates and $a(t)$ is the scale factor of the Universe and determines the expansion of the Universe. The parameter k is related with the curvature of the Universe and can take three different values:

- $k = +1$: Positive Curvature $\rightarrow$ Closed Universe,
- $k = 0$: Null Curvature $\rightarrow$ Flat Universe,
- $k = -1$: Negative Curvature $\rightarrow$ Open Universe.

This kind of metric is called the Friedmann-Robertson-Walker (FRW) metric and it is important to note that this metric is valid when the observer is in the comoving frame. The different objects of the Universe are not really in that frame since they have peculiar velocities due to gravitational interactions. That is the case of the Earth, or even our Galaxy moving to the Virgo attractor.

After studying the geometry of the Universe it is time to study the matter and the energy content. As the Universe is homogeneous and isotropic we consider a perfect fluid which energy-momentum tensor is given by

$$T^{\mu\nu} = pg^{\mu\nu} + (p+\rho)u^\mu u^\nu, \tag{2.12}$$

where p is the pressure and ρ is the energy density. For comoving coordinates we have

$$T^\mu_\nu = \mathrm{diag}(\rho, -\vec{p}), \quad T^\mu_\mu = \rho + 3p. \tag{2.13}$$

The conservation of the energy-momentum tensor leads to

$$\dot{\rho} + 3\frac{\dot{a}}{a}(\rho + p) = 0, \tag{2.14}$$

where the dot over a variable means its time derivative. This equation can be written as $d(\rho a) = pda$, so the pressure and the density are related by $p = \omega\rho$, where ω is a time-independent constant and it is different for every fluid it represents. For the case of radiation $\omega = 1/3$, while for matter we

have $\omega = 0$ and finally for dark energy $p = -\rho$. Once we have how matter and energy is represented in the Universe one can solve the Einstein equations,

$$R_{\mu\nu} - \frac{1}{2}Rg_{\mu\nu} = 8\pi G\left(T_{\mu\nu} + \Lambda g_{\mu\nu}\right), \tag{2.15}$$

where Λ is a cosmological constant. The solutions are

$$\left(\frac{\dot{a}}{a}\right)^2 = \frac{8\pi G}{3}\rho + \frac{\Lambda}{3} - \frac{k}{a^2}, \tag{2.16}$$

$$\frac{\ddot{a}}{a} = -\frac{4\pi G}{3}(\rho + 3p) + \frac{\Lambda}{3}. \tag{2.17}$$

In order to simplify from now on we call $H = \dot{a}/a$, that is the Hubble parameter. These two equations determined the evolution of the Universe, Eq. (2.16) tells us about the expansion rate of the Universe while Eq. (2.17) determines whether this expansion is accelerated or decelerated.

Using Eq. (2.16) one can define the critical density, ρ_c as the total density in a flat spacetime,

$$\rho_c = \frac{3H^2}{8\pi G}, \tag{2.18}$$

where we have obtained this expression supposing a flat Universe, $k = 0$, and neglecting the term of dark energy $\Lambda = 0$. The critical density today is approximately $\rho_c = 10^{-5}h^2$ GeV cm^{-3}, here h is the reduced Hubble constant defined by $H = 100h$km s^{-1}Mpc^{-1}, and it has a numerical value of $h = 0.673$ according with the observations of the Planck satellite [118]. Usually it is more convenient to express the densities of the different components of the Universe (matter and radiation) as its density over the critical density, $\Omega_i = \rho_i/\rho_c$ (see Section 2.1). For the specific cases of the dark energy and the curvature we have $\Omega_\Lambda = \Lambda/3H^2$ and $\Omega_k = -k/a^2H^2$. Using these different definitions of the densities we can rewrite Eq. (2.16) as

$$\Omega_{rad} + \Omega_m + \Omega_\Lambda = 1 - \Omega_k. \tag{2.19}$$

These density values are able to be measured by observational experiments. According to the Planck satellite [118] we could know that the different densities are,

$$\Omega_\Lambda = 0.685^{+0.018}_{-0.016}, \quad \Omega_m = 0.315^{+0.016}_{0.018}, \quad \Omega_k = -0.0005^{+0.0065}_{-0.0066}. \tag{2.20}$$

According with the data the curvature density is almost negligible. Using Eq. (2.19) we can obtain the radiation density nowadays that results to be of the order of $\mathcal{O}(10^{-4})$, which means that radiation does not play a role in the present configuration of the Universe, being the dominating elements the dark energy and the matter content.

Freeze-out

The Early Universe can be thought as a hot plasma of particles in thermal equilibrium where they were interacting to each other. However the Universe was expanding so the temperature of

the plasma decreased accordingly. In order to describe the evolution of the different particles in the thermal bath we must be able to describe the distribution function of a particle in thermal equilibrium at a temperature T. Using the Cosmological Principle we can reduce the degrees of freedom of the distribution function and make it function only of the time and energy, $f(\mathbf{x}, \mathbf{p}) = f(t, E)$, where $\mathbf{x}$ and $\mathbf{p}$ are 4-vectors for the time-position and energy-momentum. Depending on the nature of the particle the distribution function is

$$f_i(t, E_i) = \left(\exp(E_i - \mu_i/T) \pm 1\right)^{-1}, \tag{2.21}$$

where E_i is the energy of the particle and μ_i is the chemical potential. The sign in the distribution is positive for a Fermi-Dirac particle (fermion) and negative for a Bose-Einstein particle (boson). For the case we are considering if the particles are not relativistic and they are not under the conditions to form a Bose-Einstein condensate or Fermi degeneration we can safely use the Boltzmann statistics for all the particles, that is

$$f_i(t, E_i) = \exp\left(-(E_i - \mu_i)/T\right). \tag{2.22}$$

In the Early Universe the WIMPs, χ, were annihilating and being produced in reactions within the plasma together with different particles of the SM. When the temperature of the plasma was high enough[2] the production of pairs of DM and the annihilation of DM into SM particles were efficient since the particles had enough energy to create them.

We can define the annihilation rate, Γ_{ann}, as the rate of annihilation of DM particles,

$$\Gamma_{ann} = n_{eq}\langle\sigma v\rangle, \tag{2.23}$$

where σ is the WIMP annihilation cross section, v is the relative velocity of the DM particles that annihilate and n_eq is the number density of WIMPS in chemical equilibrium in the plasma, that in the approximation of a Boltzmann distribution is given by

$$n_{eq} = g_\chi \left(\frac{T m_\chi}{2\pi}\right)^{3/2} e^{-m_\chi/T}, \tag{2.24}$$

where g_χ are the internal degrees of freedom of χ. As the Universe expanded the temperature of the plasma decreased. That makes more difficult for the particle of the plasma to create WIMPs since it is exponentially suppressed as is indicated in Eq. (2.24), so only particles that are in the tail of the distribution have enough energy to produce DM particles. The expansion of the Universe also decreased the number density of particles, therefore if the annihilation rate is greater than the Hubble rate, $\Gamma > H$ the WIMPs remain in the plasma, however when it becomes smaller, $\Gamma < H$ the DM particles are not produced since they are chemically decoupled. After the decoupling the total number of WIMPs is constant for a comoving volume until today.

In general we can define the number density of a particle χ with a distribution function $f_\chi(t, E_\chi)$ as

$$n_\chi = \frac{g_\chi}{(2\pi)^3} \int d^3\vec{p} f(t, E_\chi). \tag{2.25}$$

[2]High enough temperature in this context means that the temperature is much higher than the WIMP mass, $T \gg m_\chi$

The temporal evolution of the number of particles is given by the Liouville operator $\mathbb{L}[f]$,

$$\mathbb{L} = \frac{d}{d\tau} = \frac{\partial x^\mu}{\partial \tau}\frac{\partial}{\partial x^\mu} + \frac{\partial p^\mu}{\partial \tau}\frac{\partial}{\partial p^\mu} = p^\mu \frac{\partial}{\partial x^\mu} - \Gamma^\mu_{\sigma\rho} p^\sigma p^\rho \frac{\partial}{\partial p^\mu}, \tag{2.26}$$

where $\Gamma^\mu_{\sigma\rho}$ is the afin connection. Given the fact that we are working in a FRW metric the Liouville operator reads,

$$\mathbb{L} = E\frac{\partial}{\partial t} - H|\vec{p}|^2 \frac{\partial}{\partial E}. \tag{2.27}$$

The evolution of the number density then,

$$\frac{g_\chi}{(2\pi)^3}\int \frac{d^3\vec{p}}{E}\mathbb{L}[f(t, E_\chi)] = \frac{dn}{dt} + 3Hn. \tag{2.28}$$

If we define the Yield as $Y = n/s$ where s is the entropy density given by $s = \frac{2\pi^2 g_*^s T^3}{45}$ where g_*^s parametrises the number of relativistic degrees of freedom, we can compute the temporal evolution of Y,

$$\frac{dY}{dt} = \frac{1}{s}\left(\frac{dn}{dt} + 3Hn\right). \tag{2.29}$$

so the number density evolution and the temporal evolution of the yield are related.

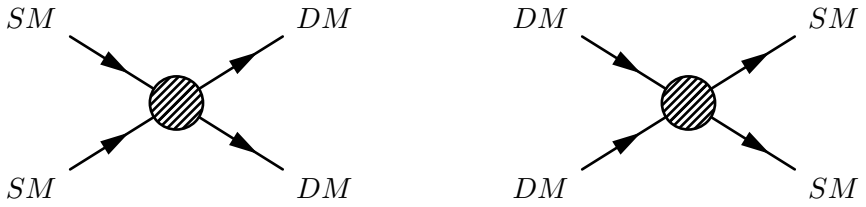

Figure 2.6: Processes that take place in the plasma of the early Universe where SM particles and DM particles are created and annihilated.

We have seen that the Liouville operator gives the temporal evolution of the number density. This evolution is also connected with the rate of particle collisions produced in the plasma. We could define a collision operator in such a way that it is related with the Liouville operator in the following way,

$$\frac{g_\chi}{(2\pi)^3}\int \frac{d^3\vec{p}}{E}\mathbb{L}[f(t, E_\chi)] = \frac{g_\chi}{(2\pi)^3}\int \frac{d^3\vec{p}}{E}\mathbb{C}[f(t, E_\chi)], \tag{2.30}$$

where $\mathbb{C}[f(t, E_\chi)]$ is the collision operator and it is defined for a reaction of the type $\chi_i\bar{\chi}_j \longleftrightarrow AB$ (see Figure 2.6) as

$$\begin{aligned}\frac{g_\chi}{(2\pi)^3}\int \frac{d^3\vec{p}}{E}\mathbb{C}[f(t, E_\chi)] = -\int d\Pi_i d\Pi_j d\Pi_a d\Pi_b (2\pi)^4\delta^4(p_i + p_j - p_a - p_b)\times \\ \left[|\overline{\mathcal{M}_{ij\to ab}}|^2 f_i f_j(1 \pm f_a)(1 \pm f_b) - |\overline{\mathcal{M}_{ab\to ij}}|^2 f_a f_b(1 \pm f_i)(1 \pm f_j)\right].\end{aligned} \tag{2.31}$$

Here $d\Pi_i$ is the Lorentz invariant phase space that reads,

$$d\Pi_i \equiv \frac{g_i}{(2\pi)^3}\frac{d^3\vec{p}}{2E_i}, \tag{2.32}$$

and $|\overline{\mathcal{M}_{ij\to ab}}|^2$ is the squared matrix element summed over the final states and averaged over the initial states. For the sake of simplicity we assume the following points:

1. CP is conserved in the WIMPs creation and annihilation processes. This assumption implies that $|\overline{\mathcal{M}_{ij\to ab}}|^2 = |\overline{\mathcal{M}_{ab\to ij}}|^2 = |\overline{\mathcal{M}}|^2$.

2. As we have assume a Maxwell-Boltzmann statistics for the particles in the plasma the factors $(1 \pm f_i) \simeq 1$ for all the species in kinetic equilibrium.

3. The particles in the plasma are in thermal equilibrium, in that sense $f_{a,b} = f^{eq}_{a,b} \simeq e^{-E_{a,b}/T}$.

4. Energy conservation reads $E_i + E_j = E_a + E_b$, this implies the next relation for the distribution function of the WIMPs and the particles in the plasma, $f_i f_j = \exp\left(-(E_i + E_j)/T\right) = \exp\left(-(E_a + E_b)/T\right) = f_a f_b$.

These assumptions simplify the computations, now the collision operator reads,

$$\frac{g_\chi}{(2\pi)^3}\int \frac{d^3\vec{p}}{E}\mathbb{C}[f(t,E_\chi)] = -\int d\Pi_i d\Pi_j d\Pi_a d\Pi_b (2\pi)^4 \times \\ \delta^4(p_i + p_j - p_a - p_b)|\overline{\mathcal{M}}|^2[f_i f_j - f_i^{eq} f_j^{eq}]. \tag{2.33}$$

Using the relation for the cross section,

$$d\sigma F = |\overline{\mathcal{M}}|^2 (2\pi)^4 \delta^4(p_i + p_j - p_a - p_b)\frac{d^3\vec{p}}{(2\pi)^3 2E_a}\frac{d^3\vec{p}}{(2\pi)^3 E_b}, \tag{2.34}$$

where $F = [(p_i \cdot p_j)^2 - m_i^2 m_j^2]^{1/2} = v 2E_i 2E_j$, with v the relative velocity between the WIMPs. Including this on Eq. (2.33) we get

$$\frac{g_\chi}{(2\pi)^3}\int \frac{d^3\vec{p}}{E}\mathbb{C}[f(t,E_\chi)] = -\langle\sigma v\rangle(n^2 - n_{eq}^2), \tag{2.35}$$

where we have used the thermal averaged cross section times velocity,

$$\langle\sigma v\rangle = \frac{\int \sigma v \frac{g_i}{(2\pi)^3} f_i d^3\vec{p}_i \frac{g_j}{(2\pi)^3} f_j d^3\vec{p}_j}{\int \frac{g_i}{(2\pi)^3} f_i d^3\vec{p}_i \frac{g_j}{(2\pi)^3} f_j d^3\vec{p}_j}. \tag{2.36}$$

Now Boltzmann equation reads

$$s\frac{dY}{dt} = \frac{dn}{dt} + 3Hn = -\langle\sigma v\rangle(n^2 - n_{eq}^2), \tag{2.37}$$

that can be rewritten in terms of the yield as

$$\frac{dY}{dt} = -s\langle\sigma v\rangle(Y^2 - Y_{eq}^2), \tag{2.38}$$

It is convenient to define a new variable $x \equiv m/T$ since the interactions are very dependent on the temperature so now we can write Eq. eq:yield as

$$\frac{dY}{dx} = -\sqrt{\frac{\pi}{45G}}\frac{g_*^{1/2} m_\chi}{x^2}[Y^2 - Y_{eq}^2], \tag{2.39}$$

where G is the gravitational constant.

When the temperature of the plasma becomes smaller than the mass of the DM particle, $T < m_{DM}$ the particles in the plasma cannot create WIMPs because they are exponentially suppressed, so the DM particles can only annihilate. However when the expansion of the Universe starts to be greater than the DM annihilation rate, $H > \Gamma$, the WIMPs cannot annihilate and its number density over the entropy density is constant, that makes the yield of DM particles to become constant up to now. This mechanism is known as *freeze-out* since the DM particles seem to be frozen from the time they decoupled from the plasma.[3] The constant value of the yield when it freezes-out is given by

$$Y_0 \approx \sqrt{\frac{45G}{g_*\pi}}\frac{x_F}{m_\chi}\frac{1}{\langle\sigma v\rangle}, \tag{2.40}$$

where $x_F = m_{DM}/T_F$, and T_F is the temperature at which the freeze-out takes place. Usually for a WIMP in the range of masses of 1-100 GeV the typical value for the freeze-out is $x_F \simeq 20$. The evolution of the yield in time, given by Eq. (2.39), is shown in Figure 2.7. The black solid lines represent the yield for DM particles. When the temperature drops (x grows) there is a point where the DM particles decoupled for some point in $x \simeq 20$. The value of the yield at the moment of decoupling depends on the thermal average cross section times the velocity. For larger values of the cross section the WIMPs remain in thermal equilibrium with the plasma longer. Given the fact that Y_0 is constant from the decoupling time up to now, the relic density is computed as

$$\Omega_\chi h^2 = \frac{\rho_\chi h^2}{\rho_c} = \frac{m_\chi n_\chi h^2}{\rho_c} = m_\chi s_0 \frac{Y_0 h^2}{\rho_c}. \tag{2.41}$$

If we assume that the DM mass is of the order of the electroweak scale ($\sim$ 100 GeV) the relic density can be computed to be

$$\Omega_\chi h^2 \approx \frac{3\times 10^{-27}\,\mathrm{cm}^3/\mathrm{s}}{\langle\sigma v\rangle}. \tag{2.42}$$

As we know by cosmological observations the relic density value nowadays is approximately $\Omega_\chi h^2 \approx 10^1$, so we get for a weak scale WIMP a thermal averaged cross section of the order $\langle\sigma v\rangle \sim 10^{-26}\,\mathrm{cm}^3/\mathrm{s}$ that is the magnitude of the weak scale interactions. This coincidence that relates the weak scale with the current relic density suggests that DM may not be too far from the TeV scale.

[3] All the quantities referred to this time are labelled with a subscript F.

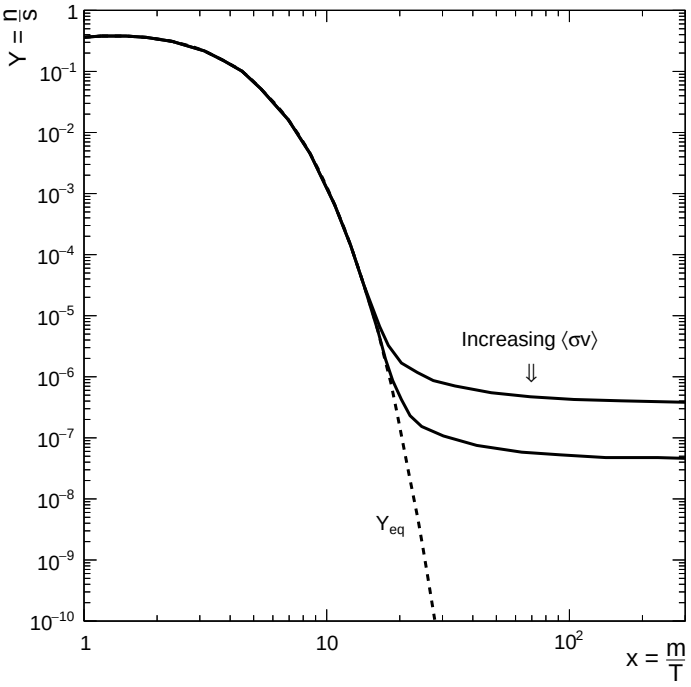

Figure 2.7: Yield evolution for DM particles with different $\langle \sigma v \rangle$ (solid black line) and yield evolution of the non-relativistic species in thermal equilibrium with the plasma (dashed black line). For larger $\langle \sigma v \rangle$ the relic density today is smaller while the time at which the freeze-out takes place occurs later. The yield for particles in thermal equilibrium with the plasma drops dramatically leaving to a negligible amount of them nowadays.

2.3. Dark Matter searches

Dark Matter particle must interact with the SM particles in order to achieve the correct relic density that is observed today. Using these interactions with ordinary matter one can try to obtain signals or even produce it in experiments. There are different methods to search for DM depending on the kind of diagram we use to detect it. Figure 2.8 shows the different diagrams involving SM and DM particles and to which search correspond. There are three different kind of searches. The first one is Direct Detection (DD). This method uses the interaction of DM particles with heavy nuclei in underground laboratories. The second way to search for DM is Indirect Detection (ID) experiments. As DM is present in the Universe there is the possibility of two DM particles to annihilate so the aim of the ID experiments is to look for the possible annihilation products in terms of cosmic rays. The last possibility is to produce DM particles directly in a collider. As they have interaction with SM particles it is possible in principle to produce them in particle accelerators, however as they are neutral they do not leave any trace in the detector, so it must be accompanied by a detectable particle in order to be *seen* as missing transverse energy in the detectors. In this Section we review the three different kind of searches and their status nowadays.

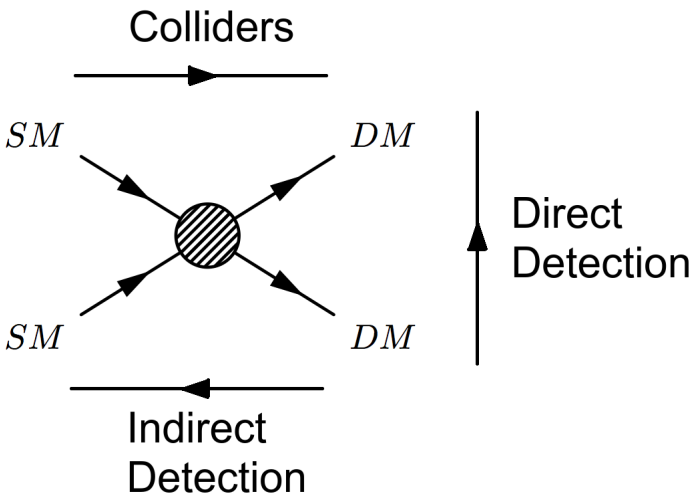

Figure 2.8: Diagram containing all the possible searches for dark matter. Direct detection experiments read the diagram from the bottom to the top, since they look for a elastic scattering of dark matter particle off nuclei. Indirect detection experiments are based on the diagram going from the right to the left side, they search for dark matter annihilation products. The last one is the colliders search, they study how the SM particles could produce DM particles so the diagram applied is the one read from left to right.

2.3.1. Direct Detection

Dark Matter particles are going through the Earth with a velocity of around 220 km/s since they are present in our Galaxy with a local density between $0.3 - 0.4$ GeV/cm^3. Given that fact one can expect that DM particles can interact with ordinary matter. Direct Detection experiments are based on the measurement of the recoil energy of the elastic scattering of a WIMP off nuclei. For a mass of the WIMP of the order of GeV the expected energy deposited is of the order of keV. In order to detect the recoil energy the detectors of the DD experiments can make use of the phonons produced by vibrations of the structure of the material, or the photons that arise when the nuclei recoil, or measuring the ionization leads by the nucleus in the material. Usually the experiments combined these properties in order to measure correctly the energy transferred by the DM particle, however they all present a threshold energy as a lower limit in which for lower energy recoil they are not sensitive. In Figure 2.9 the most stringent bounds up to now are represented. These bounds are represented in terms of solid lines with the name of the experiment attached. Those bounds are imposed in the plane (σ_p^{SI}, m_{DM}), where σ_p^{SI} is the total cross section of a WIMP-proton scattering for a Spin Independent interaction and m_{DM} is the DM mass. The five limits corresponds to five different experiments that are sensitive to different mass ranges. The CDMSlite [122], SuperCDMS [123] and CRESST-II [124] experiments have the stringent bound for masses of the DM below $m_{DM} < 5$ GeV while the LUX [125] and Panda X-II [126] experiments are more sensitive to a wider range since it can exclude WIMP masses greater than $m_{DM} > 8$ GeV. One can see that experiments are less sensitive to light masses of the WIMP, this is due to the

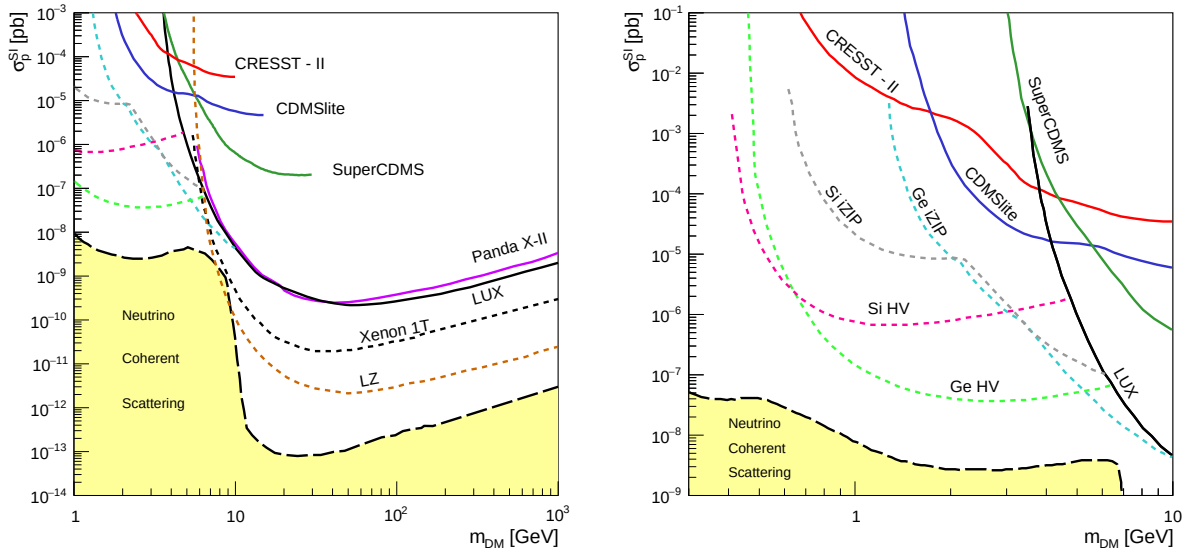

Figure 2.9: Spin independent cross section of the proton constraints for different experiments in terms of the DM mass. The most stringent bounds nowadays are depicted as solid lines and corresponds to CDMSLite [122] (blue), SuperCDMS [123] (green), CRESST-II [124] (red), LUX [125] and Panda X-II [126]. In short-dashed line the prospects of the Xenon1T [127], LZ [128] and SuperCDMS SNOLAB (Ge iZIP, Si iZIP, Ge HV, Si HV) [129] experiments are shown. The long-dashed curve shows the neutrino wall, representing the neutrino coherent scattering [130]. This line marks when the WIMP cross section becomes comparable to the one of the neutrino coherent scattering.

fact that in the scattering they produce low energy recoil in the nucleus that it cannot reach the threshold energy of the experiment. In fact in order to explore the low mass regime one must use light targets and lower the threshold. The only problem is that having light targets the experiments would be affected by more sources of background. However to probe the high mass sector heavier targets are suitable where less sources of background are found. In Figure 2.9 the experiments that cover the low mass regime, CDMSlite [122] and SuperCDMS [123], are based on Germanium while the experiments covering the high mass region, the LUX [125] and Panda X-II [126], are based on Xenon that is heavier than Germanium.

In terms of short-dashed lines the future reach of the experiments Xenon1T [127] (black) and LZ [128] (brown) are shown. These experiments will cover a range of WIMP masses similar to the LUX and Panda X-II experiments but improving the sensitivity in the cross section in two orders of magnitude in some regions. For low masses the future Germanium and Silicium based detectors in SuperCDMS SNOLAB experiments will cover a range of the WIMP mass between 0.5 GeV up to 10 GeV [129]. These four different detectors, Ge iZIP, Si iZIP, Ge HV and Si HV, are shown in right panel of Figure 2.9. The neutrino coherent scattering is also depicted as a long-dashed line covering the light yellow area in Figure 2.9. This curve represents irreducible neutrino background where the direct detection experiments lose sensitivity to the signals left by the WIMPs [130].

The experimental results of Figure 2.9 are presented as a function of the cross section per proton, i.e., the bounds are computed assuming that protons and neutrons couple equally to DM, usually called isospin conserved interactions. However, in the most general case of a DM model those couplings could be different. In this case the number of protons and neutrons of the nucleus used as a target in the direct detection experiment is important and the bounds provided by the experimental collaborations, such as the ones represented in Figure 2.9 are no longer valid in this scenario. The WIMP-nucleus cross section can be written as [131],

$$\sigma_0 = \frac{4\mu_N^2}{\pi} \left[f_p Z + f_n (A - Z) \right]^2 , \tag{2.43}$$

for a nucleus of Z protons and $A - Z$ neutrons. μ_N is the reduced mass of the nucleus and the WIMP and $f_{p,n}$ are the effective coupling of the protons and neutrons to the DM and their form is model dependent. When the interactions are isospin conserving, $f_n = f_p$, the cross section, σ_0, is dependent only the number of nucleons so it can be normalised to this number and the bounds can be expressed in terms of cross section per nucleon. However in the case of isospin violating interactions, where $f_n \neq f_p$ this is not longer valid. In fact, if one try to follow the "scattering per nucleon" scheme could be over or underestimating the bounds on the DM scattering cross section since now not only the number of nucleons but the real composition of protons and neutrons matters. For a given nucleus of Z protons and $A - Z$ neutrons the maximum cross section suppression is given by [132–135],

$$\frac{f_n}{f_p} \simeq -\frac{Z}{A - Z}. \tag{2.44}$$

In the cases where isospin violation is present the actual bounds of the direct detection experiments must be computed directly by calculating the number of events allowed by each experiment.

2.3.2. Indirect Detection

Indirect Detection experiments are based on the measurement of the final products of annihilation or decay of the DM particles. Those products may be seen as cosmic rays, photons or neutrinos that can be measured through their fluxes as excesses over the expected background. As we said before the decoupling of the DM particles from the primordial plasma make them not annihilate because of the expansion of the Universe. However there are regions in the Universe where the DM concentration is still large enough, so WIMPs can annihilate. There are three kind of indirect detection experiments depending on what they measure, gamma rays, antimatter or neutrinos.

The gamma ray experiments are very competitive in the dark matter searches when they focus on high density objects of the Universe such as the Galactic Centre or the Dwarf Spheroidal galaxies that are satellites of the Milky Way. One of the main important challenges for this kind of experiments is the understanding of all the possible astrophysical sources of gamma ray background. One of these experiments is the Fermi-LAT telescope, that is specialised in measuring gamma rays in a range of energy between tens of MeV to hundred of GeV. This experiment collects gamma ray information from a number of Dwarf Spheroidal Galaxies [136] and the Galactic Centre [137] and translate them into bounds on the thermal averaged annihilation cross section times the velocity,

$\langle\sigma v\rangle_0$, of different SM annihilation channels such as e^+e^-, $\mu^+\mu^-$, $\tau^+\tau^-$, W^+W^-, $u\bar{u}$ and $b\bar{b}$. From these searches the Fermi-LAT experiment is able to reach the regions of the parameter space of a thermal relic WIMP, assuming a typical cross section of $\langle\sigma v\rangle \simeq 3 \times 10^{26}\,\mathrm{cm}^3/\mathrm{s}$.

Other indirect detection experiments use the measurement of antimatter fluxes. The most common are the ones that study the positron and antiproton fluxes. The positron flux measured by different experiment such as AMS [138], PAMELA [139] and AMS-02 [140] indicates an excess on the cosmic-ray positrons. This could be interpreted as a hint of annihilating DM, however several arguments could explain this excess [141–144]. The antiproton cosmic ray spectrum has been also measured by different experiments such as Fermi-LAT [145] and AMS-02 [140]. Although the measured antiproton flux showed no deviation from the expected background there exist a discrepancy between this two experiments.

The last kind of indirect detection experiments are those that measure the neutrino cosmic fluxes. The most important ones are IceCube [146] and ANTARES [147]. They set constraints measuring the neutrino fluxes measured and they can translate them in terms of the spin-dependent interactions with nuclei. In that sense the bounds from these telescopes are competitive with the ones derived from the direct detection experiments.

2.3.3. Collider searches

In the previous searches the presence of DM in the Universe was used in order to detect it. However one can try to produce DM particles from their interactions with ordinary matter in a collider such as the LHC. However the only facts that we know about DM make its detection very hard. DM particles have zero electric charge, that makes impossible to be detected within a detector using the usual techniques. In fact they behave like neutrinos, so we can only infer the presence of WIMPs inside a collider through the imbalance of the total transverse momentum known as missing transverse energy, $\not{E}_T$. Nevertheless due to the stability of the DM particle it will be produced in pairs, so if only a pair of WIMPs is produced both transverse momenta will compensate leading to no signal in the detector. In order to compensate that fact if initial state radiation of a SM particle is produced together with the pair of WIMPs it is possible to detect the $\not{E}_T$ of the system and then compare the results with the SM predictions. A typical diagram of DM production together with a initial state radiation in the LHC, usually dubbed as mono-X, is illustrated in Figure 2.10. Those searches are being performed by the ATLAS and CMS detectors of the LHC, where they look for DM together produced with jets [148, 149], photons [150, 151] or other SM particles [152–159].

In order to set bounds using this mono-X searches it is usually common to apply the effective operator formalism, where the mediators are integrated out, to describe the interaction between the DM particles and the SM ones. In principle one can construct a set of different operators assuming the nature of the DM particle, whether it is a boson or a fermion, and the nature of the interaction, whether it is a scalar, pseudoscalar, vector or axial interaction. A typical term of the Lagrangian using effective operators could be

$$\frac{1}{\Lambda^2}(\bar{\chi}\gamma^\mu\chi)(\bar{q}\gamma_\mu q), \tag{2.45}$$

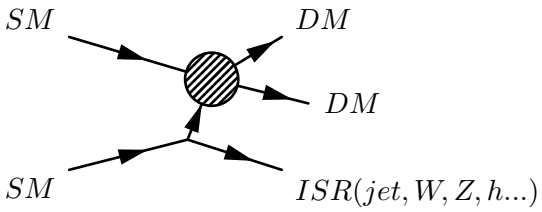

Figure 2.10: Diagram illustrating the mono-X searches for DM. The bubble represents the interaction between the DM and the SM sectors that depending on the model could be a s-channel, t-channel or u-channel.

for a fermionic DM particle and a vector interaction. Here the vector boson mediator has been integrated out and Λ is defined as the scale up to the effective theory is valid. This cut-off scale is related to the mass of the mediator and the couplings of the mediator to the DM and the SM particles by $\Lambda = M_{Z'}/\sqrt{g_\chi g_q}$ for the case of Eq. (2.45).[4] However, this interpretation is not valid for all the cases and it has a limited range of validity. The effective operator formalism is based on the fact that heavy mediators can be integrated out. This is valid when the momentum transferred in a collision is very small compared with the mass of the mediator, $Q^2 \ll m_{Z'}^2$. In this case the following expansion in the propagator of the diagram can be done,

$$\frac{g_q g_\chi}{Q^2 - m_{Z'}^2} \simeq -\frac{g_q g_\chi}{m_{Z'}^2}\left(1 + \frac{Q^2}{m_{Z'}^2}\right), \tag{2.46}$$

giving the effective operator of Eq. (2.45) when $Q^2 \ll m_{Z'}^2$. This formalism is very useful since LHC limits can be easily related with the ones coming from direct and indirect detection given the relation of Figure 2.8. In particular, if we assume that the DM is produced through a pair of quarks (as is the case of Eq. (2.45)) in the LHC the diagram responsible for that production is the same as the one of direct detection scattering, so the bounds coming from the LHC are easily translated in bounds on the plane (σ_p^{SI}, m_{DM}). However, for the present configuration of the LHC at 13 TeV of centre of mass energy, this relation holds for mediators heavier than 10 TeV [160]. For lighter mediators this estimation fails down giving to a wrong interpretation. When the mediator mass is sizeable to the momentum transferred resonant effects coming from the on-shell production of the mediator can enlarge the cross section of the process [161]. Using the effective operator formalism neither the correct cross section nor the resonance effects can be taken into account. Also when the mass of the mediator is lighter than the momentum transferred the expansion of Eq. (2.46) is no longer valid. In that sense one has to be careful when interpreting the results of LHC searches using effective operators. For that reason simplified models where the mediator is no longer integrated out are used to extract information from LHC data [160, 162–164].

Using simplified models one can also relate the different searches such as collider and direct detection searches since the diagram involved in both processes is the same but rotated $\pi/2$. In Figure 2.11 collider limits (black line) are translated to the (σ_p^{SI}, m_{DM}) plane for a simplified model where the DM particle is a Dirac fermion and it is connected to the SM through a vector boson mediator [162]. Different direct detection experiments such as LUX (red line), CDMSLite (green line) and CRESST-II (blue line) are depicted for comparison. For the values chosen in Ref. [162]

[4] Similar relations are found in the case of the other effective operators constructed for the different kind of DM particles and the different nature of the interactions.

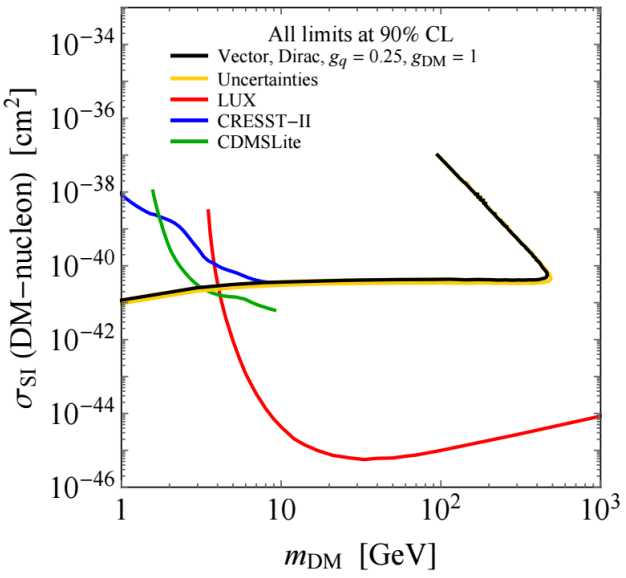

Figure 2.11: Spin independent proton cross section bounds in terms of the DM mass. Collider limits on a simplified vector-like mediator model with a Dirac fermion DM (black line) are depicted together with different bounds coming from direct detection experiments: LUX (red), CRESST-II (blue) and CDMSLite (green). Figure extracted from Ref. [162].

the collider limits are more sensitive for low masses of the DM particles where the bounds are competitive with the ones coming from the direct detection experiments CDMSLite and CRESST-II. However, for masses larger than 10 GeV LUX experiment could explore a larger region of the parameter space. In that sense, collider limits are complementary to the ones provided by direct detection experiments.

Collider searches are proved to be very efficient constraining low WIMP masses $m_{DM} < 10\,\text{GeV}$, although in order to set bounds on the DM parameter space it is usually assumed different simplified models with scalar or vector mediators. Although they go a step beyond the effective field approach and they include realistic effects such as resonance effects, it is very difficult for this kind of searches to be model independent since a way of production must be assumed or a nature of the interaction must be chosen without knowing the real nature of the DM sector.

Instead of using this formalism that would be a bottom-up approach, one can use a top-down one. In this case one can assume a particular model with a DM candidate that is connected with the SM in a specific manner and search for specific signals that the dark sector would lead without relying on the mono-X diagrams. The objective of this thesis is to take advantage of the peculiarities of a chosen model that can explain the DM problem and compared them with actual data from LHC. Those signals could vary from one model to another and go beyond the mono-X searches from simplified models. The specific connections between the SM and the DM sectors are used to elucidate signals on observables that in principle could not be related with DM, such as

the diphoton rate for the Higgs boson.

The first part of this thesis is devoted to study the signatures that mediators between the DM and the SM would leave in the detector. Two different kinds of mediator are studied. The Chapter 3 is devoted to a scalar mediator that could mix with the SM Higgs boson and is connected with the DM particles. Due to this mixing the mediator could decay into a pair of SM Higgses, leading to a characteristic signal in the detector since the SM Higgs decays are known. The specific final state $WW\bar{b}b$ is studied in detail. Expectations of this channel, fulfilling the DM constraints, in the future Run while are presented. In Chapter 4, a vector mediator is used to connect the SM and the DM sectors. Using the peculiarities of the model one can see that the mediator could be exhaustively searched in the LHC by means of its decay products. In particular dijet searches and dilepton searches are useful to set limits on the parameter space of the model.

However, if one assumes a complete model a wide variety of signals could appear in the LHC. The second part of this thesis is dedicated to the specific signals that two different models within the context of SUSY could lead in the detector. These signals under study are very dependent of the DM sector. In Chapter 5, the DM construction leads to a characteristic signal in terms of displaced vertices and long-lived charged particles. These signals are a clear effect of how the DM sector is constructed. Chapter 6 is devoted to the effects of the DM candidate on Higgs physics, in particular loop induced decays $h \to \gamma\gamma$ and $h \to \gamma Z$. This model connects the DM sector to the Higgs observables through the loops that give rise these two specific signatures. The fact that the DM particle must be in agreement with the present relic density and direct detection rates, lead to an imprint in the Higgs $\gamma\gamma$ and γZ rates.

Part I

Dark Matter Portals

3

Scalar Portal: Singlet Extension of the SM

One of the simplest extension of the SM Higgs sector is given by the addition of a real singlet field. This construction has received special attention in the literature as it can be seen in Refs. [26, 165–185]. The relevant Lagrangian for the scalar sector is written as:

$$\mathcal{L} = (D_\mu \Phi)^\dagger (D^\mu \Phi) + \frac{1}{2}\partial_\mu S\, \partial^\mu S - V(\Phi,\, S), \tag{3.1}$$

with the potential [168, 170],

$$\begin{aligned} V(\Phi,\, S) = {} & \lambda_{40}\left(\Phi^\dagger\Phi - v^2\right)^2 + \lambda_{21}\, v\left(\Phi^\dagger\Phi - v^2\right) S + \lambda_{22}\left(\Phi^\dagger\Phi - v^2\right) S^2 \\ & + \lambda_{02}\, v^2\, S^2 + \lambda_{03}\, v S^3 + \lambda_{04} S^4. \end{aligned} \tag{3.2}$$

The potential defined in Eq. (3.2) is not invariant under global $\mathbb{Z}_2$ transformations of the field S ($S \to -S$) that means that the new scalar, S, is unstable. As a consequence the singlet state cannot account to be the DM. Nevertheless, it can play a relevant role by providing a portal to DM. Let us consider then an extra singlet neutral Dirac fermion that is stable under a $\mathbb{Z}_2$ parity that enlarges the Lagrangian by

$$\bar{\psi}(i\partial\!\!\!/ - m_0)\psi + \lambda_\psi S \bar{\psi}\psi. \tag{3.3}$$

The singlet fermion is then a potential, WIMP-like, DM candidate, mediated by the singlet scalar state S.

After expanding the scalar potential $V(\Phi,\, S)$ around the real neutral vacuum expectation values (VEVs) one obtains the physical doublet and singlet scalar fields:

$$\Phi = \begin{pmatrix} 0 \\ v + \phi/\sqrt{2} \end{pmatrix}, \quad S = v_S + s. \tag{3.4}$$

For the values of the VEVs we have chosen $V(\Phi,\, S)$ such that $v \simeq 174$ GeV and $v_S = 0$.[1] In order to assure that the potential is bounded from below the conditions $\lambda_{40} > 0$, $\lambda_{04} > 0$, $\lambda_{22} > -2\sqrt{\lambda_{40}\lambda_{04}}$ over the quartic terms have to be imposed [186].

The presence of the λ_{21} term in Eq. (3.2) gives rise to the mixing of the the two scalars ϕ and s. The mass eigenstates are given by

$$\begin{pmatrix} h \\ H \end{pmatrix} = \begin{pmatrix} \cos\alpha & \sin\alpha \\ -\sin\alpha & \cos\alpha \end{pmatrix} \begin{pmatrix} \phi \\ s \end{pmatrix}, \tag{3.5}$$

[1] Note that, in a generic potential, S can be shifted to fulfill this condition.

where the mixing angle α and the mass eigenvalues read

$$\begin{aligned} \tan 2\alpha &= \frac{\lambda_{21}\sqrt{2}}{2\lambda_{02}-\lambda_{40}} \\ m^2_{H,h} &= \left(2\lambda_{40}+\lambda_{02} \pm \sqrt{2\lambda_{21}^2+(2\lambda_{40}-\lambda_{02})^2}\right) v^2. \end{aligned} \tag{3.6}$$

The stability of the vacuum is achieved by requiring $\lambda_{02} > 0$ and $4\lambda_{40}\lambda_{02} > \lambda_{21}^2$. These parameters, ($\lambda_{40}$, λ_{02}, λ_{21}), are expressed in terms of the physical ones α, m_h, m_H, and v by use of Eq. (3.6) as follows:

$$\begin{aligned} \lambda_{40} &= \frac{m_h^2 \sin^2\alpha + m_H^2 \cos^2\alpha}{8v^2}, \\ \lambda_{02} &= \frac{m_h^2 \cos^2\alpha + m_H^2 \sin^2\alpha}{4v^2}, \\ \lambda_{21} &= \frac{(m_H^2 - m_h^2)\sin 2\alpha}{2\sqrt{2}v^2}. \end{aligned} \tag{3.7}$$

The cubic and quartic interactions involving the mass eigenstates h, H can be given as functions of the physical parameters appearing in Eq. (3.6) and the three remaining couplings (λ_{22}, λ_{03}, λ_{04}). This is in contrast with the SM (or in the extended complex Higgs singlet model), where the full potential can be reconstructed from the mass (matrix) and the VEVs of the field(s). In what follows, we will assume that h, the lighter Higgs, is the SM-like Higgs discovered at the LHC having $m_h \sim 125$ GeV and its couplings approach the SM ones in the $\cos\alpha \approx 1$ limit. Thus, we will assume that H, the heavier Higgs, is the singlet-like one.

3.1. Constraints on m_H and $\sin\alpha$

If the Higgs couplings deviate from their SM values these deviations are constrained by the LHC Higgs data and by the electroweak precision observables (EWPO). We first concentrate on the latter. Within the SM, the Higgs boson contributes to the gauge bosons self-energies involved in the EWPO by mean of loop corrections that depend on the values of the couplings and the Higgs mass. In the singlet-extended Higgs model, the one loop self-energies will be given by the sum of two SM-like Higgs contributions of both states evaluated at Higgs masses, m_h and m_H, rescaled by $\cos^2\alpha$ and $\sin^2\alpha$ respectively [170] as it is illustrated in Fig. 3.2. This property can also be applied to non-universal diagrams (*e.g.*, vertex corrections) involving the Higgses and it is transmitted to the EWPO in the limit where higher order terms, $\mathcal{O}(\sin^4\alpha)$, are neglected. For that reason we evaluated predictions for the for the Z-peak observables [187] and m_W, Γ_W [188], as a function of m_H and $\sin^2\alpha$. For this purpose we have made use of the program ZFITTER [189–196] that provides different observables listed in Table 3.1. The results are presented in Figure 3.2, where 90% and 95% C.L. allowed regions in the $m_H - \sin^2\alpha$ plane are shown. The structure of these lines can be understood by noting that at $m_H = m_h$ the contour line is a vertical one since its value does not depend on the mixing angle. On the other hand, for large m_H values, the mixing angle must be small enough to compensate the non-decoupling Higgs contributions to the EWPO.

Observable	Data	Observable	Data
m_W	80.385 ± 0.015	$\sin^2\theta^\ell_{\rm eff}$	0.2324 ± 0.0012
Γ_W	2.085 ± 0.042	A_c	0.670 ± 0.027
Γ_Z	2.4952 ± 0.0023	A_b	0.923 ± 0.020
$\sigma^0_{\rm had}$	41.540 ± 0.037	$A^{0,c}_{\rm FB}$	0.0707 ± 0.0035
R^0_ℓ	20.767 ± 0.025	$A^{0,b}_{\rm FB}$	0.0992 ± 0.0016
$A^{0,\ell}_{\rm FB}$	0.0171 ± 0.0010	R^0_c	0.1721 ± 0.0030
A_ℓ	0.1499 ± 0.0018	R^0_b	0.21629 ± 0.00066

Table 3.1: Electroweak data taken from Ref. [10] used in the fit of the EWPO.

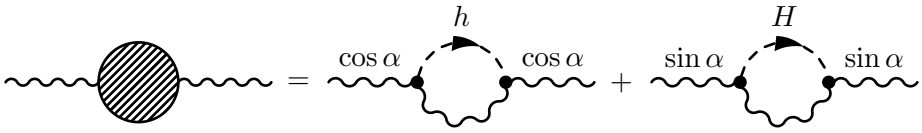

Figure 3.1: Pictorical view of the Higgs corrections to the gauge boson self energies. The contributions of the Higgses is interpreted as the sum of both diagrams where each of them is weighted with the respective reducing coupling and the Higgs mass.

It is also common to use the oblique parameters (S, T, U) instead of analyzing the complete set of observables. We expect that in the region where $m_H \lesssim 200$ GeV both methods should give a similar χ^2 value. However, for larger m_H values, the gaussian approximation to the χ^2 that is used to fit (S, T, U) and the estimation of their errors starts to break down.[2] This can be explicitly checked by evaluating χ^2 as a function of m_h using the whole Z-peak data or the oblique parameters (S, T, U).

Let us now consider the impact of the LHC Higgs data. As it was already mentioned before, the reduction of the Higgs couplings to SM fields due to the mixing translates into a common reduction of the Higgs signal-strength modifier in all channels. By applying the narrow-width approximation, one can see that this factor is given by $\cos^2\alpha$. Using Eq. (1.4), it is straightforward to derive a bound on the mixing, namely, $\sin^2\alpha < 0.076\,(0.128)$ at 90% (95%) C.L. for the 8 TeV Run. One can also consider the constraints coming from the 13 TeV data (Eq. (1.5)) and combine both results (Eq. (1.6)) that provide a constraint in the mixing angle $\sin^2\alpha < 0.060\,(0.100)$ at 90% (95%) C.L. The LHC bounds can be combined with the ones derived from the EWPO giving as a result the limits presented in Figure 3.3. The combined results using the 8 TeV data are depicted with full lines while the ones using the 8 TeV and 13 TeV data are represented by means of dashed lines. Given the fact that the LHC constraints are flat in the m_H direction they push down the EWPO bounds for low masses as it can be seen comparing Figure 3.2 with Figure 3.3. We can compare how the bounds change when the 13 TeV data are included. From Figure 3.3 it is clear that the constraints on the mixing angle coming from the combination of both LHC runs are more stringent. Although the 13 TeV data favours a larger mixing angle, the combination reduces the

[2] This is shown in Ref. [57], where a detailed calculation of Δr and m_W in the singlet-extended model is presented.

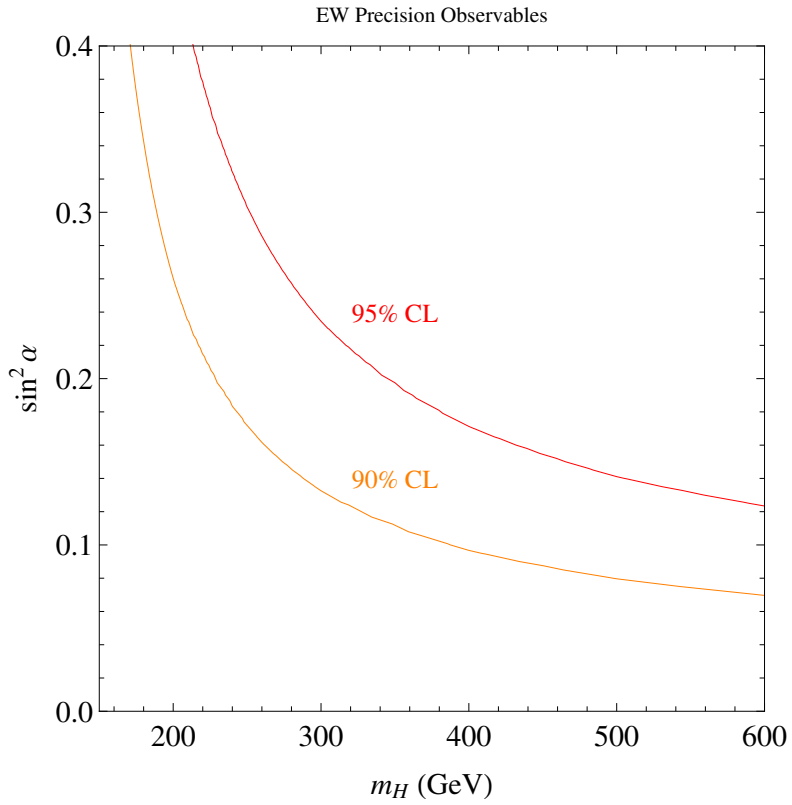

Figure 3.2: Constraints in the $m_H - \sin^2\alpha$ derived from the full set of EWPO at the Z-peak.

total error, this effect is the responsible for reducing the allowed values for the mixing angle. As we discussed above the LHC data tend to flat the constraints and this effect is stronger for low masses.

After dealing with the indirect bounds[3] on the mixing for a given m_H value, we briefly comment on the direct ones, derived from heavy Higgs boson searches. Note that, as a consequence of the mixing, the production and decay modes of the singlet-like Higgs H will be the same as those of the SM-like Higgs. However, as it has different mass, the branching ratios of the decay channels will be different. We can re-interpret ATLAS and CMS analyses for heavy Higgs searches to derive bounds on m_H and $\sin^2\alpha$. The ATLAS collaboration has presented two searches for the heavy Higgs boson. The first one uses the $H \to WW \to \ell\nu\ell\nu$ [198] decay mode and the bound corresponds to an integrated luminosity of 21 fb^{-1} at $\sqrt{s} = 8$ TeV. The second one uses the $H \to ZZ$ decay [199]. The CMS collaboration has reported two analyses on heavy Higgs searches using the $H \to ZZ$ decay channels. The first one corresponds to an integrated luminosity of 19.6 fb^{-1} at $\sqrt{s} = 8$ TeV and considers the $\ell^+\ell^- q\bar{q}$ final state [200]. The second one considers final states where both Z's decay into charged leptons, and corresponds to an integrated luminosity of 5.1 fb^{-1} at $\sqrt{s} = 7$ TeV and 19.6 fb^{-1} at $\sqrt{s} = 8$ TeV [201]. The CMS collaboration has also performed an analysis

[3]There are other constraints that can be derived by imposing perturbative unitarity of scattering amplitudes for longitudinal W bosons [177, 197]. We will ignore them since they are weaker than the other bounds [47].

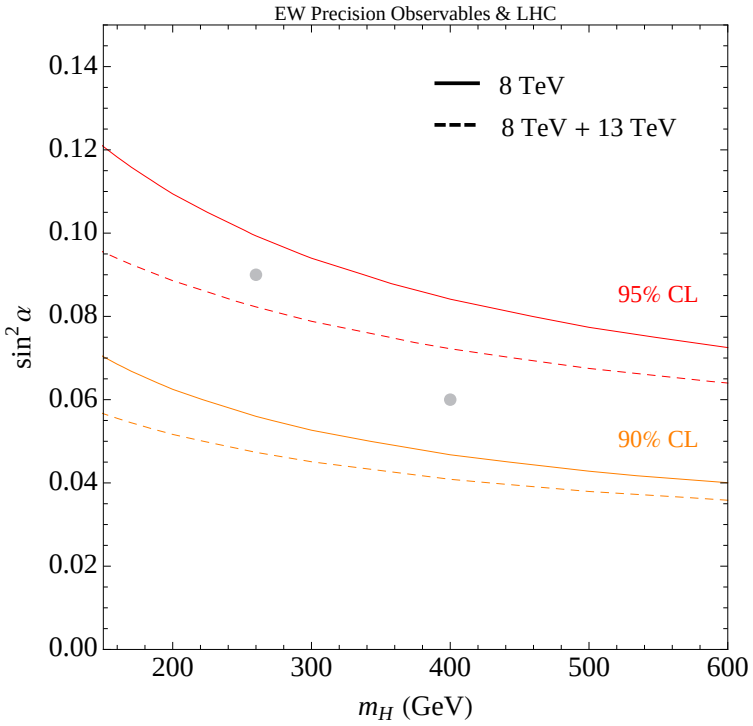

Figure 3.3: Constraints in the $m_H - \sin^2\alpha$ plane derived from the full set of EWPO at the Z-peak combined with the LHC Higgs coupling data. The constraint from the 8 TeV data is represented as full lines while the one coming from the combination of 8 TeV and 13 TeV is depicted as dashed lines. We have also drawn the two benchmark points whose LHC implications are analyzed in detail in Section 3.3.

using the channel $H \to WW \to \ell\nu\ell\nu$, obtained for the configurations of $\sqrt{s} = 7$ TeV with an integrated luminosity of 4.9 fb^{-1} and $\sqrt{s} = 8$ TeV with 19.5 fb^{-1} [202]. The results are shown in Figure 3.4, where we have assumed that H has the same branching ratios as those a SM Higgs would have for the same masses. This is certainly a good approximation if the $H \to hh$ decay process is not kinematically allowed, or $\mathrm{BR}(H \to hh) \ll 1$. On the other hand, if $\mathrm{BR}(H \to hh)$ is substantially large, these bounds have to be rescaled as indicated in the figure, and eventually will become irrelevant in the $\mathrm{BR}(H \to hh) \sim 1$ limit. In this case, the double-Higgs production process will be the main signature of the model at the LHC and deserves a detailed study.

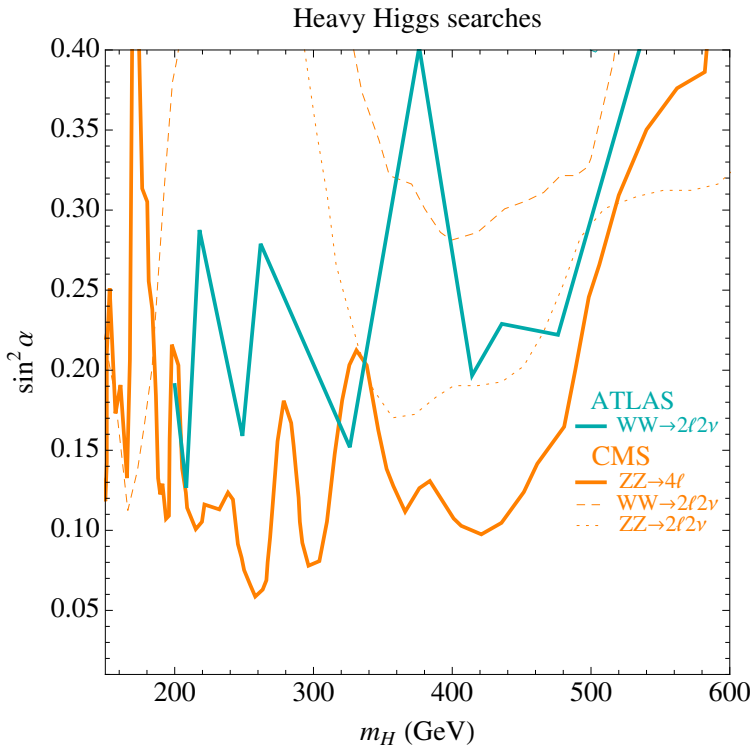

Figure 3.4: Constraints in the $m_H - \sin^2\alpha$ plane derived by ATLAS and CMS from SM-like heavy Higgs searches assuming the heavy Higgs decays as the SM one. For non-zero $\mathrm{BR}(H \to hh)$ values, the vertical axis would read $\sin^2\alpha/(1 - \mathrm{BR}(H \to hh))$.

3.2. Dark Matter with a scalar mediator

Given that the new scalar is unstable, it does not solve the dark matter problem. Nevertheless, it can play a relevant role by providing a portal to DM. In this Section we explore this possibility. The DM mass and its coupling to the new scalar will be restricted by requiring a DM relic density in agreement with the experimental value. We analyse the compatibility between this condition and the requirement of a sizable $H \to hh$ branching ratio, as assumed in the previous section.

We will consider an extra singlet neutral Dirac fermion, ψ presented above and given by Eq. (3.3). The singlet fermion is stable due to the Z_2 parity and is then a potential, WIMP-like, DM candidate. We will now explore the possibilities of this candidate to fulfil the requirements given by the relic density and direct detection experiments. In order to illustrate this we will focus on two benchmark points described by

1. $m_H = 400$ GeV, $\sin^2\alpha = 0.06$,

2. $m_H = 260$ GeV, $\sin^2\alpha = 0.09$.

Both points are allowed by EWPO and LHC constraints[4] as can be seen in Fig. 3.3 where they are depicted as grey points.[5]

Relic density

We have implemented the model in CalcHEP [203] and used the micrOMEGAs 2.4 package [204] to evaluate the DM relic density for the two benchmark points studied in the previous section. The results are displayed in Figure 3.5, where we show the DM relic density as a function of the WIMP mass, m_ψ, for different values of λ_ψ. The light red region corresponds to λ_ψ values varying from 0.001 to 1. The black solid line represents the relic density for $\lambda_\psi = 0.1$. The blue band is bounded by the allowed experimental relic density value given by Planck [118]:

$$0.1134 < \Omega h^2 < 0.1258 \;\; (95\%\,\text{C.L}) \tag{3.8}$$

Note that the correct relic density can be achieved in two regions. The first one is characterized by a DM mass close to $m_h/2$, providing an enhancement of the DM annihilation cross section due to the resonance effect. When kinematically allowed, the Higgs decay into a ψ pair becomes dominant. As the LHC constrains the Higgs invisible width, which is mainly given by

$$\Gamma(h \to \psi\bar{\psi}) = \frac{|\lambda_\psi \sin\alpha|^2}{16\pi} m_h \left(1 - \frac{4m_\psi^2}{m_h^2}\right)^{3/2}, \tag{3.9}$$

this small m_ψ window gets reduced (~ 1 GeV).

There is a much wider parameter region where the enough amount of DM annihilation can be triggered by the heavy Higgs. Around and above the region of the heavy Higgs resonance, *i.e.*$2m_\psi \gtrsim m_H$, the other annihilation channels such as $\psi\bar{\psi} \to hH$ and $\psi\bar{\psi} \to HH$ are open, thus making the DM annihilation sufficient to attain the correct relic density. For $2m_\psi < m_H$, the $H \to \psi\psi$ decay process will contribute to the decay width of the heavy Higgs boson, reducing the BR($H \to hh$) ratio and thus decreasing the resonant double Higgs production. This could affect the possibilities of finding this signal by reducing the statistical significance. However, in the region where $2m_\psi > m_H$ the results would remain unaffected. For this reason we should incorporate the constraints from the direct detection experiments in order to know which DM regions are favoured. A similar study was done in Ref. [205], that agrees with our analysis.

Direct Detection

Direct detection experiments search for DM by means of its elastic scattering off nuclei. In the absence of a positive signal, present search results translate into bounds on the WIMP-nuclei cross section for a given WIMP mass. As the elastic scattering is produced at low momentum we

[4]The benchmark point with $m_H = 260$ GeV is in a bit tension with the combination of 8 TeV and 13 TeV data.

[5]These two benchmark points are chosen within a range that is suitable for the double Higgs production detection as it will be shown in the next Section 3.3.

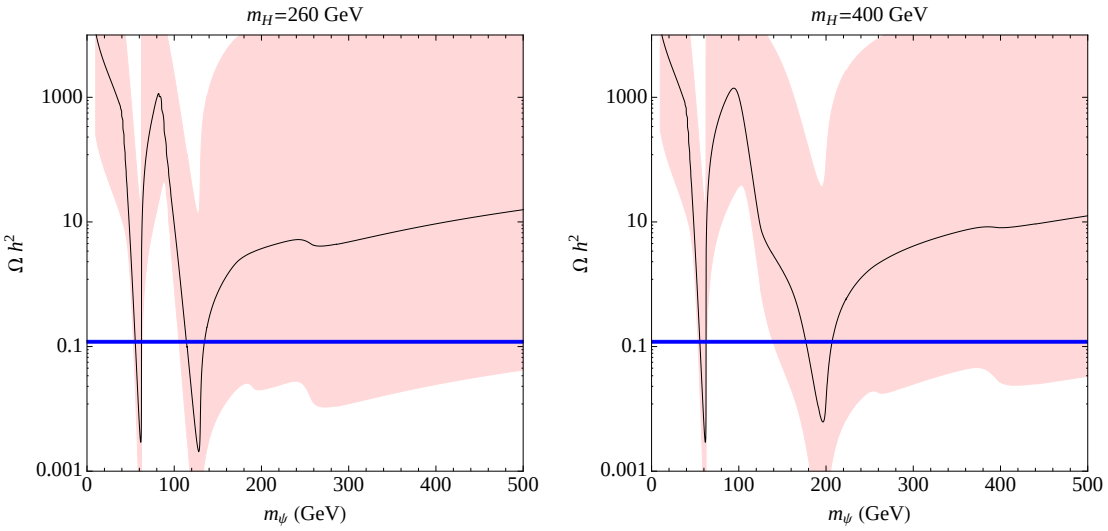

Figure 3.5: DM relic density as a function of the WIMP mass, m_ψ, for different values of λ_ψ. See the text for detailed description.

can write the interaction as an effective operator. In our case, it is induced by t-channel exchange of the Higgses and is given by:

$$\mathcal{L}_{\text{eff}} \supset \alpha_{q_i} \bar{\psi}\psi\bar{q}_i q_i, \tag{3.10}$$

with [45]

$$\frac{\alpha_q}{m_q} = \frac{\lambda_\psi \cos\alpha \sin\alpha}{v}\left(\frac{1}{m_h^2} - \frac{1}{m_H^2}\right), \tag{3.11}$$

The spin-independent elastic scattering cross section can be written as[6]

$$\sigma^{\text{SI}}_{\psi p} = \frac{1}{\pi}\frac{m_p^2}{(m_p + m_\psi)^2} f_p^2, \tag{3.12}$$

where m_p is the proton mass and f_p is defined as

$$\frac{f_p}{m_p} = \sum_{q_i=u,d,s} f^p_{Tq_i}\frac{\alpha_{q_i}}{m_{q_i}} + \frac{2}{27} f^p_{TG} \sum_{q_i=c,b,t}\frac{\alpha_{q_i}}{m_{q_i}} \tag{3.13}$$

where the quantities f_{Tq_i} represent the contributions of the light quarks to the mass of the proton. The full expressions for the spin-independent cross section can be found in Refs. [45, 48]. In Figure 3.6 the normalized spin-independent cross section is plotted as a function of the DM candidate mass for the two benchmark points. This normalized cross section, $\xi\sigma^{\text{SI}}_{\psi N}$, is the product of the spin-independent cross section and the factor ξ defined as $\xi \equiv \min\{1, \Omega_\psi h^2/0.1226\}$. This factor

[6] See, for example, Ref. [131]

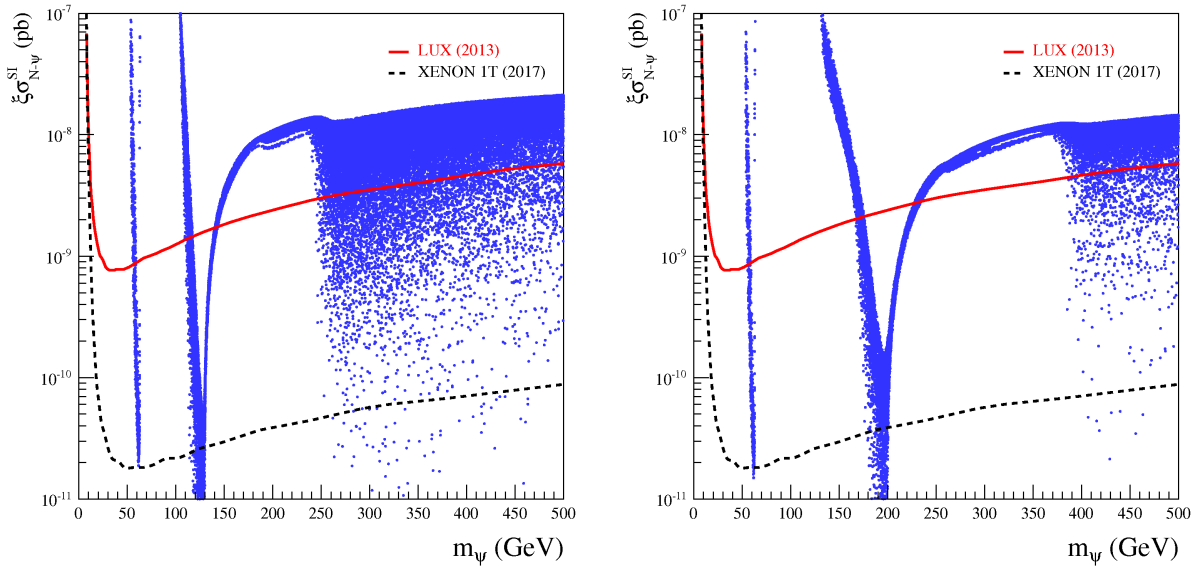

Figure 3.6: Spin independent cross section as function of the DM mass for the two different scenarios with $m_H = 260$ GeV (left) and $m_H = 400$ GeV (right). The red line represents the bounds from LUX [206] while the black dashed line corresponds to the future prospects of XENON1T [127].

accounts for situations where ψ provides only a fraction of the total amount of dark matter. In Figure 3.6 a scan over the mass and the λ_ψ parameters has been done. Only the points with a relic density equal or less than that from Planck, Eq. (3.8) are showed. The bounds imposed by LUX [206] are included as well as future prospect from XENON 1T [127].

For the light DM candidate it is difficult to have the correct relic density and avoid the bound imposed by LUX at the same time. These conditions are compatible in a small region close to half of the mass of the Higgses, so a resonant peak is present. However, this means that the decays $h \to \psi\bar{\psi}$ and $H \to \psi\bar{\psi}$ are dominant, so the model could be excluded by the LHC or would spoil the results obtained in the collider analysis. Nevertheless, we can find a region with relatively high masses of the DM candidate that fulfills both relic density and spin-independent cross section and is placed above the resonance produced by the heavy Higgs. In fact, the allowed area is induced by the opening of the $\psi\bar{\psi} \to HH$ annihilation channel, making the cross section more effective.

This analysis implies that there exists a region where DM requirements are fulfilled and is located above the heavy Higgs boson mass. Moreover the forthcoming direct detection experiment such as XENON1T are predicted to be more sensitive so a large amount of the parameter space of this model, leading to the possibility of probing it.

3.3. Double Higgs Production in the $H \to hh \to WWb\bar{b}$ channel

As we have seen above, the singlet extended SM can account for the DM problem by adding a singlet Dirac fermion to its Lagrangian. This DM candidate is in agreement with the measurements of the relic density of DM in the Universe and with the no observation of DM in direct detection experiments. Once these requirements are fulfilled we focus on the collider consequences of such a model.

The resonant double Higgs production is a distinct feature of the model we are dealing with. In this section we study this process in the forthcoming LHC run at 14 TeV. Since the Higgs production cross-section $\sigma(H)$ scales as $\sin^2\alpha$ and there is a bound on the allowed mixing for a given m_H, we can obtain the maximal value of $\sigma(H)$ as a function m_H. This is shown in Figure 3.7, where the 95% C.L. limit on $\sin^2\alpha$ has been used.

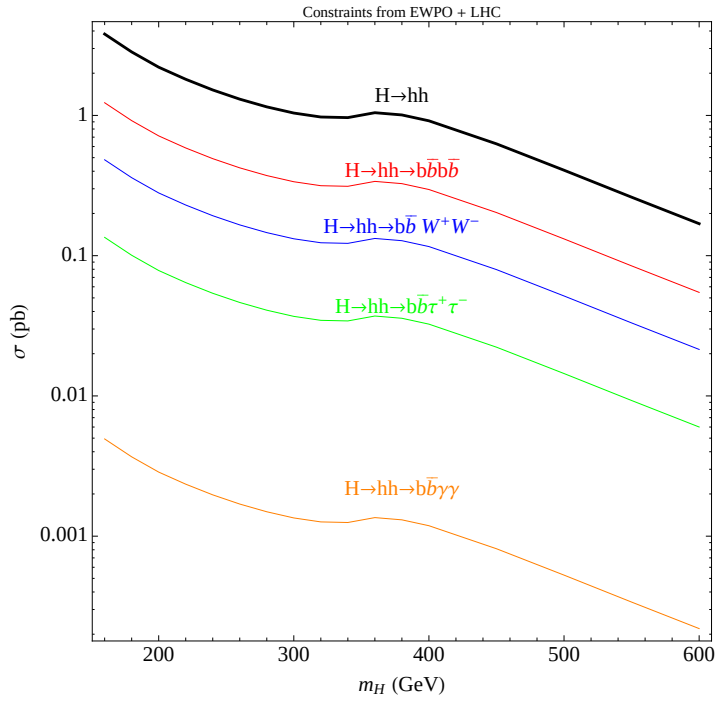

Figure 3.7: Cross-section of the double Higgs production mediated by the heavy Higgs boson evaluated at the maximal mixing angle. The black line shows the total cross section for this process while different final state cross sections are presented in colours.

In order to check the signal significance at the LHC, which will be resumed with the upgraded center-of-mass energy along the year 2015, we perform a Monte Carlo (MC) study by choosing two benchmark points. For the $H \to hh$ decay process, the largest portion of signal events will consist of the four-b-jet final state as studied in Refs. [60,61]. However, the multi-jet signature is generically vulnerable to the huge QCD backgrounds and the poor reconstruction efficiency. One can attempt to increase the purity of signal events by imposing a tight b-tagging condition, but then it would

result in a big sacrifice of the signal statistics. The ATLAS and CMS collaborations have performed searches for resonant double-Higgs production in the $b\bar{b}b\bar{b}$ final state [207, 208]. It was shown that in order to be effective in this channel the mass of the new resonance should be greater than 500 GeV to ensure two highly boosted, back-to-back $b\bar{b}$ di-jet systems [60]. For smaller masses, the product of the acceptance and the efficiency of the search decreases, thus making difficult to use this channel.

The subleading decay process is $b\bar{b}W^+W^-$, followed by fully-hadronic, semi-leptonic, and di-leptonic modes. This search channel, as it will be shown below, can be efficient in the 260 – 500 GeV range for the heavy Higgs mass.[7] Among them, the final states containing the lepton are more suitable for the search since the fully-hadronic states are liable to be in trouble due to the similar reason as in the four-b-jet signal. In leptonic signal events the missing energy originated from the neutrino prevents the direct reconstruction of the Higgs resonances. Still, provided that the light Higgs boson mass m_h is accurately known, one can obtain the neutrino four-momenta up to a two-fold ambiguity by using on-shell mass relations, as well as the missing energy condition in the case of the semi-leptonic channel:

$$(p^\nu)^2 = 0, \quad \left(p^\nu + p^\ell + p^q + p^{q'}\right)^2 = m_h^2, \quad \mathbf{p}_{\rm T}^\nu = \not{\mathbf{p}}_{\rm T}, \tag{3.14}$$

where $\not{\mathbf{p}}_{\rm T}$ is the missing transverse momenta measured in the event, and q and q' are jets from the hadronically-decaying W boson. On the other hand, the on-shell relations are not enough to constrain the neutrino momenta in the case of the di-leptonic channel, even though it provides a cleaner signal than that of the semi-leptonic one. Here we examine the discovery potential of the di-leptonic decay mode, which appears to be more challengeable due to the missing neutrinos, although it is less vulnerable to uncertainties regarding the jet reconstruction, by using various kinematic variables and an approximate reconstruction scheme. We will show the practicability and the limitation of the search strategy in the two different scenarios used before for the DM phenomenology that are characterized by

1. $m_H = 400$ GeV, $\sin^2\alpha = 0.06$,
2. $m_H = 260$ GeV, $\sin^2\alpha = 0.09$,

assuming $\mathrm{BR}(H \to hh) = 1$ for both benchmark points.[8]

The production cross-section is $\sigma(gg \to H) \times \mathrm{BR}(H \to hh) = \sigma(gg \to \phi) \times \sin^2\alpha \simeq 0.7$ (1.2) pb for $m_H = 400$ (260) GeV in the 14-TeV LHC regime. Here, ϕ is the Higgs-like scalar. $\sigma(gg \to \phi)$ has been obtained from the Higgs Cross Section Working Group in Ref. [211] assuming that the couplings of ϕ are SM-like. The search channel of interest is

$$H \to hh \to b\bar{b}\,W^+W^- \to b(p^b)\bar{b}(p^{\bar{b}}) + \ell^+(p^\ell)\ell^-(q^\ell) + \not{E}_{\rm T} \quad (\ell = e,\, \mu), \tag{3.15}$$

[7] The complementary channel to the one presented here is the $b\bar{b}\gamma\gamma$ [209, 210]. The small branching ratio of the SM Higgs decaying into two photons makes this channel challenging (see, however Refs. [62–64]).

[8] We stress that the results obtained here can be readily reinterpreted for the scenario with different $\mathrm{BR}(H \to hh)$ values.

where the source of the missing energy are the neutrinos produced by the leptonically-decaying W bosons. For the numerical simulation, we have generated the MC events using PYTHIA 8 [212], interfacing with the CT10 parton distribution functions [213] for a proton-proton collision at $\sqrt{s} =$ 14 TeV. The parton showering and the hadronization have been performed by PYTHIA 8. Then, the hadron-level data has been processed with the fast detector-simulation program DELPHES 3 [214], which reconstructs the final-state objects such as jets, isolated leptons, and the missing energy with the inclusion of detector resolution effects and tagging/fake rates. The input parameters have been adjusted for the ATLAS detector in DELPHES. FASTJET 3 [215] is employed to reconstruct jets. In our simulation, the anti-k_t jet algorithm [216] with distance parameter of 0.5 is chosen for the jet reconstruction. It is known that the tagging efficiency for the b-jet depends on the transverse momentum $p_{\rm T}$ and the pseudorapidity η of the jet object. Recent ATLAS and CMS analyses on the b-jet identification for the experimental data indicate that the efficiency can be as large as ~ 60 – 80% [217]. For the sake of a simple analysis, we assume a flat b-tagging efficiency of 70% for $p_{\rm T} > 30$ GeV and $|\eta| < 2.5$. The mis-tagging efficiency is set to be 10% for the c-jet and 1% for the light flavor as well as the gluon jet. Isolated electrons (muons) are required to have $p_{\rm T} > 13$ (10) GeV within $|\eta| < 2.4$. In order to remove fake leptons coming from the decays of hadrons, we discard the leptons lying within the angular separation $\Delta R_{\ell j} = \sqrt{\Delta\phi_{\ell j}^2 + \Delta\eta_{\ell j}^2} < 0.4$ from a jet with $p_{\rm T} > 25$ GeV. Since the tau reconstruction efficiency is relatively poor, we reject events containing the tau-jet with $p_{\rm T} > 10$ GeV. The missing transverse momentum $\not{p}_{\rm T}$ is defined as the opposite of the vector sum of all the visible particles' transverse momenta.

Having the same final states as the signal, the di-leptonic $t\bar{t}$ process is the main background. The subleading backgrounds include Drell-Yan (DY), di-boson, and the SM Higgs processes that lead to the leptonic final states and the b-jets. In addition, we consider the rare SM Higgs processes, including double-Higgs production via the gluon-gluon fusion (GGF), single-Higgs production via the vector-boson fusion (VBF), and Higgs boson production in association with a weak vector boson or a top-pair, *i.e.*, hW/Z and $ht\bar{t}$. The SM double-Higgs events have been generated by a modified PYTHIA 6 program [218] in which the matrix element calculated with HPAIR [219] is implemented, while the other processes have been generated by PYTHIA 8. We use the production cross section for the SM double-Higgs process obtained by HPAIR, which can calculate up to next-to-leading order. The $t\bar{t}$ production cross section is calculated with TOP++ 1.4 [220] at next-to-next-leading order, and the Higgs production cross sections, except that of the double-Higgs process, are obtained from Ref. [211]. For the DY and the di-boson processes, we use the leading-order cross sections calculated with PYTHIA 8 since most of them can contribute to the background by faking b-jets and can be readily removed by event selection cuts, as will be discussed shortly. In Table 3.2, we show the cross-section values used in this study.

Before going further into the analysis, let us introduce one of the main kinematic variables and the reconstruction scheme adopted to obtain the approximate values of the invisible neutrino momenta. The situation with more than one invisible particle in a collider event is common in many extensions of the SM providing a viable DM candidate. One of the most studied collider variables to search for such a new physics signature is $M_{\rm T2}$, which is a generalized transverse mass particularly known to be useful for the pair-production processes of new particles that eventually

Process	Cross section
$H \to hh$ ($m_H = 400$ GeV)	0.66
$H \to hh$ ($m_H = 260$ GeV)	1.18
$t\bar{t}$	844.43
GGF h	50.35
VBF h	4.17
hW/Z	2.39
$ht\bar{t}$	0.61
hh	0.033
DY	91130.0
Di-boson	121.0

Table 3.2: Production cross sections in pb for the signal and background processes at the 14 TeV proton-proton collision. We set $m_t = 173.5$ GeV and $m_h = 125$ GeV.

decay into the invisible particles [221, 222]. Suppose that the decay topology is like

$$pp \to Y + \overline{Y} + U \to V(p)\chi(k) + \overline{V}(q)\chi(l) + U(u), \tag{3.16}$$

where Y is a heavy unstable particle, V is a set of detectable particles such as jets or charged leptons, and χ is the invisible particle. Here, U denotes a set of particles that do not participate in the decay process of Y, like initial or final state radiations. For the new physics signature with the decay topology Eq. (3.16), the invisible momenta k and l, as well as the particle masses m_Y and m_χ, are unknown, while only the sum of their transverse components can be inferred from the deficit of total transverse momentum in the collider event, *i.e.*, the missing transverse momentum. Then, $M_{\mathrm{T}2}$ is defined as

$$M_{\mathrm{T}2} \equiv \min_{\mathbf{k}_{\mathrm{T}}+\mathbf{l}_{\mathrm{T}}=\not{\mathbf{p}}_{\mathrm{T}}} \left[\max\left\{ M_{\mathrm{T}}^{(1)},\, M_{\mathrm{T}}^{(2)} \right\} \right], \tag{3.17}$$

where $M_{\mathrm{T}}^{(i)}$ $(i = 1, 2)$ are transverse masses for the decay chains,

$$\begin{aligned} \left(M_{\mathrm{T}}^{(1)}\right)^2 &= m_V^2 + m_\chi^2 + 2\left(\sqrt{|\mathbf{p}_{\mathrm{T}}|^2 + m_V^2}\sqrt{|\mathbf{k}_{\mathrm{T}}|^2 + m_\chi^2} - \mathbf{p}_{\mathrm{T}} \cdot \mathbf{k}_{\mathrm{T}}\right), \\ \left(M_{\mathrm{T}}^{(2)}\right)^2 &= m_{\overline{V}}^2 + m_\chi^2 + 2\left(\sqrt{|\mathbf{q}_{\mathrm{T}}|^2 + m_{\overline{V}}^2}\sqrt{|\mathbf{l}_{\mathrm{T}}|^2 + m_\chi^2} - \mathbf{q}_{\mathrm{T}} \cdot \mathbf{l}_{\mathrm{T}}\right). \end{aligned} \tag{3.18}$$

Here, $\mathbf{k}_{\mathrm{T}}$, $\mathbf{l}_{\mathrm{T}}$, and m_χ are input parameters. In practice, the transverse momenta of invisible particles are uniquely determined by the minimization, whereas the invisible particle mass m_χ is a

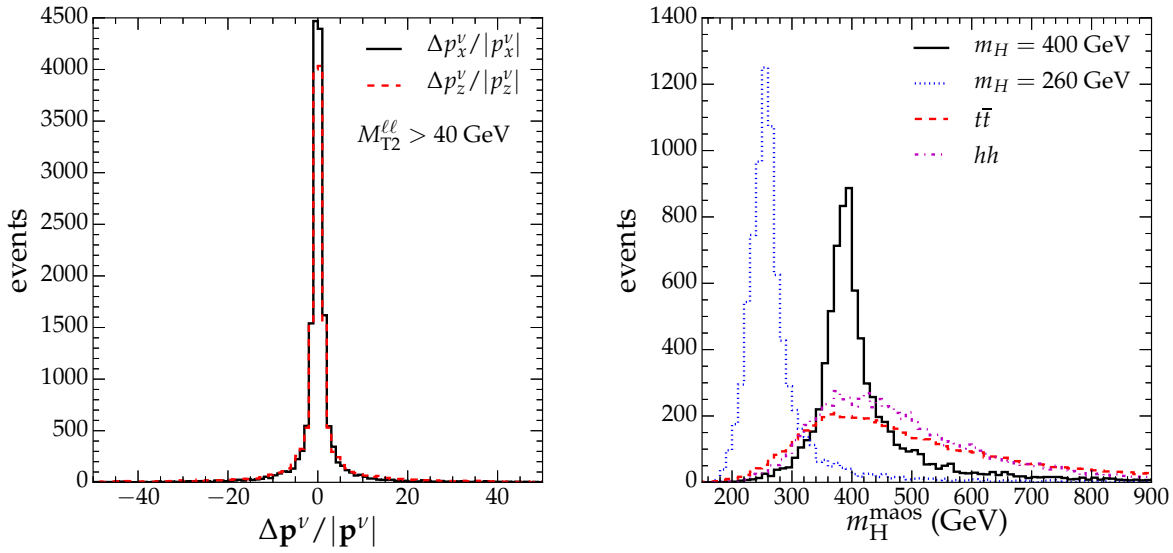

Figure 3.8: (Left panel) Difference between the MAOS momentum and the true neutrino momentum for $m_H = 400$ GeV $\Delta\mathbf{p}^\nu/|\mathbf{p}^\nu| \equiv (\mathbf{p}_\nu^{\rm maos} - \mathbf{p}_\nu^{\rm true})/|\mathbf{p}_\nu^{\rm true}|$. (Right panel) Normalized $m_H^{\rm maos}$ distributions for $m_H = 260$ and 400 GeV and the $t\bar{t}$ backgrounds using parton-level data.

constant that must be put by hand before the minimization. Once the correct m_χ value is chosen, the endpoint position of the $M_{\rm T2}$ distribution points to the parent particle mass,

$$M_{\rm T2}(m_\chi = m_\chi^{\rm true}) \leq m_Y. \tag{3.19}$$

The situation becomes simpler when the invisible particle mass is already known as in the case of SM processes, where the neutrino is the only particle escaping detection and can be safely assumed to be massless for reconstruction purposes.[9] Another notable feature of the $M_{\rm T2}$ variable is that it comes in handy even when one or both parent particles are off-shell. This has been used to measure the SM Higgs boson mass in the di-leptonic $WW^{(*)}$ channel [227, 228]. In the case when $m_h < 2m_W$, at least one of the W bosons should be produced off-shell. Then, the maximal value of $M_{\rm T2}$ is not m_W, but $\sim m_h/2$. This can be deduced by considering some special kinematic configurations, as derived in the Appendix of Ref. [3].

As mentioned above, the di-leptonic system cannot be solved by on-shell mass relations even if Higgs boson masses are known. However, there is an approximation scheme to solve the unknown neutrino momenta with the help of $M_{\rm T2}$. When the minimization has been finalized to obtain the $M_{\rm T2}$ value, a unique solution for the transverse momentum configuration is picked up. One may attempt to see the correlation between these hypothetical momentum components and the true

[9] The application of $M_{\rm T2}$ to the SM process was firstly proposed in Ref. [223] for measuring the top quark mass in the di-leptonic $t\bar{t}$ process. It is later employed and checked its efficiency in the real experimental analyses measuring the top quark mass at both Tevatron and the LHC [224–226].

ones. For a subset of events whose $M_{\rm T2}$ values are close to $M_{\rm T2}^{\rm max}$, it can be shown that the $M_{\rm T2}$ solution of the transverse momenta are very close or equal to the true momenta. This can be justified by the fact that the $M_{\rm T2}$ solution is unique while preserving kinematic constraints,[10] and the endpoint of the transverse mass corresponds to the invariant mass of the decaying system, *i.e.*, the parent particle mass. Then, by adopting the $M_{\rm T2}$ solution of the invisible transverse momenta in conjunction with known on-shell mass relations, one can calculate the longitudinal and energy components of the invisible four-momenta. This is so-called $M_{\rm T2}$-assisted on-shell (MAOS) approximation scheme [230]. One drawback of this scheme is that it cannot be applied if any of the parent particles are off-shell. However, it has been claimed that one can circumvent the on-shell mass problem by plugging the transverse mass for the decay chain instead of the invariant mass into the on-shell mass relation [227, 228, 231]. This means that the on-shell mass relations now become

$$(p + k^{\rm maos})^2 = \left(M_{\rm T}^{(1)}\right)^2, \quad (q + l^{\rm maos})^2 = \left(M_{\rm T}^{(2)}\right)^2. \tag{3.20}$$

This modified scheme guarantees that there is always a real solution for the invisible momenta since the transverse mass is bounded from above by the invariant mass, and it maintains the property that the MAOS momentum is equal to the true momentum for the endpoint events of $M_{\rm T2}$, see the left panel of Figure 3.8, where the efficiency of approximation to the invisible momenta in the modified scheme is shown. Since the light Higgs boson mass here is set at 125 GeV $< 2m_W$, one or both W bosons produced by the Higgs boson are always off-shell. In this situation, the modified MAOS scheme Eq. (3.20) can be applied. Once the MAOS momentum has been obtained, one can construct the invariant mass of the total system, which corresponds to the heavy singlet-like Higgs boson mass, given by

$$(m_H^{\rm maos})^2 \equiv \left(p^b + p^{\bar{b}} + p^\ell + q^\ell + k^{\rm maos} + l^{\rm maos}\right)^2 \simeq m_H^2. \tag{3.21}$$

Strictly speaking, the equality holds only when $k^{\rm maos} = k^{\rm true}$ and $l^{\rm maos} = l^{\rm true}$. The right panel of Figure 3.8 shows $m_H^{\rm maos}$ distributions for the heavy Higgs signal and the SM double-Higgs as well as $t\bar{t}$ backgrounds using the parton-level MC event samples. One can see that the peak position of the signal distribution clearly matches the m_H value, while broad distributions are exhibited in the non-resonant background process.

Armed with these tools, we now discuss our analysis to search for the heavy Higgs signal. After reconstructing the final-state objects, we select events that passed the basic cuts, given as follows.

- At least two isolated, opposite-sign leptons including the electron or the muon, *i.e.*, $e^\pm e^\mp$, $\mu^\pm\mu^\mp$, and $e^\pm\mu^\mp$. We further require that one of them must have $p_{\rm T} > 20$ GeV,
- At least two b-tagged jets with $p_{\rm T} > 30$ GeV,

[10] The $M_{\rm T}^{(i)}$ $(i = 1, 2)$ functions are ellipses in the phase space and the $M_{\rm T2}$ value is determined by their intersecting point in the balanced configuration. This feature can be used to seek the $M_{\rm T2}$ value by using a sophisticated algorithm proposed in Ref. [229].

- Missing energy $\not{E}_{\rm T} > 20$ GeV,
- For the opposite-sign same-flavor leptons, the event is rejected if $m_{\ell^+\ell^-} < 12$ GeV to avoid the leptons produced by decays of the hadrons. The Z-veto condition, which discards events containing $|m_{\ell^+\ell^-} - m_Z| < 15$ GeV, is also imposed.

We note that all the cut values have been chosen to optimize the signal significance. In the signal events, all the leptons are produced in the $h \to WW^*$ decay process. In this case, it is known that the spin correlations of the decay mode make the charged leptons collinear. This feature can be used to further reduce the leptonic backgrounds. We use two angular cuts: the azimuthal angular difference $|\Delta\phi_{\ell\ell}| < 1.32$ (1.57) and $\Delta R_{\ell\ell} \equiv \sqrt{(\Delta\phi_{\ell\ell})^2 + (\Delta\eta_{\ell\ell})^2} < 1.34$ (1.58) for the Higgs signal with $m_H = 400$ (260) GeV. The upper frames in Figure 3.9 show a clear separation between the signal and the $t\bar{t}$ background, particularly when $m_H = 400$ GeV. This is because the leptons can be much more boosted in the heavy Higgs events than in the light Higgs ones. The collinearity of leptons is also encoded in the other cut variables, the sum of the transverse momenta $p_{\rm T}^{\ell\ell} = |\mathbf{p}_{\rm T}^{\ell} + \mathbf{q}_{\rm T}^{\ell}|$ and the di-lepton invariant mass $m_{\ell\ell}$. In the case when $m_H = 260$ GeV, the leptons are less energetic so that $p_{\rm T}^{\ell\ell}$ is relatively soft; see the lower frames in Figure 3.9. We require that $p_{\rm T}^{\ell\ell} > 42$ (25) GeV and $m_{\ell\ell} < 60$ (47) GeV for the $m_H = 400$ (260) GeV scenarios. The $m_{\ell\ell}$ cut can also remove the $Z \to \tau^+\tau^-$ events in which the tau leptons decay leptonically.

In addition to the basic selection and the leptonic cuts, one can impose cuts on the b-jets. Recently, a boosted Higgs technique has been developed for processes like $pp \to hV$ ($V = W$, Z) [232] or $pp \to hh$ [233], followed by $h \to b\bar{b}$. In the situation where the Higgs boson is substantially boosted, the jets produced by the Higgs boson can often be considered as one fat jet, whose mass is around m_h. For very high $p_{\rm T}^h \gg m_h$, $\Delta R_{bb} \equiv \sqrt{(\Delta\phi_{bb})^2 + (\Delta\eta_{bb})^2}$ can be estimated to be

$$\Delta R_{bb} \simeq \frac{2m_h}{p_T^h}. \tag{3.22}$$

If the fat Higgs jet condition could be applied, the backgrounds, in particular the $t\bar{t}$ events, would be reduced very efficiently since the b-jets in the background can have a relatively large angular separation. In the Higgs signal, $p_{\rm T}^h$ can be as large as

$$p_{\rm T}^h = \frac{m_H}{2}\sqrt{1 - \frac{4m_h^2}{m_H^2}} \simeq 156 \text{ GeV}. \tag{3.23}$$

so $\Delta R_{bb} \simeq 1.6$ for $m_H = 400$ GeV in the rest frame of the heavy Higgs boson. The left panel in the upper frames of Figure 3.10 justifies this estimation. Normally, the fat Higgs jet is required to have $\Delta R_{bb} \sim 1.2$ – 1.5 or $p_{\rm T}^h \gtrsim 200$ GeV. Provided that the heavy Higgs boson is produced at near-threshold energy, the transverse momentum of the light Higgs has an upper bound as given in Eq. (3.23). Therefore, we expect that the boosted Higgs technique will be applicable in the case of much heavier Higgs boson with $m_H \gtrsim 490$ GeV.

In our benchmark points, it is inevitable to use the conventional kinematic cuts. Although the angular separations of the b-jets are rather sizable, they are still smaller than the backgrounds when $m_H = 400$ GeV, while the cut can be applied in the opposite way when $m_H = 260$ GeV. This

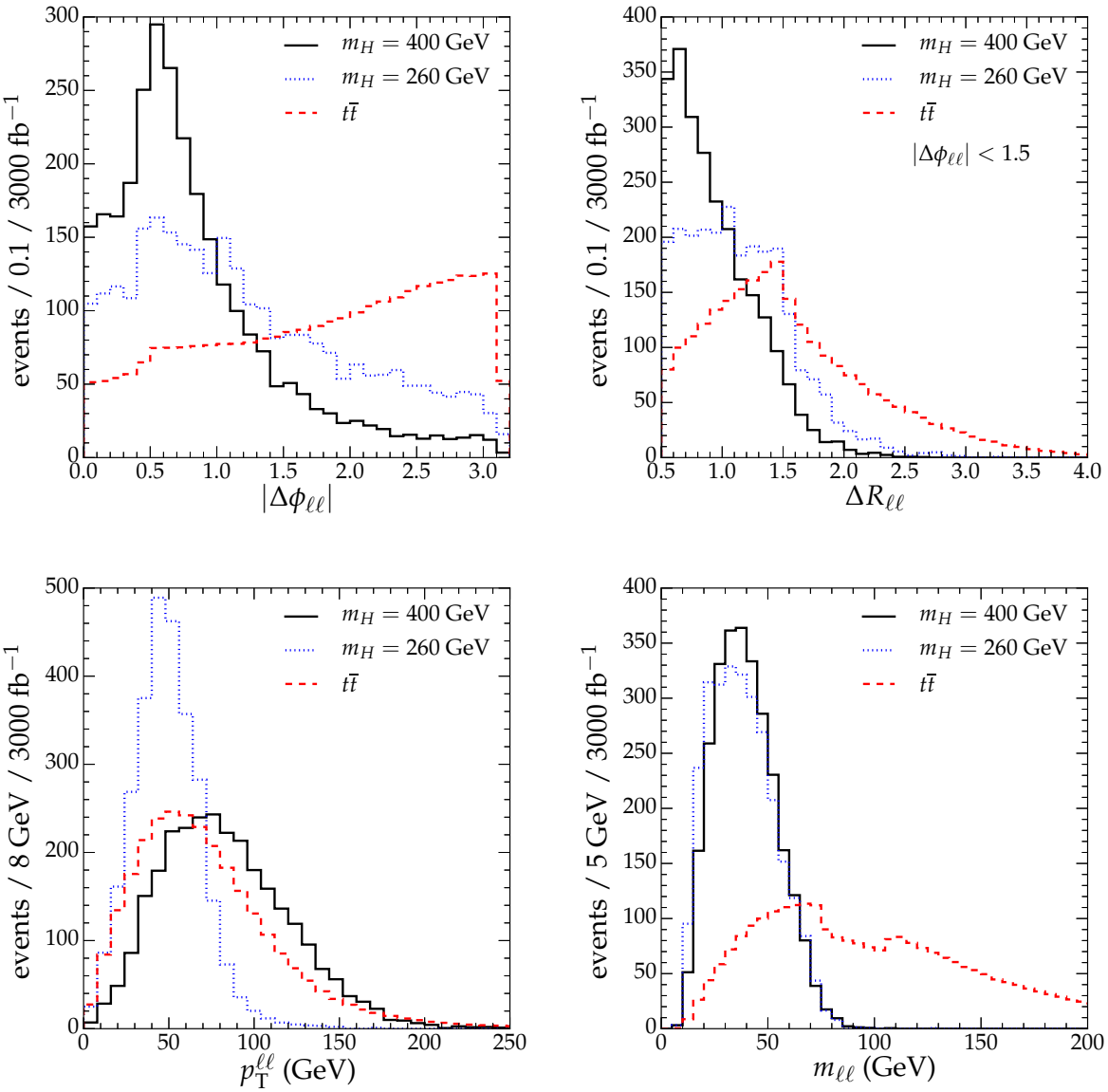

Figure 3.9: Detector-level distributions of the kinematic variables for the two charged leptons. The upper frames are (Left panel) the azimuthal angular separations and (Right panel) the $\Delta R_{\ell\ell}$ when applying the azimuthal angular cut has been imposed. The lower frames are (Left panel) the sum of transverse momenta $p_{\mathrm{T}}^{\ell\ell}$ and (Right panel) the invariant mass $m_{\ell\ell}$ distributions. Basic selection cuts are applied and all the distributions are normalized for an illustration.

can be easily deduced from Eq. (3.22), which predicts that the angular separation can be very large for the smaller p_{T}^{h} value. On the other hand, the right panel in the upper frames of Figure 3.10

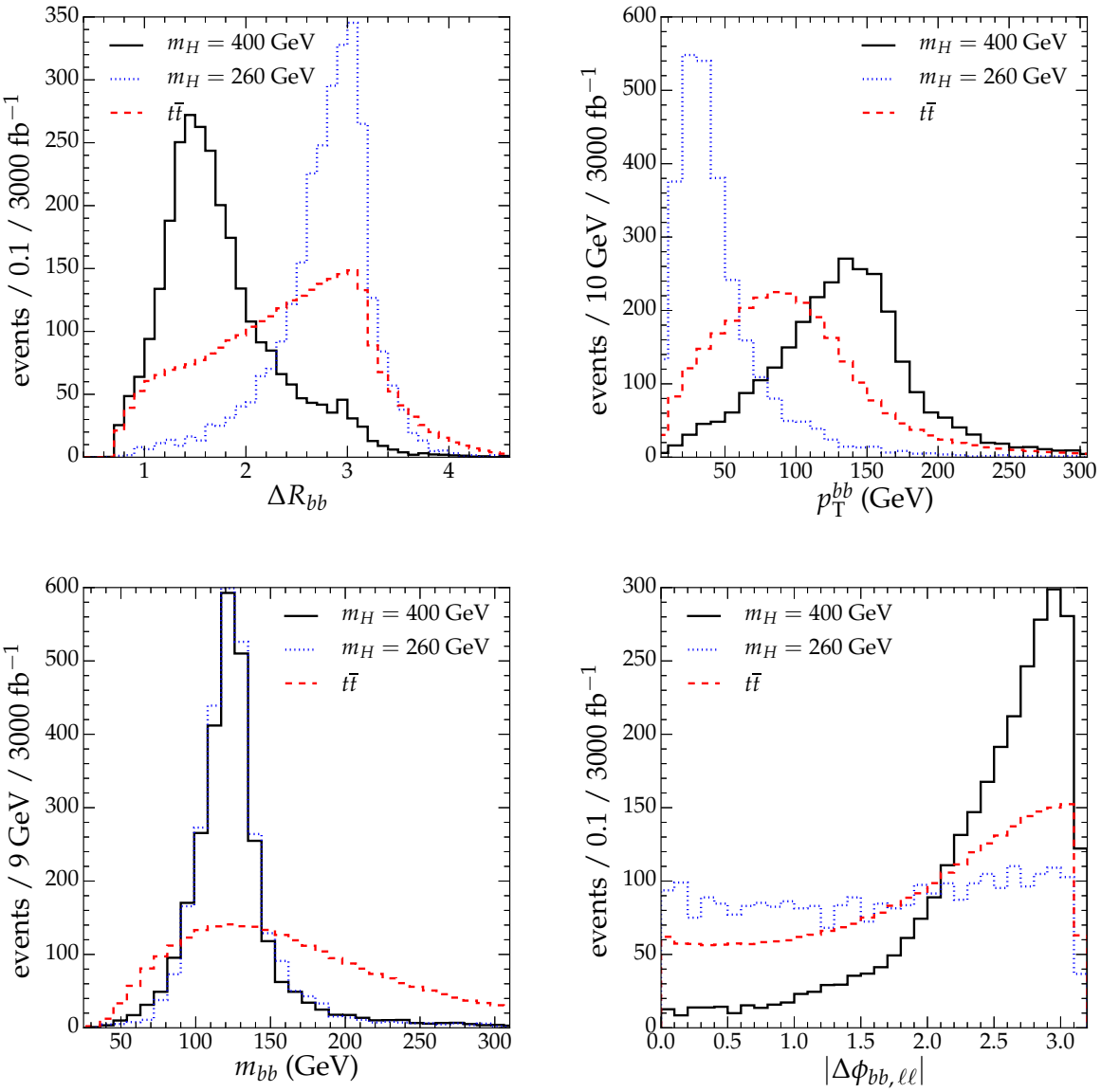

Figure 3.10: Detector-level distributions of the kinematic variables for the two b-tagged jets. The upper frames are (Left panel) ΔR_{bb} and (Right panel) the transverse momentum p_{T}^{bb}. The lower frames are (Left panel) the di-b-jet invariant mass and (Right panel) the azimuthal angular separation between $b\bar{b}$ and $\ell^+\ell^-$ systems. Basic selection cuts are applied and all the distributions are normalized for an illustration.

shows that the $m_H = 400$ GeV signal events presents much larger values of the total transverse momentum that the $m_H = 260$ GeV one for the $b\bar{b}$ system. We select events with $\Delta R_{bb} < 2.25$ and $p_{\mathrm{T}}^{bb} > 105$ GeV for $m_H = 400$ GeV, while $\Delta R_{bb} > 2.56$ without imposing any p_{T}^{bb} cut for $m_H = 260$

GeV signal events. Since the m_h value is already known, one can further impose a cut on the di-b-jet invariant mass to ensure that the b-jets are originated from the light Higgs boson. One can see that the invariant mass distributions have clear peaks around $m_h = 125$ GeV, for both benchmark points, in the left panel in the lower frames of Figure 3.10. The invariant mass is required to lie within 115 (94) GeV $< m_{bb} <$ 146 (135) GeV for $m_H = 400$ (260) GeV signal.

In the case when the heavy Higgs boson is produced near threshold, the light Higgs boson pair will be almost in a back-to-back configuration. Then, it is likely that the direction of the $b\bar{b}$ system will be well separated from that of the $\ell^+\ell^-$ system. This feature can be seen in the right panel in the lower frames of Figure 3.10, where the distributions for the absolute value of $\Delta\phi_{bb,\,\ell\ell} \equiv \cos^{-1}(\hat{\mathbf{p}}_{\rm T}^{bb} \cdot \hat{\mathbf{p}}_{\rm T}^{\ell\ell})$, where $\hat{\mathbf{p}}_{\rm T} \equiv \mathbf{p}_{\rm T}/p_{\rm T}$, are shown. We take events with $|\Delta\phi_{bb,\,\ell\ell}| > 1.92$ for the $m_H = 400$ GeV signal. This cut is not applicable to the $m_H = 260$ GeV signal, as the angular separation can be relatively small due to the small boost of each Higgs decay chain.

We now turn to the $M_{\rm T2}$ cuts. For the $2b + 2\ell + \not{E}_{\rm T}$ final state, one can construct two kinds of $M_{\rm T2}$ according to the definition for the visible + invisible system, that is, either $2\ell + \not{E}_{\rm T}$, which contains only leptons, or $2b + 2\ell + \not{E}_{\rm T}$, which contains b-jets as well as leptons when forming the visible particle system. We emphasize that $M_{\rm T2}$ is known to be applicable to systems that can be divided into two groups of visible particles, like processes depicted in the decay topology Eq. (3.16) with a pair production of heavy particles, followed by two separate decay chains. The $2\ell + \not{E}_{\rm T}$ system in the signal decay topology Eq. (3.15) can be regarded as a process of this type. In what follows, the $M_{\rm T2}$ calculated for the $2\ell + \not{E}_{\rm T}$ system is expressed as $M_{\rm T2}^{\ell\ell}$ to distinguish it from the other kind of $M_{\rm T2}$. As is derived in the Appendix of Ref. [3] for some kinematic configurations the $M_{\rm T2}^{\ell\ell}$ distribution is bounded from above by $m_h/2 < m_W$, whereas it has a maximum at m_W in the di-leptonic $t\bar{t}$ process, since both W bosons are in on-shell. The $M_{\rm T2}^{\ell\ell}$ distributions in the left panel of Figure 3.11 clearly show the endpoint structure. Another notable feature is that there are a number of events which have vanishing $M_{\rm T2}^{\ell\ell}$ for both signal and background distributions. They correspond to a trivial zero of $M_{\rm T2}^{\ell\ell}$ in the fully massless case, *i.e.*, $m_\ell = m_\nu = 0$ [234]. This happens when the missing transverse momentum $\not{\mathbf{p}}_{\rm T}$ lies on the smaller sector of the transverse plane spanned by the visible momentum vectors $\mathbf{p}_{\rm T}^{\ell}$ and $\mathbf{q}_{\rm T}^{\ell}$. In this case, the $M_{\rm T2}^{\ell\ell}$ value is taken for a momentum partition where both transverse masses in Eqs. (3.18) are vanishing. However, the fraction of events with the trivial zero of the $M_{\rm T2}^{\ell\ell}$ can be different depending on the preferred momentum configuration of the process. Due to the spin correlation and the boost, the opening angle of the charged leptons in the Higgs signal event is smaller than that in the di-leptonic $t\bar{t}$ events, as can be seen in the upper frames of Figure 3.9. This means that there are more chances to have the trivial zero of $M_{\rm T2}^{\ell\ell}$ in the $t\bar{t}$ events than in the Higgs signal. Therefore, the lower cut, as well as the upper one, can help reduce the backgrounds further. This lower cut on the $M_{\rm T2}^{\ell\ell}$ also increases the accuracy of the MAOS momenta, which will be used in the subsequent analysis. We impose the $M_{\rm T2}^{\ell\ell}$ cut as 25 GeV $< M_{\rm T2}^{\ell\ell} <$ 60 GeV for the $m_H = 260$ GeV signal. In the case when $m_H = 400$ GeV, the missing transverse momentum vector can lie inside of the opening angle of the di-lepton system when the light Higgs is fairly boosted. Therefore, we do not apply the lower cut, so only the upper cut $M_{\rm T2}^{\ell\ell} < 60$ GeV is imposed for the $m_H = 400$ GeV signal.

Once $M_{\rm T2}^{\ell\ell}$ has been calculated, one can construct the invariant mass of the $2\ell + \not{E}_{\rm T}$ system

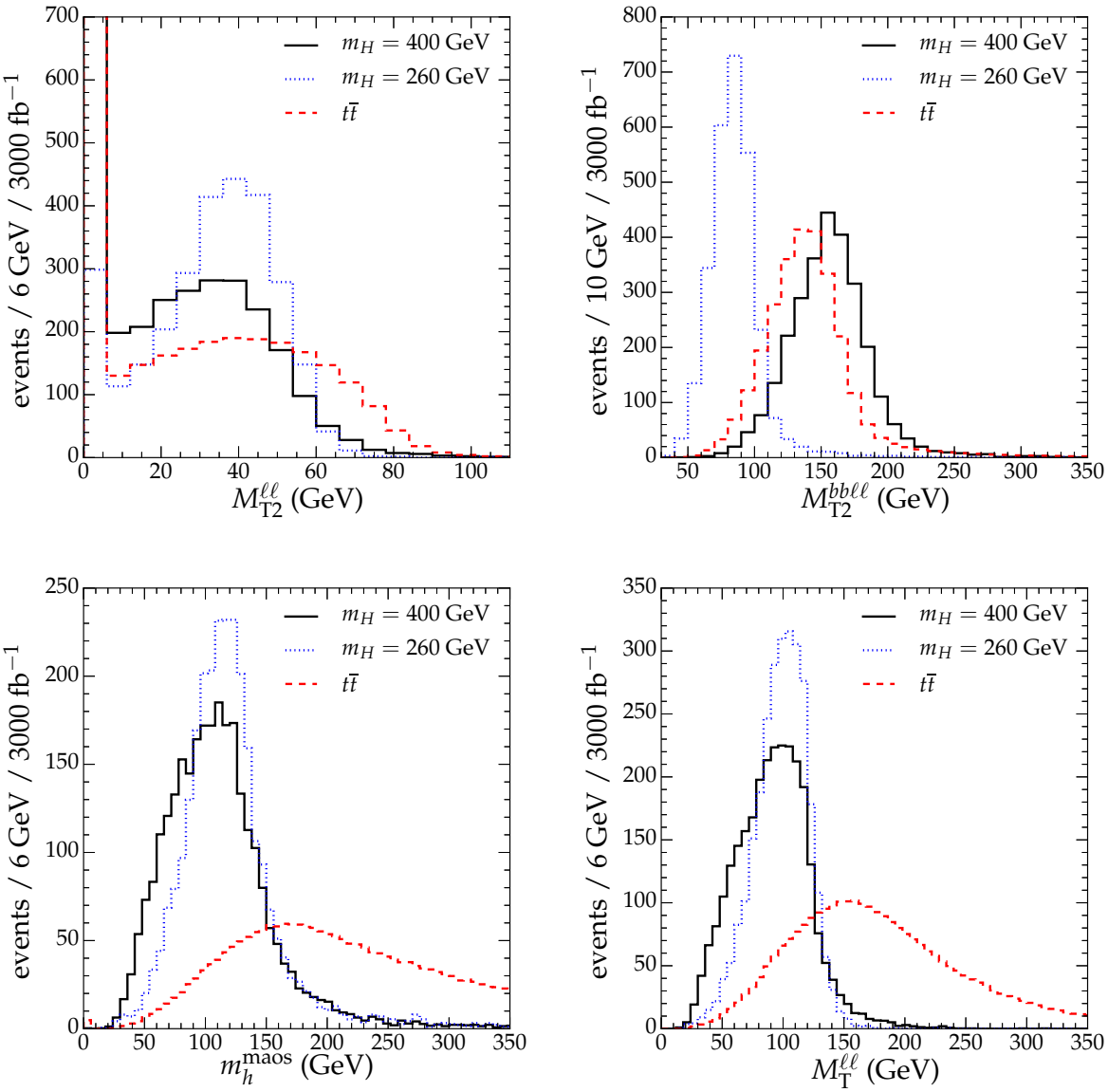

Figure 3.11: The upper frames are detector-level M_{T2} distributions for (Left panel) the $2\ell + \not{E}_{\mathrm{T}}$ and (Right panel) $2b + 2\ell + \not{E}_{\mathrm{T}}$ systems. The lower frame are (Left panel) m_h^{maos} and (Right panel) $M_{\mathrm{T}}^{\ell\ell}$ distributions for detector-level signals and backgrounds. Basic selection cuts are applied and all the distributions are normalized for an illustration.

by using the MAOS momentum of the invisible particle, given by

$$(m_h^{\mathrm{maos}})^2 \equiv \left(p^\ell + q^\ell + k^{\mathrm{maos}} + l^{\mathrm{maos}}\right)^2, \tag{3.24}$$

which equals to m_h when $k^{\mathrm{maos}} = k^{\mathrm{true}}$ and $l^{\mathrm{maos}} = l^{\mathrm{true}}$. It is shown in the lower-left panel of

Figure 3.11. One can further employ the transverse mass of the leptonic system, ignoring the unknown $m_{\nu\nu}$ value and the longitudinal momentum components of neutrinos,

$$\left(M_{\rm T}^{\ell\ell}\right)^2 = m_{\ell\ell}^2 + 2\left(\sqrt{|\mathbf{p}_{\rm T}^{\ell\ell}|^2 + m_{\ell\ell}^2}|\not{\mathbf{p}}_{\rm T}| - \mathbf{p}_{\rm T}^{\ell\ell}\cdot\not{\mathbf{p}}_{\rm T}\right), \tag{3.25}$$

which is bounded from above by m_h [235]. Since both distributions have distinguishable peak and edge structures as well as a strong correlation with m_h, we use them as cut variables demanding $m_h^{\rm maos} < 145$ GeV and 30 GeV $< M_{\rm T}^{\ell\ell} < 125$ GeV for $m_H = 400$ GeV, and 60 GeV $< m_h^{\rm maos} < 136$ GeV and 58 GeV $< M_{\rm T}^{\ell\ell} < 126$ GeV for $m_H = 260$ GeV signal events. We have not applied the lower cut on $m_h^{\rm maos}$ for $m_H = 400$ GeV since the distribution is relatively distorted due to the trivial zero solutions described above.

After counting two b-jets as well as the charged leptons among the set of visible particle system, *i.e.*, $V = b\ell$, one can define another kind of $M_{\rm T2}$ variable, denoted as $M_{\rm T2}^{bb\ell\ell}$.[11] Recall that $M_{\rm T2}$ aims at the physics of processes describable by the decay topology Eq. (3.16). The Higgs signal has a different decay topology since the invisible particle system is disjointed from the $b\bar{b}$ system. On the other hand, it is well known that the di-leptonic $t\bar{t}$ process is one of the SM processes where the $M_{\rm T2}$ variable is applicable since the decay topology is exactly the same as Eq. (3.16), and the $M_{\rm T2}^{bb\ell\ell}$ distribution is strictly bounded from above by m_t. Therefore, one can still attempt to employ $M_{\rm T2}^{bb\ell\ell}$ to reduce the $t\bar{t}$ backgrounds if the edge structure of the signal distribution has a certain amount of deviation from m_t. The $M_{\rm T2}^{bb\ell\ell}$ distributions for both, signal and $t\bar{t}$, are shown in the right panel of Figure 3.11.

Before going further, let us briefly summarize the types of the $M_{\rm T2}$ solutions for the invisible momenta. The hypothetical invisible momentum configuration that gives the $M_{\rm T2}$ value can be classified in two types. One is a balanced configuration, in which $M_{\rm T}^{(1)} = M_{\rm T}^{(2)}$ is realized, and the other is an unbalanced one, in which $M_{\rm T}^{(1)} \neq M_{\rm T}^{(2)}$ [222]. In each collider event, only one type of the momentum configuration provides the $M_{\rm T2}$ value, which can be deduced by the invariant masses of the visible particle set in the event, m_V and $m_{\overline{V}}$ in Eqs. (3.18). One can easily find that a stationary value of the transverse mass $M_{\rm T}^{(1)}$ is attained when $\mathbf{k}_{\rm T} = m_\chi \mathbf{p}_{\rm T}/m_V$ and $\mathbf{l}_{\rm T} = \not{\mathbf{p}}_{\rm T} - \mathbf{k}_{\rm T}$. Then,

$$M_{\rm T}^{(1)} = m_V + m_\chi, \tag{3.26}$$

which is called an unconstrained minimum of the transverse mass. Similarly, one can find the stationary value of $M_{\rm T}^{(2)} = m_{\overline{V}} + m_\chi$. For each stationary point, the $M_{\rm T}^{(1)}$ value can be compared to $M_{\rm T}^{(2)}$. In the case that

$$M_{\rm T}^{(1)}\Big|_{\mathbf{k}_{\rm T}=m_\chi\mathbf{p}_{\rm T}/m_V} = m_V + m_\chi > M_{\rm T}^{(2)}\Big|_{\mathbf{l}_{\rm T}=\not{\mathbf{p}}_{\rm T}-\mathbf{k}_{\rm T}}, \tag{3.27}$$

$M_{\rm T2}$ is given by the unconstrained minimum of $M_{\rm T}^{(1)}$, *i.e.*,

$$M_{\rm T2} = m_V + m_\chi. \tag{3.28}$$

[11] There is an ambiguity of how to pair one b-jet to one charged lepton because there can be two possible pairings in each event. Here, we define $M_{\rm T2}^{bb\ell\ell}$ as the smaller one between two possible values of $M_{\rm T2}^{bb\ell\ell}$. This definition matches the one used to measure the top quark mass using $M_{\rm T2}$ in Ref. [223].

This corresponds to the unbalanced configuration. On the other hand, if it is satisfied that

$$\begin{aligned} M_{\mathrm{T}}^{(1)}\Big|_{\mathbf{k}_{\mathrm{T}}=m_\chi \mathbf{p}_{\mathrm{T}}/m_V} &= m_V + m_\chi \leq M_{\mathrm{T}}^{(2)}\Big|_{\mathbf{l}_{\mathrm{T}}=\not{\mathbf{p}}_{\mathrm{T}}-\mathbf{k}_{\mathrm{T}}}, \\ M_{\mathrm{T}}^{(2)}\Big|_{\mathbf{l}_{\mathrm{T}}=m_\chi \mathbf{q}_{\mathrm{T}}/m_{\overline{V}}} &= m_{\overline{V}} + m_\chi \leq M_{\mathrm{T}}^{(1)}\Big|_{\mathbf{k}_{\mathrm{T}}=\not{\mathbf{p}}_{\mathrm{T}}-\mathbf{l}_{\mathrm{T}}}, \end{aligned} \tag{3.29}$$

then M_{T2} is given by the balanced configuration in which $M_{\mathrm{T}}^{(1)} = M_{\mathrm{T}}^{(2)}$. For a detailed discussion of the momentum configuration types and their corresponding properties of M_{T2}, see Refs. [222, 236–238].

In the case of $M_{\mathrm{T2}}^{\ell\ell}$, the M_{T2} value is always given by the balanced configuration since $m_\ell = m_\nu = 0$. On the other hand, because $m_{b\ell}$ is not a constant but a variable, there exist sort of events in which the unbalanced configuration is selected to provide the $M_{\mathrm{T2}}^{bb\ell\ell}$ value. In the di-leptonic $t\bar{t}$ process,

$$m_{b\ell} \leq \sqrt{m_t^2 - m_W^2} \simeq 154 \text{ GeV} \tag{3.30}$$

when the b quark mass is neglected. Therefore, the unbalanced $M_{\mathrm{T2}}^{bb\ell\ell}$ has a maximum value smaller than m_t, while the balanced M_{T2} value can be as large as m_t. This means that the overall $M_{\mathrm{T2}}^{bb\ell\ell}$ distribution is bounded from above by the maximum of the balanced $M_{\mathrm{T2}}^{bb\ell\ell}$ values. For the Higgs signal, the situation is different. If one considers the case when the total transverse momentum of the whole system is vanishing, or equivalently, the heavy Higgs has been produced at rest on the transverse plane, one can find that the balanced $M_{\mathrm{T2}}^{bb\ell\ell}$ value cannot exceed $m_H/2$ by a similar consideration as done in the Appendix of Ref. [3]. However, from Eq. (3.28), the unbalanced $M_{\mathrm{T2}}^{bb\ell\ell}$ has an upper bound at $m_{b\ell}^{\max}$, which can be expressed analytically as

$$m_{b\ell}^{\max} = \frac{m_H m_W}{2m_h}\left(1 + \sqrt{1 - \frac{4m_h^2}{m_H^2}}\right) \simeq 229 \text{ GeV} \tag{3.31}$$

for $m_H = 400$ GeV, while it is $\simeq 107$ GeV for $m_H = 260$ GeV. The maximum value in the above equation is achieved when one of the hypothetical neutrino momenta chosen by the $M_{\mathrm{T2}}^{bb\ell\ell}$ calculation is parallel to the momentum direction of the charged lepton sharing the same parent particle, while the other one is anti-parallel.[12] The $m_{b\ell}$ distributions for various m_H values and the $M_{\mathrm{T2}}^{bb\ell\ell}$ distributions classified by the types of the $M_{\mathrm{T2}}^{bb\ell\ell}$ solutions are shown in Figure 3.12, using the parton-level data for the sake of a numerical demonstration. This also means that the endpoint of $M_{\mathrm{T2}}^{bb\ell\ell}$, as well as the $m_{b\ell}$ distributions for the Higgs signal events, will be smaller than m_t if $m_H \lesssim 330$ GeV, and, in that case, the upper cut should be used instead of the lower one unless the upper bound value is too close to m_t. This observation may lead one to deduce that the efficiency of the $M_{\mathrm{T2}}^{bb\ell\ell}$ cut might be the similar as that of the $m_{b\ell}$ cut. However, in our numerical study, the $M_{\mathrm{T2}}^{bb\ell\ell}$ cut turns out to perform slightly better than $m_{b\ell}$. This might be because $M_{\mathrm{T2}}^{bb\ell\ell}$ incorporates the effect of the missing momentum and its correlation with the visible momenta. We set the event

[12] We note that $m_{b\ell}^{\max}$ for the Higgs signal is not a global maximum for all possible $b\ell$ pairings, but the maximum for a pair which leads to the smaller value of $M_{\mathrm{T2}}^{bb\ell\ell}$.

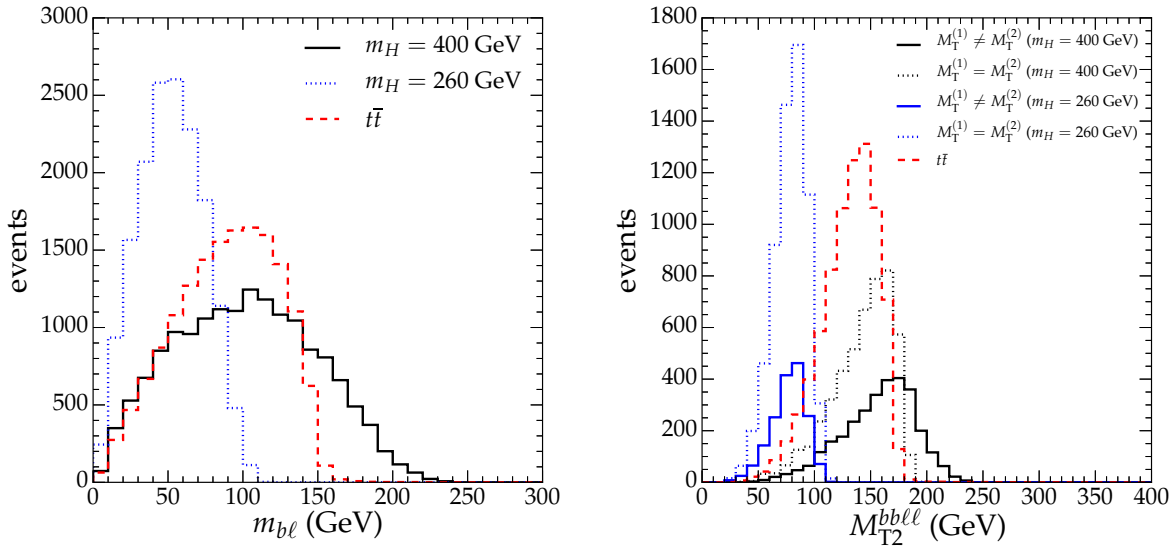

Figure 3.12: Parton-level distributions for (Left panel) $m_{b\ell}$ when $m_H = 260$ and 400 GeV and (Right panel) $M_{\rm T2}^{bb\ell\ell}$ classified by the types of the invisible momentum configuration chosen by the $M_{\rm T2}$ calculation. See the text for detailed explanation. For a comparison, distributions for the di-leptonic $t\bar{t}$ process are shown.

selection cut value as $M_{\rm T2}^{bb\ell\ell} > 165$ GeV for $m_H = 400$ GeV and $M_{\rm T2}^{bb\ell\ell} < 96$ GeV for $m_H = 260$ GeV signals.

When considering final-state particles all together, the simplest kinematic variables that one can construct are the invariant mass of the total visible system, $m_{bb\ell\ell}$, and the transverse mass of the full system including the missing energy. Since the full visible + invisible system has a fixed invariant mass, *i.e.*, m_H, the invariant mass of the visible system also has a dependency on m_H for its maximal value. One can find that

$$m_{bb\ell\ell}^2 \leq \frac{m_H^2}{2}\left(1 + \sqrt{1 - \frac{4m_h^2}{m_H^2}}\right) \simeq (377\ \text{GeV})^2 \tag{3.32}$$

for $m_H = 400$ GeV, whereas there is no definite cut-off in the $t\bar{t}$ background since $m_{t\bar{t}}$ is a variable of the event in the hadron collider, see the left panel of Figure 3.13. Since the lower bound is fixed as $m_{b\bar{b}} = m_h = 125$ GeV in the signal events, only the upper cut on $m_{bb\ell\ell}$ variable can be applied. For the benchmark point with $m_H = 400$ (260) GeV, we set the cut as $m_{bb\ell\ell} < 395$ (200) GeV. This cut becomes important in the case of a heavy Higgs with lower mass value, like in the case of $m_H = 260$ GeV, since it is capable of taking more stronger cut value. The other useful kinematic variable is the transverse mass of the full system, defined as

$$\left(M_{\rm T}^{bb\ell\ell}\right)^2 = m_{bb\ell\ell}^2 + 2\left(\sqrt{|\mathbf{p}_{\rm T}^{bb\ell\ell}|^2 + m_{bb\ell\ell}^2}|\not{\mathbf{p}}_{\rm T}| - \mathbf{p}_{\rm T}^{bb\ell\ell}\cdot\not{\mathbf{p}}_{\rm T}\right), \tag{3.33}$$

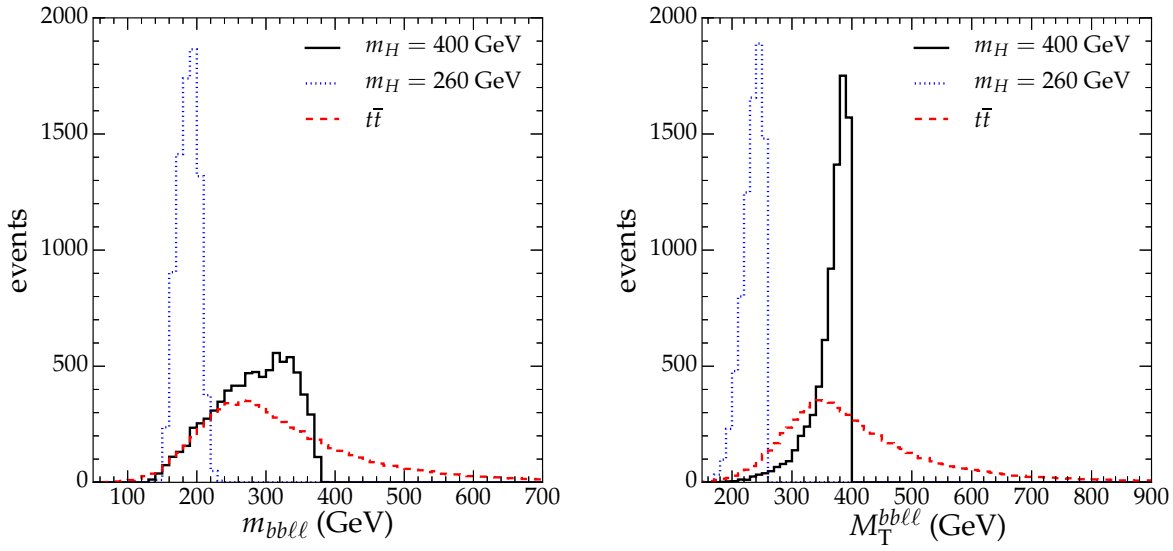

Figure 3.13: Normalized distributions for (Left panel) $m_{bb\ell\ell}$ and (Right panel) $M_{\rm T}^{bb\ell\ell}$ distributions for $m_H = 260$ and 400 GeV and the $t\bar{t}$ backgrounds using parton-level data.

where $\mathbf{p}_{\rm T}^{bb\ell\ell} \equiv \mathbf{p}_{\rm T}^{b} + \mathbf{p}_{\rm T}^{\bar{b}} + \mathbf{p}_{\rm T}^{\ell} + \mathbf{q}_{\rm T}^{\ell}$ is the total visible transverse momentum. Here, the unknown $m_{\nu\nu}$ is ignored. When all the visible particles are on the transverse plane and the neutrino momentum vectors are collinear, so that the $m_{\nu\nu}$ is vanishing, the transverse mass is equivalent to the invariant mass of the full system, *i.e.*, m_H. This means that the transverse mass is bounded from above by m_H, as can be seen in the right panel of Figure 3.13. In the real situation, the endpoint of the distribution is often smeared by the backgrounds and/or poor reconstruction efficiency of the final-state objects. Still, since the peak position is near the endpoint, it can provide an lower bound on m_H. On the other hand, the transverse mass has some correlation with the MAOS invariant mass, as discussed in Ref. [228]. They select the similar types of events in the phase space, and the efficiency is comparable to each other. We use both two variables to suppress backgrounds and define the signal region.

Combining all the cuts discussed so far, we examine their effects on the signal and the backgrounds by investigating how the cross sections are changing by applying them. See Tables 3.3 and 3.4 for $m_H = 400$ and 260 GeV, respectively. The unlisted backgrounds turned out to be almost negligible after applying the initial cuts. In summary, although the production cross section for $m_H = 400$ GeV is smaller than that of $m_H = 260$ GeV, the signal can be distinguished by several angular cut variables, as well as the cut on $M_{\rm T2}^{bb\ell\ell}$. We have found a set of kinematic variables useful for the search. Eventually, the scenarios with a relatively lighter singlet-like Higgs boson are quite difficult to probe by using the kinematic event variables. In this case, one can still attempt to combine the search results from the other channels like $bb\tau\tau$ and $bbZZ$, which have the next-to-subleading branching fractions, or a multivariate analysis, like the performed in Ref. [233]. If m_H

Selection cuts	$H \to hh$	$t\bar{t}$	GGF h	$ht\bar{t}$	hh	DY	VV	$\hat{\sigma}_{3000}$
Basic selection	0.54	3560.36	0.15	0.072	0.024	272.41	0.90	0.48
$\Delta\phi_{\ell\ell}$, $\Delta R_{\ell\ell}$, $p_{\rm T}^{\ell\ell}$	0.40	562.02	0.11	0.015	0.019	33.56	0.047	0.90
$m_{\ell\ell}$, $M_{\rm T2}^{\ell\ell}$	0.36	314.95	0.097	0.009	0.017	11.20	0.0	1.1
$m_h^{\rm maos}$, $M_{\rm T}^{\ell\ell}$	0.33	237.96	0.097	0.007	0.015	11.20	–	1.2
ΔR_{bb}, $p_{\rm T}^{bb}$	0.23	73.03	0.008	0.002	0.012	3.73	–	1.4
m_{bb}	0.14	16.24	0.0	$\simeq 0.0$	0.007	0.0	–	1.9
$\Delta\phi_{bb,\,\ell\ell}$, $m_{bb\ell\ell}$	0.13	11.99	–	–	0.005	–	–	2.1
$M_{\rm T2}^{bb\ell\ell}$	0.059	1.31	–	–	0.004	–	–	2.8
Signal region	0.048	0.70	–	–	$\simeq 0.0$	–	–	3.1

Table 3.3: Cut flow of signals for $m_H = 400$ GeV and the main backgrounds in fb. See the text for detailed description of the event selection cuts applied. VV denotes the di-boson processes ($V = W$, Z). $\hat{\sigma}_{3000}$ is the signal significance calculated with a Poisson probability at 3000 fb^{-1} integrated luminosity. The signal region is defined by 345 GeV $< M_{\rm T}^{bb\ell\ell} <$ 425 GeV and 350 GeV $< m_H^{\rm maos} <$ 430 GeV.

is much larger than 400 GeV, it is expected that the boosted Higgs technique approach is more promising.

Up to now, we have assumed that BR($H \to hh$) ~ 1. This can be fulfilled in a large (λ_{22}, λ_{03}, λ_{03}) parameter-space region. We now relax this condition and suppose that the SM Higgs-like decays originated by the mixing are non-negligible. In this case, for a given m_H value, we can evaluate bounds on the mixing using the ATLAS and CMS data on heavy Higgs searches [239], as shown in Figure 3.4. The most stringent exclusion limit comes from the CMS search [200, 201]. This search is focused on the combination of the $4\ell/2\ell 2\tau$ final states in the $H \to ZZ$ channel assuming that the heavy Higgs only decays into SM particles, *i.e.*, BR($H \to hh$) is vanishing. The maximal mixing angle allowed by this search for $m_H = 260$ GeV is $\sin^2\alpha < 0.06$ (95% C.L.), while for $m_H = 400$ GeV it is $\sin^2\alpha < 0.11$ (95% C.L.). If BR($H \to hh$) is non-vanishing, the latter constraints become weaker. The excluded $\sin^2\alpha$ values for given BR($H \to hh$) are represented in the light gray region of Figure 3.14 for both $m_H = 260$ GeV and $m_H = 400$ GeV. On the other hand, the constraints imposed by the EWPO and the LHC, shown as dark gray region in Figure 3.14, are independent of BR($H \to hh$). This is because they come from the modification of the couplings, parameterized by the mixing angle α, while the ones derived from the heavy Higgs searches depend directly on the value of BR($H \to hh$). One can also see the interplay between direct and indirect constraints in Figure 3.14. For $m_H = 260$ GeV, the direct search result on $H \to ZZ$ imposes the most stringent bound, up to BR($H \to hh$) ~ 0.4. For larger values of BR($H \to hh$), the LHC + EWPO limits are the most important ones since the direct search limit

Selection cuts	$H \to hh$	$t\bar{t}$	GGF h	$ht\bar{t}$	hh	DY	VV	$\hat{\sigma}_{3000}$
Basic selection	0.48	3560.36	0.15	0.072	0.024	272.41	0.90	0.43
$\Delta\phi_{\ell\ell}$, $\Delta R_{\ell\ell}$, $p_{\rm T}^{\ell\ell}$	0.28	818.01	0.15	0.020	0.022	48.51	0.095	0.70
$m_{\ell\ell}$, $M_{\rm T2}^{\ell\ell}$	0.21	206.23	0.11	0.006	0.007	0.0	0.0	0.80
$m_h^{\rm maos}$, $M_{\rm T}^{\ell\ell}$	0.19	140.69	0.08	0.004	0.005	–	–	0.88
ΔR_{bb}, m_{bb}	0.104	6.65	0.008	$\simeq 0.0$	$\simeq 0.0$	–	–	2.21
$m_{bb\ell\ell}$	0.009	3.03	0.008	–	–	–	–	2.82
$M_{\rm T2}^{bb\ell\ell}$	0.083	2.29	0.0	–	–	–	–	2.99
Signal region	0.083	2.19	–	–	–	–	–	3.06

Table 3.4: Cut flow of signals for $m_H = 260$ GeV and the main backgrounds in fb. See the text for detailed description of the event selection cuts applied. $\hat{\sigma}_{3000}$ is the signal significance calculated with a Poisson probability at 3000 fb^{-1} integrated luminosity. The signal region is defined by $180\ \text{GeV} < M_{\rm T}^{bb\ell\ell} < 265$ GeV and $185\ \text{GeV} < m_H^{\rm maos} < 305$ GeV.

weakens. For $m_H = 400$ GeV the direct limit is not as stringent as the indirect ones, which impose an upper bound of $\sin^2\alpha < 0.084$, independently of the BR($H \to hh$) value.

We can use the discovery reach of the 14 TeV LHC [240] for the Higgs boson search using the decay channel $H \to ZZ \to 4\ell$ to estimate the detectability of the two m_H values as a function of the mixing and the BR($H \to hh$).[13] In Figure 3.14, we show the 3σ and 5σ significance lines for this channel for the integrated luminosity of 3000 fb^{-1}. These lines show that for low values of BR($H \to hh$) this search is able to resolve a large portion of the mixing angle values, leaving a small window of possible values. The sensitivity of this channel begins to decrease for BR($H \to hh$) > 0.6, just in the region where the double Higgs production, in particular the channel above mentioned, becomes relevant. In Figure 3.14, we have included the 3σ equivalent line for the $H \to hh \to b\bar{b}WW^*$ channel. It is important to note that both channels are complementary since they are very dependent on the value of BR($H \to hh$). As a remark, the ATLAS collaboration has performed a search of heavy Higgses using the channel $H \to hh \to b\bar{b}\gamma\gamma$ [241]. The results are not shown because the exclusion limit is well above the ones of Figure 3.14.

[13] We assume that BR($H \to hh$) + BR($H \to$ SM particles) = 1.

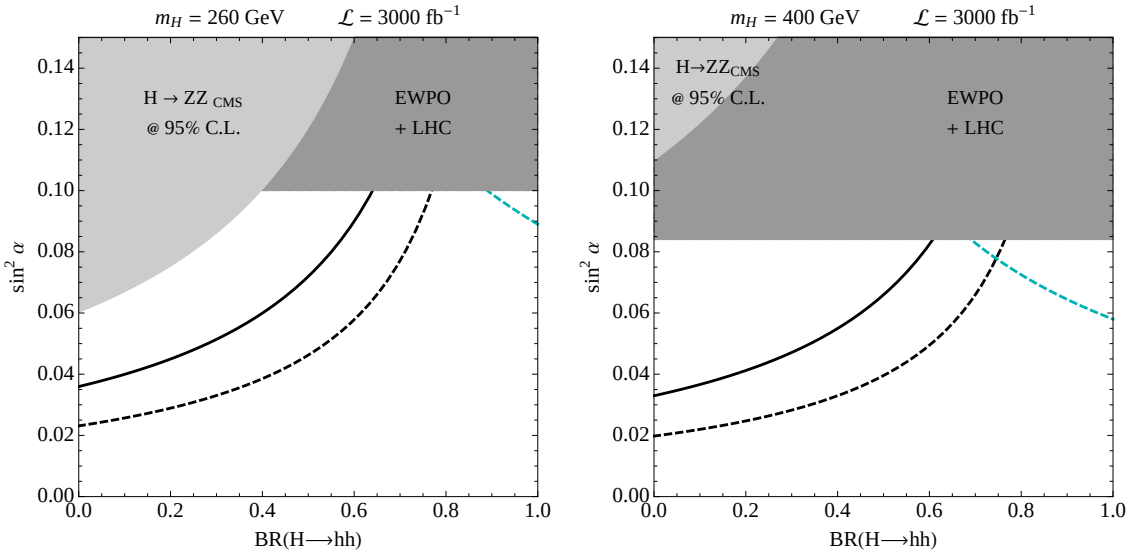

Figure 3.14: The dashed line delimits the 3σ significance region in the $\sin^2\alpha - \mathrm{BR}(H \to hh)$ plane for the $H \to hh \to b\bar{b}WW^* \to 2b + 2\ell + 2\nu$ ($\ell = e, \mu$) process for the integrated luminosity of 3000 fb^{-1}. The solid (dashed) black curve corresponds to the 5σ (3σ) for the $H \to ZZ \to 4\ell/2\ell 2\tau$ channels. Dark grey shaded region is the 95% C.L. CMS exclusion bounds and the light grey region is the one for EWPO + LHC.

4

Vector Portal: Stückelberg

Extra abelian gauge factors are among the most common extensions of the SM [49], and also among the best motivated from string theory, where massive extra $U(1)$ gauge bosons appear ubiquitously (for reviews see e.g. Refs. [66, 242–246]). In fact, when one tries to implement a visible sector with the SM gauge group in, say, intersecting brane models, one generically obtains not $SU(3)_c \times SU(2)_L \times U(1)_Y$, but rather $U(3)_c \times U(2)_L \times U(1)^p$ which contains several extra abelian factors (including the centers of $U(3)_c$ and $U(2)_L$).

The models we will consider along this Chapter are based on this type of string constructions. The symmetry structure of this scenario can be represented schematically in the following form,

$$\underbrace{SU(3)_c \times SU(2)_L \times U(1)_{\rm v}^n}_{\Psi_{\rm v}} \;\times\; \underbrace{U(1)_{\rm h}^m \times G_{\rm h}}_{\Psi_{\rm h}} \tag{4.1}$$

where the $U(1)_{\rm v}^n$ are n abelian gauge factors to which the visible matter fields $\Psi_{\rm v}$ couple. All of the corresponding gauge bosons acquire a mass through the Stückelberg mechanism, except for a particular linear combination of them that corresponds to hypercharge and remains massless (in the phase of unbroken electroweak symmetry). $U(1)_{\rm h}^m$ are m abelian gauge factors (some of which could be massless) to which only hidden matter $\Psi_{\rm h}$ couples, and $G_{\rm h}$ represents the semi-simple part of the hidden gauge group.

As mentioned, these type of scenarios can fairly easily be implemented in models of intersecting D6-brane of type IIA string theory. Intuitively, each sector consists of several intersecting stacks of branes wrapping 3-cycles of a six-dimensional compactification space. Each stack hosts a $U(N)$ gauge factor and chiral matter arises at the brane intersections. Different sectors arise from brane stacks that do not intersect each other and can hence be separated in the internal space (see Fig. 4.1).

The extra abelian gauge bosons of Eq. (4.1) can provide a portal into the hidden sector in two different ways. The most thoroughly studied is a small kinetic mixing of a light hidden gauge boson with the visible massless photon [247–255]. This generates an effective coupling of DM with visible fields which is proportional to their electric charge, and hence, the DM particles only couple to protons and do not couple to neutrons. From the point of view of direct DM searches, this is very important, since the elastic scattering of DM off nucleons only receives contributions from protons. This is, the ratio between the coupling of DM to neutrons and protons vanishes, $f_n/f_p = 0$.

The second mechanism, which will be the main subject of this Chapter, was pointed out in Refs. [33, 34] (see also Refs. [256–259]). It results from the mixing of massive $U(1)$s of the visible sector with $U(1)$s of the hidden one. Despite living in different sectors, the $U(1)$ gauge bosons $A_{\rm v}^n$ and $A_{\rm h}^m$ often have Stückelberg couplings to the same axions, e.g. RR closed string axions in type II string models. As a consequence the resulting mass matrix can be highly non-diagonal. The

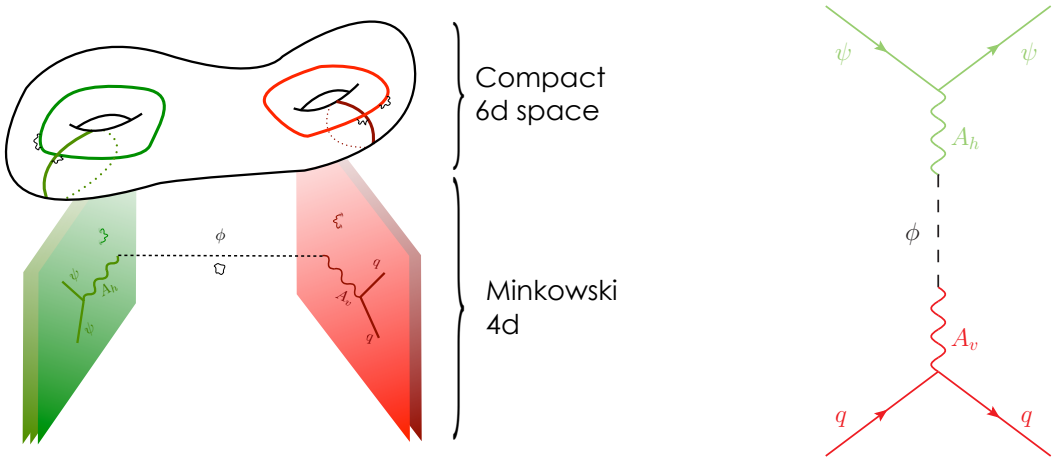

Figure 4.1: Left: Schematic representation of a hidden sector scenario Eq. (4.1) with intersecting D-branes. Green and red branes do not intersect each other and hence host different sectors. Right: Diagram contributing to the elastic scattering of hidden sector DM, ψ, off quarks. The mediator of this interaction is a mixing of different string axions, ϕ, and the vectors A_v and A_h.

'physical' Z' eigenstates obtained upon diagonalization of the kinetic and mass matrices are largely mixed combinations of $A_{\rm v}^n$ and $A_{\rm h}^m$ and hence couple simultaneously to both, visible and hidden, matter sectors. This mass mixing is a tree-level effect that provides an effective portal into hidden sectors, provided the associated Z' bosons are light enough.

Despite the potentially complex gauge and matter structure of the hidden sector, it seems reasonable to assume that it hosts a Dirac fermion ψ that plays the role of DM in the Universe. The stability of these particles is easily guaranteed by the perturbatively conserved $U(1)_h^m$ symmetries or by non-perturbatively exact discrete subgroups thereof, or simply because they are the lightest particles of the whole sector. In any case, their interaction with the SM fermions will be driven by the exchange of a Z' boson. For DM direct detection experiments the leading interaction of the elastic scattering of ψ with quarks is depicted in the right panel of Fig. 4.1. Following this reasoning, it is clear that the charges of the SM fermions under the $U(1)_{\rm v}^n$ groups that mix with the hidden sector will determine the prospects for detecting ψ in these experiments.

In this Chapter we study the phenomenology of a class of scenarios of this kind that can be embeded into well known string theory constructions. In particular, we focus on the isospin violation character of the DM interactions with protons and neutrons induced by the Z' bosons. As we will see, isospin violation could distinguish these Stückelberg portal models from other popular setups, such as the Higgs or scalar portal discussed in the previous Chapter or the Z-mediation scenarios.

4.1. Effective Lagrangian and Z' eigenstates

In this section we review the general constructions of Refs. [33, 34, 259] which describe the mixing mechanism of massive $U(1)$ gauge bosons from different sectors, the so-called Stückelberg

portal. We begin with a discussion in terms of the effective field theory, and describe later on the string implementation of such setup.

Non-diagonal $U(1)$ mass matrix

The abelian sector of the construction sketched in Eq. (4.1) can generically be described by the Lagrangian

$$\mathcal{L} = -\frac{1}{4}\vec{F}^T \cdot f \cdot \vec{F} - \frac{1}{2}\vec{A}^T \cdot M^2 \cdot \vec{A} + \sum_\alpha \overline{\psi}_\alpha \left(i\partial\!\!\!/ + \vec{Q}_\alpha^T \cdot \vec{A}\!\!\!/ \right) \psi_\alpha \tag{4.2}$$

where the vector $\vec{A}^T = (A_1 \dots A_{n+m})$ encodes all the $U(1)$ gauge bosons of the system, with field strength $\vec{F} = d\vec{A}$. In this normalization the gauge coupling constants are absorbed in the kinetic matrix f. In hidden sector scenarios, the charge vectors $\vec{Q}_\alpha$ of a given matter field ψ_α will have non-zero entries only for one of the sectors (either visible or hidden), while the kinetic and mass matrices f and M can have off-diagonal entries that mix both sectors. We are interested in particular in the mixings induced by the mass matrix M.

The mass terms for Abelian gauge bosons $\vec{A}$ can be generated by either the Higgs or the Stückelberg mechanisms. In both cases the crucial term in the Lagrangian is the coupling of $\vec{A}$ to a set of pseudo-scalar periodic fields $\phi^i \sim \phi^i + 2\pi$ whose covariant kinetic terms read

$$\mathcal{L}_M = -\frac{1}{2} G_{ij} \left(\partial\phi^i - k_a^i A^a \right) \left(\partial\phi^i - k_b^j A^b \right) . \tag{4.3}$$

Here, G_{ij} corresponds to a positive-definite kinetic matrix (the metric in the space of ϕ^i fields), which in our conventions has dimension of (mass)^2. The factors k_a^i encode the non-linear gauge transformations

$$\vec{A} \to \vec{A} + d\vec{\Lambda} \qquad \Longrightarrow \qquad \phi^i \to \phi^i + k_a^i \Lambda^a . \tag{4.4}$$

The statement that the gauge symmetry group is compact ($U(1)$ rather than $\mathbb{R}$) implies that the transformations must be periodic $\Lambda \sim \Lambda + 2\pi$, and hence that the k_a^i factors (as well as the matter charges $\vec{Q}_\alpha$ of Eq. (4.2)) must be quantized. In fact, under the appropriate normalization they can be assumed to be integers, k_a^i, $Q_\alpha^a \subset \mathbb{Z}$. In the case of the Higgs mechanism, the axion-like fields ϕ^i are identified with the phases of Higgs fields H^i, and the k_a^i factors are simply the charges of the latter under the $U(1)_a$ groups. It is not surprising that these are integer quantities. What is perhaps less obvious is that even for axions not related to a Higgs fields, one can still associate $U(1)$ integer "charges" that determine their gauge transformations.

The $U(1)$ gauge bosons get a mass by absorbing the axions, ϕ^i, through the Lagrangian Eq. (4.3). After gauge fixing the $U(1)$ symmetries, the mass term of Eq. (4.2) is generated, and the corresponding mass matrix takes the form

$$M^2 = K^T \cdot G \cdot K . \tag{4.5}$$

It is easy to see that this matrix can be highly non-diagonal and have off-diagonal entries that mix hidden and visible sectors. This can happen with particular strength if the mixing is induced by the integer matrix K of axionic charges.

The dynamical origin of the mixing is the simultaneous coupling of vector bosons from different sectors to the same axions (see figure 4.1). As a toy model, consider two $U(1)$ gauge bosons, a visible A_v and a hidden A_h, that couple to an axion with charges +1 and -1, respectively, i.e. $K = \binom{+1}{-1}$, whose kinetic matrix is $G = m^2$. The resulting mass matrix of the $U(1)$ bosons would read $M^2 = m^2 \left(\begin{smallmatrix} 1 & -1 \\ -1 & 1 \end{smallmatrix}\right)$. The resulting physical eigenstates are obviously highly mixed combinations of A_v and A_h that hence couple with similar strength to both sectors.

In the following we generalize this simple example to the case where several gauge bosons mix with each other by absorbing several axions with mixed charges.

Diagonalization and eigenstates

In order to study the properties of the system described by the Lagrangian of Eq. (4.2), it is convenient to move to a basis in which the gauge bosons have a canonical kinetic term and a diagonal mass matrix. The former can be obtained by a linear transformation:

$$\vec{A} \equiv \Lambda \cdot \vec{A}' \tag{4.6}$$

such that $\Lambda^T \cdot f \cdot \Lambda = 1$. In the case with no kinetic mixing, i.e. $f = \mathrm{diag}(g_1^{-2}, \ldots, g_N^{-2})$, the transformation matrix is simply $\Lambda = \mathrm{diag}(g_1, \ldots, g_N)$. For the moment we need not assume such simplification, and we work with a general kinetic matrix f.

The Lagrangian in terms of the transformed bosons $\vec{A}'$ reads

$$\mathcal{L} = -\frac{1}{4}\vec{F}'^2 - \frac{1}{2}\vec{A}'^T \cdot \Lambda^T \cdot M^2 \cdot \Lambda \cdot \vec{A}' + \overline{\psi}\left(i\partial\!\!\!/ + \vec{Q}_\psi^T \cdot \Lambda \cdot \vec{A}\!\!\!/\,'\right)\psi\,. \tag{4.7}$$

Notice that with this new normalization, what appears in the matter coupling to the gauge boson is no longer just the charges Q, but products of these and coupling constants g (and possible kinetic mixing parameters).

We need now an orthogonal transformation $\mathcal{O}$ that diagonalizes the mass matrix $\tilde{M}^2 \equiv \Lambda^T \cdot M^2 \cdot \Lambda$. That is, we need to find a basis of orthonormal eigenvectors

$$\tilde{M}^2 \cdot \vec{v_i} = m_i^2 \vec{v_i} \qquad \Longrightarrow \qquad \mathcal{O} = (\vec{v_1}\ \vec{v_2}\ \ldots\ \vec{v_N})\,. \tag{4.8}$$

Conveniently, we define $\vec{v_i}' \equiv \Lambda \cdot \vec{v_i}$. The transformation $\vec{A}' \equiv \mathcal{O} \cdot \vec{A}''$ brings the Lagrangian to a standard form with canonical kinetic term and diagonal mass matrix:

$$\mathcal{L} = -\frac{1}{4}F''^2_i - \frac{1}{2}m_i^2 A''^2_i + \sum_\alpha \overline{\psi}_\alpha \left(i\partial\!\!\!/ + \vec{g'}_\alpha^T \cdot \vec{A}\!\!\!/\,''\right)\psi_\alpha \tag{4.9}$$

The coupling of a vector A_i'' to the matter field ψ_α is given by a linear combination of the original charges:

$$g'^{(i)}_\alpha = \vec{Q}_\alpha^T \cdot \vec{v}'_{(i)}\,. \tag{4.10}$$

Notice the important fact that, for massless eigenvectors, $\vec{v_i}'$ are precisely the zero eigenvectors of the original mass matrix M^2, i.e. they satisfy $K \cdot \vec{v_i}' = 0$. Since the entries of the matrix K are

integer numbers, the entries of the massless eigenvectors $\vec{v_i}'$ will be also integers, up to an overall normalization factor. The corresponding gauge bosons will be massless, have quantized charges, and if the form of the matrix K is appropriate, will couple exclusively to one sector of the theory. They are hence perfect candidates to play the role of the SM hypercharge.

These last remarks do not apply to massive eigenstates, for which $M^2 \cdot \vec{v_i}' \neq \alpha_i \vec{v_i}'$. Generically, given the non-diagonal character of the mass matrix M^2, all of the entries of the massive eigenvectors $\vec{v_i}$ will be non-zero and of the same order. The physical massive gauge bosons A_i'' will be hence a linear combination of both visible and hidden bosons and they will act as portals into hidden sectors.

Before concluding this section let us write down an important condition on the vectors $\vec{v_i}$. The orthogonality of the transformation matrix $\mathcal{O}$ of Eq. (4.8) translates into the condition

$$\vec{v_i}^{\,T} \cdot \vec{v_j} = \delta_{ij} \qquad \Longrightarrow \qquad \vec{v_i}'^{\,T} \cdot f \cdot \vec{v_j}' = \delta_{ij} \,. \tag{4.11}$$

We will have to take this condition into account in the phenomenological analysis carried out in the following sections.

The string theory interpretation

As mentioned in the introduction, one nice feature of the Stückelberg portal is that it finds a natural implementation in string theory, and a particularly intuitive one in models of intersecting D-branes. A detailed study and explicit examples in the setup of toroidal orientifolds of type IIA string theory can be found in the original references [33, 34]. Here, we briefly describe where the different fields and couplings arise in such models (for general reviews on these type of string compactifications, see e.g. Refs. [66, 242–244]).

In type IIA orientifold compactifications, gauge bosons arise from open strings living on D6-branes that span the four non-compact dimensions, and wrap three-cycles of the six dimensional compactification space X_6 (usually a Calabi-Yau manifold). A stack of N overlapping such branes usually hosts a gauge group $U(N) \cong SU(N) \times U(1)$. Chiral matter fields arise at the intersections of two stacks. Hence, in order to obtain hidden sector scenarios, one has to choose carefully the cycles wrapped by the branes to make sure that stacks from different sectors do not intersect with each other.

The abelian gauge bosons living in such stacks couple not only to open strings, but also to closed strings which include the graviton, and also Ramond-Ramond (RR) axions that arise from the reduction of RR three forms along three-cycles of X_6. Being associated to closed strings that propagate in the bulk of the compactification, it is natural to consider that such RR axions couple to gauge fields from different sectors. These couplings are of the Stückelberg type given in Eq. (4.3) and generate masses for the gauge bosons. The charge matrix K is determined by the wrapping numbers of the branes around odd cycles of X_6 (odd with respect to the orientifold projection), and can be engineered in such a way that the mass matrix is highly non-diagonal.

The matrix G that also enters in the formula for the mass matrix M^2 and is identified with the complex structure moduli space metric of the compactification space X_6, times a string scale factor M_s^2. Unfortunately, except for the simplest compactifications, this metric is unknown.

Nevertheless, as long as some RR axion has non-zero charges under $U(1)$ groups from different sectors, the mixing induced by the mass matrix M^2 is expected to be strong and results in physical Z' bosons that couple visible and hidden sectors.

The final ingredient in the Lagrangian of Eq. (4.2) is the kinetic matrix f. At tree level, this matrix is diagonal $f = \text{diag}(g_1^{-2}, \ldots, g_N^{-2})$, with the couplings determined by the volume of the cycles wrapped by the corresponding branes. Loop corrections can generate off-diagonal terms that produce small kinetic mixings among different $U(1)$s.

The fate of the $U(1)$ gauge bosons in this type of models is to gain a mass of the order of the string scale, suppressed by the square of the gauge coupling factor, $m_{Z'} \propto g^2 M_s^2$. This is expected to be very large in a broad class of string constructions. Nevertheless, several mechanisms have been proposed to lower the Z' masses, including large volume and anisotropic compactifications, or eigenvalue repulsion effects [33, 252, 260]. The conclusion is that, although not generic, Z' masses at scales as low as the TeV, or even smaller, can be achieved in several setups.

At energy scales much lower than the Z' boson masses, the corresponding $U(1)$ symmetries become effectively global. They are in fact perturbatively exact symmetries of the effective Lagrangian, and they are broken only by highly suppressed non-perturbative effects [261–263]. Therefore, the $U(1)$ symmetries that extend the visible sector gauge group in realistic D-brane constructions should find an interpretation in terms of known approximate global symmetries of the SM, such as Baryon or Lepton number.

Interestingly, these extra $U(1)$ groups are generically anomalous symmetries of the SM. It is well known, however, that these anomalies are cancelled by a generalized Green-Schwarz mechanism, in which the RR axions, ϕ^i, and the Stückelberg couplings of Eq. (4.3) play a crucial role. Although the gauge bosons associated to such anomalous $U(1)$s are not considered too frequently in the phenomenological literature, they are a key (and in fact most often unavoidable) ingredient of realistic constructions with open strings.

In the following, we take the Stückelberg portal string constructions we have described in this section as a motivation, and study some of their phenomenological consequences.

SM fermion couplings to Z'

As in Refs. [33, 34], we focus on visible sectors realized as in Ref. [264], the so-called *Madrid quivers*, which provide some of the simplest realistic models of intersecting D6-branes. In order to reproduce the SM one introduces four stacks of branes yielding a $U(3)_A \times U(2)_B \times U(1)_C \times U(1)_D$ visible gauge group. The intersection numbers of these branes are chosen in such a way that the model reproduces the SM chiral spectrum and is free of anomalies (with anomalies of extra $U(1)$ factors cancelled by the Green-Schwarz mechanism).

In Table 4.1 the charges of the SM particles under the four visible $U(1)$ factors are presented. These charges can be interpreted in terms of known global symmetries of the SM. In particular, Q_A and Q_D are proportional to baryon and lepton number, respectively. With these charge assignments, the hypercharge corresponds to the linear combination

$$Q^Y = \frac{1}{6}\left(Q_A - 3Q_C + 3Q_D\right) . \tag{4.12}$$

One has to make sure that such a combination remains as a massless gauge symmetry of the system (before electroweak symmetry breaking), i.e. that it corresponds to a zero eigenstate of the mass matrix M^2. Following the discussion below Eq. (4.10), one has to make sure hence that the matrix of axionic charges K has an eigenvector $\vec{v_Y}' = (1, 0, -3, 3; 0, \ldots, 0)$ with zero eigenvalue. The first entries of this vector correspond to the visible sector, and the latter to the hidden one, so that hypercharge couples exclusively to visible matter. In fact, this condition can be implemented in type II string constructiones by simple topological requirements on the wrapping numbers of the visible branes. Therefore, according to Eq. (4.10), the hypercharge coupling to a matter field ψ_α reads

$$g_\alpha^Y = e\, Q_\alpha^Y = \frac{e}{6}\left(Q_{\alpha A} - 3Q_{\alpha C} + 3Q_{\alpha D}\right) . \tag{4.13}$$

In general, the remaining three visible $U(1)$ gauge bosons acquire masses by the Stückelberg mechanism, and as stressed in the previous section, they can have strong mass mixing with hidden $U(1)$ bosons. In this Thesis we are interested in the phenomenology induced by the lightest of the resulting physical Z' bosons whose contribution to the DM interaction with SM particles is dominant. Since we cannot know the explicit form of the mass matrix M^2 for generic string compactifications (in particular because of the lack of control of the G matrix that enters the Lagrangian) we will simply parametrise the couplings of the lightest Z' boson to the matter fields ψ_α by a linear combination

$$g_\alpha^{Z'} = a\, Q_{\alpha A} + b\, Q_{\alpha B} + c\, Q_{\alpha C} + d\, Q_{\alpha D} + \sum_{i=1}^{m} h_i\, Q_{\alpha i}^{(h)} \tag{4.14}$$

where we have included the contributions from hidden $U(1)$ factors. The parameters a, b, c, d and h_i are precisely the entries of the vector $\vec{v}'_{Z'} = (a, b, c, d; h_1, \ldots)$ of Eq. (4.10). For massive Z' bosons these are continuous parameters and as already stressed, they are all generically different from zero. Furthermore, notice that, by definition, $\vec{v}'_{Z'} \equiv \Lambda \cdot \vec{v}_{Z'}$, where $\vec{v}_{Z'}$ is a normalized vector. Since at tree level $\Lambda = \mathrm{diag}(g_1, \ldots, g_N)$, one can see that the parameters a, b, c, d and h_i will be proportional to the original gauge coupling constants, and hence perturbative.

The parameters a, b, c and d, which in turn determine the effective couplings of visible matter to DM, are nevertheless, not completely arbitrary. On the one hand, they must be orthogonal to the hypercharge assignment in the sense of Eq. (4.11). Neglecting possible kinetic mixing effects, i.e. taking $f = \mathrm{diag}\,(g_a^{-2} \ldots\, g_d^{-2} \ldots)$, the orthogonality condition reads

$$\frac{a}{g_a^2} + \frac{3b}{g_c^2} - \frac{3d}{g_d^2} = 0\,. \tag{4.15}$$

On the other hand, the vectors $\vec{v}^{\,(i)}$ must be properly normalized, yielding

$$\frac{g_Y^2}{36}\left(\frac{1}{g_a^2} + \frac{9}{g_c^2} + \frac{9}{g_d^2}\right) = 1\,, \tag{4.16}$$

$$\frac{a^2}{g_a^2} + \frac{b^2}{g_b^2} + \frac{c^2}{g_c^2} + \frac{d^2}{g_d^2} + \sum_{i=1}^{m} \frac{h_i^2}{g_{h_i}^2} = 1\,, \tag{4.17}$$

Matter field	Q_A	Q_B	Q_C	Q_D	Y
Q_L	1	-1	0	0	1/6
q_L	1	1	0	0	1/6
U_R	-1	0	1	0	-2/3
D_R	-1	0	-1	0	1/3
L	0	-1	0	-1	-1/2
E_R	0	0	-1	1	1
N_R	0	0	1	1	0

Table 4.1: SM spectrum and $U(1)_i$ charges in the four stack models of Ref. [264]. Anomaly cancellation requires the three quark families to be divided into two Q_L doublets and two antidoublets q_L of $U(2)_B$ i.e. they differ in their $U(1)_B$ charge. We assign the up and down quarks to the antidoublets.

for the Z and Z' respectively. Notice that in the second expression the factor $\sum_{i=1}^{m} h_i^2/g_{h_i}^2$ encodes all the possible interactions of the Z' with matter living in the hidden sector. Given the potential complexity of this sector, which we will not fully specify in this Thesis, Eq. (4.17) reduces to a bound on the visible sector couplings

$$\frac{a^2}{g_a^2} + \frac{b^2}{g_b^2} + \frac{c^2}{g_c^2} + \frac{d^2}{g_d^2} < 1\,. \tag{4.18}$$

Furthermore, the couplings g_i can be related to the SM gauge coupling constants by means of the following relations [260, 264]:

$$g_a^2 = \frac{g_3^2}{6}\,, \quad g_b^2 = \frac{g_2^2}{4}\,, \quad \left(\frac{1}{g_a^2} + \frac{9}{g_c^2} + \frac{9}{g_d^2}\right) = 36 g_Y^{-2}\,, \tag{4.19}$$

where g_3 and g_2 refers to the $SU(3)_{QCD}$ and $SU(2)_L$ coupling constants, respectively. These relations arise from the fact that $U(1)_A$ and $U(1)_B$ are just the center of the groups from which the $SU(3)_{QCD}$ and $SU(2)_L$ gauge factors of the SM arise.[1]

Now we have all the necessary information to build the couplings of the Z' to the SM particles. In virtue of Eq. (4.14) and Table 4.1, the left and right handed (first and second family) of quarks have the following couplings,

$$\begin{aligned} g_{u_L}^{Z'} &= (a+b)\,, \qquad g_{u_R}^{Z'} = (-a+c)\,, \\ g_{d_L}^{Z'} &= (a+b)\,, \qquad g_{d_R}^{Z'} = (-a-c)\,, \end{aligned} \tag{4.20}$$

which can be used to define the vectorial coupling as the sum of the left and right components,

$$\begin{aligned} C_u^V &= g_{u_L}^{Z'} + g_{u_R}^{Z'} \;\; = (b+c)\,, \\ C_d^V &= g_{d_L}^{Z'} + g_{d_R}^{Z'} \;\; = (b-c)\,, \end{aligned} \tag{4.21}$$

[1] Note that these relations should be evaluated at the compactification scale. The running of the coupling constants from this scale to the electroweak scale, at which isospin violating properties of DM are defined, can be simply reabsorbed into the definition of the parameters a, b, c and d.

and the axial coupling as the difference,

$$\begin{aligned} C_u^A &= g_{u_L}^{Z'} - g_{u_R}^{Z'} &= (2a+b-c)\,, \\ C_d^A &= g_{d_L}^{Z'} - g_{d_R}^{Z'} &= (2a+b+c)\,. \end{aligned} \tag{4.22}$$

Similarly, according to Table 4.1, for the third family of quarks the vectorial couplings are given by

$$\begin{aligned} C_t^V &= (-b-c)\,, \\ C_b^V &= (-b+c)\,, \end{aligned} \tag{4.23}$$

whereas the axial couplings are given by

$$\begin{aligned} C_t^A &= (2a-b-c)\,, \\ C_b^A &= (2a-b+c)\,. \end{aligned} \tag{4.24}$$

Finally, for the three families of leptons the vector and axial couplings can be written as

$$\begin{aligned} C_\ell^V &= (-b-c)\,, \\ C_\ell^A &= (-b+c-2d)\,, \end{aligned} \tag{4.25}$$

respectively. Note that in all cases, the vectorial couplings are independent of a as well as of d, as was to be expected from the aforementioned interpretation of the charges Q_A and Q_D in terms of baryon and lepton number. The axial couplings, on the other hand do depend on a and d. This fact will have a remarkable impact on the LHC bounds as we will see later.

4.2. Isospin violation Dark Matter from the Stückelberg mechanism

As we have seen previously, the different charges of the SM particles under the $U(3)_A \times U(2)_B \times U(1)_C \times U(1)_D$ visible gauge group, together with the mixing of the corresponding abelian bosons, gave rise to very generic vector and axial couplings to the Z' boson. As a consequence, a DM particle living in the hidden sector, ψ, will couple to each SM fermion through the Z' in a different manner. This fact can be translated into a different coupling strength of ψ to protons and neutrons, and thus, to a rather flexible amount of isospin violation f_n/f_p (a_n/a_p). This is very important from the point of view of DM direct detection experiments [132].

Direct detection experiments are based on the elastic scattering of DM particles off nucleons inside an underground detector which shields it from cosmic rays. These experiments are tremendously sensitive to the recoil energy released by a nucleus of the target material when a DM particle hits it. Since the interaction between the nucleon and the DM particle occurs in the non relativistic limit (the relative velocity of the system in the lab frame is of the order of hundreds of km/s), the energy deposited in the detector after the collision is very small, of the order $\mathcal{O}(10)$ keV. Depending on the nature of the DM particles, and the mediator of its interaction with quarks, there exist many different operators that contribute to this interaction. For a Dirac fermion

DM with a Z' gauge boson mediator, its interactions with quarks can be divided into the so-called spin-independent (SI) interactions, arising from scalar and vector interactions with quarks, and spin-dependent (SD) interactions that originate from axial-vector interactions. Let us now analyse either cases separately.

SI interactions

The spin independent contribution to the total cross section of the DM-nucleus elastic scattering arises from scalar and vector couplings. For an interaction mediated by a vector boson exchange, the effective Lagrangian for the interaction of ψ with nucleons (protons (p) and neutrons (n)) can be written as,

$$\mathcal{L}_{SI}^{V} = f_p(\bar{\psi}\gamma_\mu\psi)(\bar{p}\gamma^\mu p) + f_n(\bar{\psi}\gamma_\mu\psi)(\bar{n}\gamma^\mu n), \tag{4.26}$$

where f_p and f_n are the vector couplings of ψ to the protons and neutrons, respectively. These quantities depend on the nucleon quark content. For a vector interaction the only quarks that play a role are those of the valence (up and down), while for a scalar interaction the sea quarks are also important for the entire process. Since the up and down quarks are not present in the proton and neutron in the same fraction, one can express f_p and f_n as follows [265],

$$f_p = 2b_u + b_d, \quad f_n = b_u + 2b_d, \tag{4.27}$$

where b_u and b_d are the effective vector couplings of the up and down quarks to the DM particles.[2] After integrating out the Z' boson, these couplings can be easily written as,

$$b_{(u,d)} = \frac{hC_{(u,d)}^{V}}{2m_{Z'}^2}\,, \tag{4.28}$$

with h being the coupling strength of the Z' boson to ψ, and $m_{Z'}$ the mass of the lightest Z' boson.

Using now the expressions for the vector couplings of the Z' to up and down quarks, given in Eq. (4.21), it is straightforward to deduce that,

$$\begin{aligned} b_u &= \frac{hC_u^V}{2m_{Z'}^2} = \frac{h}{2m_{Z'}^2}\,(b+c)\,, \\ b_d &= \frac{hC_d^V}{2m_{Z'}^2} = \frac{h}{2m_{Z'}^2}\,(b-c)\,. \end{aligned} \tag{4.29}$$

These two expressions make obvious that in this framework the ratio between the coupling of ψ to protons and neutrons i.e. the amount of isospin violation f_n/f_p, according to Eq. (4.27), is given by

$$\frac{f_n}{f_p} = \frac{(3b-c)}{(3b+c)} = \frac{(3b/c-1)}{(3b/c+1)}\,. \tag{4.30}$$

Interestingly, the the total amount of isospin violation depends exclusively on the ratio between the parameters b and c which, as mentioned before, are continuous and different from zero, generating

[2] Not to be confused with the coupling b associated with the $U(1)_B$ symmetry.

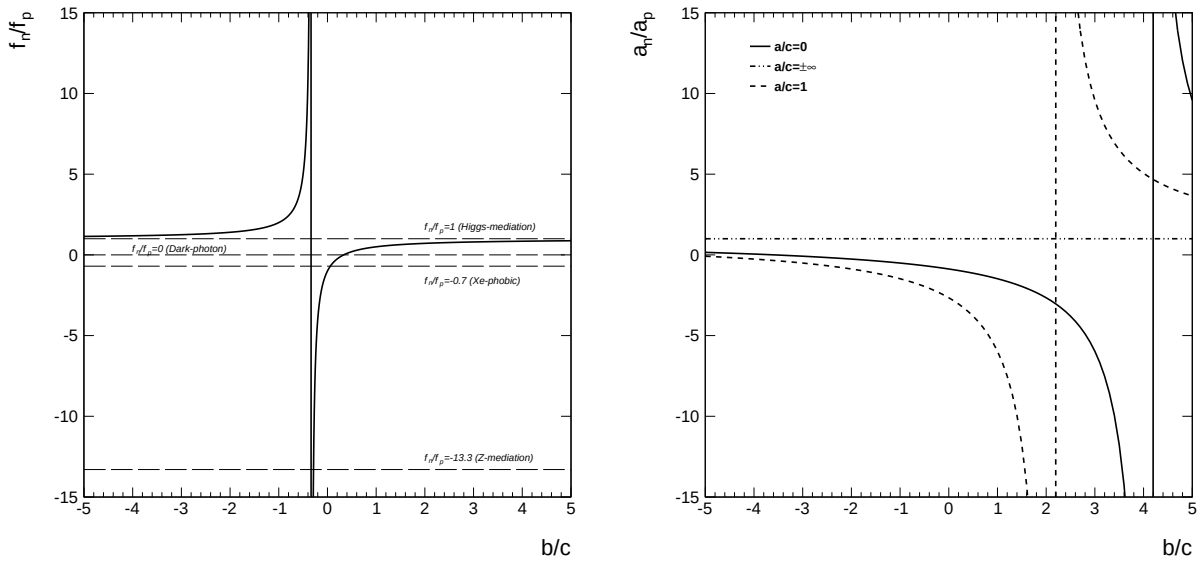

Figure 4.2: Left: Amount of isospin violation for SI interactions, f_n/f_p, as a function of b/c (solid line). Some representative values of f_n/f_p are shown as horizontal dashed lines. Right: Ratio between the coupling of DM to neutrons and protons, a_n/a_p, for the SD interactions as a function of b/c. For a/c we have taken different limits, $a/c \to 0$ (solid line), $a/c \to \pm\infty$ (dot dashed line), and $a/c = 1$ (dashed line).

a ratio f_n/f_p different from ± 1. This is a consequence of the introduction of $U(1)$ gauge groups in the visible sector to reproduce the global symmetries of the SM. In particular, the parameter b corresponds to a chiral $U(1)$ symmetry of the Peccei-Quinn type, with mixed $SU(3)$ anomalies; while c is related precisely to the weak isospin symmetry $U(1)_C$ [264]. Isospin violation and chirality are the key properties why these new groups generate a general isospin violation in the currents related to the Z' interaction.

In Figure 4.2 (left panel) the quantity f_n/f_p is shown as a function of b/c according to Eq. (4.30). We have shown some noteworthy theoretical benchmark values of this ratio as well, like Z mediation and dark photon scenarios, $f_n/f_p = -13.3$ and $f_n/f_p = 0$, respectively. The value of $f_n/f_p \approx -0.7$ is the so-called Xe-phobic dark matter scenario to which Xe-based detectors are poorly sensitive[3]. Interestingly, we notice that our construction naturally generates isospin violating couplings $f_n/f_p \neq 1$ for any value of the parameters b and c. These parameters are expected to be of the same order, $|b/c| \sim \mathcal{O}(1)$, which defines a region in which the value of f_n/f_p is subject to important changes (for values around $b/c = -1/3$). This precisely highlights the flexibility in the isospin violation patterns found in these constructions.

All this together can be taken as a clear and testable prediction of this kind of constructions. It also would be distinguishable from other hidden DM scenarios. For instance, if the portal between the visible and the hidden sector occurs via a Higgs boson, the value of f_n/f_p would be generally 1, since the Higgs boson can not differentiate chiralities of the quarks.[4]

It is worth noting that, although the type of constructions we are considering, based on the visible gauge group $U(3)_A \times U(2)_B \times U(1)_C \times U(1)_D$, lead to a flexible amount of isospin violation (generically $f_n/f_p \neq \pm 1$),[5] there is a well known class of alternative type II string models in which the gauge group $U(2)_B$ is replaced by $USp(2)_B \cong SU(2)_B$ [267]. In such models, the $U(1)_B$ factor, which was crucial in our discussion, is absent. One could realise the Stückelberg portal scenario in such constructions, and follow steps similar as the ones we have taken here. The only difference one would find is that the parameter b would be identically zero, and hence that the DM interactions with the nucleons would automatically satisfy $f_n/f_p \equiv -1$.

SD interactions

Let us now move to consider the case of SD interactions. As we have mentioned above, these interactions arise from the axial-vector couplings of DM to protons and neutrons, and thus, occur when the DM particles have a spin different from zero. In terms of the effective Lagrangian we can write,

$$\mathcal{L}_{SD} = a_p(\bar{\psi}\gamma_\mu\gamma_5\psi)(\bar{p}\gamma^\mu\gamma_5 p) + a_n(\bar{\psi}\gamma_\mu\gamma_5\psi)(\bar{n}\gamma^\mu\gamma_5 n), \tag{4.31}$$

[3] This is a consequence of the ratio between the number of protons and neutrons in xenon isotopes

[4] In type II 2HDM for $\tan\beta \approx 1$ there can be deviations [266].

[5] In the models we discuss, the values $f_n/f_p = \pm 1$ can only be reached in the limits $b/c \to 0$ and $b/c \to \infty$, which although not excluded, are not particularly preferred. This provides a remarkable and potentially measurable distinction of these constructions from other portals.

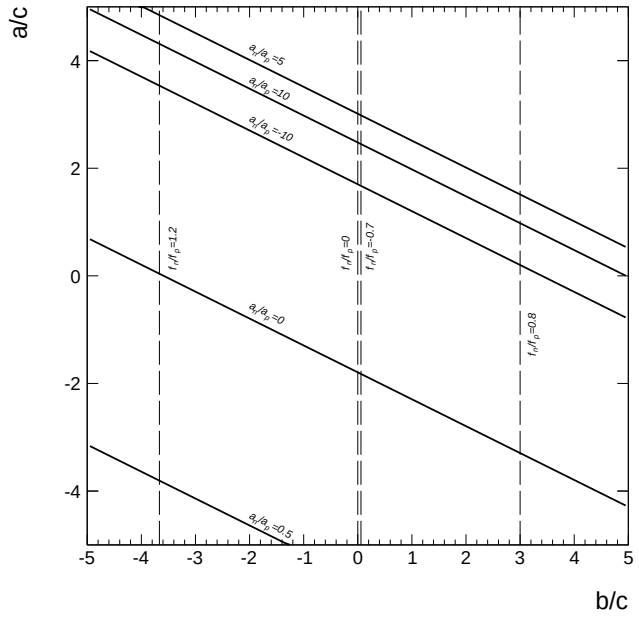

Figure 4.3: Ratio between the coupling of DM to neutrons and protons for the SD interactions as a function of b/c. For a/c we have take different limits, $a/c \to 0$ (black line), $a/c \to \infty$ (blue line), and $a/c = 1$ (gray line).

where the parameters $a_{p(n)}$ are the couplings of DM to protons (neutrons), and can be expressed in the following way [131],

$$a_p = \sum_{q=u,d,s} \frac{\alpha_q^A}{\sqrt{2}G_F}\Delta_q^p = \frac{h}{2\sqrt{2}G_F m_{Z'}^2}\left[C_u^A\Delta_u^p + C_d^A(\Delta_d^p + \Delta_s^p)\right], \tag{4.32}$$

$$a_n = \sum_{q=u,d,s} \frac{\alpha_q^A}{\sqrt{2}G_F}\Delta_q^n = \frac{h}{2\sqrt{2}G_F m_{Z'}^2}\left[C_u^A\Delta_u^n + C_d^A(\Delta_d^n + \Delta_s^n)\right], \tag{4.33}$$

where α_q^A is the effective axial coupling of DM to quarks and G_F denotes the Fermi coupling constant. Operators for axial-vector interactions in the nucleon are related to those involving quarks through the quantities $\Delta_q^{p(n)}$, which relate the spin of the nucleon to the operator $\langle p(n)|\bar{q}\gamma^\mu\gamma_5 q|p(n)\rangle$. For these we have taken the values from Ref. [268].

Now, we can take the ratio between the coupling to protons and neutrons, which gives

$$\frac{a_n}{a_p} = \frac{\Delta_u^n + \frac{2a/c+b/c+1}{2a/c+b/c-1}(\Delta_d^n + \Delta_s^n)}{\Delta_u^p + \frac{2a/c+b/c+1}{2a/c+b/c-1}(\Delta_d^p + \Delta_s^p)}. \tag{4.34}$$

As one can see from the previous expression, unlike for f_n/f_p, this ratio also depends on a/c not only on b/c, and hence, there is one more degree of freedom respect to the SI case.

In Figure 4.2 (right panel), the ratio a_n/a_p is depicted as a function of b/c according to Eq. (4.34) for different values of the ratio a/c. In the limit of $a/c \to \infty$ (dot dashed line), we find the case of $a_n/a_p = 1$, similar to the case of the SI interactions in the limit $b/c \to \infty$. While, for the cases $a/c \to 0$ (solid line) and $a/c = 1$ (dashed line), the values of a_n/a_p are generally different from ± 1. Notice that in this case one can also define the Xe-phobic scenario for a_n/a_p. However, it depends on the ratio between the zero momentum expectation values of the spin for protons and neutrons in xenon which are of the order of $\mathcal{O}(10^{-2})$ (using the latest calculations [269]), and for simplicity it is not included in Figure 4.2.

Finally, in order to rearrange the results for both SI and SD interactions, in Figure 4.3 we show the plane a/c versus b/c. As we have seen before, these two ratios determine the amount of isospin violation in DM interactions for both the SI and SD contributions. On the one hand, the dashed vertical lines represent some values of f_n/f_p, which are independent of a/c, as in Figure 4.2. On the other hand, the solid lines denote some values for a_n/a_p. Remarkably, in the region shown, where the values of a, b and c are in general of the same order, the DM interactions are isospin violating in both types of interactions. Furthermore, we see that very high values of the neutron component (with respect to the proton component) can be reached, although, the variation of either f_n/f_p or a_n/a_p is very abrupt in this region (see also Figure 4.2). This is important for direct detection experiments that use target materials in which the ratio between the neutron and proton contribution is significantly different than one. For instance, in Xe-based detectors such as LUX, the SD component is dominated by the neutron scatterings due to the dominance of the neutrons in the total spin of the ^{129}Xe and ^{131}Xe isotopes.

4.3. Detecting Z' mediators in the LHC

The production and the subsequent decay of a Z' boson into SM particles might leave distinctive signal of new physics that can be searched at colliders, and in particular at the LHC. The ATLAS detector at the LHC searched for high mass resonances decaying into a $\mu^+\mu^-$ or an e^+e^- pair for energies above the Z pole mass, at a center of mass energy $\sqrt{s} = 8$ TeV and luminosities of 20.5 fb^{-1} and 20.3 fb^{-1} for dimuons and dielectrons resonances, respectively [270]. These results are consistent with the SM predictions allowing to place an upper limit on the signal cross section times the corresponding branching fraction of the process $pp \to Z' \to \mu^+\mu^-(e^+e^-)$.[6] There are also searches for dijet resonances and monojets plus missing energy that receive additional contributions from the presence of a Z' boson, both at the LHC and Tevatron colliders, and hence, they can be used to place constraints on this kind of models as well [271–273].

In the model presented here, the coupling of the Z' boson to leptons and quarks contributes to the appearance of dimuon, dielectron and dijet resonances, and thus, these searches can constraint the parameter space. In order to include these bounds to determine which regions are allowed in light of these searches, we have followed the approach given in Ref. [274]. In the narrow width approximation, the dilepton production in proton-proton collisions mediated by the Z' can be

[6] Although these results can be used to place constraints on other models of new physics, we are interested in its application for the search of a Z' boson.

written as,

$$\sigma_{l^+l^-} \simeq \left(\frac{1}{3} \sum_q \frac{dL_{q\bar{q}}}{dm^2_{Z'}} \times \widehat{\sigma}(q\bar{q} \to Z') \right) \times \mathrm{BR}(Z' \to l^+l^-)\,, \tag{4.35}$$

where $dL_{q\bar{q}}/dm^2_{Z'}$ denotes the parton luminosities, $\widehat{\sigma}(q\bar{q} \to Z')$ is the peak cross section for the Z' boson, and $\mathrm{BR}(Z' \to l^+l^-)$ is the branching ratio for the Z' decaying into a lepton pair. A close inspection of the previous expression reveals that there is a part which only depends on the model parameters, and the remaining part that only depends on the kinematics of the process. Hence, it can be factorized as,

$$\sigma_{l^+l^-} = \frac{\pi}{48s} \mathcal{W}_{Z'} \left(s, m^2_{Z'}\right) \times \mathrm{BR}(Z' \to l^+l^-)\,, \tag{4.36}$$

where the function $\mathcal{W}_{Z'}$ is given by:

$$\mathcal{W}_{Z'} = \sum_{q=u,d,c,s} c_q \omega_q \left(s, m^2_{Z'}\right)\,. \tag{4.37}$$

The coefficients c_q are the sums of the squares of the vector and axial couplings, $(C_q^V)^2 + (C_q^A)^2$, to the corresponding quarks. Notice that we do not include the contributions from the bottom and top quarks, since they can be safely neglected in the production process. In this limit, provided that the first and second quark families share the same charges under the $U(3)_A \times U(2)_B \times U(1)_C \times U(1)_D$ gauge symmetry group (see Section 4.1), the function $\mathcal{W}_{Z'}$ can be written as a sum of the up and down doublet components of the quarks as

$$\mathcal{W}_{Z'} = c_{up}\omega_{up} \left(s, m^2_{Z'}\right) + c_{down}\omega_{down} \left(s, m^2_{Z'}\right)\,. \tag{4.38}$$

In the previous expression we have reabsorbed a factor 2 in the definition of the ω functions. This factor corresponds to the sum of the up and charm quarks contribution to the up component and, in the same way, for the down and strange quarks for the down component.

Using the Eqs. (4.36) and (4.38) one can easily write the production cross section of a dilepton pair mediated by the Z' in proton proton collisions at leading order (LO) as,

$$\sigma^{LO}_{l^+l^-} = \left[c_{up}\tilde{\omega}_{up} \left(s, m^2_{Z'}\right) + c_{down}\tilde{\omega}_{down} \left(s, m^2_{Z'}\right)\right] \times \mathrm{BR}(Z' \to l^+l^-)\,, \tag{4.39}$$

where $\tilde{\omega}_{up,down} = (\pi/48s)\omega_{up,down}$.

Before moving to the phenomenological analysis of the BM points, let us write the partial

widths of the Z' boson decay into SM particles and ψ as a function of the model parameters as,

$$\Gamma_{l\bar{l}} = \frac{m_{Z'}}{12\pi}c^2\left[\left(1+\frac{b}{c}\right)^2\left(1+\frac{2m_l^2}{m_{Z'}^2}\right)+\left(1-\frac{b}{c}-2\frac{d}{c}\right)^2\left(1-\frac{4m_l^2}{m_{Z'}^2}\right)\right]\sqrt{1-\frac{4m_l^2}{m_{Z'}^2}}, \quad (4.40)$$

$$\Gamma_{\nu\bar{\nu}} = \frac{m_{Z'}}{6\pi}c^2\left(\frac{b}{c}+\frac{d}{c}\right)^2, \quad (4.41)$$

$$\Gamma_{u\bar{u}(c\bar{c})} = \frac{m_{Z'}}{4\pi}c^2\left[\left(1+\frac{b}{c}\right)^2\left(1+\frac{2m_{u(c)}^2}{m_{Z'}^2}\right)+\left(1+\frac{b}{c}+2\frac{a}{c}\right)^2\left(1-\frac{4m_{u(c)}^2}{m_{Z'}^2}\right)\right]\sqrt{1-\frac{4m_{u(c)}^2}{m_{Z'}^2}}, \quad (4.42)$$

$$\Gamma_{d\bar{d}(s\bar{s})} = \frac{m_{Z'}}{4\pi}c^2\left[\left(1-\frac{b}{c}\right)^2\left(1+\frac{2m_{d(s)}^2}{m_{Z'}^2}\right)+\left(1+\frac{b}{c}+2\frac{a}{c}\right)^2\left(1-\frac{4m_{d(s)}^2}{m_{Z'}^2}\right)\right]\sqrt{1-\frac{4m_{d(s)}^2}{m_{Z'}^2}}, \quad (4.43)$$

$$\Gamma_{t\bar{t}} = \frac{m_{Z'}}{4\pi}c^2\left[\left(1-\frac{b}{c}\right)^2\left(1+\frac{2m_t^2}{m_{Z'}^2}\right)+\left(1+\frac{b}{c}-2\frac{a}{c}\right)^2\left(1-\frac{4m_t^2}{m_{Z'}^2}\right)\right]\sqrt{1-\frac{4m_t^2}{m_{Z'}^2}}, \quad (4.44)$$

$$\Gamma_{b\bar{b}} = \frac{m_{Z'}}{4\pi}c^2\left[\left(1+\frac{b}{c}\right)^2\left(1+\frac{2m_b^2}{m_{Z'}^2}\right)+\left(1-\frac{b}{c}+2\frac{a}{c}\right)^2\left(1-\frac{4m_b^2}{m_{Z'}^2}\right)\right]\sqrt{1-\frac{4m_b^2}{m_{Z'}^2}}, \quad (4.45)$$

$$\Gamma_{\psi\bar{\psi}} = \frac{m_{Z'}}{6\pi}h^2\left(1-\frac{m_\psi^2}{m_{Z'}^2}\right)\sqrt{1-\frac{4m_\psi^2}{m_{Z'}^2}}, \quad (4.46)$$

where l and ν refer to the three families of leptons and neutrinos, respectively. These expressions and the SM couplings of the Z', given in Section 4.1, allow us to evaluate the LHC bounds as a function of the parameters a/c and b/c.

It is important to note that other searches could constraint this kind of mediators such as monojets, $\bar{t}t$ production or monolepton. For a detailed study of the monojets and $\bar{t}t$ production constraints see Ref. [275].

4.4. Isospin violating DM in light of the LHC and LUX results

As we have shown previously, this kind of constructions generally predict isospin violating DM. The relations between the proton and neutron contributions for SI and SD interactions depend on the couplings a, b and c, and more specifically, in their relations.

According to Eqs. (4.21)-(4.25), all couplings of the Z' to SM fermions can be written in terms of the four parameters $a\,, b\,, c\,, d$. In light of this, it is obvious that certain combinations of these parameters will affect the predicted values of some constrained experimental observables. Furthermore, as pointed out in Section 4.1, there are some constraints on these parameters that come from the building of the Z and Z' bosons in this model. This Section is aimed at exploring the impact that these constraints have on the allowed values of a/c and b/c, and hence, on the experimentally allowed values of f_n/f_p and a_n/a_p. Needless to say, these regions will depend on certain assumptions on the DM mass and its coupling h, the Z' mass, d/c, and c, and for this reason we will concentrate on six representative benchmark (BM) points. The values used for each of these parameters are shown in Table 4.2.

	c	d/c	h	m_ψ (GeV)	$m_{Z'}$ (TeV)
BM1	0.01	1	0.1	50	1
BM1a	0.01	2	0.05	50	1
BM2	0.1	3	0.5	500	3
BM2a	0.05	5	0.25	500	3
BM3	0.1	1	0.1	2000	3
BM3a	0.25	1	0.2	2000	3

Table 4.2: Input parameters for each BM point.

It is legitimate to ask whether the mass scales that appear in such BMs can arise in consistent string compactifications. As we have already mentioned at the end of Section 4.1, Z' masses of the order of the TeV, although not generic, can be achieved in several ways without much difficulty. On the other hand, notice that the DM particles are charged, often chirally, not only under $U(1)$ hidden groups, but also under non-abelian factors, i.e. the $G_{\rm h}$ in Eq. (4.1). Therefore, the mass of the field ψ is related to possible strong coupling dynamics and symmetry breaking patterns (e.g. a hidden Higgs mechanism) of the hidden non-abelian gauge sector. In this sense, it is quite natural to consider DM masses in the GeV-TeV range, at least as natural as having visible sectors reproducing the masses of the SM particles.

Given the potential complexity of the matter and gauge structure of the hidden sector, it seems reasonable to asume that there could be some mechanisms, either thermal or non-thermal, to account for the relic abundance of ψ other than annihilation through the Z' channel. This highlights the dependence of the DM abundance on the particular details of the hidden sector dynamics, which we want to keep as generic as possible. Nevertheless, it is worth mentioning that, in general, annihilation cross sections through the Z' channel are lower than the thermal value, and thus indirect detection bounds on the annihilation cross section are generally far from our predictions.

The only contributions to the phenomenology of the model that do not depend on any further assumption on the hidden sector are direct DM searches and LHC searches for resonances[7]. The former only depends on the coupling of ψ to quarks by the exchange of a Z' boson (see Figure 4.1), while the latter depends on the coupling of Z' to SM particles (quarks and leptons) and the coupling h. In the following, we will determine the experimentally allowed regions of a/c and b/c in the six BM points shown in Table 4.2 taking into account the limits from LUX and the LHC.

LUX and LHC limits

The recent null results of the LUX collaboration [206] have placed a very stringent upper limit on the elastic scattering of DM off protons, reducing significantly the parameter space allowed

[7] Hadronic decays [52, 276] and the muon anomalous magnetic moment [265, 277] do not depend either on any further assumption and can affect the allowed values of parameters a, b and c. However, we have checked that these constraints are not competitive with LUX and LHC in the region of the parameter space considered in this Thesis.

in many theories that provide DM candidates. This limit has been extracted by assuming a scalar DM candidate (zero SD contribution) and $f_n/f_p = 1$, which are the typical assumptions that the collaborations use in order to compare their results within a unified framework. However, this prevents us from using this result directly, since none of these two assumptions hold for the DM candidate analysed in this Chapter. Therefore, in order to implement this bound properly we have simulated the LUX experiment, and we have calculated for a given point of the parameter space if it is allowed at 90% C.L. using the Yellin's maximum gap method [278]. To such end, we calculate the predicted total number of events in LUX considering the SI and SD components and computing the f_n/f_p, a_n/a_p ratios. To calculate the 90% C.L. exclusion using the maximum gap method, we consider that LUX experiment has observed zero candidate events in the signal region[8].

To calculate the total number of expected signal events in a Xe-based detector we have followed the prescription of Ref. [279] in the S1 range 2-30 PE for an exposure of 10065 kg days, using the acceptance shown in the bottom of Fig. 1 of Ref. [206] plus an extra 1/2 factor to account for the 50% of nuclear recoil acceptance. We use the S1 single PE resolution to be $\sigma_{PMT} = 0.37$ PE [280], a 14% of photon detection efficiency, and the absolute scintillation efficiency digitized from Ref. [206]. For the DM speed distribution, we use the standard isothermal Maxwellian velocity distribution, with $v_0 = 220$ km/s, $v_{esc} = 544$ km/s, $\rho_0 = 0.3$ GeV/cm^3 and $v_e = 245$ km/s, as the one used by the LUX collaboration [206]. As pointed out in Ref. [281] the effect of the form factors can also induce important differences in the expected number of events. In this Chapter we use the Helm factor for the SI component and the SD structure functions given in Ref. [269] for the SD component.

To show explicitly the dependence of the SI and SD elastic scattering cross sections on the parameters of the model, namely, on the ratios a/c and b/c, let us write them as,

$$\sigma_p^{SI} = \frac{4}{\pi}\mu_p^2 f_p^2 = \frac{\mu_p^2 h^2}{\pi m_{Z'}^4}\,(3b+c)^2\,, \tag{4.47}$$

$$\sigma_p^{SD} = \frac{24 G_F^2}{\pi}\mu_p^2 a_p^2 = \frac{3\mu_p^2 h^2}{\pi m_{Z'}^4}[(2a+b-c)\Delta_u^p + (2a+b+c)(\Delta_d^p + \Delta_s^p)]^2. \tag{4.48}$$

Notice that in order to calculate the neutron contributions one has to multiply by $(f_n/f_p)^2$ the SI component and by $(a_n/a_p)^2$ the SD component, whose expressions are given in Eqs. (4.30) and (4.34). Let us mention at this point the existing relation between the SI and the SD elastic cross sections. From the previous equations, and the corresponding neutron counterparts, one can easily see that the contribution from the SD cross section to the total number of expected events dominates if $|a/c| \gg |b/c|$ and $|a/c| \gg 1$. However, for a given of c the ratio a/c cannot be arbitrarily large due to the normalization Eq. (4.18). In fact, it can be shown that for the SD component to be dominant in LUX for the range of m_ψ considered and when $|b/c| < 5$ (the region shown in the figures) then $a/c \gtrsim 100$. Using the values of c shown in Table 4.2, such high values of a/c do not satisfy the Eq. (4.18), and hence, they are not considered.

[8] Actually, LUX observed one candidate event that was marginally close to the background region in the $\log_{10}(S2/S1) - S1$ plane. Thus our result of the exclusion is closer to the actual LUX limit when considering zero observed events.

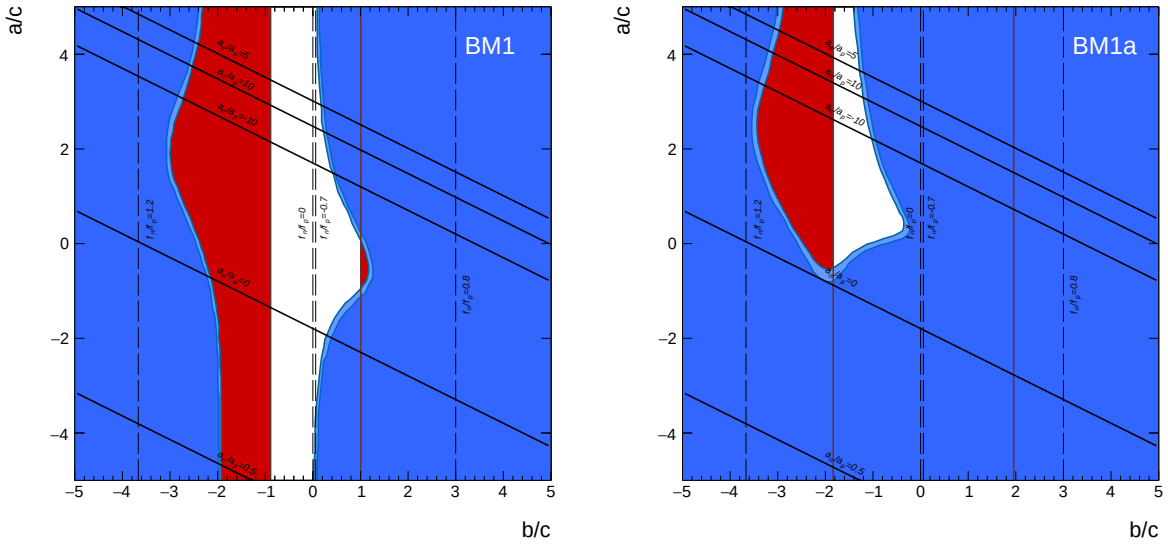

Figure 4.4: a/c versus b/c for BM1 (left) and BM1a (right). As in Figure 4.3 we show some values of the ratios f_n/f_p and a_n/a_p. The LUX bound excludes all the region depicted in red. LHC bounds rule out different regions for e^+e^- (light blue) and $\mu^+\mu^-$ resonances (darker blue). In this BM point, dijet resonances do not constrain.

In order to compute the constraints from LHC searches we make use of the dimuon, dielectron and dijet resonance searches . In that sense we make use of the formalism described in Section 4.3. To extract the functions $\tilde{\omega}$ at $\sqrt{s} = 8$ TeV we have benefited from `CalcHEP 3.6.22` [203] using the parton distribution functions `CTEQ6L` to be consistent with the LHC analysis [270]. Furthermore, in order to include Next-to-LO effects, we have used the K-factor given in Ref. [282]. Remarkably, this approach can be used to calculate not just the bounds for dilepton but also for dijet resonances just by substituting $\text{BR}(Z' \to l^+l^-)$ (valid for dilepton in the previous expressions) by $\text{BR}(Z' \to q\bar{q})$, where a sum over all quarks (except for the top quark [273]) must be performed. Finally, to include properly the dijet resonance searches, the cross section times the branching fraction must be multiplied by a factor $A = 0.6$ which accounts for the efficiency of the detector [273].

Results

Let us start analysing BM1 and BM1a. These BM points correspond to a low mass dark matter candidate, with a mass of 50 GeV and a Z' boson of 1 TeV. In Figure 4.4 we show the plane a/c-b/c with some values of the ratios f_n/f_p and a_n/a_p for BM1 (left panel) and BM1a (right panel). We have superimposed the 90% C.L. LUX exclusion region (shown in red) that rules out high values of $|b/c|$, while in blue we show the exclusion regions from the LHC searches for e^+e^- (light blue) and $\mu^+\mu^-$ resonances (darker blue). As we have anticipated previously, the LUX limit does not depend on the specific value of a/c since in this region of the parameter space the SI contribution of the elastic scattering dominates over the SD one. For BM1, LUX excludes the regions $b/c \lesssim -0.9$ and $b/c \gtrsim 1.0$, which correspond to the regions in which the proton and neutron

components of the SI elastic cross section are similar, $|f_n/f_p| \approx 1$. To understand this behaviour note that the proton contribution given in Eq. (4.47) decreases very fast around $b/c = -1/3$, faster than f_n/f_p (due to f_p^2). This means that, although in the allowed region the neutron contribution to the SI cross section dominates with values of f_n/f_p that can be very large (see also left panel of Figure 4.2), it also decreases, and thus, the LUX limit weakens. For BM1a, since the value of h has been decreased respect to BM1, the coupling of ψ to the Z' also diminishes and then the LUX limits are able to constrain much less parameter space, namely, it rules out the region $|b/c| \gtrsim 1.9$.

Unlike direct detection limits, LHC bounds depend on the value of a/c. First of all, we show that for BM1 when $|a/c| \lesssim 2$, both e^+e^- and $\mu^+\mu^-$ bounds are less stringent. This can be understood from Eqs. (4.43) and (4.44). The second term in both expressions is minimized when $b/c \approx -2a/c$ which is translated into a minimization of the production cross section of the Z' (see also Eq. (4.38)) and thus, both limits are less stringent. Besides, LHC limits are stronger for positive values of b/c as a consequence of the dominance of the $\tilde{\omega}_{up}$ function over the corresponding function of the down component and hence, the production through the up component cancels out the first term of Eq.(4.43) for $b/c \approx -1$. LHC limits are stronger for BM1a for two reasons. First, the increasing of d/c makes the Z' coupling to leptons higher and then the corresponding branching ratio is increased. Second, a smaller value of h makes the Z' boson less *invisible*, which is translated into an increase of both, its production cross section and its branching ratio into SM particles. Remarkably, LHC limits rule out a big portion of the parameter space allowed by LUX, including the Xe-phobic value of f_n/f_p, and it leaves only a small region allowed corresponding to positive values of a/c and $-2 \lesssim b/c \lesssim -1$.

Interestingly, the allowed regions for both BMs represent isospin violating DM scenarios in which the neutron contribution of the SI component might be much higher than the corresponding proton component but both are generally small in order to evade LUX bounds. For the SD component in BM1, the values of a_n/a_p are not restricted while for BM1a, the allowed region encodes a_n/a_p generally larger than one. In conclusion, there exists an outstanding complementarity between LHC and direct detection searches for these BM points. While LUX is more stringent than the LHC for negative values of b/c, the LHC is more constraining for positive ones, and for BM1a also for negative a/c, which highlights the power of combining different experiments in the search for new physics.

Let us move now to BM2 and BM2a. These BM points entail a much heavier DM candidate with respect to the previous ones, now $m_\psi = 500$ GeV, and a Z' boson of 3 TeV, heavier than before as well. In this region of DM masses, direct detection experiments start to lose their sensitivity very rapidly, so we have increased the DM coupling h in order for the LUX limit to play a role. Besides, by augmenting d/c we have increased the decay width of the Z' boson into leptons, which makes dilepton constraints more stringent. In Figure 4.5 the plane a/c-b/c is depicted for these BM points. Notice that in this case dijet searches at the LHC are shown as dark blue regions with oval-like shapes and are specially important in the upper left corner of the BM2 case.

As in the previous BMs, LUX limits are very stringent in this case, specially for BM2, and again are independent of a/c (dominated by SI interactions). LUX rules out the zone $|b/c| \gtrsim 0.4$ for BM2 and $|b/c| \gtrsim 1.7$ for BM2a, since for the latter the values of both c and h are smaller. For BM2, the reason for this behaviour is the same as before: in the region not excluded, although the

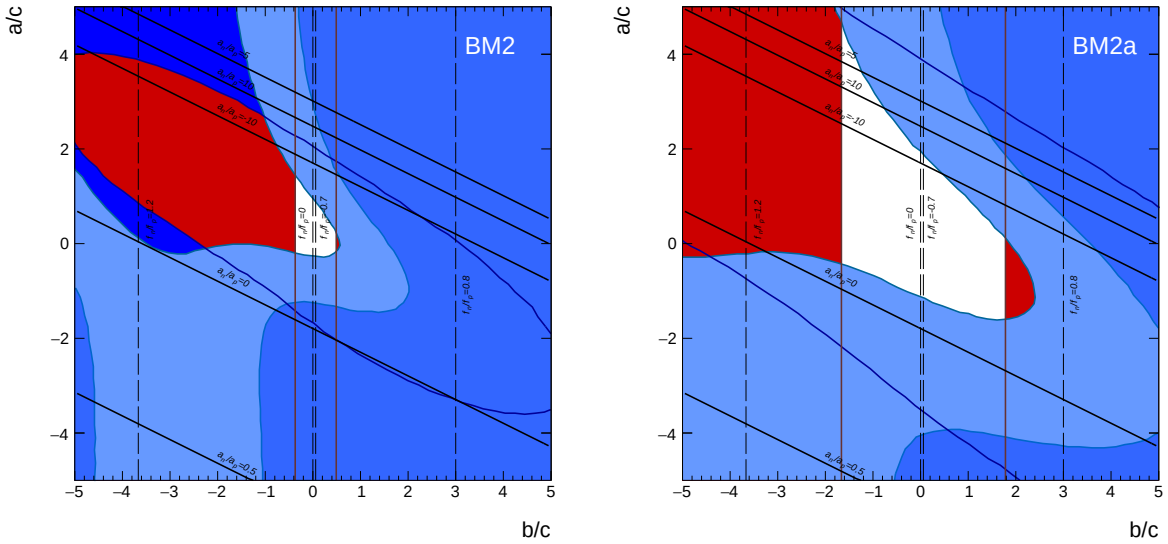

Figure 4.5: Same as Figure 4.4 but for BM2 (left) and BM2a (right). In this case the exclusion region from dijet resonances at the LHC is shown in dark blue.

neutron contribution is much higher than the proton contribution, both cross sections are small. LHC limits from dilepton resonances are now very well differentiated and more stringent as a consequence of the increase of d/c (respect to BM1 and BM1a). The difference between e^+e^- and $\mu^+\mu^-$ channels is more notably and comes from the different sensitivity of the ATLAS detector to these channels at this Z' mass, since its coupling to each of these leptons is identical. Finally, dijet resonance searches appear in these cases as more constraining than dileptons and LUX in a small region of the parameter space (the upper left corner in the left panel of Figure 4.5). The shape of this constraint is due to the squares of the couplings to quarks, involved either in the production mechanism or in the subsequent decay of the Z'. This can be understood as a *leptophobic* behaviour of the Z' in this region of BM2, while we have not found such feature in BM2a due to the increase of d/c which makes the Z' more *leptophilic*.

To end with these BM points, as it is shown in Figure 4.5, there is only a tiny region allowed for BM2, while for BM2a the region is considerably bigger. In terms of isospin violation in the SI interactions, it corresponds to neutron dominance as in the previous cases. Remarkably, the Xe-phobic scenario ($f_n/f_p = -0.7$) remains allowed by both LHC and LUX in the two BMs analysed. For the SD interactions, the ratio a_n/a_p is found to range between 1 and -10, approximately, and thus, it can be concluded that in general all interactions in direct detection experiments would be dominated by neutrons. The complementarity between direct DM searches and the LHC now takes a new shape. LUX rules out the values of b/c stronger than LHC in all cases, however, the LHC is able to constrain high values of $|a/c|$. Surprisingly, this complementarity is able to delimit the allowed portions of the parameter space so strongly that the we have obtained closed regions.

To end with the analysis, we study two BMs in which the decay of the Z' into DM particles is kinematically forbidden, BM3 and BM3a, unlike for BM1(a) and BM2(a). Our results are shown

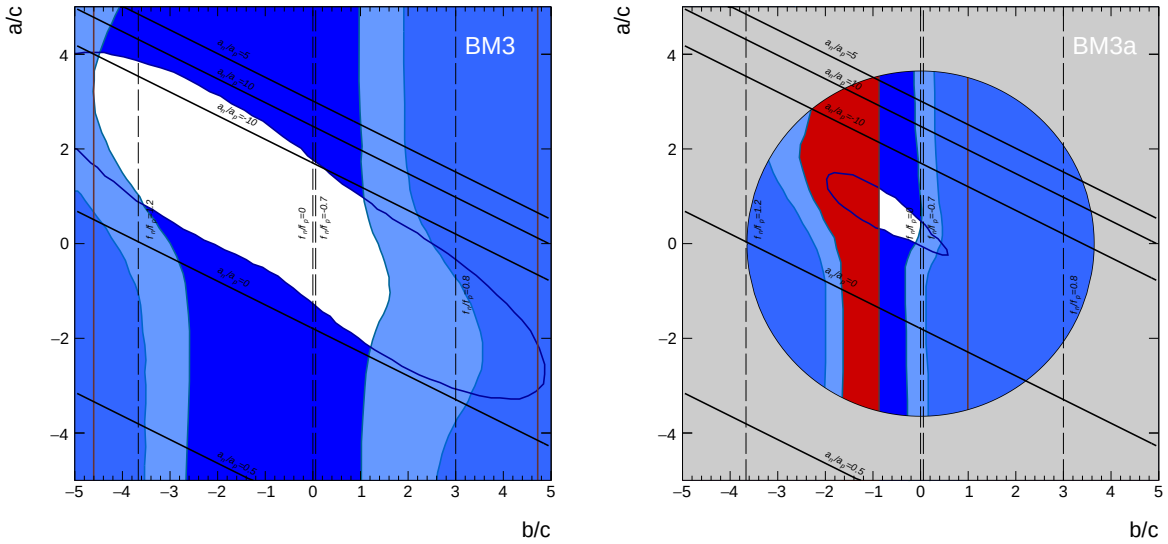

Figure 4.6: Same as Figure 4.5 but for BM3 (left) and BM3a (right). The grey region on the right panel do not satisfy Eq. (4.18) and thus, its is not phenomenologically viable.

in Figure 4.6 for BM3 (left panel) and for BM3a (right panel). The choice of the parameters is such that for BM3, LUX limits are not very constraining, while for BM3a the increase of c and h makes LUX very restrictive. However, for the latter a new constraint, very strong, has appeared. The grey area denotes a forbidden region because it does not satisfy Eq. (4.18). This is a consequence of the value of c in this case, which is the bigger of all BMs.

Since the Z' boson cannot decay into DM particles in BM3 and BM3a, the branching ratios into SM particles are increased, and therefore, we expect LHC limits to constrain very severly. Notably, for BM3 dijet bounds dominate the region $-3 \lesssim b/c \lesssim -1$. The value used for d/c in these BMs makes that for b/c relatively small the Z' boson behaves as *leptophobic*, which results in a decrease in sensitivity of the dilepton searches. As soon as $|b/c|$ increases this behaviour disappears and dilepton bounds are dominant over the dijet ones. In most of the region allowed the SI elastic scattering cross section is dominated by neutrons, except for the region close to $b/c \approx 1$. The ratio a_n/a_p allowed is very similar to those in the previous BM points.

For BM3a, shown in the right panel of Figure 4.6, we find that only a very small region is allowed. The region extending from $b/c \approx -1$ up to $b/c \approx 0$, and from $a/c \approx 0$ to $a/c \approx 1$. From a point of view of complementarity, this region is exceptionally exemplifying since it is delimited by all the searches. The upper and lower regions are bounded by dijet searches, the left by LUX and the right by dilepton searches. This is a consequence of increasing c while keeping the ratio d/c constant. In this case, the SI cross section is dominated by neutrons and the SD proton cross section is similar to the neutron component but with $a_n/a_p \approx -1$.

Part II

Supersymmetric Dark Matter

5

Next to - MSSM with RH sneutrinos

The NMSSM with RH neutrino and sneutrino states was introduced in Refs. [93–96]. It was there shown that the RH sneutrino can be the LSP and a viable candidate for dark matter within the category of WIMPs, since the correct relic abundance can be obtained in wide regions of the parameter space, including the possibility that the RH sneutrino is very light [97].

The superpotential of this model reads

$$W = W_{\rm NMSSM} + \lambda_N S N N + y_N L \cdot H_2 N, \tag{5.1}$$

where flavour indices are omitted and the dot denotes the $SU(2)_L$ antisymmetric product. The Lagrangian contains new soft-supersymmetry breaking parameters as follows

$$-\mathcal{L} = -\mathcal{L}_{\rm NMSSM} + {m_{\tilde{N}}}^2 |\tilde{N}|^2 + \left(\lambda_N A_{\lambda_N} S \tilde{N}^2 + y_N A_{y_N} \tilde{L} H_2 \tilde{N} + \text{H.c.}\right). \tag{5.2}$$

In total, five new free parameters are included, namely a soft sneutrino mass $m_{\tilde{N}}$, two Yukawa couplings λ_N and y_N, and two trilinear parameters A_{λ_N} and A_{y_N}. After radiative Electroweak symmetry-breaking takes place the Higgs fields take non-vanishing VEVs. In particular the VEV of the singlet, v_s, triggers an effective μ parameter which provides an elegant solution to the μ problem of the MSSM. At the same time, an effective Majorana mass is generated for the RH neutrino,

$$M_N = 2\lambda_N v_s \ , \tag{5.3}$$

which is therefore of the order of the electroweak scale.

The neutrino mass matrix can then be written in terms of the above quantities as

$$M_\nu = \begin{pmatrix} 0 & \mathbf{y}_N v_2 \\ \mathbf{y}_N^T v_2 & 2\lambda_N v_s \end{pmatrix} = \begin{pmatrix} 0 & M_D \\ M_D^T & M_N \end{pmatrix}. \tag{5.4}$$

In general M_D is a $3 \times k$ matrix and M_N is a $k \times k$ matrix, where k is the number of RH neutrinos. In this Chapter, for simplicity, we consider only one RH neutrino with equal mixings with the three left-handed neutrinos[1]. In the limit where the neutrino Yukawa is small, the diagonalization of the above mass matrix yields two eigenstates which are almost approximately pure gauge eigenstates. The lightest of these would correspond to ordinary left-handed neutrinos, $\nu_1 = \nu_L$, whereas the heavier one is a pure RH neutrino $\nu_2 = N$, with masses as follows,

$$m_{\nu_L} = \frac{y_N^2 v_2^2}{2\lambda_N v_s}, \qquad M_N = 2\lambda_N v_s \, . \tag{5.5}$$

[1]The properties of a general construction, with three RH neutrinos, would be affected by the specific texture of the Yukawa matrix. Although this would have a profound effect on the resulting neutrino phenomenology, the presence of displaced vertices would be treated in a similar fashion to the analysis in this Chapter.

Notice that in order to reproduce the smallness of the left-handed neutrinos the value of y_N has to be small, of the order of the electron Yukawa, $y_N \sim 10^{-6}$, typical of a low-scale see-saw mechanism. As we will see in the next section, the smallness of this parameter is responsible for the presence of displaced vertices or long-lived charged particles.

We will express neutrino mass eigenstates in terms of the mixing matrix, N^ν as follows,

$$\nu_i = N^\nu_{iL}\nu_L + N^\nu_{iR}N\,, \tag{5.6}$$

and identify $\nu_1 \approx \nu_L + N^\nu_{1R}N$ and $\nu_2 \approx N^\nu_{2L}\nu_L + N$. The mixing between LH and RH neutrino mass eigenstates, as obtained from the diagonalization of Eq. (5.4), is proportional to y_N and therefore small, $N^\nu_{1R} = N^\nu_{2L} = \frac{y_N v_2}{2\lambda_N v_s}$.

Regarding the sneutrino sector, the mass eigenstates are also a linear superposition of the LH and RH gauge eigenstates, $\tilde{\nu}_L$ and $\tilde{N}$, respectively. We can use a similar description in terms of the mixing matrix $N^{\tilde{\nu}}$ as follows,

$$\tilde{\nu}_i = N^{\tilde{\nu}}_{iL}\tilde{\nu}_L + N^{\tilde{\nu}}_{iR}\tilde{N}\,. \tag{5.7}$$

As in the case of the neutrinos, the left-right mixing terms are proportional to y_N (the complete expression can be found in Ref. [96]) and are therefore very small. For this reason the mass eigenstates are almost pure LH or RH fields, $\tilde{\nu}_1 \approx N^{\tilde{\nu}}_{2L}\tilde{\nu}_L + \tilde{N} \approx \tilde{N}_1$ and $\tilde{\nu}_2 \approx \tilde{\nu}_L + N^{\tilde{\nu}}_{2L}\tilde{N} \approx \tilde{\nu}_L$, with $N^{\tilde{\nu}}_{2L}$, $N^{\tilde{\nu}}_{1R} = \mathcal{O}(y_N)$. Notice that in this case we identify the lightest eigenstate with the lighter RH sneutrino, $\tilde{N}_1$. In terms of the rest of the parameters the lighter RH sneutrino mass reads

$$m^2_{\tilde{N}_1} = m^2_{\tilde{N}} + |2\lambda_N v_s|^2 + |y_N v_2|^2 \pm 2\lambda_N \left(A_{\lambda_N} v_s + (\kappa v_s^2 - \lambda v_1 v_2)^\dagger\right), \tag{5.8}$$

where the sign in front of $2\lambda_N$ is chosen opposite to the sign of $2\lambda_N \left(A_{\lambda_N} v_s + (\kappa v_s^2 - \lambda v_1 v_2)^\dagger\right)$.

In this construction, the on-shell production of RH neutrinos can lead to the occurrence of displaced vertices. Moreover, if the NLSP is the lighter stau, it can also behave as a long-lived charged particle if produced on-shell. In both cases the lifetime of the corresponding particle is a function of the neutrino Yukawa, y_N, as we will see in the next section, and since $y_N \sim 10^{-6}$ particles tend to be long-lived.

5.1. RH-sneutrino Dark Matter

Given the fact that the RH-sneutrino fulfils all the important properties of a viable DM candidate it is possible to be the DM particle. There exist different attempts in the literature to present the sneutrino as a well candidate for DM, for instance the Left-Handed sneutrino appearing in the MSSM, however it was shown in Ref. [79] that the LH sneutrino coupling with the Z boson was high enough to produce a quick annihilation in the Early Universe and also to a high rate in the scattering cross section off nuclei. In order to evade this problem a mixed state of LH and RH sneutrino was proposed so tuning the mixing one can control annihilation rates [283–288].

In this model a pure RH sneutrino state is considered. Two important aspects are crucial for the RH sneutrino to be a good candidate to DM. The first one is the flexibility in the mass of

the RH sneutrino. In Eq. (5.8) the mass of the RH-sneutrino is shown as a function of different parameters of the model. It is easily seen that achieving a specific mass of the RH-sneutrino can be obtained tuning the different parameters of the model. The other aspect to be taken into account is the Higgs sector. The Higgs couples to RH-sneutrinos through the term SNN of Eq. (5.1). The strength of this interaction modifies the different annihilation rates of the RH-sneutrinos being the responsible of the different DM properties such as the relic density and also the direct detection rates. Being the Higgs sector the main responsible of the connection between the DM sector and the SM one[2] the final states of the RH-sneutrino annihilation are W^+W^-, ZZ, $f\bar{f}$, $H_i^0H_j^0$, $H_i^+H_j^-$, $A_a^0A_b^0$, ZA_a^0, $W^\pm H^\mp$, gg, $Z\gamma$, $\gamma\gamma$ and NN. All these channels contribute to the annihilation rate in the Early Universe and determine the present relic density. Furthermore the fermionic channel is the responsible of the direct detection cross section. Consequently if the fermionic channel is the dominant one, there is a correlation between different processes. However, if this correlation implies that one of the DM results is unfavoured the other annihilation channels could help to alleviate this. For that reason the RH-sneutrino is a viable and attractive candidate for DM. In Refs. [97–100] an exhaustive and detailed DM analysis of the model has been performed showing the different characteristics and possibilities of the RH-sneutrino in view of the different DM experiments.

5.2. Constraints on the Higgs invisible decay width

The recently discovered Higgs particle at the LHC has a mass of 126 GeV and SM-like branching ratios [8, 289]. Within the NMSSM a scalar Higgs with these properties can be obtained in wide regions of the parameter space [290–304]. In fact, the presence of an extra scalar Higgs field induces new contributions to the Higgs mass from the $\lambda S H_u H_d$ term in the superpotential, which allows to get a fairly heavy Higgs boson while reducing the fine-tuning with respect to the situation in the MSSM. The Higgs sector of the NMSSM is very rich, and the presence of a lighter scalar Higgs is also allowed, provided that it is mostly singlet-like. All these features are still valid in our construction, however, when implementing constraints on the resulting Higgs phenomenology one has to be aware that the presence of light RH neutrinos or sneutrinos can contribute significantly to the invisible decay width of the scalar Higgses [97]. For the reduced signal strength of the Higgs to di-photon mode, $R_{\gamma\gamma}$, we use $0.23 \leq R_{\gamma\gamma} \leq 1.31$, the latest CMS results at 2σ [305][3]. The remaining reduced signal strengths are also constrained according to the CMS results of Ref. [305] (see Refs. [307, 308] for the equivalent ATLAS results). Notice that these measurements indirectly entail a strong bound on the invisible and non-standard decay modes of the SM-like Higgs boson [309–316], which in our case affects the decay modes $h_{SM}^0 \to H_1^0H_1^0$, $h_{SM}^0 \to A_1^0A_1^0$, $h_{SM}^0 \to \tilde{\chi}_i^0\tilde{\chi}_i^0$, and especially, $h_{SM}^0 \to NN$ and $h_{SM}^0 \to \tilde{N}_1\tilde{N}_1$.

[2]There are other diagrams connecting the DM and the SM sectors, however they are proportional to the neutrino Yukawa, y_N that is negligible compared with the other couplings such as λ_N

[3]For ATLAS the same limit including all systematics is $0.95 \leq R_{\gamma\gamma} \leq 2.55$ [306, 307].

The decay width of a scalar Higgs into a RH sneutrino pair or a RH neutrino pair is [97],

$$\Gamma_{H_i^0\to\tilde{N}_1\tilde{N}_1} = \frac{|C_{H_i^0\tilde{\nu}\tilde{\nu}}|^2}{32\pi m_{H_i^0}}\left(1-\frac{4{m_{\tilde{N}_1}}^2}{m^2_{H_i^0}}\right)^{1/2}, \tag{5.9}$$

$$\Gamma_{H_i^0\to NN} = \frac{\lambda_N^2 (S^3_{H_i^0})^2}{32\pi} m_{H_i^0}\left(1-\frac{4{M_N}^2}{m^2_{H_i^0}}\right)^{3/2}, \tag{5.10}$$

where the Higgs-sneutrino-sneutrino coupling reads [96]

$$C_{H_i^0\tilde{\nu}\tilde{\nu}} = \frac{2\lambda\lambda_N m_W}{\sqrt{2}g}\left(\sin\beta S^1_{H_i^0}+\cos\beta S^2_{H_i^0}\right)+\left[(4\lambda_N^2+2\kappa\lambda_N)v_s+\lambda_N\frac{A_{\lambda_N}}{\sqrt{2}}\right]S^3_{H_i^0}. \tag{5.11}$$

In terms of these, the branching ratio into invisible and non-SM channels reads,

$$\mathrm{BR}(h^0_{SM}\to inv) = \frac{\Gamma_{h^0_{SM}\to inv}}{\Gamma_{NMSSM}+\Gamma_{h^0_{SM}\to inv}}, \tag{5.12}$$

where Γ_{NMSSM} is the Higgs decay width in all other possible NMSSM products and is calculated using the code `NMSSMTools`. $\Gamma_{h^0_{SM}\to inv}$ accounts for all non-standard decays of the Higgs boson, which in our model should comprise decays into pairs of RH neutrinos, RH sneutrinos, neutralinos, and scalar and pseudoscalar Higgs bosons, i.e., $\Gamma_{h^0_{SM}\to inv} = \Gamma_{h^0_{SM}\to\tilde{N}_1\tilde{N}_1}+\Gamma_{h^0_{SM}\to NN}+\Gamma_{h^0_{SM}\to\tilde{\chi}_i^0\tilde{\chi}_i^0}+\Gamma_{h^0_{SM}\to H_1^0H_1^0}+\Gamma_{h^0_{SM}\to A_1^0A_1^0}$. In the scenarios considered in this chapter the neutralinos and lightest CP-even and CP-odd Higgses are heavier than $m_{h^0_{SM}}/2\approx 62$ GeV, and therefore only the contributions from decays into RH neutrinos and sneutrinos are important.

From the expressions above it is clear that if the decay into RH neutrinos is kinematically allowed then large values of λ_N can lead to a sizable contribution to the invisible decay, being therefore very constrained. On the other hand, regarding the Higgs decay into two RH sneutrinos, the Higgs-sneutrino-sneutrino coupling is a more complicated function, involving λ_N, A_{λ_N}, and $m_{\tilde{N}}$, and accidental cancellations might occur. In general, however, large λ_N is also more constrained.

Throughout this Chapter we consider input parameters defined at the electroweak scale, so no running is performed. The supersymmetric spectrum and Higgs phenomenology is computed using `NMSSMTools` [317–319], which we have modified to incorporate the RH neutrino and sneutrino sector. We also include a condition on the stability of the corresponding vacuum following the analysis of Ref. [320]. The decay width for the RH neutrino has been calculated using `CalcHEP 3.4` [203]. We incorporate the most recent experimental constraints on the masses of supersymmetric particles, as well as on low-energy observables (which are also computed using `NMSSMTools`). In particular, we consider the recent measurement of the branching ratio of the $B_s\to\mu^+\mu^-$ process by the LHCb [321] and CMS [322] collaboration, which implies $1.5\times10^{-9}<\mathrm{BR}(B_s\to\mu^+\mu^-)<4.3\times10^{-9}$ at 95% CL. Also, for the $b\to s\gamma$ decay, we require the 2σ range $2.89\times10^{-4}<\mathrm{BR}(b\to s\gamma)<4.21\times10^{-4}$, where theoretical and experimental uncertainties have been added in quadrature [323–327]. We also impose the constraint on the branching ratio of the $B^+\to\tau^+\nu_\tau$ decay at 2σ, $0.85\times10^{-4}<\mathrm{BR}(B^+\to\tau^+\nu_\tau)<2.89\times10^{-4}$ [328]. Regarding the supersymmetric contribution to the muon anomalous magnetic moment, a_μ^{SUSY}, experimental data using e^+e^- suggest that there is a deviation

from the SM value [329–333]. However, if tau data is used, this discrepancy is smaller [332]. In our analysis we compute this quantity but do not impose any constraints on it. Following the recent observations, we demand the presence of a Higgs boson with a mass of 126 GeV and SM-like couplings [8, 289]. Finally, some analysis suggest the existence of a second singlet-like Higgs boson with a mass around 98 GeV [334–336], a possibility that we also consider in one example.

Table 5.1 shows the input parameters for three NMSSM scenarios, labelled S1, S2 and S3, that will be used in this Chapter and that pass all the constraints mentioned above. We also indicate the RH sneutrino relic density and spin-independent scattering cross section off nucleons [4], σ^{SI}. Part of the resulting supersymmetric spectrum (corresponding to the Higgs, stau and neutralino/chargino sectors) is shown, together with the corresponding values for some low-energy observables. In scenario S1 the SM Higgs is the second-lightest one, $h^0_{SM} = H^0_2$, whereas in scenarios S2 and S3 it is the lightest one, $h^0_{SM} = H^0_1$.

Since we have chosen small values of $\tan\beta$, the value of $\mathrm{BR}(B_S \to \mu^+\mu^-)$ is very close to the SM value and this constraint is not very important in ours scan. On the other hand, $\mathrm{BR}(b \to s\gamma)$ has a more serious impact on the NMSSM parameter space (see e.g., Ref. [76]). Finally, in the low $\tan\beta$ regime the contribution to the muon anomalous magnetic moment is not sufficient to account for the deviation observed in e^+e^- data.

In Refs. [96, 97] it was shown that the RH sneutrino relic density can be adjusted by playing with the free parameters λ_N, A_{λ_N} and $m_{\tilde{N}}$ without significantly affecting the NMSSM phenomenology. For this reason, in this analysis we do not impose any constraint on the relic abundance of the RH sneutrino.

We have constructed a chi-squared function, $\chi^2(\mu)$, for the total visible signal strength, μ, using the data for the signal strengths of each individual process given by ATLAS and CMS. In order to be conservative we assume that $\mu = 1 - \mathrm{BR}(h^0_{SM} \to inv)$, which holds if the Higgs is totally SM-like except for the new decays. This means that new contributions (apart from those of the SM) to the Higgs production are assumed to be zero. Although this is not always true for SUSY models, this implies a stronger bound on the invisible Higgs branching ratio. The minimum of the function is achieved for a non-zero value of the invisible Higgs branching ratio, and the 1σ and 2σ values are given by $\chi^2 = \chi^2_{min} + \Delta\chi^2$, with $\Delta\chi^2 = 1$, and 4 respectively. With this prescription, we obtain $\mathrm{BR}(h^0_{SM} \to inv) < 0.15(0.27)$ at $1\sigma(2\sigma)$, consistent with other recent analyses [310–316].

We illustrate in Figure 5.1 the effect of these bounds on the (λ_N, $m_{\tilde{N}}$) plane corresponding to scenarios S1 and S2 of Table 5.1. For each of these we consider two examples with $A_{\lambda_N} = -150$ GeV and -250 GeV. The light (dark) blue area corresponds to the region excluded due to an excess in the invisible branching ratio of the SM-like Higgs. The constraints from the invisible Higgs decay are very dependent on the RH sneutrino parameters. In Figure 5.1 the RH sneutrino mass increases with the soft mass parameter $m_{\tilde{N}}$ (along semicircular trajectories that depend on λ_N). The dark gray area corresponds to regions of the parameter space for which $m^2_{\tilde{N}_1} < 0$ and the light gray area

[4] We only give these quantities for information, since we have not applied dark matter constraints in this Chapter. Most of the points have a relic density very close to the value obtained by Planck data and a value of σ^{SI} that is just above or below the current upper bound obtained by the LUX, XENON100 and SuperCDMS direct detection experiments [123, 206, 337]. Direct detection limits are more important for points with light RH sneutrino, such as S1a and S1b, and some of us will reanalyse the viability of light RH-sneutrinos in the light of these bounds [98].

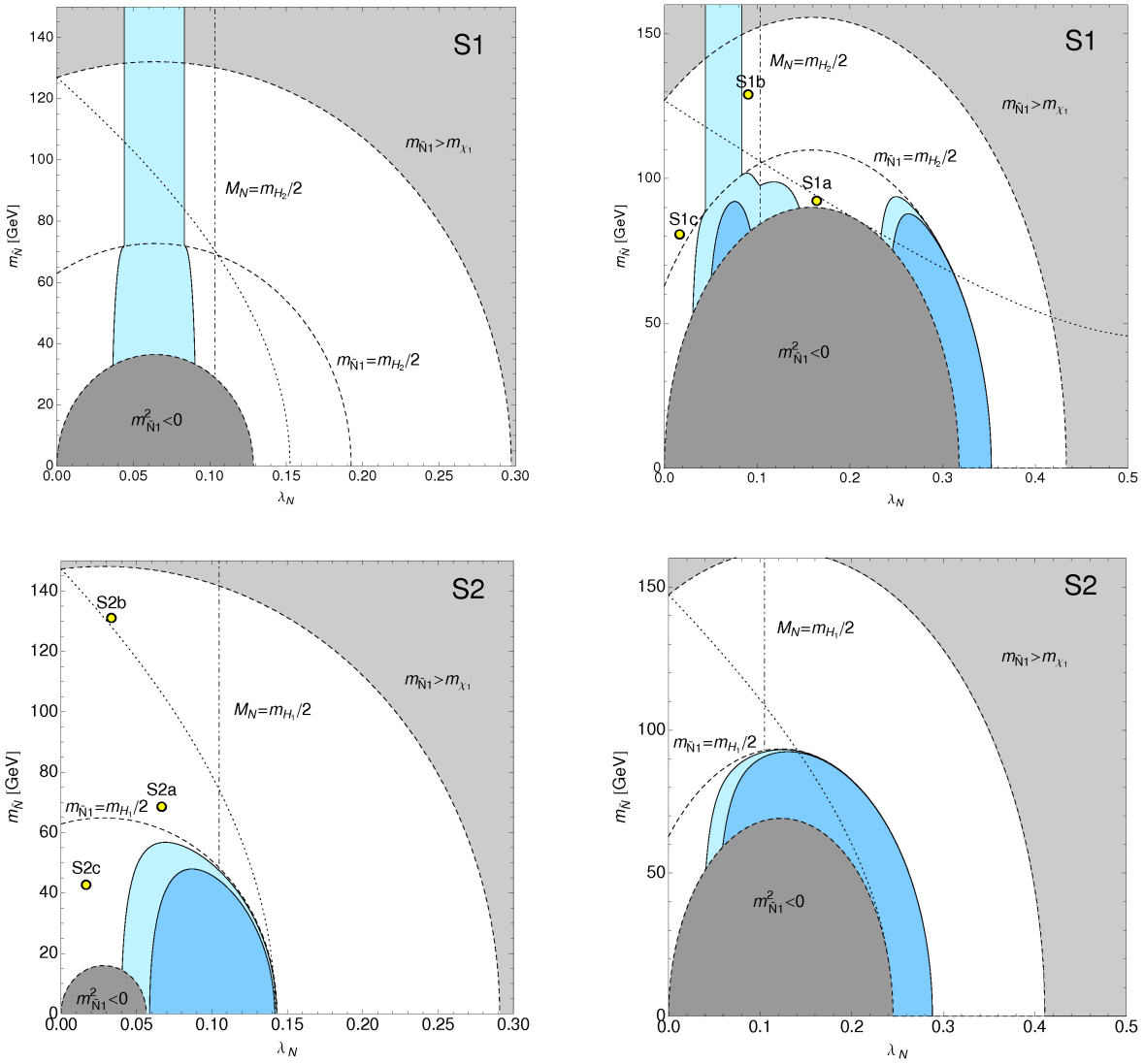

Figure 5.1: Constraints on the $(\lambda_N,\, m_{\tilde{N}})$ plane from the invisible branching ratio of the SM-like Higgs for S1 (upper row) and S2 (lower row). From left to right, the trilinear term is $A_{\lambda_N} = -150,\, -250$ GeV. Dark (light) blue areas correspond to the regions of the parameter space where BR$(h^0_{SM} \to inv) > 0.15(0.27)$, corresponding to the 1σ and 2σ exclusion limit by ATLAS and CMS. Dark gray areas are ruled out since the RH sneutrino mass-squared is negative. Dashed lines indicate the curves along which the RH sneutrino mass is constant and $m_{\tilde{N}_1} = m_{\tilde{\chi}^0_1}$, $m_{\tilde{N}_1} = m_{h^0_{SM}}/2$ from top to bottom. The vertical dot-dashed line corresponds to $M_N = m_{h^0_{SM}}/2$. Finally, points to the left and below the dotted line satisfy $m_{\tilde{N}_1} + M_N < m_{\tilde{\chi}^0_1}$. Yellow dots correspond to the various benchmark points, defined in Table 5.1, that are used in the analysis.

Scenarios	**S1**	**S2**	**S3**
$\tan\beta$	2.0	2.5	2.7
$M_1,\ M_2,\ M_3$	500, 650, 1950	300, 600, 1800	345, 575, 2500
$m_{L,E}$	300	250	1000,350
$m_{Q,U,D_{1,2}}$	2000	2000	2000
m_{Q,U,D_3}	1500	2000	2000
A_E	-1000	-1000	750
$A_{U,D}$	2000	2300	2550
μ	152	180	595
$\lambda,\ \kappa$	0.50, 0.27	0.60, 0.40	0.58, 0.34
$A_\lambda,\ A_\kappa$	283, -220	265, -50	1189, -225
$m_{H_1^0},\ m_{H_2^0},\ m_{H_3^0}$	99.5, 125.8, 358.6	125.7, 225.7, 446.2	125.8, 656.9, 1650.5
$m_{A_1},\ m_{A_2}$	254.1, 348.9	181.0, 432.8	501.5, 1644.9
$m_{\tilde{\chi}_1^0},\ m_{\tilde{\chi}_2^0},\ m_{\tilde{\chi}_3^0}$	127.0, 176.3, 200.1	147.3, 206.9, 277.9	335.7, 528.9, 611.2
$m_{\tilde{\chi}_4^0},\ m_{\tilde{\chi}_5^0}$	492.3, 674.3	306.8, 627.6	665.5, 740.7
$m_{\tilde{\chi}_1^\pm},\ m_{\tilde{\chi}_2^\pm}$	144.9, 674.1	173.6, 627.5	530.6, 676.5
$m_{\tilde{\tau}_1},\ m_{\tilde{\tau}_2}$	290.5, 312.9	245.9, 259.5	352.0, 1000.8
$\mathrm{BR}(b\to s\gamma)$	$4.244^{+0.436}_{-0.631}\times10^{-4}$	$3.984^{+0.381}_{-0.578}\times10^{-4}$	$3.307^{+0.256}_{-0.456}\times10^{-4}$
$\mathrm{BR}(B_s\to\mu^+\mu^-)$	$3.676^{+2.567}_{-1.891}\times10^{-9}$	$3.677^{+2.568}_{-1.892}\times10^{-9}$	$3.677^{+2.568}_{-1.892}\times10^{-9}$
$\mathrm{BR}(B^+\to\tau^+\nu_\tau)$	$1.316^{+1.316}_{-0.748}\times10^{-4}$	$1.316^{+1.316}_{-0.748}\times10^{-4}$	$1.318^{+1.318}_{-0.749}\times10^{-4}$
a_μ^{SUSY}	$2.717^{+2.906}_{-2.528}\times10^{-10}$	$4.592^{+2.938}_{-2.938}\times10^{-10}$	$5.142^{+2.818}_{-2.637}\times10^{-10}$
Benchmark Points	**S1a** **S1b** **S1c**	**S2a** **S2b** **S2c**	**S3a** **S3b**
λ_N	0.165 0.091 0.017	0.067 0.033 0.017	0.083 0.151
$m_{\tilde{N}}$	92.2 128.9 80.6	68.5 130.9 42.5	190.7 179.2
A_{λ_N}	−250 −250 −250	−150 −150 −150	−500 −750
y_N	10^{-7} 10^{-6} 10^{-5}	10^{-6} 10^{-6} 10^{-5}	10^{-7} 10^{-7}
$m_{\tilde{N}_1}$	20 100 70	70 130 40	200 65
M_N	100 55 10	40 20 10	170 310
$\Omega_{\tilde{N}_1}h^2$	0.356 0.155 21.2	0.684 0.838 65.6	0.729 0.047
$\sigma^{\mathrm{SI}}\times10^7$	2.4 2.0 6.9×10^{-4}	7.4×10^{-3} 5.4×10^{-4} 1.4×10^{-3}	1.1×10^{-3} 3.3×10^{-2}

Table 5.1: Input parameters of the NMSSM at the electroweak scale that define the three scenarios S1, S2 and S3 used in this Chapter. The resulting masses of the scalar and pseudoscalar Higgses are indicated, together with the neutralinos, charginos, and the lighter stau, as well as the values of some low energy observables with the corresponding theoretical error. For each scenario, a number of representative benchmark points are defined by the corresponding values of the soft RH sneutrino mass, $m_{\tilde{N}}$, soft trilinear parameter, A_{λ_N}, coupling λ_N, and Yukawa coupling y_N. We also indicate the RH sneutrino mass, $m_{\tilde{N}_1}$ and RH neutrino mass M_N, as well as the RH sneutrino relic density and spin-independent scattering cross section off nucleons (in pb). All the masses are given in GeV.

is the one with $m_{\tilde{N}_1} > m_{\tilde{\chi}_1^0}$, above which the RH sneutrino is no longer the LSP. Dashed lines correspond to trajectories with a constant $m_{\tilde{N}_1}$. In all the examples we observe that $\Gamma_{h^0_{SM}\to\tilde{N}_1\tilde{N}_1}$ becomes larger when A_{λ_N} and λ_N increase and more regions are excluded. Above the line with $m_{\tilde{N}_1} = m_{h^0_{SM}}/2$ the Higgs cannot decay into a RH sneutrino pair and is therefore less constrained.

On the other hand, the RH neutrino mass increases with λ_N and so does the decay width $\Gamma_{h^0_{SM}\to NN}$ (see eq. (5.10)). This gives rise to a vertical excluded area for S1 in the range $0.04 \lesssim \lambda_N \lesssim 0.09$ which is independent of A_{λ_N}. In example S2 the decay width $\Gamma_{h^0_{SM}\to NN}$ is reduced since the SM-like Higgs has a smaller singlet component and therefore does not violate the experimental bound. The vertical dot-dashed line corresponds to $M_N = m_{h^0_{SM}}/2$ so to the right of this line the Higgs decay into a RH neutrino pair is kinematically forbidden.

Finally, points in the area to the left and below the dotted line satisfy $m_{\tilde{N}_1} + M_N < m_{\tilde{\chi}^0_1}$. In this area the neutralino NLSP can undergo the two-body decay $\tilde{\chi}^0_1 \to \tilde{N}_1 N$, whereas to the right and above the dotted line the dominant decay is $\tilde{\chi}^0_1 \to \tilde{N}_1 \nu_L$.

We have selected various representative benchmark points for each scenario, which are indicated in the plot by means of a yellow dot, labelled as S1a, S1b, S1c, S2a, S2b, and S2c, and with parameters defined at the bottom of Table 5.1.

5.3. Displaced Vertices

RH neutrino production

RH neutrinos can be produced at the end of a decay chain together with a RH sneutrino, when the latter is the LSP. If the wino-like neutralino and wino-like chargino are light, the leading production channel is $pp \to \tilde{\chi}_i \tilde{\chi}^\pm_j$ (through a very off-shell W). Both neutralino and chargino subsequently decay into the RH sneutrino LSP in very short chains (e.g., $\tilde{\chi}_i \to \tilde{N}_1 N$ and $\tilde{\chi}^\pm_j \to W^\pm \tilde{\chi}^0_1 \to W^\pm \tilde{N}_1 N$).

RH neutrinos can also be produced directly in the decay of a scalar Higgs boson. This is a very clean channel, however it can be suppressed. On the one hand, the production of a Higgs particle is proportional to its doublet component (which determines the Higgs coupling to SM particles), but the decay of the Higgs into RH neutrinos is only sensitive to its singlet component. Notice also that the $h^0_{SM} \to NN$ branching ratio is also constrained to be small from the recent bounds on invisible Higgs decays.

Both production mechanisms are illustrated in Figure 5.2. The RH neutrino eventually decays into Standard Model particles. Notice that depending on the masses of the particles involved, the RH neutrino can be produced on-shell or be an off-shell mediator of higher order decays. We can define three potential scenarios.

(I) $M_N < m_{\tilde{\chi}^0_1} - m_{\tilde{N}_1}$

In this case, the lightest neutralino two-body decay $\tilde{\chi}^0_1 \to \tilde{N}_1 N$ is kinematically allowed. This proceeds very rapidly, since the coupling $C_{\tilde{\nu} N \tilde{\chi}_i}$ is not Yukawa suppressed. In this case, the RH neutrino and sneutrino are produced on-shell and the on-shell RH neutrino can be long-lived.

(II) $m_{\tilde{\chi}^0_1} - m_{\tilde{N}_1} < M_N < m_{\tilde{\chi}^0_1} + m_{\tilde{N}_1}$

The neutralino two-body decay $\tilde{\chi}^0_1 \to \tilde{N}_1 N$ is not possible, but it can proceed through a

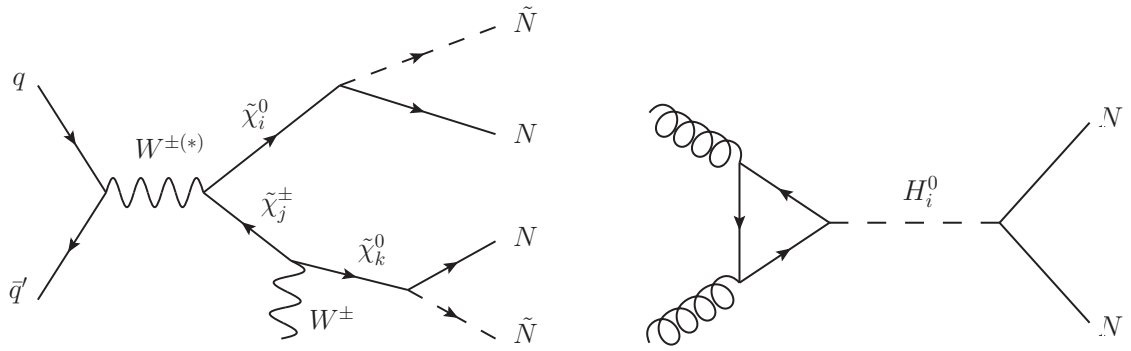

Figure 5.2: Different possibilities for the production of RH sneutrinos. On the left, a neutralino/chargino pair is produced after the original collision and undergoes a short decay chain that ends in the production of a RH neutrino/sneutrino. On the right, a pair of RH neutrinos is produced in the decay of a Higgs boson.

virtual RH neutrino into a multi-body final state, where the virtual RH neutrino vertex introduces a factor y_N^2 in the total neutralino decay width. However, the two-body decay $\tilde{\chi}_1^0 \to \tilde{N}_1 \nu_L$ is always kinematically allowed and dominates the decay width. Although it is suppressed by the mixing between the left and right neutrino components (and therefore also introduces a factor y_N^2), it is favoured by the phase space with respect to the possibility discussed above. Since the decay products of the neutralino are invisible, this scenario does not leave any displaced vertex (and is indistinguishable from the production of neutralino dark matter). This implies that for this range of RH neutrino masses we cannot consider the production mechanism through a neutralino-chargino pair.

On the other hand, this does not affect RH neutrinos produced through Higgs decays.

(III) $m_{\tilde{\chi}_1^0} + m_{\tilde{N}_1} < M_N$

Finally, if RH neutrinos are heavy enough that the decay channel $N \to \tilde{\chi}_1^0 \tilde{N}_1$ is kinematically allowed, then no displaced vertices are expected, since $\tilde{N}_1$ is stable and, as explained above, $\tilde{\chi}_1^0 \to \tilde{N}_1 \nu_L$ is the dominant decay channel for the lightest neutralino.

RH neutrino decays

If the RH neutrino is heavy enough, it can undergo a two-body decay into $W^{\pm} l^{\mp}$, $Z\nu_L$, or $H_i^0 \nu_L$. The decay width corresponding to all these channels is proportional to y_N^2, which enters either through the LR mixing of the neutrino (in the cases $N \to W^{\pm} l^{\mp}$ and $N \to Z\nu_L$) or in the

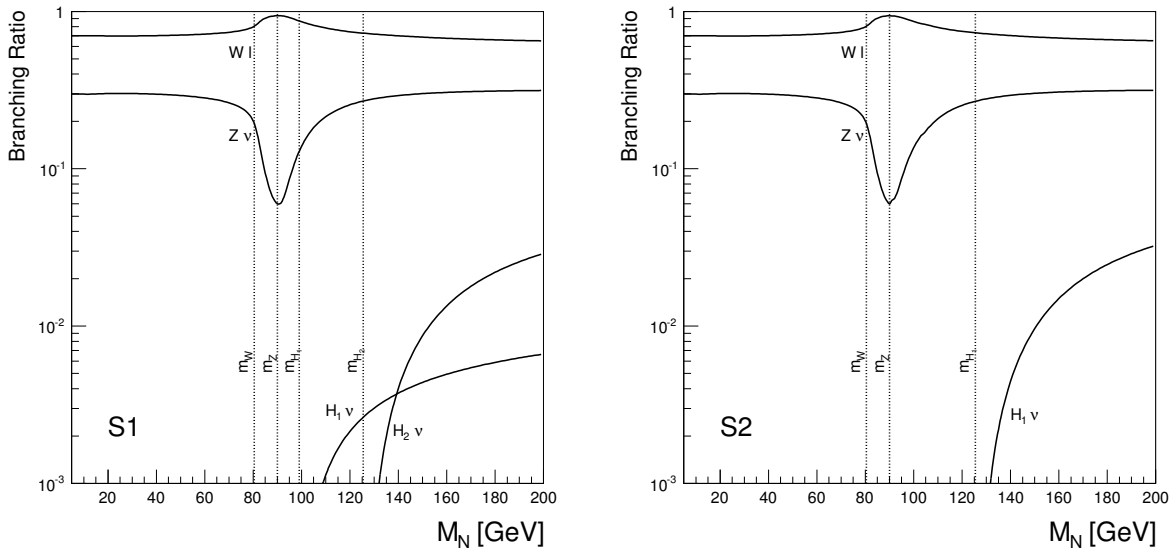

Figure 5.3: Branching ratios of the RH neutrino as a function of its mass for scenario S1 (left) and S2 (right).

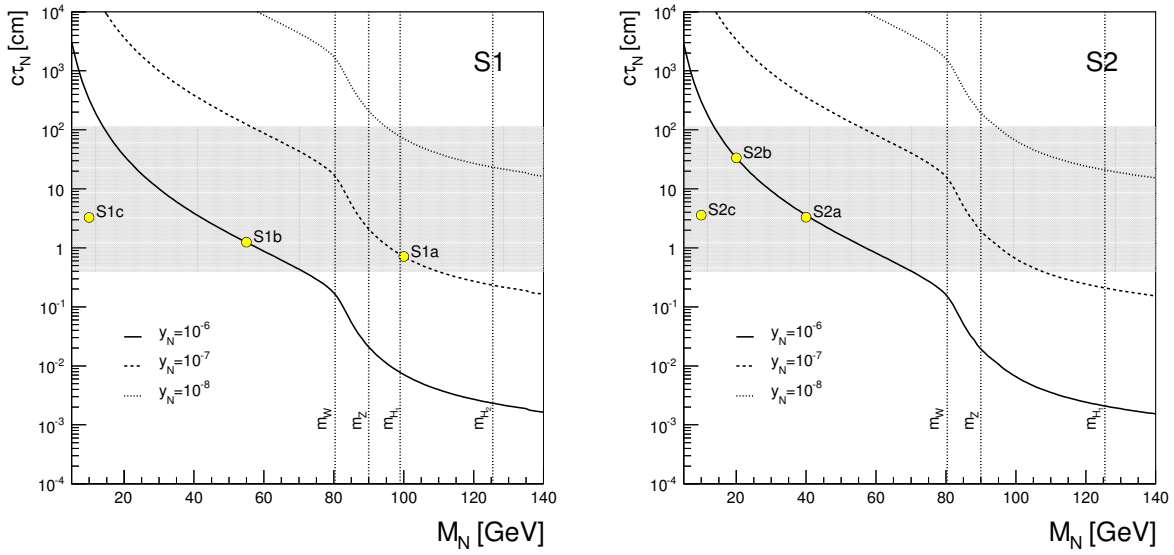

Figure 5.4: Decay length of the RH neutrino as a function of its mass for benchmark points S1 (left) and S2 (right). It is important to note that the decay length is independent of the sneutrino mass. The different lines represent different values of the neutrino Yukawa coupling. The shaded area corresponds to the range in lengths that could lead to an observable displaced vertex in the ATLAS inner detector.

coupling with the Higgs (in the case of $N \to H_i^0 \nu_L$),

$$\Gamma_{N\to Wl} = \frac{y_N^2 v_2^2 g^2}{64\pi}\frac{M_N}{m_W^2}\left(1-\frac{m_W^2}{{M_N}^2}\right)^2\left(1+\frac{2m_W^2}{{M_N}^2}\right), \tag{5.13}$$

$$\Gamma_{N\to Z\nu_L} = \frac{y_N^2 v_2^2 g^2}{64\pi}\frac{M_N}{m_W^2}96\left(1-\frac{m_Z^2}{{M_N}^2}\right)^2\left(1+\frac{2m_Z^2}{{M_N}^2}\right), \tag{5.14}$$

$$\Gamma_{N\to H_i^0\nu_L} = \frac{y_N^2 (S^2_{H_i^0})^2}{8\pi} M_N \left(1-\frac{m_{H_i^0}^2}{{M_N}^2}\right)^2, \tag{5.15}$$

Process	Signature
$N \to W^{\pm} l_i^{\mp} \to \nu_j l_j^{\pm} l_i^{\mp}$	$2\ell(+\not{E}_T)$
$\to q\bar{q}' l_i^{\mp}$	ℓjj
$N \to Z\nu_i \to \nu_i l_j^{\pm} l_j^{\mp}$	$2\ell(+\not{E}_T)$
$\to \nu_i q\bar{q}$	$2j(+\not{E}_T)$
$N \to H_i^0 \nu_i \to \nu_i l_j^{\pm} l_j^{\mp}$	$2\ell(+\not{E}_T)$
$\to \nu_i q\bar{q}$	$2j(+\not{E}_T)$
$\to \nu_i \gamma\gamma$	$2\gamma(+\not{E}_T)$

Table 5.2: Potential signatures at the LHC corresponding to the different production mechanisms, where $\ell = e^{\pm}$, $\mu^{\pm}$ and j stands for hadronic jets. As explained in the text, it is difficult to measure the missing transverse energy, $\not{E}_T$, associated with a displaced vertex.

where $S^2_{H_i^0}$ is the up component of the Higgs H_i^0. Therefore, we expect this particle to be long-lived, and give rise to a displaced vertex that could be observed through the resulting charged SM particles. Notice in this sense that the channels $Z\nu_L$ and $H_i^0\nu_L$ are only observable through the decay products of the Z and H_i^0 bosons.

For lighter N, we can only have three-body decays through virtual $W^{\pm}$, Z or H_i^0. For the same reasons as above, the decay width is proportional to y_N^2 but now is further suppressed by the phase space, thus leading to a larger lifetime. We have computed the corresponding lifetime using `CalcHEP 3.4`.

Thus, in terms of the parameters of the model, the RH neutrino lifetime is only a function of its mass, sensitive to the details of the Higgs sector, and modulated by y_N^2. We illustrate the results with two numerical examples, denoted benchmark points S1 and S2, with parameters defined in Table 5.1. The resulting decay length and branching ratios are displayed as a function of the RH neutrino mass on the left and right panels of Figure 5.3 and Figure 5.4, respectively. The shaded area corresponds to the range in distances that we expect the ATLAS inner detector can resolve for a displaced vertex. We indicate by means of dotted vertical lines the masses of the gauge bosons and H_1^0, below which two-body decays are no longer possible.

As we observe, for a wide range of values for the RH neutrino mass and the neutrino Yukawa, the RH neutrino decay length is within the range that can be resolved in ATLAS. Also, we have found that in general the decay through a virtual or on-shell W dominates the decay width, and this will determine our choice of signals to analyse.

Signals at the LHC

The displaced vertex originating from the late decay of a RH neutrino is observable through the decay products of the $W^{\pm}$, Z, and H_i^0 bosons.

The observation of a displaced vertex depends on the reconstruction of the tracks of the charged particles produced. Usually at least two charged tracks are needed to reconstruct a secondary vertex. Important parameters for the reconstruction are the total distance from the primary

vertex, L_{xy}, and the impact parameter, $d_0 = L_{xy} \sin\theta$, where θ is the angle described by the trajectory of the displaced vertex with respect to the beam line. An illustrative scheme of a displaced vertex is represented in Fig. 5.5. The resolution of the vertices in the pixel tracker for both ATLAS and CMS detectors is of the order of hundred μm, however as the displaced vertices must be distinguished from primary ones, usually $|d_0| \gtrsim 2-4$ mm and $L_{xy} \gtrsim 4-8$ mm is imposed [338–341]. These cuts also remove completely the SM background, as it was shown in Refs. [339–342]. In fact, in Ref. [341] it was shown through MC simulation studies that the selection on $|d_0| > 2$ mm can remove 98% of all tracks from the primary pp vertices. Although in their searches for displaced vertices ATLAS and CMS use the whole detector volume, the identification of a displaced vertex decreases when d_0 grows [338, 339, 341]. In our analysis we will therefore restrict our searches to the inner detector[5] and for each simulated event we impose impose a cut on the decay length of the RH neutrino, 10 mm $< c\tau_N <$100 cm.

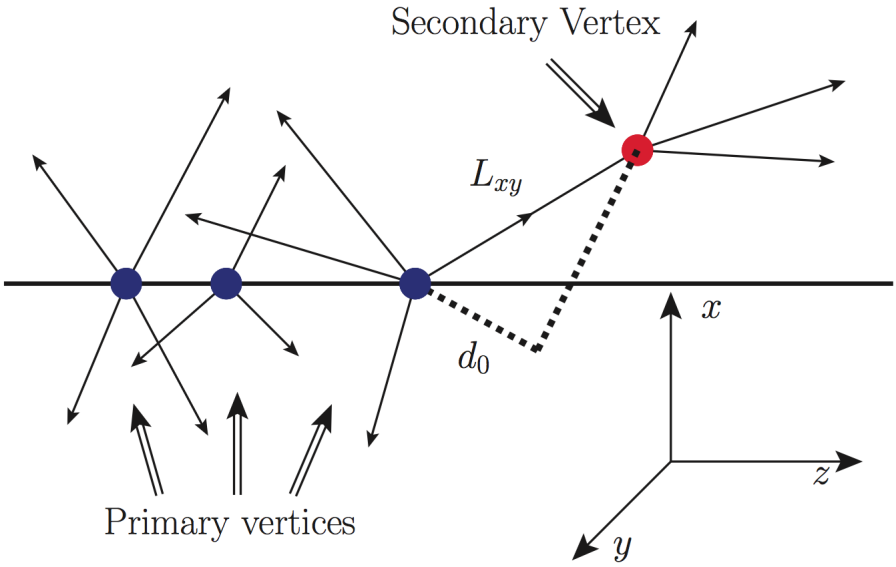

Figure 5.5: Illustrative scheme of a displaced vertex with different primary vertices.

The results for current searches for displaced vertices using the ATLAS or CMS detector can be found in Refs. [338–340] and Ref. [341], respectively. The efficiencies shown there are dependent on the distance where the displaced vertex takes place. In some points the reconstruction efficiency could be as large as 30%, but in general this efficiency is smaller.

In Table 5.2 we detail the potential signatures[6] As mentioned in the previous section, we expect the contribution from $N \to W^{\pm} l^{\mp}$ to be dominant and therefore we concentrate on the two signatures $N \to 2\ell + \not{E}_T$ and $N \to \ell jj$. Notice however that $N \to 2\ell + \not{E}_T$ also receives contributions from processes in which the mediator is either the Higgs or the Z boson and this will be taken into account. It is important to observe that the emitted neutrinos contribute to the missing energy

[5] For CMS(ATLAS) the inner detector has a radius of 110 (108.2) cm [343, 344].
[6] Similar signatures have been described in singlino decays in the $\mu\nu$SSM [345].

of the total event. The missing energy cannot be associated to the displaced vertex itself (as the neutrino cannot be detected). For this reason, $\not{E}_T$ is not a good variable in our study and we only focus on the properties of the visible particles that originate in the displaced vertices (leptons and jets).

- $2l(+\not{E}_T)$

  In principle one could think of using the transverse mass, defined as

  $$m_T^2 = \left(\sqrt{M_{vis}^2 + \vec{p}_{T,vis}^{\,2}} + \not{E}_T^V\right)^2 - \left(\vec{p}_{T,vis} + \vec{\not{p}}_T^{\,V}\right)^2, \tag{5.16}$$

  where M_{vis}^2 is the invariant mass of the visible system, $\vec{p}_{T,vis}$ is the transverse momentum vector of the visible system, $\not{E}_T^V$ is the missing transverse energy of the vertex and $\vec{\not{p}}_T^{\,V}$ is the vector of the missing transverse energy. However, in practice we would not be able to measure the missing transverse energy that comes from the displaced vertex. Notice for example that it would be very difficult, if not impossible, to determine the original interaction from which the long-lived RH neutrinos originated.

  For this reason, we try to make use of only the visible particles. It was shown in Refs. [346–348] that the invariant mass for the dileptonic system presents an endpoint which is sensitive to relations between the particles involved. When applied to the process $N \to Wl/Z\nu_L/H_i^0\nu_L \to ll\nu_L$, it can be shown that if the intermediate particle is produced on-shell, an edge in the resulting distribution will be present for,

  $$\left(m_{l_1 l_2}^{edge}\right)^2 = ({M_N}^2 - m_X^2)\,, \tag{5.17}$$

  where $X = W, Z, H_i^0$. If the intermediate particle is produced off-shell, the distribution is expected to have an endpoint at

  $$\left(m_{l_1 l_2}^{end-point}\right)^2 = (M_N - m_{\nu_L})^2 \simeq {M_N}^2. \tag{5.18}$$

  Since there are different intermediate particles for the decay of the RH neutrino, one expects various edges, which might be difficult to distinguish. Also, the invariant mass of two leptons will have resonant peaks for the Z and for the H_i^0. We can avoid these two problems if we only consider the final states coming from the W boson. This can be done by requiring two leptons with different flavours that arise from the same displaced vertex. We thus eliminate leptons coming from the Z and H_i^0 channels that could spoil the mass reconstruction. Furthermore, as mentioned above, the W boson decay is favoured being the main branching ratio of the RH neutrino.

- ljj

  A plausible strategy to obtain information about the RH neutrino that produces the displaced vertex is to analyse the two jets plus the lepton arising from the same vertex. If we are able

	$\sigma^{8\text{TeV}}_{H^0_i}$	$\sigma^{8\text{TeV}}_{\tilde{\chi}^\pm_j \tilde{\chi}^0_i}$	$\sigma^{13\text{TeV}}_{H^0_i}$	$\sigma^{13\text{TeV}}_{\tilde{\chi}^\pm_j \tilde{\chi}^0_i}$	M_N	$m_{\tilde{N}_1}$	$m_{\tilde{\chi}^0_1}$
S1a	2×10^{-5}	0.87	3×10^{-4}	1.94	100	20	127
S1b	0.89	–	2.06	–	55	100	127
S1c	0.54	0.87	1.24	1.94	10	70	127
S2a	0.004	0.25	0.22	0.65	40	70	147
S2b	0.034	–	0.48	–	20	130	147
S2c	0.009	0.25	0.29	0.65	10	40	147

Table 5.3: Contributions to the production cross section of a RH neutrino pair from Higgs decays ($\sigma^{8\text{TeV}}_{H^0_i}$) and neutralino/chargino pair-production ($\sigma^{8\text{TeV}}_{\tilde{\chi}^\pm_j \tilde{\chi}^0_i}$) at the LHC with a centre of mass energy of 8 TeV and 13 TeV. For convenience, the masses of the particles involved are also indicated. The production cross sections are given in pb while the masses are in GeV. In benchmark points S1b and S2b the neutralino decay into RH neutrino and RH sneutrino is kinematically forbidden and neutralino/chargino production is not considered.

to reconstruct these three elements it is easy to calculate the invariant mass of the system, defined as

$$m^2_{jjl} = (p^\mu_{j_1} + p^\mu_{j_2} + p^\mu_l)(p_{j_1\mu} + p_{j_2\mu} + p_{l\mu}), \tag{5.19}$$

where p^μ_i are the Lorentz vectors of the different particles. Since the decay width of the RH neutrino is much smaller than its mass $\Gamma_N \ll M_N$, this variable presents a kinematical peak near the pole mass of the RH neutrino.

We are not aware of algorithms that simulate the reconstruction of displaced vertices at the detector level. Thus we have carried out our data simulation at parton level using `CalcHEP`. In order to simulate the detector effects on the reconstruction of the energies of leptons and jets, we assume that the nominal energies are smeared with a Gaussian distribution such that

$$\frac{\sigma}{E} = \frac{a}{\sqrt{E/\text{GeV}}} \oplus b\,, \tag{5.20}$$

where $\oplus$ denotes sum in quadrature. For electrons we have $a_\ell = 5\%$, and $b_\ell = 0.55\%$, whereas jets are much more difficult to reconstruct and we will take $a_j = 100\%$ and $b_j = 5\%$ [344]. Muons are measured in the muon chambers and the smearing is applied to their transverse momentum.

For each of the benchmark points in scenarios S1 and S2 in Table 5.1 we have simulated the production of RH neutrinos in proton-proton collisions with the corresponding LHC configuration, considering the two production mechanisms detailed in Subsec. 5.3. The production cross sections are specified in Table 5.3. Then, the generated event samples have been scaled to the given luminosity. We consider the current LHC values, with a centre of mass energy of 8 TeV and an integrated luminosity of $\mathcal{L} = 20$ fb^{-1}, as well as a future scenario with 13 TeV and $\mathcal{L} = 100$ fb^{-1}.

The following basic cuts are imposed in order to single out the signals.

- In order to clearly discriminate the displaced vertices from b-jets, that usually have a $c\tau \sim$ 4mm [349], we require the displacement to be sufficiently large (but still contained within the

	$\sqrt{s} = 8$ TeV, $\mathcal{L} = 20\,\text{fb}^{-1}$					$\sqrt{s} = 13$ TeV, $\mathcal{L} = 100\,\text{fb}^{-1}$				
	ee	$\mu\mu$	$e\mu$	ejj	μjj	ee	$\mu\mu$	$e\mu$	ejj	μjj
S1a	9	10	17	36	40	95	101	195	393	427
S1b	26	25	46	24	33	241	223	434	224	293
S1c	25	43	64	0	0	317	547	813	2	3
S2a	30	25	49	46	52	528	438	882	804	893
S2b	2	2	4	0	1	32	31	57	5	7
S2c	1	2	3	0	0	21	33	51	0	0

Table 5.4: Number of events that pass all the cuts for the LHC configurations $\sqrt{s}$ = 8 TeV, $\mathcal{L} = 20\,\text{fb}^{-1}$ and $\sqrt{s}$ = 13 TeV, $\mathcal{L} = 100\,\text{fb}^{-1}$. An efficiency of 20% is assumed in the reconstruction of displaced vertices.

inner detector). We thus require the presence of *two* displaced vertices with $10\,\text{mm} < c\tau < 100\,\text{cm}$.

- For isolated electrons we require $p_T > 10$ GeV and for muons $p_T > 6$ GeV and $|\eta_\ell| < 2.5$.

- For each jet we require $p_T > 15$ GeV and $|\eta_j| < 2.5$.

- The criterion for considering a particle or a jet isolated is $\Delta R > 0.4$, where $\Delta R \equiv \sqrt{(\Delta\eta)^2 + (\Delta\phi)^2}$, with $\Delta\phi$ and $\Delta\eta$ being the azimuthal angular separation and the rapidity difference between two particles. We also make sure that the particles from one displaced vertex are isolated with respect to those of the other.

These cuts are designed in order to remove the SM model background. As it is shown in Refs. [339–342] the main SM background is due to $\gamma^*/Z^* \to \ell^+\ell^-, Z^*Z^*$. The cut imposed in the decay length is very effective and it can be seen that when it is combined with the condition that the invariant mass of two leptons are greater than 5 GeV, the SM background can be totally removed. Our cut in the decay lenght is more restrictive so we make sure that we remove the SM background. We do not impose the cut on the invariant mass of the two leptons since in our scenarios the neutrinos are heavier than 5 GeV and a possible residual of background does not affect to the endpoint of the invariant mass distribution.

As it was pointed out before, the reconstruction efficiency of the displaced vertices is very poor. In our analysis we use the estimations for ATLAS and CMS and will assume that the efficiency is 20%.

The number of signal events after all the cuts are applied is given in Table 5.4 for each benchmark point and each signal ($\ell\ell$ and ℓjj). We would like to remind the reader at this point that we are considering that the RH neutrino has equal mixings with the three left-handed neutrinos. Deviations from this assumption would imply variations in the relative rates for electron and muon signals.

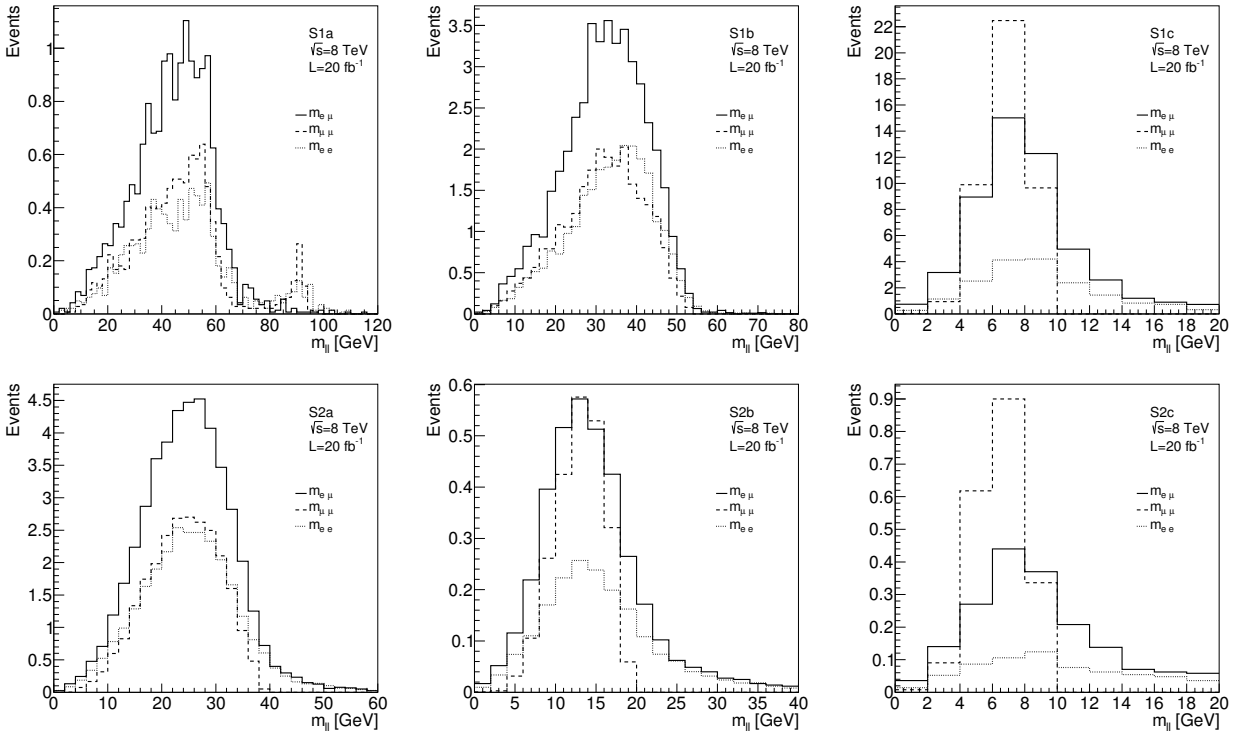

Figure 5.6: Two-lepton invariant mass distribution, $m_{\ell\ell}$, for the benchmark points S1a, S1b and S1c (upper row) and S2a, S2b and S2c (lower row) corresponding to the LHC with a centre of mass energy of $\sqrt{s} = 8$ TeV and an integrated luminosity of $\mathcal{L} = 20$ fb^{-1}. The solid line corresponds to the $m_{e\mu}$, the dashed line represents $m_{\mu\mu}$, and the dotted line is m_{ee}.

Results

Let us first analyse the results obtained for the current LHC configuration, with a centre of mass energy of $\sqrt{s} = 8$ TeV and $\mathcal{L} = 20$ fb^{-1}. We represent in Figure 5.6 the resulting two-lepton invariant mass distribution for benchmark points S1a, S1b and S1c (upper row) and S2a, S2b and S2c (lower row). The different lines represent the contributions coming from the different channels, $e\mu$ (solid), $\mu\mu$ (dashed), and ee (dotted). As it was explained above we expect that these distributions present an end-point defined by the kinematics of the system.

In the particular case of S1a, where the W boson is produced on-shell, we can see an edge around $m_{\ell\ell}^{edge} = \sqrt{{M_N}^2 - m_W^2} \simeq 60$ GeV. For this case, the Z peak is present for the same flavour channels. Although this peak is smaller (due to the smaller branching ratio in RH neutrino decays), its observation would allow us to distinguish this distribution from that of a 60 GeV RH neutrino[7]. However, for this LHC configuration this peak is actually not observable.

In the rest of the benchmark points the W boson is produced off-shell and the end-point of the invariant mass distribution is at the RH neutrino mass. Nevertheless, the reconstruction of the

[7] A 60 GeV RH neutrino would decay through off-shell bosons and present an end-point at its mass.

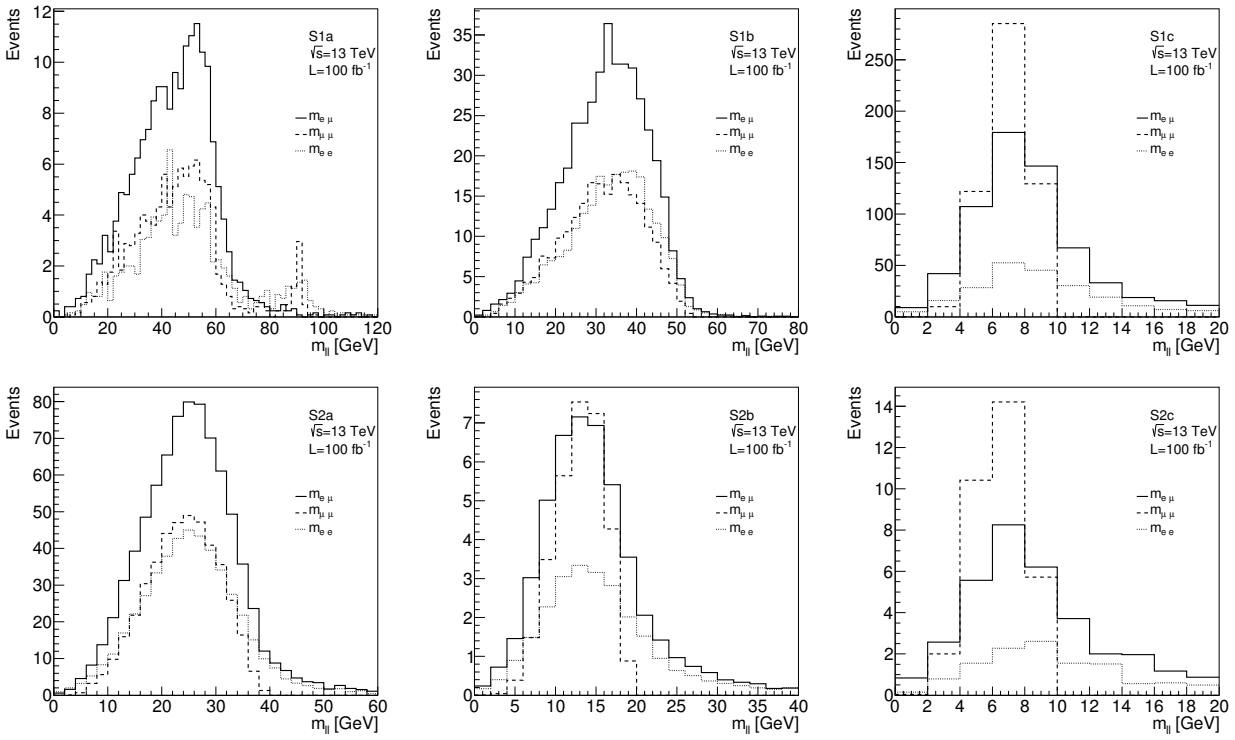

Figure 5.7: The same as in Figure 5.6, but for the LHC with a centre of mass energy of $\sqrt{s} = 13$ TeV and an integrated luminosity of $\mathcal{L} = 100$ fb^{-1}.

mass of the RH neutrino could be difficult because the smearing in the lepton energies spoils the tail of the distributions.

Scenarios in which the RH neutrino mass is small, such as S1c, S2b, and S2c are generally difficult to observe since most of the leptons produced fail to pass the cuts on their transverse energy. Also, the smearing on the tail of the dilepton-mass distribution is more severe, due to the small values of the lepton p_T. Notice however that case S1c benefits from a sizable production rate and the signal would be very clear.

The expected results for the LHC with a centre of mass energy of $\sqrt{s} = 13$ TeV and an integrated luminosity of $\mathcal{L} = 100$ fb^{-1} are shown in Figure 5.7. The same qualitative results are obtained, but now the number of events is larger and some benchmark points can be probed more easily. For example, the Z peak in benchmark point S1a features 5 events. As this peak is observed in the dimuon channel, we do not expect a depletion in the number of events due to hadronization. Also, since the detector effects are already taken into account through Eq. (5.20), we expect that such Z peak would be observable for that scenario in the next configuration of the LHC. This is also the case of some examples with low masses, such as S2b and S2c, although the small statistics would make it difficult to determine the end-point of the distributions to extract the RH neutrino mass.

Let us now turn our attention to the $N \to jj\ell$ signal. In Figure 5.8 we have represented the

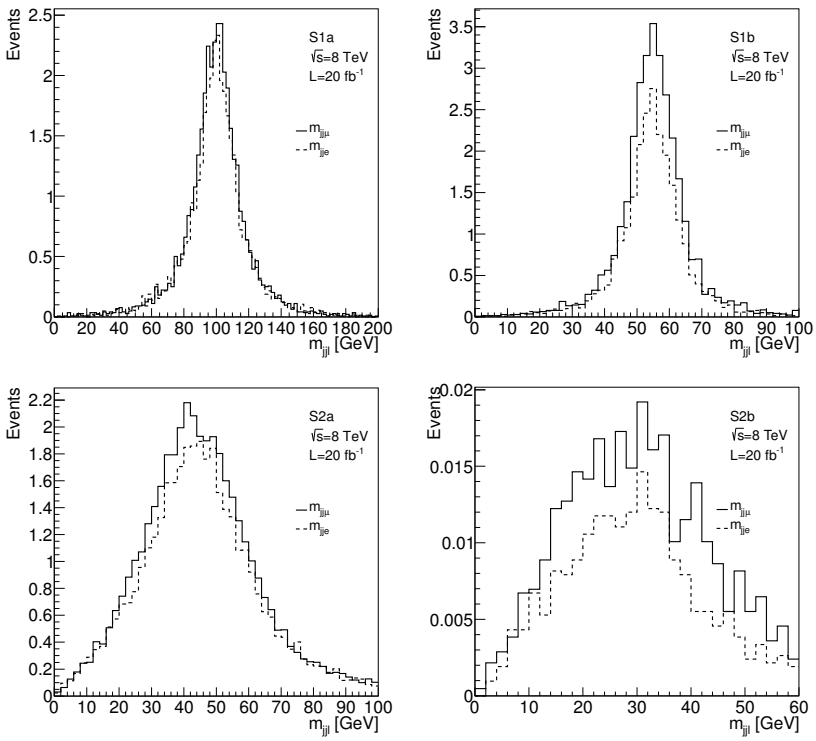

Figure 5.8: Invariant mass distribution for two jets and one lepton, $m_{jj\ell}$, for the benchmark points S1a, S1b (upper row), and S2a S2b (lower row) corresponding to the LHC with a centre of mass energy of $\sqrt{s} = 8$ TeV and an integrated luminosity of $\mathcal{L} = 20$ fb^{-1}. The solid line corresponds to the $m_{jj\mu}$ and the dashed line represents m_{jje}.

two-jets one-lepton invariant mass distribution $m_{jj\ell}$ for the different benchmark points for a LHC configuration of $\sqrt{s} = 8$ TeV and an integrated luminosity of $\mathcal{L} = 20$ fb^{-1}. For this distribution, a peak with a maximum centered in the RH neutrino mass is expected. We can see that this is the case in benchmark points S1a, S1b, and S2a. From these distributions, the RH neutrino mass can be determined with a certain precision, and compared with the results obtained from the study of the $m_{\ell\ell}$ distribution. For S2a we can see that the invariant mass distribution is centered around the mass of the RH neutrino, $M_N = 40$ GeV, however the width of the distribution is larger. Although the jets can pass the cuts, they have a small energy and cannot be reconstructed properly due to the smearing effects.

If the RH neutrino mass is small (as in benchmark points S1c, S2b, and S2c), the jets are less energetic and are more affected by the cut in p_T. For these three benchmark points, the jets and leptons cannot fulfill the cut requirements and no events would be observed (see Table 5.4).

If we now consider the future LHC configuration, with a centre of mass energy of $\sqrt{s} = 13$ TeV and an integrated luminosity of $\mathcal{L} = 100$ fb^{-1}, the number of events increases and the reconstruction of the RH neutrino mass is clearer. We show the corresponding distributions of $m_{jj\ell}$ in Figure 5.9. We can observe that the reconstruction for the benchmarks in scenario S2 is less precise, as explained above, due to the smaller energy of the resulting jets. Benchmark point S2b is now observable (with

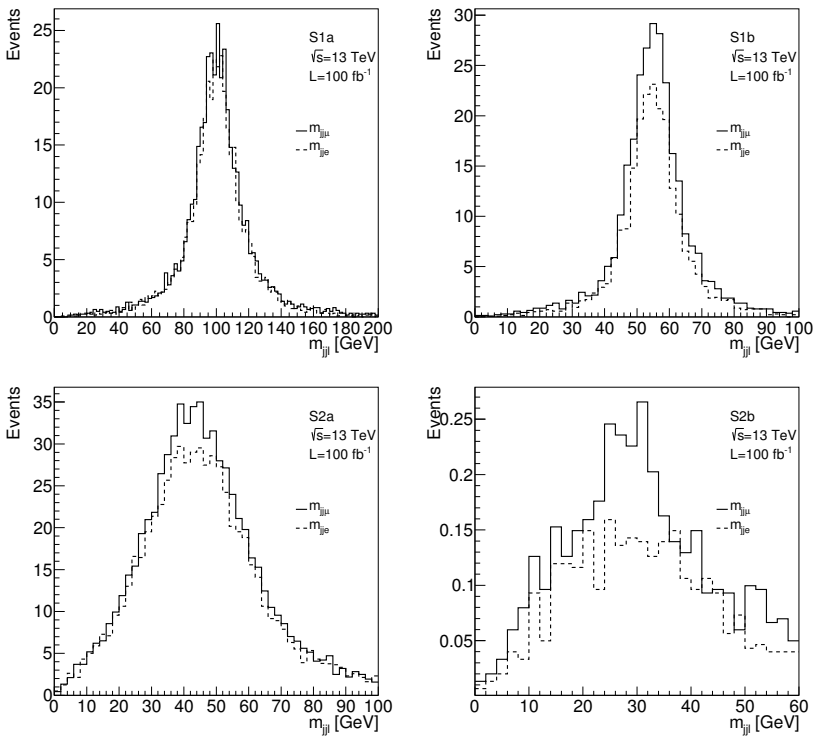

Figure 5.9: The same as in Figure 5.8, but for the LHC with a centre of mass energy of $\sqrt{s} = 13$ TeV and an integrated luminosity of $\mathcal{L} = 100$ fb^{-1}.

approximately 12 events), however both S1c and S2c remain unobservable and are therefore not shown.

Notice that the results from Refs. [338–341] are the present constraints from the LHC on displaced vertices. Some of these searches share the same signatures with this model. As these searches are done in the $\sqrt{s} = 7$ TeV with luminosities less than $\mathcal{L} = 5$ fb^{-1} and they impose strong cuts in the p_T of the objects that arise from the displaced vertex we found that our benchmark points agree with the lack of signals that these searches found.

Also, due to the fact that some of the RH neutrinos could decay promptly, the decay objects could contribute to multilepton signals in standard ATLAS and CMS searches for supersymmetry [350,351]. We have simulated the expected number of multilepton events coming from RH neutrino decays with an impact parameter smaller than $|d_0| < 0.2$ mm, and observed that this number is smaller than one in all the benchmark points. This means that the present searches on multilepton signals do not constrain our scenarios.

It should finally be mentioned that displaced vertices can also appear in R-parity violating (RPV) supersymmetric models [352]. For example, this is the case for a realization of these scenarios with trilinear RPV through a $\lambda'' UDD$ term in the superpotential [353] can induce displaced vertices [354]. However, the final states in these RPV models are different to the ones observed in our scenario, as they originate from different couplings. In particular, the LLE operator leads only

to $2\ell + \not{E}_T$, the LQD operator leads only to ℓjj and $jj + \not{E}_T$, and the UDD operator leads only to jjj.

Similarly, bilinear RPV models with $\Delta W = \mu_i L_i H_u$, can also account for non-vanishing neutrino masses through the neutralino-neutrino mixing. The final state produced at the displaced vertex in these scenarios from the decay of unstable neutralinos would be $2\ell + \not{E}_T$ and $jj + \not{E}_T$ by ν_L), where in both cases the missing energy is due to the production of a ν_L [355], however we would not observe any ℓjj events.

Contrary to trilinear and bilinear RPV, in our scenario the $2\ell + \not{E}_T$ and ℓjj signatures have the same origin (the decay of the long-lived N). As we have shown, from the reconstructed end-point in the two-lepton invariant mass distribution ($m_{\ell\ell}$) and the peak in the two-jets one lepton invariant mass distribution ($m_{\ell jj}$) we would reconstruct the same value of the RH neutrino mass. This is a valuable cross-check that would allow us to discriminate our scenario from the above mentioned RPV models.

5.4. Long-lived charged particles

A charged and long-lived particle can leave a distinctive track at the LHC that could be identified as corresponding to a particle heavier than a muon. In our construction, this can be the case, for example, of the lighter stau, which eventually decays into the RH sneutrino.

There are various contributions to the stau decay, depending on its mass:

- $\tilde{\tau}_1 \to W \tilde{N}_1$

  This is the only two-body decay channel which is kinematically allowed when $m_{\tilde{\tau}} \geq m_W + m_{\tilde{N}_1}$. It is suppressed by the mixing in the sneutrino sector, which is proportional to y_N.

- $\tilde{\tau}_1 \to q_i \bar{q}_j \tilde{N}_1$, $\nu_L l \tilde{N}_1$

  These processes are mediated by a virtual W boson that connects to a $q_i \bar{q}_j$ pair or $\nu_L l$. As in the former example, the sneutrino arises through the mixing with $\tilde{\nu}_L$, which is proportional to y_N.

- $\tilde{\tau}_1 \to \tau N \tilde{N}_1$

  This process is mediated by a neutralino χ_i^0 and is not Yukawa suppressed.

As in the case of the neutralino NLSP, the first two channels include a dependence on the neutrino Yukawa through the mixing of the RH sneutrino with the LH ones, and this implies a small decay width and a long lifetime, which in general would allow the stau to escape the detector. Notice however that the third channel is not Yukawa suppressed and therefore dominates when it is kinematically allowed (when $m_{\tilde{\tau}_1} > m_\tau + M_N + m_{\tilde{N}_1}$).

For concreteness, we will study scenario S3 in Table 5.1, which features a stau NLSP. In Figure 5.10 we represent the corresponding (λ_N, $m_{\tilde{N}}$) plane for two choices of the trilinear parameter $A_{\lambda_N} = -500$ and -750 GeV and indicate the areas that are excluded by the constraint on the invisible Higgs decay. As in scenarios S1 and S2, wide regions of the parameter space are available.

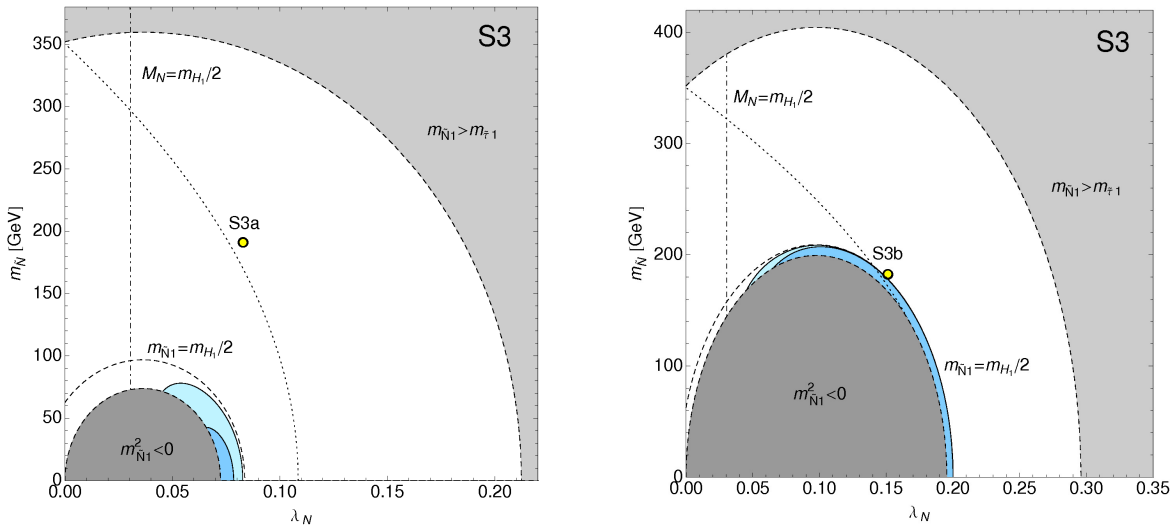

Figure 5.10: Constraints on the $(\lambda_N,\, m_{\tilde{N}})$ plane from the invisible branching ratio of the SM-like Higgs for scenario S3. From left to right, the trilinear term is $A_{\lambda_N} = -500$, and -750 GeV. The same colours and lines as in Figure 5.1 are used. Points to the left and below the dotted line satisfy $m_{\tilde{\tau}_1} > m_\tau + M_N + m_{\tilde{N}_1}$. Yellow dots correspond to the selected benchmark points.

Points to the left and below the dotted line satisfy $m_{\tilde{\tau}_1} > m_\tau + M_N + m_{\tilde{N}_1}$ and correspond to areas in which the stau can decay promptly.

We have computed the different contributions to the stau lifetime for two examples, based on scenario S3, where the RH neutrino mass has been fixed to 170 and 310 GeV. The results are represented in Figure 5.11 as a function of the RH sneutrino mass. We observe that the stau decays outside the detector for the whole range of relevant values of the neutrino Yukawa, $y_N \approx 10^{-6}$–10^{-8}, and RH sneutrino masses, except for the region with a light RH sneutrino for which the $\tilde{\tau}_1 \to \tau N \tilde{N}_1$ decay is kinematically open[8]. We have chosen two benchmark points, S3a and S3b, with a stau mass $m_{\tilde{\tau}_1} = 352$ GeV and parameters defined in Table 5.1. The stau lifetime for both is represented by yellow circles in Figures 5.10 and 5.11.

For each example we have simulated the production of long-lived staus in proton-proton collisions. The main production of the stau NLSP comes from the decay chains originated after the creation of neutralino/chargino pairs as illustrated in Figure 5.12. We consider the current LHC configuration with a centre of mass energy of 8 TeV and an integrated luminosity of $\mathcal{L} = 20\,\text{fb}^{-1}$, and the future one, with a centre of mass energy of 13 TeV and $\mathcal{L} = 100\,\text{fb}^{-1}$. The total neutralino/chargino production cross sections for each centre of mass energy ($\sigma^{8,13\,\text{TeV}}_{\tilde{\chi}^\pm_j \tilde{\chi}^0_i}$) is written in Table 5.5. In both benchmark points the lighter neutralino decays as $\tilde{\chi}^0_1 \to \tau\tilde{\tau}_1$ with a branching ratio which is approximately 100% (notice that since we have chosen a heavy RH neutrino, the direct decay $\tilde{\chi}^0_1 \to N\tilde{N}_1$ is kinematically forbidden and $\tilde{\chi}^0_1 \to \tilde{N}\nu_L$ is suppressed by y_N).

[8]For $y_N = 10^{-6}$ the stau can decay inside the detector for small RH sneutrino masses. However, the decay takes place in the calorimeter and not in the inner detector. We consider this possibility difficult to identify and do not consider it in the analysis.

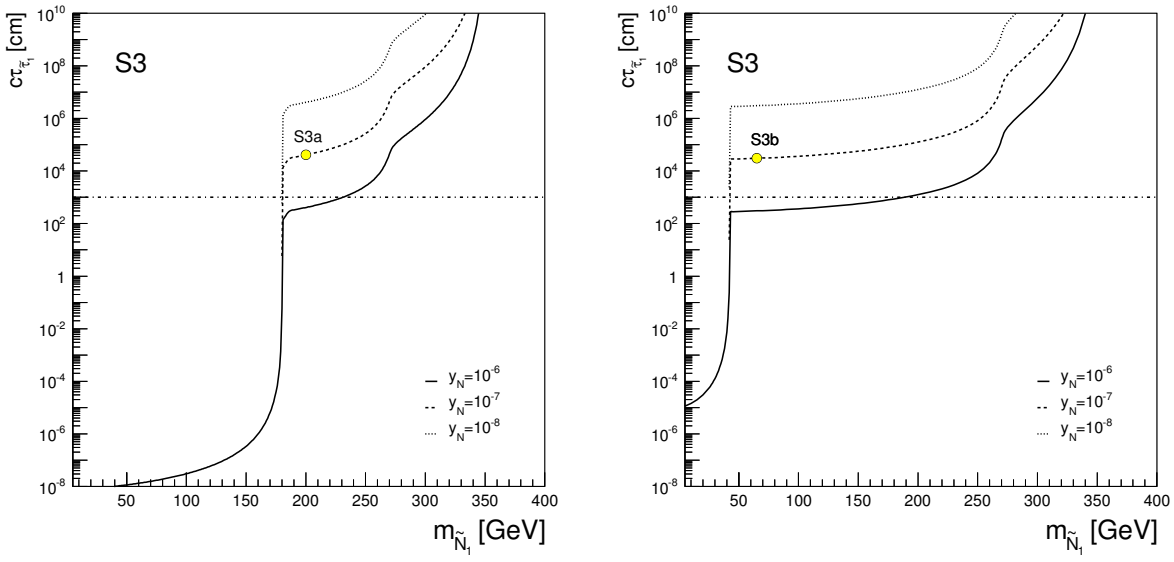

Figure 5.11: Decay length of the lighter stau NLSP as a function of the RH sneutrino mass for scenario S3 with a fixed RH neutrino mass of 170 GeV (left) and 310 GeV (right). The different lines represents different values of the neutrino Yukawa coupling. The dot-dashed line at $c\tau = 10^3$ cm represents the approximate radius of the ATLAS detector. Yellow circles denote benchmark points S3a and S3b.

We impose the following basic cuts, aimed at reducing the background (mostly due to high p_T muons) [356].

- We require *two* staus which escape the detector ($c\tau > 10\,\text{m}$).
- In order to discriminate heavy long-lived staus from muons, the measured $\beta \equiv v/c$ is required to be less than 0.95.
- We impose $p_T > 50$ GeV and $|\eta| < 2.5$ for each long-lived stau.

The trigger efficiency for heavy long-lived sleptons is estimated to be larger than 60% [356]. In our calculation we impose this value, in order to be conservative. Current searches exclude long-lived staus lighter than $m_{\tilde{\tau}_1} \approx 342$ GeV, a bound that we also take into account.

The resulting number of events that pass all the cut is displayed in Table 5.5 for benchmark points S3a and S3b and considering the current and future LHC configurations. As we observe, none of these benchmark points are observable in the current LHC configuration, since the number of events is below 2 (thereby being in agreement with the negative results of current searches). However, they could be probed in the future with a higher energy and luminosity, for which as many as 30 events could be obtained.

Upon detection, the mass of the stau can be determined using $m_{\tilde{\tau}} = p/\gamma\beta$, where p is the magnitude of the momentum vector of the long-lived particle, $\vec{p}$, and β and γ are the usual relativistic factors. Notice however that this would not be sufficient to identify this scenario and

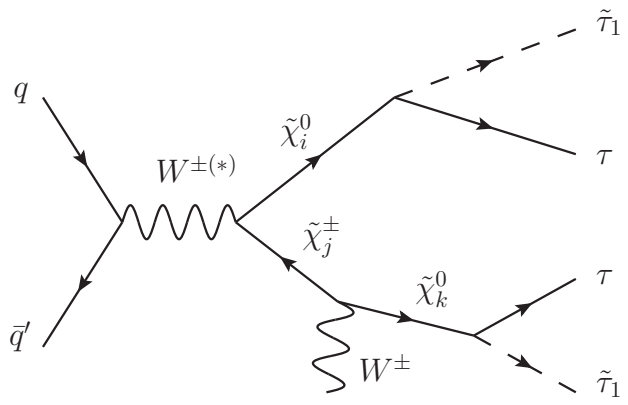

Figure 5.12: Long-lived stau production considered in this model. A neutralino/chargino pair is produced after the original collision and undergoes a short decay chain that ends in the production of long-lived staus and tau leptons.

	$\sqrt{s} = 8$ TeV, $\mathcal{L} = 20\,\text{fb}^{-1}$ $\sigma^{8\,\text{TeV}}_{\tilde{\chi}_j^{\pm}\tilde{\chi}_i^0} = 1.17$ fb	$\sqrt{s} = 13$ TeV, $\mathcal{L} = 100\,\text{fb}^{-1}$ $\sigma^{13\,\text{TeV}}_{\tilde{\chi}_j^{\pm}\tilde{\chi}_i^0} = 4.77$ fb
S3a	1.7	30.3
S3b	1.5	28.9

Table 5.5: Number of events that pass all the cuts for the LHC configurations $\sqrt{s}$ = 8 TeV, $\mathcal{L} = 20\,\text{fb}^{-1}$ and $\sqrt{s}$ = 13 TeV, $\mathcal{L} = 100\,\text{fb}^{-1}$. An efficiency of 60% is assumed in the trigger cut.

distinguish it from other possibilities with long-lived charged particles such as the MSSM or NMSSM (when the mass-difference between the stau NLSP and the neutralino LSP is smaller than the tau mass), gauge mediated supersymmetry breaking (GMSB) models in which a stau NLSP decays into a tau and a gravitino LSP, or various R-parity breaking models.

Another analysis of long-lived staus in the MSSM with sneutrinos (which mixed LH-RH states) has been presented in Ref. [357] in which the origin of the long stau lifetime is due to a small mass gap between the LSP and the NLSP. In our case, the stau lifetime is controlled by the small neutrino Yukawa, thereby providing more flexibility in the choice of sparticle masses. In any case, since this signature would be the same, it would be difficult to use it to discriminate between these two scenarios.

6

Triplet extension of the MSSM

6.1. Generic Features of the TMSSM

In the TMSSM the matter content of the MSSM is extended by a $Y = 0$ $SU(2)_L$-triplet superfield

$$\Sigma = \begin{pmatrix} \xi^0/\sqrt{2} & \xi_2^+ \\ \xi_1^- & -\xi^0/\sqrt{2} \end{pmatrix} . \tag{6.1}$$

In comparison with the MSSM, the TMSSM superpotential and soft-breaking Lagrangian contain respectively two and three extra renormalizable terms [101, 102]:

$$W_{\text{TMSSM}} = W_{\text{MSSM}} + \lambda H_1 \cdot \Sigma H_2 + \frac{1}{2}\mu_\Sigma \,\text{Tr}\,\Sigma^2 , \tag{6.2}$$

$$\mathcal{L}_{\text{TMSSM}_{\text{SB}}} = \mathcal{L}_{\text{MSSM}_{\text{SB}}} + m_4^2 \,\text{Tr}(\Sigma^\dagger \Sigma) + \left[B_\Sigma \,\text{Tr}(\Sigma^2) + \lambda A_\lambda H_1 \cdot \Sigma H_2 + \text{h.c.}\right] , \tag{6.3}$$

where $A \cdot B \equiv \epsilon_{ij} A^i B^j$ with $\epsilon_{21} = -\epsilon_{12} = 1$ and $\epsilon_{22} = \epsilon_{11} = 0$. For sake of simplicity we assume no sources of CP violation and consequently all parameters are taken as real.

In general the neutral scalar component ξ^0 acquires a VEV $\langle \xi^0 \rangle$. Electroweak precision observables impose $\langle \xi^0 \rangle \lesssim 4\,\text{GeV}$ at 95% CL [104, 358] which, unless of a tuning on the parameters, corresponds to the hierarchy

$$|A_\lambda|, \, |\mu| \, , |\mu_\Sigma| \lesssim 10^{-2} \frac{m_\Sigma^2 + \lambda^2 v^2/2}{\lambda v} , \tag{6.4}$$

with $m_\Sigma^2 \equiv m_4^2 + \mu_\Sigma^2 + B_\Sigma \mu_\Sigma$. For A_λ, μ and μ_Σ at the electroweak scale, such a hierarchy requires $m_\Sigma \gtrsim 2\,\text{TeV}$ [104] [1]. As a consequence, the mixing between the MSSM Higgs sector and the scalar triplet is rather small and it can be safely neglected for $m_\Sigma \gtrsim 5\,\text{TeV}$ [103]. These values of m_Σ as well as the hierarchy in eq. (6.4) will be assumed in the following. This in particular allows to take $\langle \xi^0 \rangle \approx 0$.

As the Σ scalar components decouple from the Higgs fields H_1 and H_2, which interact with the down and up right-handed quarks respectively, the Higgs sector at the electroweak scale looks like the one of the MSSM with some $\mathcal{O}(\lambda^2 v^2)$ shifts in the tree-level mass spectrum. By imposing

[1] For discussions on the naturalness of such a hierarchical scenario see refs. [103, 104].

the minimization conditions for the electroweak symmetry breaking, it turns out [104]

$$m_3^2 = m_A^2 \sin\beta\cos\beta \ , \tag{6.5}$$
$$m_Z^2 = \frac{m_2^2 - m_1^2}{\cos 2\beta} - m_A^2 + \lambda^2 v^2/2 \ , \tag{6.6}$$
$$m_A^2 = m_1^2 + m_2^2 + 2|\mu|^2 + \lambda^2 v^2/2 \ , \tag{6.7}$$
$$m_H^\pm = m_A^2 + m_W^2 + \lambda^2 v^2/2 \ , \tag{6.8}$$

where $\tan\beta = v_2/v_1$, $v = \sqrt{v_1^2 + v_2^2} = 174\,\text{GeV}$, m_Z and m_W are the Z and W vector boson masses, and m_1^2, m_2^2 and m_3^2 are the usual MSSM soft parameters of the Higgs fields $H_{1,2}$ whose neutral components are decomposed as $H_i^0 = v_i + (h_i + i\chi_i)/\sqrt{2}$. Moreover, the CP-even squared mass matrix in the basis (h_2, h_1) is given by

$$\mathcal{M}_{h,H}^2 = \begin{pmatrix} m_A^2\cos^2\beta + m_Z^2\sin^2\beta & (\lambda^2 v^2 - m_A^2 - m_Z^2)\sin\beta\cos\beta \\ (\lambda^2 v^2 - m_A^2 - m_Z^2)\sin\beta\cos\beta & m_A^2\sin^2\beta + m_Z^2\cos^2\beta \end{pmatrix} . \tag{6.9}$$

The contributions $\mathcal{O}(\lambda^2 v^2)$ lift the lightest eigenvalue m_h^2 and the little hierarchy problem can be then alleviated with respect to the MSSM. This can be easily seen in the limit $m_A \to \infty$ where

$$m_{h,tree}^2 = m_Z^2\cos^2 2\beta + \frac{\lambda^2}{2} v^2 \sin^2 2\beta \ . \tag{6.10}$$

The $\mathcal{O}(\lambda^2 v^2)$ term can provide a sizeable boost to m_h. In particular, no large radiative corrections are required to catch $m_h \simeq 126\,\text{GeV}$ for large λ and small $\tan\beta$ [2].

On the other hand, some rather large radiative corrections to the Higgs sector are unavoidable due to the lack of experimental evidence of stops and gluinos. Within the specific assumptions the experimental analyses are based on [359], stop and gluino bounds in the presence of any lightest neutralino mass are quite stringent, namely $m_{\tilde{t}} \gtrsim 650\,\text{GeV}$ and $M_3 \gtrsim 1.4$ TeV [360–362] (for loopholes see e.g. refs. [363, 364]). Their radiative corrections to the Higgs sector are then sizeable and need to be stabilized at the expense of a certain amount of fine tuning in the model (for details see e.g. ref. [365]).

A further important source of tuning comes from the triplet if m_Σ is large. We require this to be subdominant to the gluino and stop ones in order to alleviate the little hierarchy problem as much as possible. Notice that this condition does not prevent from $m_\Sigma > m_{\tilde{t}}$ since triplets have less degrees of freedom and (typically) smaller coupling to $H_{u,d}$ than stops. In this respect, the parameter choice $m_\Sigma \gtrsim 5\,\text{TeV}$, $m_{\tilde{t}} \gtrsim 650\,\text{GeV}$ and $\lambda \lesssim 1$ is allowed [103, 104].

In order to simplify our analysis, we will restrict the parameter space to a subset where all the above issues are taken into account. We will focus on the parameter region

$$m_\Sigma = \quad 5\,\text{TeV} \ , \quad A_t = A_b = 0 \ , \quad M_3 = 1.4\,\text{TeV} \ , \quad m_A = 1.5\,\text{TeV} \ , \tag{6.11}$$
$$\lambda \lesssim 1 \ , \quad \tan\beta \sim \mathcal{O}(1) \ , \quad \widetilde{m} \gtrsim 750\,\text{GeV} \ , \tag{6.12}$$

[2] Nevertheless, large values of λ generate a Landau pole and the TMSSM may require an ultraviolet completion to maintain perturbativity up to the unification scale.

with $\widetilde{m} = m_U = m_D = m_Q$. This choice indeed *(i)* alleviates the little hierarchy problem as it boosts m_h with subdominant Σ radiative corrections. Moreover, as far as μ_Σ and μ are not too large, it *(ii)* naturally satisfies the hierarchy (6.4) and *(iii)* allows to neglect the mixing between the Σ scalars and the low energy sector. All sleptons are considered heavy enough not to interact with the relevant SUSY spectrum; numerically they have been taken to be 3 TeV. The precise parameter space we consider is defined in section 6.4, together with all observational constraints used in this analysis.

The Higgs Mass

Nowadays the LHC measurement of the Higgs mass is very accurate. The most recent analyses present 2-σ uncertainties of about 1% on the central value $m_h \simeq 125.6\,\text{GeV}$ [305, 308]. Such accuracy goes much further than the typical precision that beyond-the-SM theoretical papers achieve. These works indeed are more aimed to capture the qualitative features of new frameworks than to accurately evaluate their predictions.

In this spirit, seminal works on the TMSSM have analyzed the Higgs sector at tree-level approximation [101, 102, 366]. Dominant one-loop corrections coming from stops and scalar triplets, as well as one-loop contributions from heavy Higgsinos and Triplinos, have been included only recently [103, 104, 367]. Despite these efforts, the theoretical uncertainties on the TMSSM Higgs mass spectrum is far from being comparable with the experimental one.

A pragmatic approach to this problem is to absorb the (potentially large) theoretical error on m_h into an effective uncertainty on the high energy parameters, especially on the m_U, m_Q and m_Σ soft-breaking terms (and on the trilinear parameters if they are allowed to be large). It is however problematic to quantify the latter uncertainty and how it propagates to the physical observables. For instance, big effects can arise in the DM relic density in the neutralino-stop coannihilation region, or in the SI cross-section when stop mediation dominates the interaction. On the other hand, less dramatic effects arise when the parameters absorbing the Higgs theoretical uncertainty provide sub-leading corrections to the observables. In order to reduce these uncertainties, here we improve the recent TMSSM Higgs mass calculations [103, 104, 367] and consider loop effects in the whole mass spectrum.

For this purpose we use the `SARAH-3.3.0` program [368, 369] to obtain the full two-loop Renormalization Group Equations (RGEs). The code, which works in the $\overline{\text{DR}}$ renormalization scheme, also provides the full one-loop ElectroWeak-Symmetry Breaking (EWSB) conditions and full one-loop spectrum to which we include some $\mathcal{O}(h_t^2 g_3^2)$ and $\mathcal{O}(h_t^4)$ two-loop contributions.

The RGEs are solved numerically by the `SPheno-3.2.4` [370, 371] code. The solution fulfills the above EWSB conditions at the electroweak scale m_Z, as well as some experimental constraints (e.g. the quark mass spectrum; for details see refs. [370, 371]). It is univocally determined once we choose the values of the residual free parameters of the theory [3]. These inputs are given (and we will quote them) at the SUSY renormalization scale, Q.

Once the RGEs are solved, all running parameters and couplings at the scale Q are known.

[3] The quantities M_1^2, M_2^2 and A_λ are fixed as functions of the other parameters through the EWSB equations with $B_\Sigma = 0$.

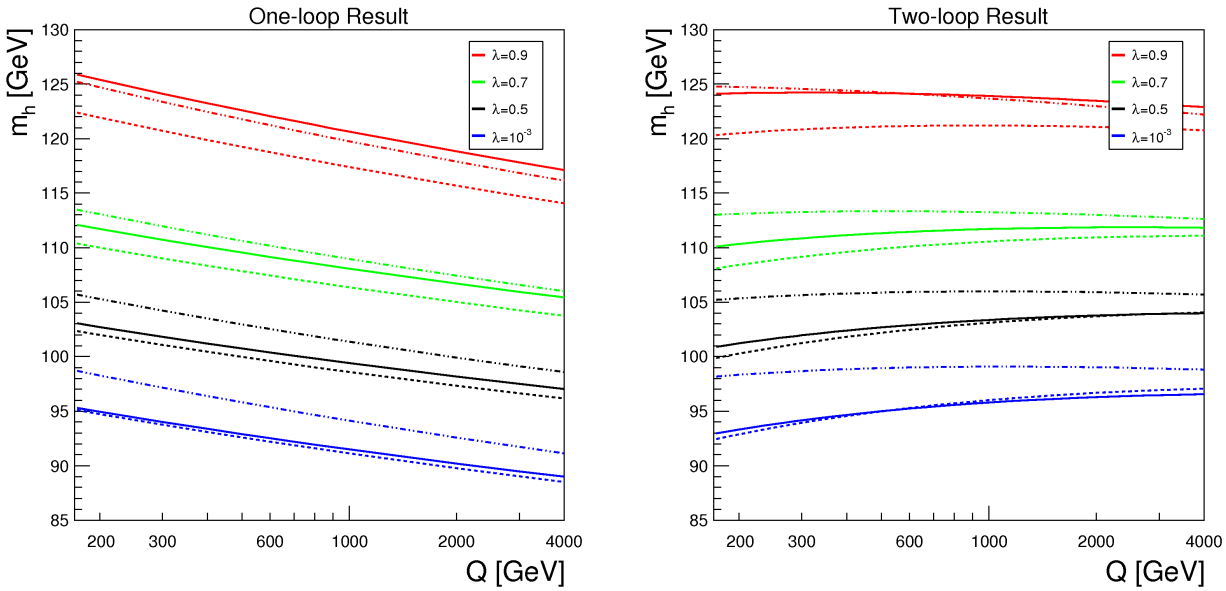

Figure 6.1: *Left:* The Higgs mass m_h as a function of the SUSY renormalization scale Q in the one-loop approximation. *Right:* Same as left in the two-loop approximation. Same color identifies same input value of λ, as labelled. A subset of parameters is fixed at: $\mu_\Sigma = M_1 = 150$ GeV, $m_A = 1.5$ TeV, $m_\Sigma = 5$ TeV, $A_t = A_b = 0$ and $M_3 = 1.4$ TeV. Solid lines (dashed lines) [dotted-dotted-dashed lines] are evaluated for $\widetilde{m} = 700$ GeV and $\mu = M_2 = 300$ GeV ($\widetilde{m} = 700$ GeV and $\mu = M_2 = 1$ TeV) [$\widetilde{m} = \mu = M_2 = 1$ TeV].

These are used to determine the pole mass spectrum. In this way, we determine the pole mass m_h at full one-loop plus $\mathcal{O}(h_t^2 g_3^2) + \mathcal{O}(h_t^4)$ two-loop order on top of the two-loop RGE resummation [4].

The renormalization scale dependence $m_h(Q)$ highlights the improvement in the Higgs mass calculation and it is presented in Figure 6.1 for several values of λ and the parameter setting in eq. (6.11) with $\mu_\Sigma = M_1 = 150\,\text{GeV}$. In the figure solid (dotted) [dotted-dotted-dashed] lines are plotted for $\widetilde{m} = 700\,\text{GeV}$ and $\mu = M_2 = 300\,\text{GeV}$ ($\widetilde{m} = 700\,\text{GeV}$ and $\mu = M_2 = 1\,\text{TeV}$) [$\widetilde{m} = \mu = M_2 = 1\,\text{TeV}$]. The scale dependence is strongly reduced by going from one-loop (left panel) to two-loop (right panel) order. The addition of the $\mathcal{O}(h_t^2 g_3^2) + \mathcal{O}(h_t^4)$ contributions is then crucial to improve the result, as it is well known in the MSSM [5] (cf. curves at $\lambda = 10^{-3}$), whereas the undetermined $\mathcal{O}(\lambda^2 h_t^2)$ corrections seem to be subdominant even at $\lambda \approx 1$.

Figure 6.1 also guides in the choice of Q. The $\mathcal{O}(h_t^2 g_3^2) + \mathcal{O}(h_t^4)$ corrections are minimized at Q nearby the electroweak scale, and $m_h(Q \approx m_t)$ is then expected to be quite stable under further radiative corrections. Although the exact number slightly depends on the parameter choice, for concreteness we fix $Q = m_t$ in the rest of the analysis.

[4] We include the $\mathcal{O}(h_t^2 g_3^2)$ and $\mathcal{O}(h_t^4)$ two-loop effects since we expect $\mathcal{O}(h_t^2 \lambda^2)$ corrections to be subdominant in the regime $\lambda \lesssim 1$ and small $\tan\beta$ due to the color factors and $h_t^2 = m_t^2/\sin^2\beta \lesssim \lambda^2$. These $\mathcal{O}(h_t^2 g_3^2)$ and $\mathcal{O}(h_t^4)$ corrections match with those of the MSSM and are therefore easy to implement in `SPheno` (for details see ref. [372] and references therein).

[5] Notice that the lines with very small λ reproduce the MSSM result except of modifications due to the extra $SU(2)_L$-charged content provided by the triplet.

A last comment concerns the chargino and neutralino parameters. As shown in the figure, if (part of) the chargino spectrum is heavy, relevant negative corrections to m_h can arise [367]. For instance, depending on the value of λ, m_h is lowered by about $1 \div 4$ GeV by moving $\mu = M_2$ from 300 GeV to 1 TeV when $\widetilde{m} = 700\,\text{GeV}$ and $\mu_\Sigma = M_1 = 150\,\text{GeV}$ (c.f. dotted and solid curves of Figure 6.1). Of course, this decrement can be compensated by modifying either $(\lambda, \tan\beta)$ and/or by increasing $\widetilde{m}$, as the dotted-dotted-dashed lines highlight.

6.2. Higgs signatures

Since our aim is to explore the qualitative capabilities of the TMSSM, in particular those related to DM features, we do not look for interplay of Higgs production and decay widths to overcome the LHC bounds. We instead try to work well within the ballpark allowed by data, that is, we attempt to reproduce a SM-like Higgs sector.

The first step in this direction is to fix the tree-level Higgs couplings to SM fields. They are SM-like if, on the top of our assumption $m_\Sigma \gg m_h$, it occurs either *(i)* m_A is much larger that m_h or *(ii)* $\tan\beta$ and λ have values within the so-called alignment region [104]. Here we focus on the first possibility. In this case results are independent of the specific choice of m_A and we can thus fix $m_A = 1.5\,\text{TeV}$ without lack of generality.

The second step is to check the radiative corrections to the Higgs couplings coming from non-SM particles. For our parameter choice, given in eqs. (6.11) and (6.12), loop corrections to tree-level interactions are negligible. They may instead be responsible of important deviations from the SM in loop-induced processes. For gluon fusion, which is the main Higgs production mechanism at LHC, no relevant deviation arises in our analysis since squarks are assumed rather heavy and $\tan\beta$ is small. Therefore, the total Higgs production is SM-like. On the contrary, charginos may be light and eventually the $\Gamma(h \to \gamma\gamma)$ and $\Gamma(h \to Z\gamma)$ widths may depart from their SM values. However, these two processes are not yet well measured due to lack of statistics and of indirect impact on other processes: in practice $\Gamma(h \to \gamma\gamma)$ and $\Gamma(h \to Z\gamma)$ are so small that they play no role in the branching ratios of other Higgs decays. For this reason we do not force them to be SM-like, as we aim to do with the dominant Higgs channels.

Finally, one has to guarantee that no new relevant Higgs decay process is open. This typically occurs when the mass of the lightest neutralino is sufficiently small to allow for the $h \to \widetilde{\chi}_1^0\widetilde{\chi}_1^0$ channel. In such a case, any signal strength $R_{XY} \equiv \text{BR}(h \to XY)/\text{BR}_{\text{SM}}(h \to XY)$ calculated by disregarding the invisible width, should be corrected by the factor $1 - \text{BR}(h \to \widetilde{\chi}^0\widetilde{\chi}^0)$ [6]. As the branching ratio $\text{BR}(h \to \widetilde{\chi}^0\widetilde{\chi}^0)$ is bounded by ATLAS and CMS analyses [373, 374], it is worth to estimate it.

[6] This definition of R_{XY} is based on the fact that the Higgs production is SM-like for the setting in eqs. (6.11) and (6.12).

The $h \to \widetilde{\chi}_1^0 \widetilde{\chi}_1^0$ channel

The Higgs decay channel into a pair of lightest neutralinos is open for $m_{\widetilde{\chi}_1^0} < m_h/2$. Its width is given by

$$\Gamma(h \to \widetilde{\chi}_1^0 \widetilde{\chi}_1^0) = \frac{G_F m_W^2}{2\sqrt{2}\pi}\, m_h \left(1 - \frac{4m_{\widetilde{\chi}_1^0}^2}{m_h^2}\right)^{3/2} g_{h\chi_1^0\chi_1^0}^2 \,, \tag{6.13}$$

where

$$g_{h\chi_1^0\chi_1^0} = (N_{12} - \frac{g_1}{g_2} N_{11})(\sin\beta N_{14} - \cos\beta N_{13}) + \frac{\lambda}{g_2} N_{15}(N_{14}\sin\beta + N_{13}\cos\beta)\,. \tag{6.14}$$

Here the quantities N_{1i} are the components of the lightest (unitary) eigenvector of the neutralino mass matrix $\mathcal{M}_{\widetilde{\chi}^0}$ which is determined at one-loop after the RGEs flow achieved via `SPheno` and `SARAH` as explained in section 6.1. The quantity $m_{\widetilde{\chi}_1^0}$ is the pole mass of the lightest eigenstate of $\mathcal{M}_{\widetilde{\chi}^0}$. At tree level $\mathcal{M}_{\widetilde{\chi}^0}$ reduces to

$$\mathcal{M}_{\widetilde{\chi}^0}^{tree} = \begin{pmatrix} M_1 & 0 & -\frac{1}{2}g_1 v_1 & \frac{1}{2}g_1 v_2 & 0 \\ 0 & M_2 & \frac{1}{2}g_2 v_1 & -\frac{1}{2}g_2 v_2 & 0 \\ -\frac{1}{2}g_1 v_1 & \frac{1}{2}g_2 v_1 & 0 & -\mu & -\frac{1}{2}v_2\lambda \\ \frac{1}{2}g_1 v_1 & -\frac{1}{2}g_2 v_2 & -\mu & 0 & -\frac{1}{2}v_1\lambda \\ 0 & 0 & -\frac{1}{2}v_2\lambda & -\frac{1}{2}v_1\lambda & \mu_\Sigma \end{pmatrix} . \tag{6.15}$$

Notice that due to the LEP chargino mass constraint $m_{\widetilde{\chi}_1^+} \gtrsim 100\,\text{GeV}$, a lightest neutralino with mass $m_{\widetilde{\chi}_1^0} < m_h/2$ must be predominantly Bino. The coupling $g_{h\chi_1^0\chi_1^0}$ is then dominated by the Higgsino and Bino mixings, namely $N_{11}N_{13}$ and $N_{11}N_{14}$. Consequently, for a given set of parameters, the experimental constraint on $\text{BR}(h \to \widetilde{\chi}_1^0\widetilde{\chi}_1^0)$ turns out to be a lower bound on μ.

When $m_{\widetilde{\chi}_1^0}$ is even smaller, namely lighter than $m_Z/2$, also the LEP bound $\Gamma(Z \to \widetilde{\chi}_1^0\widetilde{\chi}_1^0) \lesssim 2\,\text{MeV}$ [187] has to be taken into account. As the constraint on $\text{BR}(h \to \widetilde{\chi}_1^0\widetilde{\chi}_1^0)$, it imposes a lower bound on μ once the other parameters are fixed. We quantify it by the expression

$$\Gamma(Z \to \widetilde{\chi}_1^0\widetilde{\chi}_1^0) = \frac{1}{12\pi}\frac{G_F}{\sqrt{2}} m_Z^3 \left(1 - \frac{4m_{\widetilde{\chi}_1^0}^2}{m_Z^2}\right)^{3/2} \left(|N_{13}|^2 - |N_{14}|^2\right)^2 \,. \tag{6.16}$$

Moreover, when Higgsinos are extremely heavy and the lightest (Bino-like) neutralino is below the threshold of about 20 GeV, the further channel $h \to \widetilde{\chi}_2^0\widetilde{\chi}_1^0$ may be kinematically open without any dangerous enhancement to the invisible width of the Higgs or Z bosons. However, being μ very large, the chargino $\widetilde{\chi}_1^\pm$ and the neutralino $\widetilde{\chi}_2^0$ are almost degenerate. The LHC analysis on three leptons plus missing energy [360] excludes the parameter region of this scenario where $\widetilde{\chi}_2^0$ mostly decays into $Z^{(*)}\widetilde{\chi}_1^0$. In the remaining region where the channel $\widetilde{\chi}_2^0 \to h^{(*)}\widetilde{\chi}_1^0$ competes, it is instead unclear what the experimental limits are. Determining them would require a specific analysis that goes beyond the scope of this study and we then conservatively focus on the region with $\text{BR}(h \to \widetilde{\chi}^0\widetilde{\chi}^0) = \text{BR}(h \to \widetilde{\chi}_1^0\widetilde{\chi}_1^0)$.

The $h \to \gamma\gamma$ channel

Since the Higgs production is SM-like, the diphoton signal strength $R_{\gamma\gamma}$ depends only on $\mathrm{BR}(h \to \gamma\gamma)$. For our setting in eqs. (6.11) and (6.12) only charginos can induce deviations from the SM prediction of $\Gamma(h \to \gamma\gamma)$. Their contributions to $R_{\gamma\gamma}$ have been already calculated by means of the low-energy approximation [103, 104] or in the M_2 decoupling limit [102], starting from the tree-level chargino mass matrix

$$\mathcal{M}^{tree}_{\widetilde{\chi}^\pm} = \begin{pmatrix} M_2 & g_2 v \sin\beta & 0 \\ g_2 v \cos\beta & \mu & -\lambda v \sin\beta \\ 0 & \lambda v \cos\beta & \mu_\Sigma \end{pmatrix} . \tag{6.17}$$

It has been observed that maximal diphoton enhancement occurs when all chargino mass parameters are light (compatibly with the chargino mass bound) and moreover, in the regime of very small $\tan\beta$ and large λ (linked one to each other by the Higgs mass constraint), when Triplino and Higgsino mass parameters are degenerate [104].

In the present analysis we improve the previous estimate by including loop-corrections in $\mathcal{M}_{\widetilde{\chi}^\pm}$. In many cases these radiative contributions increase the lightest chargino mass by about 10% with respect to its tree-level value. They can hence be important when one cuts the allowed parameter space due to the LEP bound $m_{\widetilde{\chi}_i^\pm} \gtrsim 100\,\mathrm{GeV}$.

When only charginos provide new (sizeable) contributions to the diphoton channel and the Higgs production is SM-like, $R_{\gamma\gamma}$ is given by

$$R_{\gamma\gamma} = \left| 1 + \frac{A^{\gamma\gamma}_{\widetilde{\chi}^\pm_{1,2,3}}}{A^{\gamma\gamma}_W + A^{\gamma\gamma}_t} \right|^2 , \tag{6.18}$$

$$A^{\gamma\gamma}_{\widetilde{\chi}^\pm_{1,2,3}} = \sum_{i=1}^{3} \frac{2 M_W}{\sqrt{2}\, m_{\widetilde{\chi}_i^\pm}} (g^L_{h\widetilde{\chi}_i^+\widetilde{\chi}_i^-} + g^R_{h\widetilde{\chi}_i^+\widetilde{\chi}_i^-}) A_{1/2}(\tau_{\widetilde{\chi}_i^\pm}) , \tag{6.19}$$

where $A_{1/2}$ is the spin-1/2 scalar function (see e.g. ref. [375] for its explicit expression) with argument $\tau_{\widetilde{\chi}_i^\pm} = m_h^2/4m^2_{\widetilde{\chi}_i^\pm}$, and $g_{h\widetilde{\chi}_i^+\widetilde{\chi}_i^-}$ is the lightest Higgs effective coupling to charginos. The quantities $A^{\gamma\gamma}_W$ and $A^{\gamma\gamma}_t$ are the W-boson and top-quark contributions whose values are respectively -8.3 and 1.9 for $m_h \simeq 126\,\mathrm{GeV}$.

In the procedure we apply, which corresponds to the one `SPheno` and `SARAH` employ, $R_{\gamma\gamma}$ is calculated by plugging the chargino pole masses into $A_{1/2}(\tau_{\widetilde{\chi}_i^\pm})$. Moreover, the couplings $g^R_{h\widetilde{\chi}_i^+\widetilde{\chi}_i^-}$ and $g^L_{h\widetilde{\chi}_i^+\widetilde{\chi}_i^-}$ are the particular case $i = j$ of the expressions

$$g_{h\widetilde{\chi}_i^+\widetilde{\chi}_j^-} = \; g^L_{h\widetilde{\chi}_i^+\widetilde{\chi}_j^-}\, P_L \; + \; g^R_{h\widetilde{\chi}_i^+\widetilde{\chi}_j^-}\, P_R \tag{6.20}$$

with

$$g^L_{h\widetilde{\chi}_i^+\widetilde{\chi}_j^-} = \frac{1}{\sqrt{2}} \left[\left(U_{j1} V_{i2} - \frac{\lambda}{g_2} U_{j2} V_{i3} \right) \sin\beta + \left(U_{j2} V_{i1} + \frac{\lambda}{g_2} U_{j3} V_{i2} \right) \cos\beta \right] , \tag{6.21}$$

$$g^R_{h\widetilde{\chi}_i^+\widetilde{\chi}_j^-} = \frac{1}{\sqrt{2}} \left[\left(U_{i1} V_{j2} - \frac{\lambda}{g_2} U_{i2} V_{j3} \right) \sin\beta + \left(U_{i2} V_{j1} + \frac{\lambda}{g_2} U_{i3} V_{j2} \right) \cos\beta \right] , \tag{6.22}$$

where U and V are the unitary matrices diagonalizing the one-loop chargino mass matrix $\mathcal{M}_{\widetilde{\chi}^\pm}$ such that $U\mathcal{M}_{\widetilde{\chi}^\pm}V^T = \text{diag}(m_{\widetilde{\chi}_1^\pm}, m_{\widetilde{\chi}_2^\pm}, m_{\widetilde{\chi}_3^\pm})$.

The $h \to Z\gamma$ channel

LHC constraints on $R_{Z\gamma}$ are still very weak [376, 377]. Nevertheless, the $h \to Z\gamma$ channel, likewise the $h \to \gamma\gamma$ decay, is worth to analyze since it is particularly sensitive to new colorless electrically-charged particles which do not change the Higgs production. At the best of our knowledge, in the TMSSM the $R_{Z\gamma}$ signal strength has never been calculated.

Similarly to the case of $R_{\gamma\gamma}$, for our setting (6.11) and (6.12) only charginos can move $\Gamma(h \to Z\gamma)$ from its SM value. This leads to

$$R_{Z\gamma} = \left| 1 + \frac{A^{Z\gamma}_{\widetilde{\chi}^\pm_{1,2,3}}}{A^{Z\gamma}_W + A^{Z\gamma}_t} \right|^2 . \tag{6.23}$$

The contributions $A^{Z\gamma}_W$ and $A^{Z\gamma}_t$ have been first obtained in refs. [378, 379]. They can be expressed in term of Passarino-Veltman three-point functions and turn out to be $A^{Z\gamma}_W = -12$ and $A^{Z\gamma}_t = 0.6$ for $m_h \simeq 126\,\text{GeV}$ [380].

In the TMSSM the chargino contribution comes from triangular loops where all three chargino mass-eigenstates run in and can be flipped from one to another at the vertices (both clockwise and anti-clockwise helicity directions must be taken into account). No flipping however occurs at the vertex involving the photon. For this reason only up to two chargino mass-eigenstates run inside a given loop and each diagram involves a loop integration that is formally similar to those arising in the MSSM calculation (where only two charginos exist). Consequently the study of the $\Gamma(h \to Z\gamma)$ is a straightforward generalization to three charginos of the MSSM expression given in ref. [380].

In the view of the above considerations, we can generalize the procedure of ref. [380] and we obtain

$$A^{Z\gamma}_{\widetilde{\chi}^\pm_{1,2,3}} = \sum_{j,k=1}^{3} \frac{g_2\, m_{\widetilde{\chi}^\pm_j}}{g_1\, m_Z}\, f\Big(m_{\widetilde{\chi}^\pm_j}, m_{\widetilde{\chi}^\pm_k}, m_{\widetilde{\chi}^\pm_k}\Big)\, (g^L_{h\widetilde{\chi}^+_j\widetilde{\chi}^-_i} + g^R_{h\widetilde{\chi}^+_j\widetilde{\chi}^-_i})(g^L_{Z\widetilde{\chi}^+_j\widetilde{\chi}^-_i} + g^R_{Z\widetilde{\chi}^+_j\widetilde{\chi}^-_i}) \,, \tag{6.24}$$

in which: f is a linear combination of Passarino-Veltman functions defined in ref. [380]; $m_{\widetilde{\chi}^\pm_j}$ are pole masses; $g^L_{h\widetilde{\chi}^+_j\widetilde{\chi}^-_i}$ and $g^R_{h\widetilde{\chi}^+_j\widetilde{\chi}^-_i}$ are provided in eqs. (6.21) and (6.22); $g^L_{Z\widetilde{\chi}^+_j\widetilde{\chi}^-_i}$ and $g^R_{Z\widetilde{\chi}^+_j\widetilde{\chi}^-_i}$ are given by

$$g^R_{Z\chi^+_i\chi^-_j} = -\left(V_{i1}V^*_{j1} + \frac{1}{2}V_{i2}V^*_{j2} + V_{i3}V^*_{j3} - \delta_{ij}s^2_W\right) , \tag{6.25}$$

$$g^L_{Z\chi^+_i\chi^-_j} = -\left(U_{i1}U^*_{j1} + \frac{1}{2}U_{i2}U^*_{j2} + U_{i3}U^*_{j3} - \delta_{ij}s^2_W\right) . \tag{6.26}$$

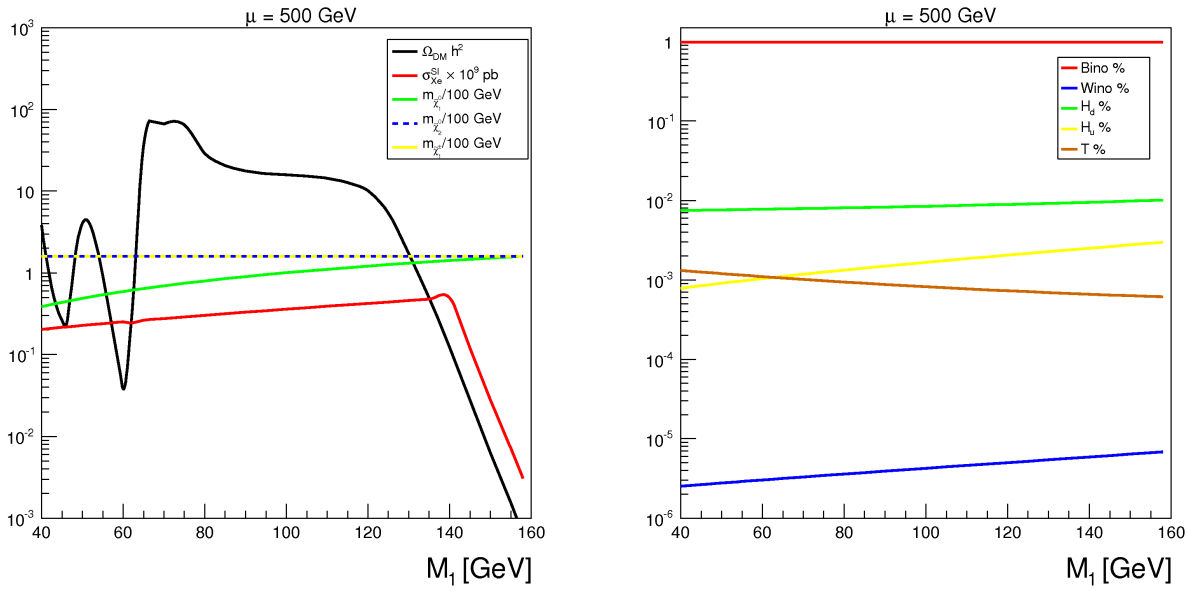

Figure 6.2: *Left:* Dependence of several physical quantities on M_1: the black line denotes $\Omega_{\rm DM}h^2$, the red $\sigma^{SI}_{Xe} \times 10^9$pb, the green the LSP, the blue $m_{\widetilde{\chi}^0_2}$, the yellow $m_{\widetilde{\chi}^\pm_1}$. The lightest chargino is degenerate with the next-to-lightest neutralino. *Right:* Component of LSP as a function of M_1: in red is the Bino fraction, in brown the Triplino, in yellow and green the two Higgsino components and in blue the Wino fraction (as labelled in the caption). In both panels $\mu = 500$ GeV, $M_2 = 1.5$ TeV, $\mu_\Sigma = 180$ GeV, $\tan\beta = 2.9$ and $\lambda = 0.88$.

6.3. Dark Matter Phenomenology of the TMSSM

In this section we present the TMSSM phenomenology in the presence of a neutralino DM candidate. As previously motivated, we require that no supersymmetric particle but neutralinos and charginos interferes during freeze-out, to achieve the correct relic density. To understand the relevant consequences of introducing the Triplino component, we first analyze the Wino decoupling limit.

In Figure 6.2 (left panel) the behaviors of the lightest-neutralino relic density and SI cross-section (black and red lines, respectively) for the limit $M_2 \gg 1\,\text{TeV}$ are depicted as a function of M_1. The corresponding masses $m_{\widetilde{\chi}^0_1}, m_{\widetilde{\chi}^0_2}, m_{\widetilde{\chi}^\pm_1}$ (left panel) and the lightest neutralino compositions (right panel) are also displayed by the mark code reported in the legends. The choice $\mu = 500\,\text{GeV}$, $\mu_\Sigma = 180\,\text{GeV}$, $\tan\beta = 2.9$ and $\lambda = 0.88$ is assumed. The SI cross-section is normalized to 10^{-9} pb, which is close to the maximum of LUX sensitivity given by $\sigma^{\rm SI} \lesssim 8 \times 10^{-10}\,\text{pb}$ at $m_{\widetilde{\chi}^0_1} \sim 50$ GeV [206].

It results that at low M_1 the lightest neutralino, which is almost pure Bino, overcloses the Universe until it reaches the Higgs resonance. In this region the lightest neutralino can provide the correct relic density and, moreover, its SI cross-section is below the LUX upper bound (i.e. the red curve is below 0.8). This occurs because the Higgsino components in the coupling $g_{h\chi^0_1\chi^0_1}$ is enough suppressed to be compatible with LUX results. The Higgs pole region is only mildly sensitive to the

presence of the Triplino. For different parameter configurations, the correct relic density is achieved also at the Z boson resonance. We will discuss these two poles more in detail in section 6.3.

Above the Higgs resonance, the relic density increases until it reaches the opening of the W^+W^- annihilation channel and then decreases. It reaches the experimental value when the coannihilation with the lightest chargino $\widetilde{\chi}_1^\pm$ (and marginally with $\widetilde{\chi}_2^0$) becomes efficient enough. Since the field $\widetilde{\chi}_1^\pm$ is dominantly Triplino (we are assuming $\mu \gg \mu_\Sigma$), the coannihilation cross section strictly depends on the tuning between μ_Σ and M_1. In particular, the correct relic density occurs for $M_1 < \mu_\Sigma$ and the LSP is Bino-like (cf. right panel). Since in this region also the LUX constraint is fulfilled, it results that in the TMSSM a well-tempered Bino-Triplino neutralino can be a good DM candidate.

The behaviors of the relic density and SI cross section shown in the figure is then a proof of concept for the DM in the TMSSM. Indeed we find two qualitatively-different regions where the LSP satisfies the DM constraints. In the next two sections we discuss them in detail, still in the M_2 decoupling limit.

Well-tempered 'Bino-Triplino' neutralino

As it is well known, in MSSM scenarios with well-tempered neutralinos the correct relic density is achieved by a tuning of the Bino and Wino (or Higgsino) mass parameters to get an opportune balance between the large annihilation cross-sections of the Bino and the small ones of the Wino (or Higgsino) [105]. In the TMSSM with M_2 above the TeV scale, the role of the Wino is replaced by the Triplino, which still has gauge interactions with the W bosons. but suppressed by the chirality factors

$$-\tfrac{i}{2}g_2\Big(2U^*_{j1}N_{i2} + 2U^*_{j3}N_{i5} + \sqrt{2}U^*_{j2}N_{i3}\Big)\Big(\gamma_\mu \cdot \tfrac{1-\gamma_5}{2}\Big) \tag{6.27}$$

$$+\ -\tfrac{i}{2}g_2\Big(2N^*_{i2}V_{j1} + 2N^*_{i5}V_{j3} - \sqrt{2}N^*_{i4}V_{j2}\Big)\Big(\gamma_\mu \cdot \tfrac{1+\gamma_5}{2}\Big) \tag{6.28}$$

The channels contributing to the relic density are the chargino annihilation into W^+W^-, ZZ followed by the coannihilations $\widetilde{\chi}_1^0\widetilde{\chi}_1^\pm \to ZW^\pm, q\bar{q}'$. The relevance of the former processes with respect to the latter ones depends on the exact hierarchy between M_1 and μ_Σ. The μ parameter is instead constrained by LUX. Indeed, due to the LUX bound the Higgsino components of the LSP have to be small in order to suppress the $g_{h\widetilde{\chi}_1^0\widetilde{\chi}_1^0}$ coupling that is the main responsible for the SI cross section via Higgs exchange. This is illustrated in Figure 6.3, where the SI cross section is plotted as a function of μ_Σ.

In all panels of the figure we fix $\tan\beta = 2.9$, $\lambda = 0.88$ and $M_2 = 1.5\,\text{TeV}$. Besides the quantities shown in Figure 6.2, also the values of $R_{\gamma\gamma}$ are displayed (for the color code of each quantity see the legend). At each point the parameter M_1 is adjusted just below μ_Σ to reproduce the observed relic density. For $\mu = 300$ GeV (top panels), the LSP is mostly Bino but the amount of its subdominant components vary at different μ_Σ. For light LSPs, the Triplino mixing is comparable to the Higgsino ones and the SI cross section is below the LUX limit. As soon as both Higgsino components reach the Triplino one, the SI cross-section is excluded by the LUX bound. By increasing μ to 500 GeV (bottom panels), the Higgsino mixings at a given μ_Σ become smaller than

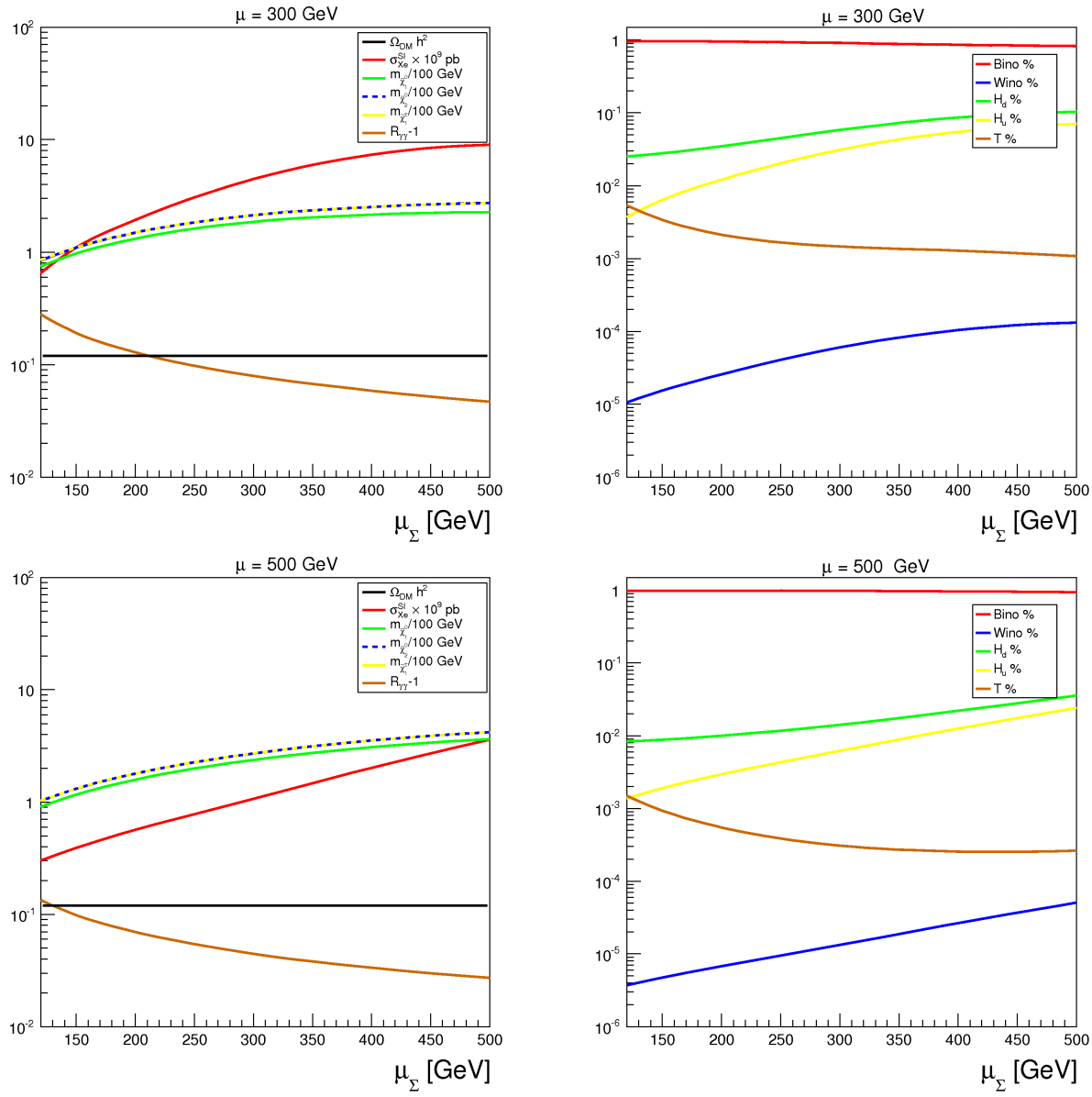

Figure 6.3: *Top left*: Dependence of σ^{SI}_{Xe} (red line), $R_{\gamma\gamma} - 1$ (brown line), $m_{\widetilde{\chi}^0_1}$ (green line), $m_{\widetilde{\chi}^\pm_1}$ (yellow line) and $m_{\widetilde{\chi}^0_2}$ (blue line) on μ_Σ. M_1 is adjusted to satisfy $\Omega_{\rm DM}h^2 = 0.12$ (black solid line) for the well-tempered neutralino. The other parameters are $\mu = 300\,$GeV, $\lambda = 0.88$, $\tan\beta = 2.9$ and $M_2 = 1.5$ TeV. *Top right*: LSP composition as a function of μ_Σ, as labelled in the caption. The other parameters are as in the left panel. *Bottom:* As above but for $\mu = 500$ GeV.

in the $\mu = 300\,$GeV case, and the SI remains below the LUX bound in a wider range: $\widetilde{\chi}^0_1$ satisfies all DM constraints in the mass range of $90 \div 200$ GeV. The Higgsino components tend to be always larger than the Triplino one, as the Triplino connects with the Bino only via the Higgsino mixing

(see Eq. (6.15)). The figure confirms as well that the mechanism that provides the relic density is a balance between annihilation and coannihilation with the lightest chargino, as both particles are close in mass. The contribution of $\widetilde{\chi}_2^0$ in coannihilation is marginal and depends strongly on the exact mixing.

Of course, the minimal μ value that LUX allows depends on the parameters that we have kept fixed in the figure. In particular, the LUX bound on μ becomes stronger at small $\tan\beta$ (see Eq. (6.14)). This anti-correlation is discussed more in detail in section 6.4. However, we can anticipate that it affects negatively the enhancements of both $\gamma\gamma$ and $Z\gamma$ Higgs signals. Indeed, as previously discussed, large $R_{\gamma\gamma}$ and $R_{Z\gamma}$ require either $\tan\beta$ and μ to be small. This is confirmed by the brown line in the left panel of Figure 6.3: for the considered parameter set, the maximal $R_{\gamma\gamma}$ drops as μ goes from 300 GeV to 500 GeV.

DM at the Higgs and Z resonances

The Higgs and Z boson resonances are fine-tuned regions as they rely on the fact that for $M_1 \sim m_h/2$ and $M_1 \sim m_Z/2$ the annihilation cross-section gets enhanced, hence decreasing the relic density. We first comment on the Higgs pole.

The case of the Higgs resonance is peculiar because the phenomenology of the LSP can be reconducted to one coupling only. The vertex Bino-Higgsino-Higgs is responsible for both the annihilation ($\widetilde{\chi}_1^0\widetilde{\chi}_1^0 \to h \to q\bar{q}$) and the SI scattering cross-section since the neutralino is mostly pure Bino. Hence the key parameters are M_1 and μ, whereas there is a minor dependence on both μ_Σ and M_2. Similarly to the case of the well-tempered neutralino, the μ parameter is constrained by the LUX bound, as illustrated in Figure 6.4 where at each point M_1 is tuned at the Higgs resonance to achieve the observed relic density. (The plotted quantities and their color code are as in Figure 6.3). Indeed for $\mu = 300$ GeV (top panels), the SI cross-section is only marginally compatible with the LUX constraint at large μ_Σ and clearly a small decrease in μ will exclude these points (cf. top and bottom left panels). The behavior of the SI cross-section is only mildly dependent on μ_Σ, as it is almost flat over all μ_Σ range. This is even more manifest for $\mu = 500$ GeV (lower panels). For such a μ value the SI cross section is well below the experimental bound. From the right panels it is clear that the LSP is almost pure Bino and that the the dominant annihilation channels is a Higgs exchange on s-channel. Indeed, due to the large mass gap between the lightest neutralino and the other charginos and neutralinos (left panel), coannihilation is completely irrelevant.

In the Higgs resonance region one might expect to have large $R_{\gamma\gamma}$ and $R_{Z\gamma}$ signal strengths because the DM phenomenology is not tightly bounded to the Triplino component. In other words the μ_Σ parameter is not correlated to $\sigma_{\rm Xe}^{\rm SI}$ or $\Omega_{\rm DM}h^2$, and therefore can take low values such that the lightest chargino mass is close to the LEP bound. However, the anti-correlation between $\tan\beta$ and μ mentioned in section 6.3, is present in this region as well. Therefore, the enhancement in the $R_{\gamma\gamma}$ turns out to be at most $\sim 10\%$ for $\mu = 300$ GeV and negligible for $\mu = 500$ GeV, as indicated by the brown line in the left panel of Figure 6.4. We will discuss this issue in detail in section 6.4.

A similar reasoning applies to the Z resonance region, with the difference that in that region the process that fixes the relic density, which is proportional to the Z-Higgsino coupling of the LSP (given in Eq. (6.16)), is uncorrelated from the SI elastic cross-section.

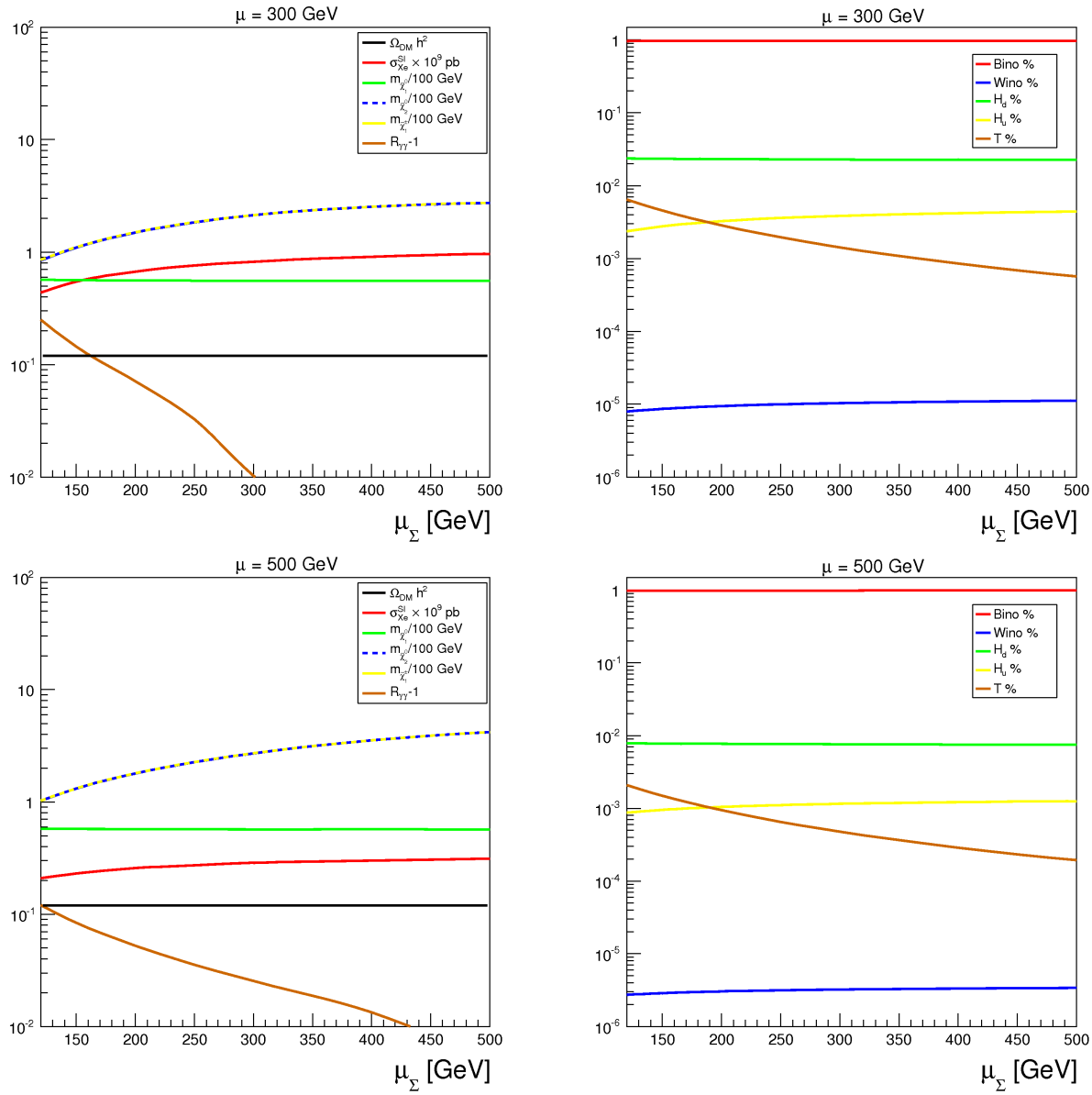

Figure 6.4: *All panels:* Same as Figure 6.3 for the Higgs pole. M_1 is chosen to satisfy the relic density and to be $M_1 \simeq m_h/2$.

6.4. Numerical analysis setup

The TMSSM involves several free parameters. Some of them have to be fixed for practical purposes but play no role in our analysis. This is the case for the whole slepton sector whose masses are assumed above the TeV scale not to interfere with the chargino and neutralino phenomenology we analyze. Other parameters have a minor impact, and their choice given in eq. (6.11) is motivated

Table 6.1: Nested Sampling (NS) parameters and their prior ranges. The priors are flat over the indicated range.

NS parameters	Prior range
$\log_{10}(M_1/\text{GeV}), \log_{10}(\mu_\Sigma/\text{GeV})$	$1 \to 3$
$\log_{10}(\mu/\text{GeV}), \log_{10}(M_2/\text{GeV})$	$2 \to 3$
$\widetilde{m}/\text{TeV}$	$0.63 \to 2$
$\log_{10}(\tan\beta)$	$0 \to 1$
λ	$0.5 \to 1.2$

in section 6.1. Some have to satisfy the EWSB conditions (as explained in section 6.1), and finally only the followings are still undetermined:

$$\{\theta_i\} = \{M_1, M_2, \mu, \mu_\Sigma, \widetilde{m}, \tan\beta, \lambda\}\,. \tag{6.29}$$

To accomplish an efficient sampling on these seven parameters, we adopt an approach based on Bayes' theorem

$$p(\theta_i|d) \propto \mathcal{L}(d|\theta_i)\pi(\theta_i)\,, \tag{6.30}$$

where d are the data under consideration, $\mathcal{L}(d|\theta_i)$ is the likelihood function and $p(\theta_i|d)$ is the posterior Probability Distribution Function (PDF). The function $\pi(\theta_i)$ is the prior PDF, it is independent of data and describes our belief on the values of the theoretical parameter, before the confrontation with experimental results.

All priors $\pi(\theta_i)$ used in the analysis and their ranges of variation are summarized in Table 6.1. A flat prior is assumed for the stop parameter $\widetilde{m}$, with an upper bound at 2 TeV in order not to introduce a large electroweak fine-tuning. For gaugino, Higgsino and Triplino masses, we instead consider logarithm priors and values below the TeV scale. Such a choice is aimed to improve the statistics in the parameter space where charginos tend to be close to their LEP mass bound, may enhance $R_{\gamma\gamma}$ and $R_{Z\gamma}$, and may open the window of the lightest neutralino DM particle. For the same purpose, and in order not to barely reproduce a MSSM-like phenomenology, we also impose $\tan\beta$ smaller than 10. A similar reasoning applies for the chosen range for λ. Within such values we expect to fully cover the TMSSM parameter region where the little hierarchy problem is alleviated (with respect to the MSSM) and perturbation theory does not break down before the GUT scale [103]. On the other hand, we neither exclude a priori scenarios with Landau poles at the PeV scale because these may be avoided in ultraviolet completions of the TMSSM.

The likelihood function is the conditional probability of the data given the theoretical parameters. The data d used in $\mathcal{L}(d|\theta_i)$, which are the observables and constraints summarized in Table 6.2, are as follows.

Collider data: We require the lightest CP-even Higgs mass m_h to be compatible with the ATLAS and CMS measurements [305, 381], which we (indicatively) combine by a statistical mean. Its uncertainty is dominated by the theoretical error, which is estimated to be around 3 GeV [372]. We also assume chargino and stop masses that fulfill the bounds $m_{\widetilde{\chi}_1^\pm} > 101$ GeV [358] and

Table 6.2: Summary of the observables and constraints used in this analysis.

Type	Observable	Measurement/Limit	Ref.
Collider data	m_h	125.85 ± 0.4 GeV (exp) ± 3 GeV (theo)	[305, 381]
	$\Gamma(Z \to \widetilde{\chi}_1^0 \widetilde{\chi}_1^0)$	< 2 MeV	[358]
	$m_{\widetilde{t}_1}$	> 650 GeV (LHC 90% CL)	[360]
	$m_{\widetilde{\chi}_1^+}$	> 101 GeV (LEP 95% CL)	[358]
DM data	$\Omega_{\rm DM} h^2$	0.1186 ± 0.0031 (exp) $\pm 20\%$ (theo)	[118]
	$\sigma_{\rm Xe}^{SI}$	LUX (90% CL)	[206]

$m_{\widetilde{t}_1} > 650$ GeV [360]. Finally, we require the invisible decay width of the Z boson to be smaller than 2 MeV [187].

DM data: We impose the lightest neutralino relic abundance to match $\Omega_{\rm DM} h^2$ measured by Plank [118], as we are interested only in single-component DM. Notice that the experimental error on this observable has become incredibly smaller than the theoretical one, hence we consider an additional 20% of theoretical uncertainty [382]. Furthermore, we enforce the neutralino SI cross-section off nuclei, σ_n^{SI}, to be compatible with the LUX direct detection exclusion bound [206] at 90% CL. For the theoretical prediction of the SI cross-section mediated by the Higgs boson, we do not introduce uncertainties related to the strange quark content of the nucleon: we fix the ratio of nucleon mass and strange quark mass to be $f_s = 0.053$ MeV, accordingly to ref. [383] (for effects due to different choices of f_s and similar quantities such as $\sigma_{\pi n}$ see e.g. refs. [384–388]).

For either the relic density and the Higgs mass we use a Gaussian likelihood function whose peak corresponds to the measured central value and whose width reproduces the standard deviation of the measurement (explicit quantities are quoted in Table 6.2). For the σ_n^{SI} constraint we instead implement a Heaviside likelihood function. The DM constraints are implemented in the likelihood function $\mathcal{L}_{\rm DM}(d|\theta_i)$, the collider constraints are implemented in the likelihood function $\mathcal{L}_{\rm Coll}(d|\theta_i)$ and the full likelihood is simply the product of every individual likelihood associated to an experimental result. Finally, the above stop and chargino mass limits as well as the constraint on the Z-boson invisible width are absorbed into the prior PDFs: each parameter point generating a TMSSM mass spectrum that violates these bounds is discarded.

For some given values of the theoretical inputs θ_i the collider and DM observables are computed by means of some public codes. We briefly summarize the programming procedure. We employ `SARAH-3.3.0` and `SPheno-3.2.4` to calculate the TMSSM mass spectrum (where radiative corrections are taken into account as described in section 6.1). Also $\Gamma(Z \to \widetilde{\chi}_1^0 \widetilde{\chi}_1^0)$, BR$(h \to \widetilde{\chi}_1^0 \widetilde{\chi}_1^0)$, $R_{\gamma\gamma}$ and $R_{Z\gamma}$ are determined by dint of `SPheno-3.2.4` along the lines of section 6.2 (for $R_{Z\gamma}$ we also use the Passarino-Veltman functions that are implemented in the `CPsuperH2.3` libraries [389]). Afterward, the `SPheno-3.2.4` output is elaborated by `micrOMEGAs_2.4.5` [268]. In this way we compute the DM observables listed in Table 6.2.

To explore the parameter space we link `SPheno` and `micrOMEGAs_2.4.5` to the nested sampling algorithm `MultiNest_v3.2` [390] (with specifications of 4000 live points and tolerance parameter set

to 0.5). This algorithm produces the posterior samples from distributions with a large number of parameters and with multi-modal likelihoods more efficiently than Markov Chain Monte Carlo. At practical level we run two samples: for analyzing the Higgs phenomenology we use only $\mathcal{L}_{\rm Coll}(d|\theta_i)$ (sample 1), whereas when exploring the DM constraints as well, we use the full likelihood (sample 2). `MultiNest_v3.2` might however populate with an insufficient number of points regions where the likelihood is flat. This is relevant for the $R_{\gamma\gamma}$ and $R_{Z\gamma}$ observables, as we do not impose constraints on their values in the likelihood function. To address this issue we run two additional samples with $\mathcal{L}(d|\theta_i)_3 = \mathcal{L}_{\rm Coll}(d|\theta_i) \times \mathcal{L}_{\gamma\gamma}(d|\theta_i)$ and $\mathcal{L}(d|\theta_i)_4 = \mathcal{L}_{\rm Coll}(d|\theta_i) \times \mathcal{L}_{\rm DM}(d|\theta_i) \times \mathcal{L}_{\gamma\gamma}(d|\theta_i)$ (for the case without and with the DM constraints respectively, sample 3 and sample 4). These two likelihood functions include a *fake* information associated to an extra Gaussian likelihood function $\mathcal{L}_{\gamma\gamma}(d|\theta_i)$ with $R_{\gamma\gamma} = 1.6 \pm 0.2$ to ensure a efficient exploration of region with large $h \to \gamma\gamma$ and $h \to \gamma Z$ signal strengths [7]. We do not provide a statistical analysis of the samples but show the result for points drawn randomly from the posterior PDF, which are provided in the `*post_equal_weight.dat` file constructed by `MultiNest_v3.2`, hence we can safely combine the samples originating from different run with different likelihood functions. Before discussing our findings, let us mention some experimental bounds that we do not enforce in the sampling phase.

Different bounds on BR($h \to \widetilde{\chi}_1^0 \widetilde{\chi}_1^0$) exist in the literature [310, 311, 313, 314, 373, 374]. Imposing any of them would make our results of difficult interpretation if a different bound should be considered. We thus prefer not imposing any cut on BR($h \to \widetilde{\chi}_1^0 \widetilde{\chi}_1^0$) and just presenting its value in the results we present.

We are also aware of the bounds on the chargino and neutralino masses based on simplified models: in scenarios with $m_{\widetilde{\chi}_1^0} \lesssim 100\,\text{GeV}$ and $m_{\widetilde{\chi}_1^\pm} \simeq m_{\widetilde{\chi}_2^0}$, data analyses impose $m_{\widetilde{\chi}_1^\pm} \gtrsim 350\,\text{GeV}$ at 95% CL if $\widetilde{\chi}_2^0$ decays 100% into Z boson, or $m_{\widetilde{\chi}_1^\pm} \gtrsim 170\,\text{GeV}$ if $\widetilde{\chi}_2^0$ decays 100% into h boson [391,392]. However, due to its not straightfoward intepretation in the generic TMSSM parameter space, we do not impose such constraints. Instead, in the post processing phase of the samples we verify that these bounds do not apply in the interesting ballpark of our analysis. Indeed, in particular when we achieve a relevant diphoton enhancement, the fields $\widetilde{\chi}_2^0$ and $\widetilde{\chi}_2^\pm$ are mixed states and consequently *(i)* their masses are not degenerate and *(ii)* the neutralino decay channels into Z and h bosons can compete especially due the Triplino component and its potentially sizeable coupling λ.

Finally, we also consider the $B_s \to \mu^+\mu^-$ and $B \to X_s\gamma$ observables and the neutralino Spin-Dependent (SD) cross-section off protons and neutrons. We use `SPheno-3.2.4` and `micrOMEGAs_2.4.5` respectively to calculate them. As expected in scenarios with low $\tan\beta$, these B-meson signatures are in full agreement with experiments [327, 393]. We will compare the results for SD cross-section with COUPP and XENON100 limits [394, 395] on proton and neutron respectively and comment them in section 6.6.

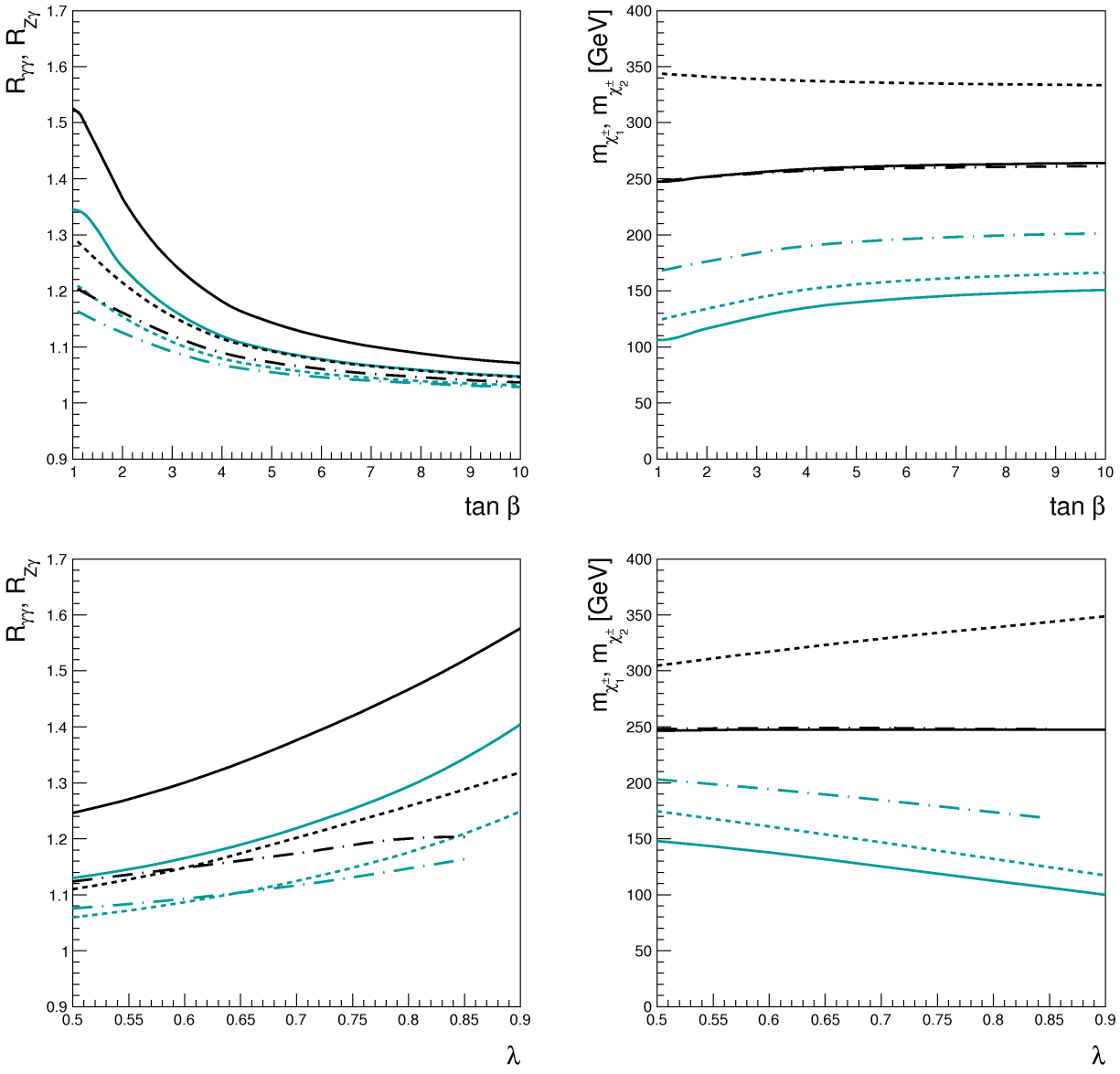

Figure 6.5: *Top left*: Analytic behavior of $R_{\gamma\gamma}$ (black) and $R_{Z\gamma}$ (turquoise) as a function of $\tan\beta$ for $\lambda = 0.85$. The solid lines are for $\mu = \mu_\Sigma = M_2 = 230\,\text{GeV}$ (scenario A), the dashed lines stand for $\mu = \mu_\Sigma = 230\,\text{GeV}, M_2 = 1\,\text{TeV}$ (scenario B) and the dot-dash lines for $\mu_\Sigma = M_2 = 230\,\text{GeV}, \mu = 400\,\text{GeV}$ (scenario C). *Top right:* Dependence on $\tan\beta$ of the lightest (turquoise) and next to lightest (black) chargino masses, which contribute to the $R_{\gamma\gamma}$ and $R_{Z\gamma}$ shown in the left panel (the solid/dashing code is as in the left panel). *Bottom:* Same as above as a function of λ for $\tan\beta = 1.1$

6.5. $R_{Z\gamma}$ and $R_{\gamma\gamma}$ without DM contraints

Within the TMSSM, the possibility of achieving sizeable enhancements in $R_{\gamma\gamma}$ has been previously highlighted in refs. [103, 104]. These analyses were performed by considering tree-level chargino masses and low-energy limit approximations. They were moreover carried out for some illustrative parameter regions. In this section we extend the previous analysis focused on the $m_A \gg m_h$ regime [103]. In particular, we explore a broader parameter space (but still keeping large m_A) and we include the radiative effects discussed in section 6.2. We also present our findings for $R_{Z\gamma}$ in Eq. (6.23).

Before reporting the result of the full parameter sampling, it is educative to understand the role of some inputs. The essential parameter dependence of $R_{\gamma\gamma}$ and $R_{Z\gamma}$ is shown in the left panels of Figure 6.5. In the figure we assume the setting in eq. (6.11), as well as $\lambda = 0.85$ in the upper plot and $\tan\beta = 1.1$ in the lower one. At each point the stop parameter $\widetilde{m}$ is adjusted to obtain $m_h = 126\,\text{GeV}$. The signal strengths $R_{\gamma\gamma}$ and $R_{Z\gamma}$ (black and turquoise lines, respectively) are calculated for three chargino mass settings: $\mu = \mu_\Sigma = M_2 = 230\,\text{GeV}$ (solid curves; scenario A), $\mu = \mu_\Sigma = 230\,\text{GeV}, M_2 = 1\,\text{TeV}$ (dashed curves; scenario B) and $\mu_\Sigma = M_2 = 230\,\text{GeV}, \mu = 400\,\text{GeV}$ (dotted-dashed curves; scenario C). The corresponding chargino masses $m_{\widetilde{\chi}_1^\pm}$ and $m_{\widetilde{\chi}_2^\pm}$ are presented in the right panels by employing the same mark code of the left plots.

For the parameter choice considered in the figure, the enhancement in $h \to \gamma\gamma$ is always larger than the one in $h \to Z\gamma$. Moreover, $R_{\gamma\gamma}$ and $R_{Z\gamma}$ are strongly correlated and a sizeable enhancement in $R_{\gamma\gamma}$ requires a departure from the SM also in the $h \to Z\gamma$ channel. These behaviors will be confirmed in the results of the full parameter sampling.

As Figure 6.6 shows, in each scenario the largest $R_{\gamma\gamma}$ and $R_{Z\gamma}$ are achieved by reducing $\tan\beta$ and increasing λ, which also corresponds to requiring less tuning in the electroweak sector (cf. eq. (6.10)). The enhancement is mostly due to the decrease of $m_{\widetilde{\chi}_1^\pm}$ and the consequent smaller suppression of the loop functions in eqs. (6.18) and (6.24) (cf. right panels of the figure; the masses $m_{\widetilde{\chi}_{2,3}^\pm}$ are large in the three scenarios and hence provide a subleading effect). However, also the coupling $g_{h\widetilde{\chi}_1^\pm\widetilde{\chi}_1^\pm}$ plays an important role. This can be deduced by comparing $R_{\gamma\gamma}$ (or $R_{Z\gamma}$) in different scenarios in correspondence to the same $m_{\widetilde{\chi}_1^\pm}$ value. For instance, for $\lambda = 0.85$ both scenario A with $\tan\beta \simeq 10$ and scenario B with $\tan\beta \simeq 1.1$ have the same chargino mass $m_{\widetilde{\chi}_1^\pm} \simeq 150\,\text{GeV}$ but quite different $R_{\gamma\gamma}$. These observations are in agreement with previous results obtained for $R_{\gamma\gamma}$ [103, 396, 397].

A last remark concerns the parameter range of Figure 6.5. We do not enter the regime of $\tan\beta \simeq 1$ and $\lambda \gtrsim 1$ to achieve larger enhancements. Besides the reasons previously provided, there is a further issue that imposes such a restriction: the more the tree-level Higgs mass is boosted, the smaller the radiative corrections have to be not to overstep the $m_h \simeq 126\,\text{GeV}$ constraint. In particular, this may require stop masses below the bound of Table 6.2, as it happens in scenario C at $\lambda \gtrsim 0.85$ with $\tan\beta \lesssim 1.1$. Of course, slightly bigger enhancements would exist by allowing for $m_{\widetilde{t}} \ll 650\,\text{GeV}$ and/or $m_\Sigma \ll 5\,\text{TeV}$. However, since prooving the experimental suitability of

[7] We check that the upper bounds on $R_{\gamma\gamma}$ and $R_{Z\gamma}$ we will obtain do not change by requiring large $R_{Z\gamma}$ instead of high $R_{\gamma\gamma}$.

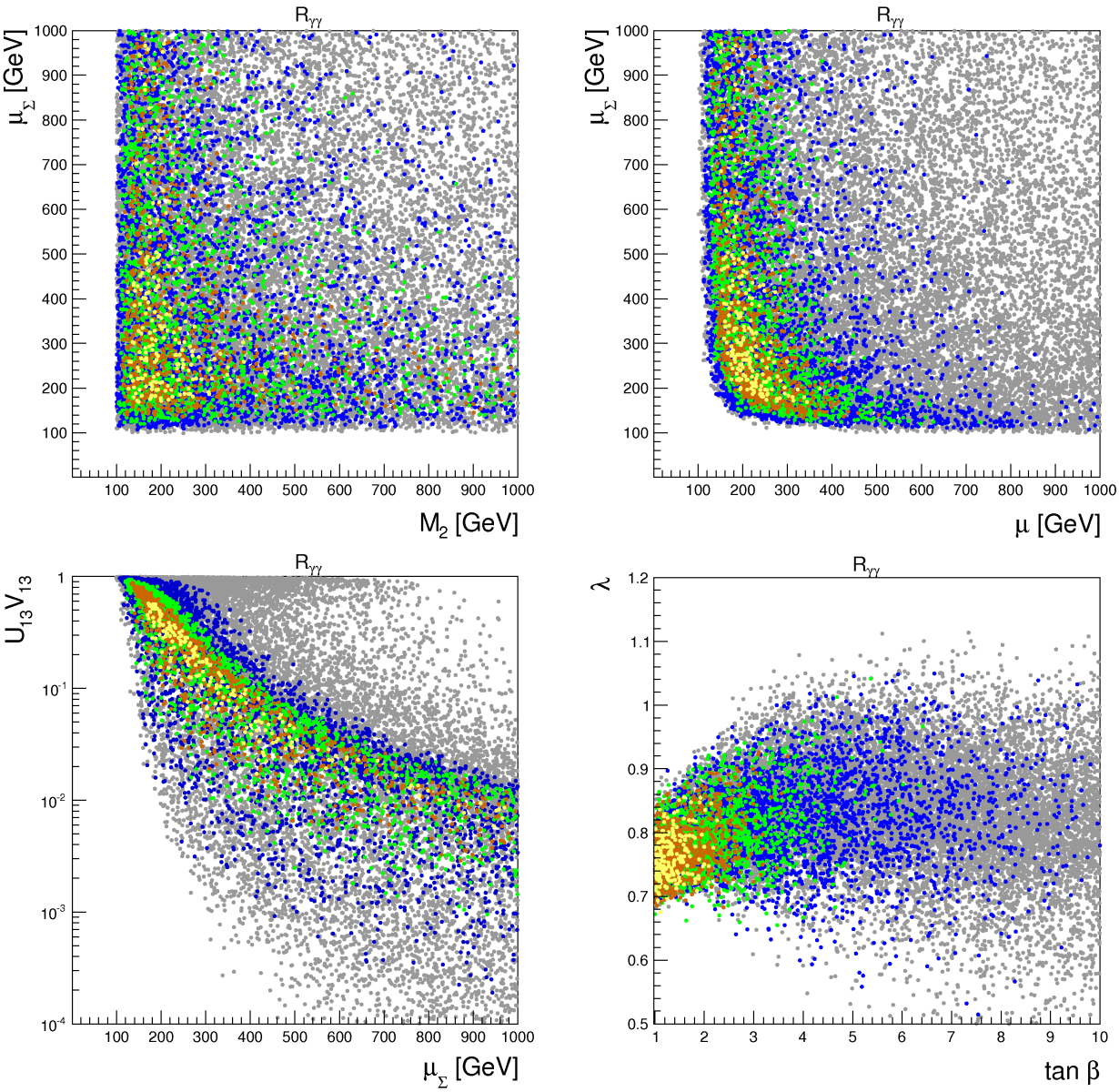

Figure 6.6: *Top left:* $R_{\gamma\gamma}$ (third direction) projected in the $\{\mu_\Sigma - M_2\}$-plane. The values of $R_{\gamma\gamma}$ are encoded in the colors: $R_{\gamma\gamma} < 1.1$ in gray, $1.1 \leq R_{\gamma\gamma} < 1.2$ in blue, $1.2 \leq R_{\gamma\gamma} < 1.3$ in green, $1.3 \leq R_{\gamma\gamma} < 1.4$ in brown, and $R_{\gamma\gamma} \geq 1.4$ in yellow. *Top right:* Same as left in the $\{\mu_\Sigma - \mu\}$-plane. *Bottom left and right:* Same as top left for the Triplino component of the lightest chargino as a function of μ_Σ and $\{\lambda - \tan\beta\}$-plane respectively.

such modifications would require specific collider analyses, and lowering m_Σ may also increase the electroweak fine tuning, we do not further discuss this possibility.

The two samples obtained with $\mathcal{L}_{\text{Coll}}(d|\theta_i)$ are presented in Figure 6.6. The amount of diphoton enhancement is encoded in the color of the points: $R_{\gamma\gamma} < 1.1$ in gray, $1.1 < R_{\gamma\gamma} < 1.2$ in

blue, $1.2 < R_{\gamma\gamma} < 1.3$ in green, $1.3 < R_{\gamma\gamma} < 1.4$ in brown, and $R_{\gamma\gamma} > 1.4$ in yellow (this color code will be maintained in the rest of the Chapter). The bottom left panel of the figure proves that the presence of the Triplino is fundamental to achieve $R_{\gamma\gamma} \gtrsim 1.3$. Indeed, if the Triplino component of the lightest chargino is negligible, $R_{\gamma\gamma}$ falls to MSSM-like values, i.e. $R_{\gamma\gamma} \lesssim 1.2$ [396] [8]. However, in some extreme cases, Triplino effects may be still present even when μ_Σ is quite large and the Triplino component of the lightest chargino is subdominant (but not negligible), as the case $\mu_\Sigma \simeq 900\,\text{GeV}$ and $R_{\gamma\gamma} \gtrsim 1.4$ shows.

The features of the parameter regions where the yellow points accumulate can be explained as follows. As observed in Figure 6.5, large diphoton enhancements are allowed for small $\tan\beta$ and rather large λ (cf. bottom right panel). In such a case, the relation $\lambda > g_2$ arises. Consequently, in the Higgs-chargino-chargino coupling the contribution proportional to λ can push $g^{L,R}_{h\widetilde{\chi}_1^\pm\widetilde{\chi}_1^\pm}$ above the maximal value obtained in the MSSM. This of course occurs only if both Triplino and Higgsino components are unsuppressed. Large $R_{\gamma\gamma}$ enhancements then require μ and μ_Σ at the electroweak scale (cf. top right panel). On the other hand, also the MSSM-like contribution of the Higgs-chargino-chargino coupling can provide an additional boost to $g^{L,R}_{h\widetilde{\chi}_1^\pm\widetilde{\chi}_1^\pm}$ if the Wino mixing is sizeable. Therefore, also M_2 has to be small to achieve maximal enhancements (cf. top left plot). In particular, in order to minimally suppress the loop function $A_{1/2}(\tau_{\widetilde{\chi}_i^\pm})$, the parameters have to be correlated in such a way that $m_{\widetilde{\chi}_1^\pm} \approx 101\,\text{GeV}$.

The effect of the Higgs and stop mass constraints is pointed out in the bottom right panel of the figure. The region with small λ and small $\tan\beta$ is not populated because the tree-level Higgs mass (6.10) is very small. In such a case, only large stop loop corrections to m_h could push it up to 126 GeV, but such corrections are not allowed due to the $\widetilde{m}$ range of Table 6.1. On the contrary, in the upper empty area with small $\tan\beta$, the tree-level Higgs mass is too large. In this case stop loop corrections have to be small not to overstep the Higgs mass constraint, but they are incompatible with the bound $m_{\widetilde{t}_1} > 650\,\text{GeV}$. Curiously, the mass bound cuts off most of the parameter space where the TMSSM exhibits a Landau pole at a scale $Q \lesssim 10^8\,\text{GeV}$ (see ref. [103] for estimates of the Landau pole scale). We stress however that the border of this empty region could be mildly moved by considering larger values of M_2, μ, and μ_Σ than those in Table 6.1. Heavier charginos would indeed provide bigger (negative) radiative correction to m_h that should be compensated by slightly larger stop masses to keep $m_h \approx 126\,\text{GeV}$ [367].

Although Figure 6.6 presents only $R_{\gamma\gamma}$ results, the above considerations apply also to $R_{Z\gamma}$. Indeed, in the TMSSM $R_{\gamma\gamma}$ and $R_{Z\gamma}$ are tightly correlated. This is proven in Figure 6.7, which displays the values of $R_{\gamma\gamma}$ and $R_{Z\gamma}$ arising in the samples 1 and 2. Since the sampling also explores the region with small M_1, the $h \to \widetilde{\chi}_1^0\widetilde{\chi}_1^0$ channel can be open. Depending on the value of $\text{BR}(h \to \widetilde{\chi}_1^0\widetilde{\chi}_1^0)$, the points in the figure are colored as follows: $\text{BR}(h \to \widetilde{\chi}_1^0\widetilde{\chi}_1^0) < 1\%$ in light blue, $1\% \leq \text{BR}(h \to \widetilde{\chi}_1^0\widetilde{\chi}_1^0) < 20\%$ in violet, $20\% \leq \text{BR}(h \to \widetilde{\chi}_1^0\widetilde{\chi}_1^0) < 50\%$ in dark yellow and $\text{BR}(h \to \widetilde{\chi}_1^0\widetilde{\chi}_1^0) \geq 50\%$ in red (this color code will be followed in the rest of the Chapter).

In the left panel of the figure, the light blue area is not aligned with the remaining region. We have investigated the origin of this feature and it seems related to the different kinds of con-

[8] This MSSM upper bound on $R_{\gamma\gamma}$ is obtained by assuming a mass spectrum similar to ours, where only charginos can enhance the diphoton rate. Due to different crucial assumptions, we do not compare our results to those of refs. [83, 397].

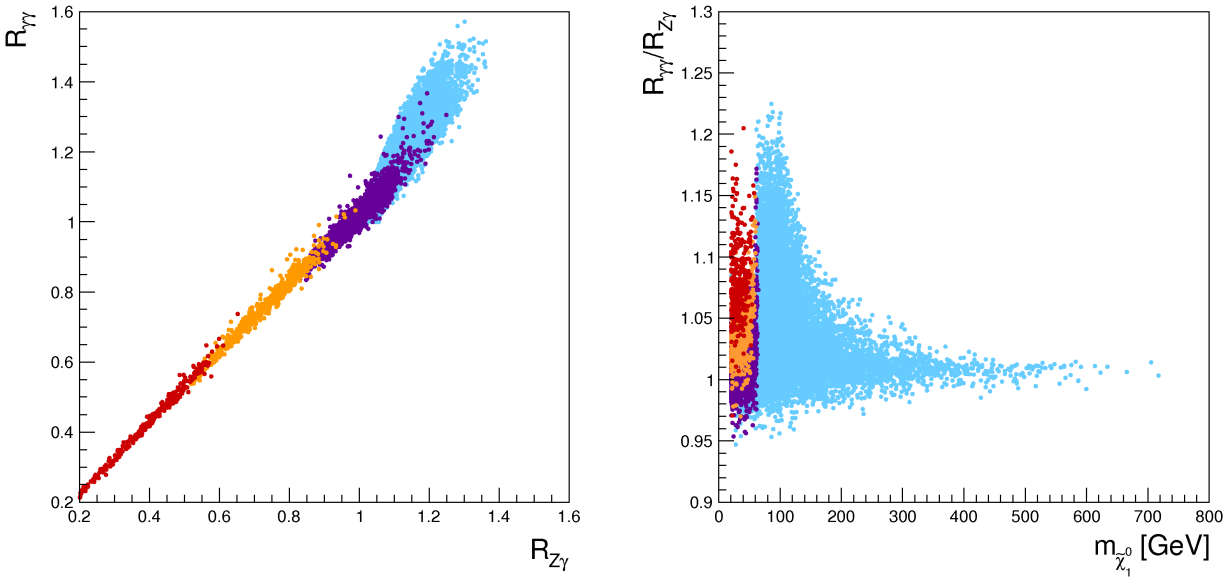

Figure 6.7: Correlation between $R_{\gamma\gamma}$ and $R_{Z\gamma}$ for the equal weight posterior sample. The color code is: light blue for $\mathrm{BR}(h \to \widetilde{\chi}_1^0\widetilde{\chi}_1^0) < 1\%$, violet for $1\% < \mathrm{BR}(h \to \widetilde{\chi}_1^0\widetilde{\chi}_1^0) < 20\%$, dark yellow for $20\% < \mathrm{BR}(h \to \widetilde{\chi}_1^0\widetilde{\chi}_1^0) < 50\%$ and red for $\mathrm{BR}(h \to \widetilde{\chi}_1^0\widetilde{\chi}_1^0) > 50\%$.

figurations of chargino parameters in that region. In fact, in the upper-left part of the light blue area, the typical chargino configuration yields to very large $g^{L,R}_{h\widetilde{\chi}_1^0\widetilde{\chi}_1^0}$ (for $M_1 \lesssim 100\,\mathrm{GeV}$). Therefore, only when $m_{\widetilde{\chi}_1^0}$ is tuned just below the $m_h/2$ threshold, $\mathrm{BR}(h \to \widetilde{\chi}_1^0\widetilde{\chi}_1^0)$ is small. Unless of this rare accident, $\mathrm{BR}(h \to \widetilde{\chi}_1^0\widetilde{\chi}_1^0)$ is either huge or zero. Consequently, for the configurations of chargino parameters that populate the upper-left part of the light blue area, $R_{\gamma\gamma}$ and $R_{Z\gamma}$ are typically either larger or much smaller than one, and an empty region at $R_{\gamma\gamma} \approx 1$ and $R_{Z\gamma} \approx 0.9$ is thus produced.

The opposite effect instead occurs in the lower part of the light blue region: the typical chargino parameters yield tiny $g^{L,R}_{h\widetilde{\chi}_1^0\widetilde{\chi}_1^0}$ and hence $\mathrm{BR}(h \to \widetilde{\chi}_1^0\widetilde{\chi}_1^0)$ is small for very most of the values that M_1 can assume. For these configurations of chargino parameters, therefore, $R_{\gamma\gamma}$ and $R_{Z\gamma}$ do not jump from one value to a very different one at the threshold $m_{\widetilde{\chi}_1^0} \sim m_h/2$ but slowly change as function of M_1. For this reason the violet region is abundantly populated by such chargino configurations.

Finally, let us summarize the most striking result of this section. From our analysis we obtain the following TMSSM bounds (see Figure 6.6):

$$R_{\gamma\gamma} \lesssim 1.6\,, \qquad R_{Z\gamma} \lesssim 1.4\,, \qquad 0.95 \lesssim R_{\gamma\gamma}/R_{Z\gamma} \lesssim 1.2 \qquad \text{(no DM obs.)} \tag{6.31}$$

and we stress the tight degree of correlation between the two loop-induced processes.

6.6. Constraints on $R_{\gamma\gamma}$ and $R_{Z\gamma}$ from DM phenomenology

DM in the TMSSM: global survey

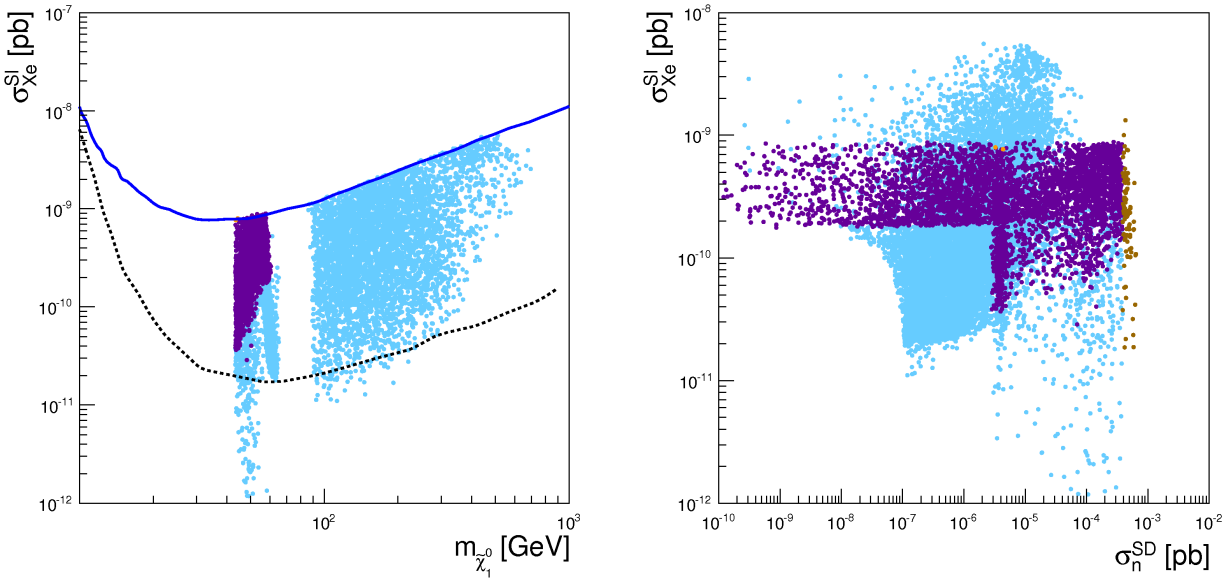

Figure 6.8: *Left:* Equal weight posterior sample in the $\{\sigma^{\rm SI}_{\rm Xe} - m_{\widetilde{\chi}^0_1}\}$-plane. The solid blue line stands for the LUX exclusion limit, while the black dotted line is the projected sensitivity of XENON1T. The color code is as in Figure 6.7 and indicates the Higgs into invisible branching ratio percentage when the channel is open. *Right:* Same as left in the $\{\sigma^{\rm SI}_{\rm Xe} - \sigma^{\rm SD}_{n}\}$-plane. The brown points stand for points at odds with the XENON100 exclusion bound for $\sigma^{\rm SD}_n$.

In this section we present the results of a comprehensive sampling of the TMSSM parameter space, using the likelihood $\mathcal{L}_{\rm DM}(d|\theta_i)$ and the prior ranges described in section 6.4.

Figure 6.8 (left panel) shows the mass value for which the LSP is a viable DM candidate compatible with LUX (blue solid). As discussed above, there are two separate regions: one with the resonances at $40\,{\rm GeV} \lesssim m_{\widetilde{\chi}^0_1} \lesssim 70\,{\rm GeV}$, and one with a well-tempered neutralino at $m_{\widetilde{\chi}^0_1} \gtrsim 90\,{\rm GeV}$. The apparent upper limit at about 600 GeV is an artifact of the prior range choice for the mass parameters. Notice that almost all the parameter space is in the sensitivity range of XENON1T [127] (black dotted line), so an effective TMSSM might be probed by DM direct searches in 5-7 years time [9]. In our sample the minimal values of $\sigma^{\rm SI}_{\rm Xe}$ correspond to the contribution to the SI cross-section due to squarks exchange, when the Higgsino component start to be negligible. The value is similar in all the sample as the squark sector is kept heavy. More interestingly, the requirement of having the LSP as good DM candidate sets as well an upper bound on the Higgs invisible branching ratio ${\rm BR}(h \to \widetilde{\chi}^0_1\widetilde{\chi}^0_1) < 20\%$ (violet points), which is comparable to current LHC bounds [310, 311, 313, 314] (indeed there are the very few dark yellow points with

[9] However, we stress that the accuracy of the present analysis does not allow for refined comparison between the TMSSM and XENON1T. Indeed, our estimate of the SI cross section does not take into account loop-induced corrections of the order of $\mathcal{O}(10^{-11})$ pb [398].

BR($h \to \widetilde{\chi}_1^0\widetilde{\chi}_1^0$) > 20%). This illustrates the complementarity between DM direct searches and colliders: significant values of the Higgs invisible width can be fully probed by XENON1T.

In the right panel of Figure 6.8 we show the $\sigma^{\rm SI}_{\rm Xe}$ versus the SD cross-section on neutron (which is equivalent to the one on proton). As in the previous figures, violet points represent parameter configurations with BR($h \to \widetilde{\chi}_1^0\widetilde{\chi}_1^0$) > 1%, whereas brown points correspond to SD cross-section values at odds with the XENON100 exclusion bound, whose strongest limit $\sigma_n^{\rm SD} \lesssim 3\times10^{-4}$ pb is at $m_{\widetilde{\chi}_1^0} \sim 50$ GeV. We do not remove the brown points from our samples as the nuclear uncertainties on the structure functions for the nucleons are large and can affect the predicted number of events by a factor of 3-4 [281, 395, 399]. In addition the predictions for the SD on proton give the same value, however these values are below the COUPP sensitivity, which reaches the maximum at $\sigma_p^{\rm SD} \sim 5\times10^{-3}$ pb for $m_{\widetilde{\chi}_1^0} \sim 40$ GeV. These points with large $\sigma_{p,n}^{\rm SD}$ are associated to the t-channel Z boson exchange and arise when Higgsino components are sizable. They correspond to the Z resonance region, where the coupling $g_{Z\widetilde{\chi}_1^0\widetilde{\chi}_1^0}$ is large. In the case of SD scattering there is a one-to-one correspondence with the annihilation cross-section mediated by the Z boson. The main bulk of the sample is however below the current SD bounds, because the coupling to the Z boson tends to be suppressed for most of the LSP composition, being predominantly Bino-like. The sharp cut on the upper values of SD and SI when the Higgs channel into invisible is open is due to the LUX bounds. XENON1T will be less sensitive to SD interaction (perhaps $\sim 10^{-6}$ pb), hence the model is more likely to be tested with the SI cross-section and the brown points will all be probed, independently of the nuclear uncertainties.

When M_2 is decreased to the same scale as the other chargino parameters, the phenomenology of the DM is wider and the tight bound on the lower limit of μ described above (sections 6.3 and 6.3) is relaxed by the additional admixture with the Wino component. This is illustrated in Figure 6.9, where we display the LSP mass versus the neutralino and chargino parameters as labelled. From the top left panel, it is clear that the LSP is mostly Bino, as $m_{\widetilde{\chi}_1^0}$ and M_1 follow each other over all the allowed range. From the other three panels it is striking that the Higgs and Z resonances are mostly independent from M_2 and μ_Σ as they can acquire approximately any allowed value.

The case of the well-tempered neutralino, where all possible combinations of compositions for the are available, is more interesting. Indeed the LSP can be mixed Bino-Triplino, as discussed above, but it can never be Triplino dominated because the LSP would be the corresponding chargino. Successful DM candidates can also show up as MSSM-like states, that is Bino-Wino, in which case the relic density is achieved by neutralino annihilation into W^+W^- and coannihilation with the lightest chargino producing $q\bar{q}'$. These MSSM-like scenarios are however less appealing because the condition $M_1 \sim M_2$ is not recovered by the usual supersymmetry-breaking mechanisms. Of course, a large portion of the parameter space presents mixed Bino-Triplino-Wino LSP, for which the dominant annihilation and coannihilation channels are $\widetilde{\chi}_1^0\widetilde{\chi}_{1,2}^0 \to W^+W^-$ and $\widetilde{\chi}_1^0\widetilde{\chi}_1^\pm \to q\bar{q}'$. Due to the LUX bound only μ larger than about 300 GeV is allowed. Moreover, the relic density is achieved by a mixture of annihilation and coannihilation. More specifically the main processes are $\widetilde{\chi}_1^0\widetilde{\chi}_1^0 \to hZ, q\bar{q}$ and $\widetilde{\chi}_1^0\widetilde{\chi}_1^\pm \to ZW^\pm$. Instead, when all components (Bino-Triplino-Wino-Higgsino) in the LSP are sizable, the main annihilation channels are the following: $\widetilde{\chi}_1^\pm\widetilde{\chi}_1^\pm \to W^\pm W^\pm$, $\widetilde{\chi}_1^0\widetilde{\chi}_1^\pm \to hW^\pm$ and $\widetilde{\chi}_1^0\widetilde{\chi}_1^0 \to hZ$.

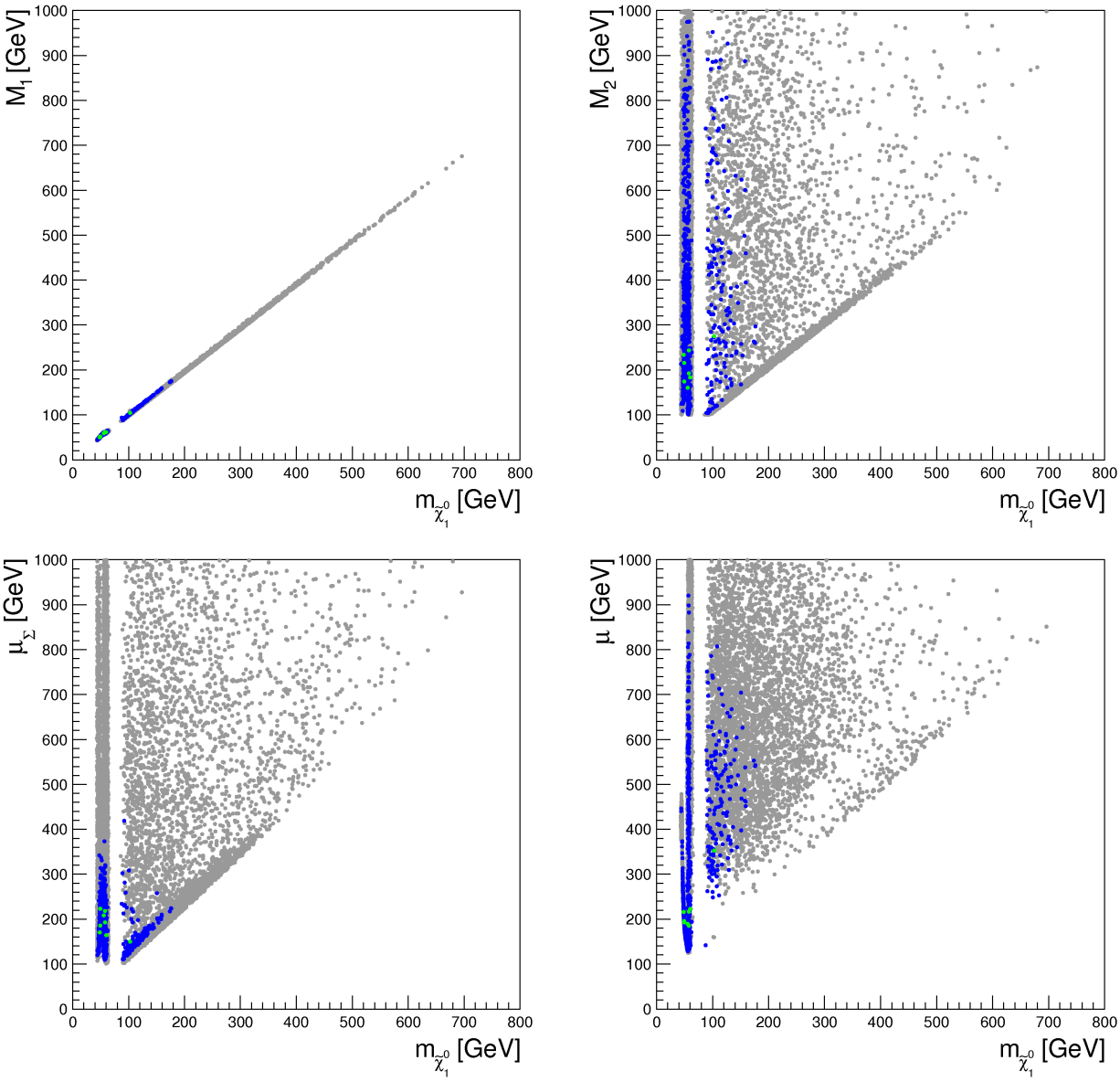

Figure 6.9: *Top left*: M_1 dependence of the mass of the LSP $m_{\tilde{\chi}_1^0}$. *Top right:* Same as left for M_2. *Bottom:* Same as top left for μ_Σ and μ. The color code is as in Figure 6.6.

DM implications on $R_{\gamma\gamma}$ and $R_{Z\gamma}$

Figure 6.10 shows the $\gamma\gamma$ signal strength versus the $Z\gamma$ one, similarly to Figure 6.7. The possible $R_{\gamma\gamma}$ and $R_{Z\gamma}$ that can be achieved in the TMSSM where the DM constraints are satisfied, are displayed in cyan. They are superposed to the points of Figure 6.7 where no DM observable is imposed (here displayed in green). The DM constraints alleviate the change in slope that arises

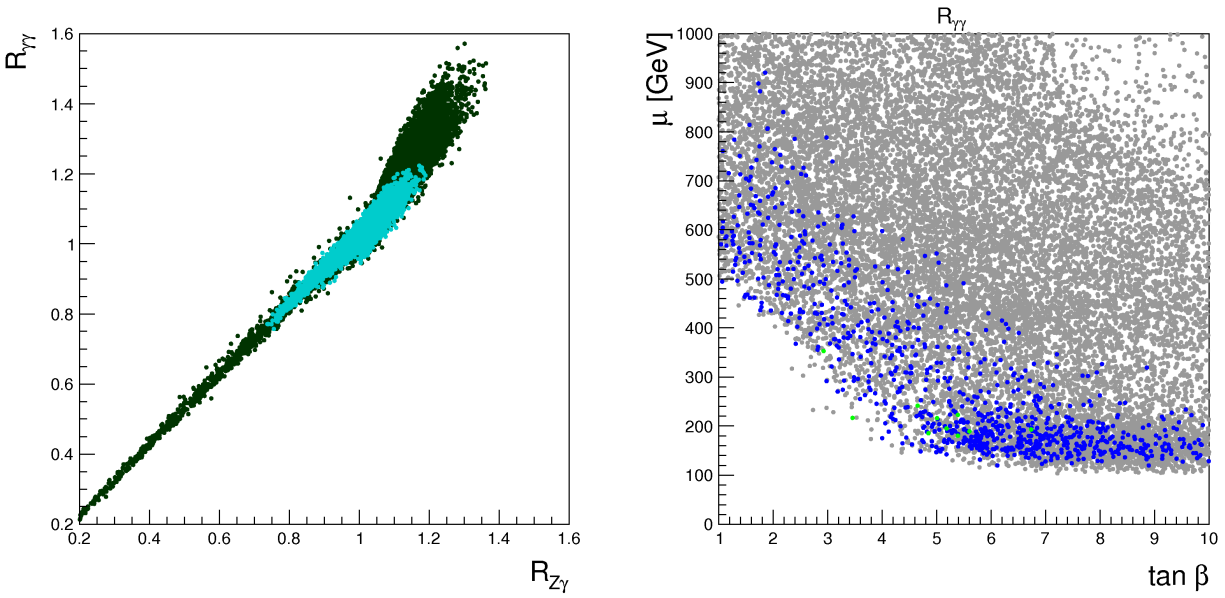

Figure 6.10: *Left*: Correlation between $R_{\gamma\gamma}$ and $R_{Z\gamma}$ for the equal weight posterior sample for the no DM case (green points) and for the DM case (cyan points). *Right:* Correlation between $\tan\beta$ and μ for the equal weight posterior sample for the DM case. Same color code as in Figure 6.6.

in the correlation plot without DM constraints (cf. left panel of Figure 6.7): the cyan points follow a smooth pattern with respect to the dark green ones. As previously discussed, the missing dark green zone in the upper part of that plot is due to a Higgs branching ratio varying very fast as soon as it is kinematically open. There, to get small reduction in the signal strength, M_1 should lie exactly on the threshold value, which is a very infrequent situation. On the contrary, with the LSP being DM, the relic density constraint requires $M_1 \sim m_{h,Z}/2$ (or the well-tempered neutralino conditions) and therefore a large portion of the sampled parameter space is concentrated in the pole regions.

On the other hand, on general basis, the DM constraints are not encouraging about the collider Higgs phenomenology. Indeed, our analysis leads to

$$R_{\gamma\gamma} \lesssim 1.25 \ , \qquad R_{Z\gamma} \lesssim 1.2 \qquad \text{(with DM obs.)} \ . \tag{6.32}$$

The most stringent constraint on the parameter space where large $R_{\gamma\gamma}$ and $R_{\gamma\gamma}$ are achieved, is the LUX bound on SI cross-section, which rules out the configurations where either μ and $\tan\beta$ are simultaneously small: the anti-correlation between these two variables is striking from the right panel of Figure 6.10 [10]. In particular, for $\tan\beta \simeq 1$ the LSP is a viable DM candidate only for $\mu > 500$ GeV, i.e. it is incompatible with the ballpark that provides the largest possible enhancements (see Figure 6.7). The possibility of achieving sizeable loop-induced decays of the Higgs and at the same time a successful neutralino DM particle, starts arising at $\tan\beta \gtrsim 3$ and $\mu \gtrsim 300$ GeV: this is exactly the region that saturates the bounds in eq. (6.32), as shown by the

[10] This correlation is proper of the MSSM and has been noticed for instance in ref. [400].

green points in the right panel (these points have $R_{\gamma\gamma} > 20\%$). The mild enhancement of 10% is viable in all $\tan\beta$ range, as it is due to small values of μ_Σ. This is illustrated in Figure 6.11. In the left panel we show the projection of the $R_{\gamma\gamma}$ values as a function of λ and $\tan\beta$: the range of the Triplino coupling λ that provides the enhancements is limited with respect to Figure 6.7, being scattered at around $0.8 \div 0.9$. Signal strengths larger than one can only be achieved for small values of μ_Σ (central panel); they are however only marginally sensitive to M_2. The same points are instead concentrated to both small values of μ and μ_Σ (right panel) and they mostly correspond to the Higgs and Z resonance regions. This is confirmed by looking at the same sparse green/blue points in Figure 6.9, which are mostly concentrated at values of $m_{\tilde{\chi}_1^0}$ around $40 \div 70\,\text{GeV}$.

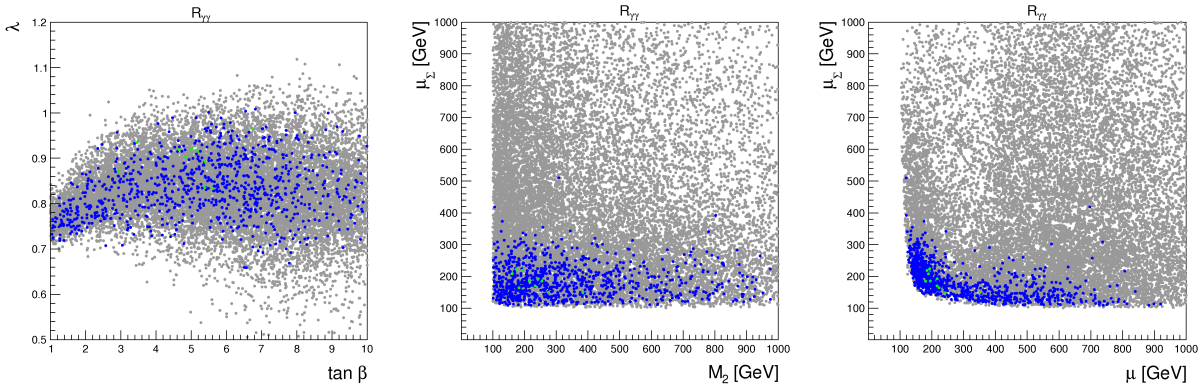

Figure 6.11: *Left:* $R_{\gamma\gamma}$ (third direction) projected in the $\{\lambda - \tan\beta\}$-plane. Same color code as in Figure 6.6. *Central and right:* Same as left in the $\{\mu_\Sigma - M_2\}$ and $\{\mu_\Sigma - \mu\}$ planes.

7

Conclusions

7.1. English

In this Thesis we have studied the collider phenomenology perspective from which one can address the DM problem. As we know, DM is approximately the 27% of the content of the Universe and it is the 85% of the total amount of matter in the Universe, however, its nature is still unknown. The most favoured perspective is the fact that the DM is a particle that interacts weakly with the SM content, the well-known WIMP DM. Taken into account this assumption, a huge amount of possibilities appears under different models extending the SM in order to account for a dark sector. On the one hand, one can choose a simple scenario where the DM sector and the SM one are coupled through a particle that plays the role of mediator. This kind of constructions are usually dubbed portals. In Part I we have shown two constructions differing in the nature of the mediator, either a scalar or a vector boson.

In Chapter 3 we explore the singlet-extended model. This is the simplest extension of the SM scalar sector that connects to the dark sector. It predicts a universal deficit in the Higgs boson couplings to the SM fermions and gauge bosons caused by the mixing between the two neutral scalar states. In the coming years, the LHC will further explore the properties of the Higgs boson by looking for possible deviations from the SM predictions [401]. In particular, after the high-luminosity upgrade, LHC is expected to deliver 3000 fb^{-1} at 14 TeV [402]. This would allow to measure the $\gamma\gamma$, WW, ZZ, $b\bar{b}$, and $\tau^+\tau^-$ Higgs couplings within a 2 – 8% error [401, 402]. Alternatively, a new contribution to the invisible Higgs width would imply the reduction of the visible Higgs decays, which can also be interpreted as a generic Higgs coupling deficit. The direct production and detection of the new Higgs would certainly elucidate this point. Since the relevant cross section depends on the mass and the mixing of the extra Higgs state, we have first reviewed the present experimental bounds on these two parameters. Concerning the constraints by EWPO, we have improved previous analysies by using the full set of electroweak observables instead of the oblique parameters (S, T), since the last ones only provide an accurate descriptions of the heavy Higgs effects in the $m_H \sim m_h$ region.

In order to illustrate the detection of the direct heavy Higgs production, we have chosen two benchmark points compatible with present bounds, in particular, the LHC Higgs data and the EWPO. We have studied the resonant SM Higgs boson pair production in the $hh \to b\bar{b}\, WW \to$

$b\bar{b}\ell^+\nu\ell^-\bar{\nu}$ decay channel. The main background to the signal is the di-leptonic $t\bar{t}$ process. Besides some basic selection cuts, we have applied M_{T2} cuts to the $2\ell + \not{E}_{\mathrm{T}}$ or $2b + 2\ell + \not{E}_{\mathrm{T}}$ systems in order to optimise the signal significance. Using the di-leptonic channel alone, a significance $\sim 3\sigma$ for 3000 fb^{-1} can be achieved at the 14 TeV LHC for $m_H = 400$ GeV if the mixing is close to its present limit and $\mathrm{BR}(H \to hh) \approx 1$. A lower branching ratio or a smaller mixing angle would require combining various hh decay channels. The complementarity between $H \to hh$ and $H \to ZZ$ channels is studied for arbitrary $\mathrm{BR}(H \to hh)$ values.

We have also checked that it is possible to extend the model by including a DM candidate. The next generation of direct detection experiments will be capable of probing a large amount of the parameter space of the model.

In Chapter 4, we have performed a thorough study of phenomenological features of hidden sector scenarios with Stückelberg Z' portals that arise as low energy effective actions of certain type II string compactifications with intersecting branes. For our purposes, the crucial property of these constructions is the unavoidable extension of the SM gauge group by several ('anomalous') abelian gauge bosons which gain a mass and can mix with analogous bosons from hidden sectors.

Many interesting phenomenological properties of such setups are determined by the charges of the SM spectrum under the extra $U(1)$s of the visible sector, together with a handful of mixing parameters (a, b, c, d). The possible choices for the charges are rather scarce, due to the necessary identification of these symmetries with approximate global symmetries of the SM. We have focussed on a particular gauge structure, the *Madrid models* that arises in a large class of intersecting brane constructions. Some other configurations are possible, and they could be studied in analogy. We believe, nevertheless, that our analysis covers a significant portion of the landscape of semi-realistic brane models.

Once the extra visible $U(1)$ bosons mix with those from the hidden sectors, the lightest Z' mass eigenstate generates interactions between DM and SM fermions. A particularly appealing and characteristic feature of such models, is the natural appearance of rich patterns of isospin violating DM interactions, which contrasts with other simple portals traditionally considered in the literature. We have explored the prospects for f_n/f_p and a_n/a_p in six different BM points of the parameter space of these constructions, incorporating LHC and LUX bounds showing that in general values of these ratios tend to be dominated by the neutron contribution. Target materials with more sensitivity to neutron interactions are thus very suitable to explore these scenarios.

Generically, this setup provides isospin violating couplings both in the SI and SD interactions. We have confronted our prospects with LUX and LHC bounds for a set of BM points. By using our own simulation of the LUX experiment, we have performed a check of the exclusion regions for each point using the maximum gap method. This has allowed us to analyse consistently a general scenario with SI and SD (proton and neutron contributions) interactions as well as in general cases of isospin violating couplings of DM. For the LHC we have calculated, for each point of the parameter space, the production cross section of a Z' boson times the branching ratio of a specific decay. With this, we have included ATLAS searches for dilepton (e^+e^- and $\mu^+\mu^-$) and dijet resonances. Remarkably, all regions experimentally allowed entail much higher neutron than proton cross sections for the SI interactions while for the SD the situation is less constrained.

The findings of this work open the door to a generic scenarios in which the signals in dir-

ect detection experiments can be dominated by neutrons. Moreover, we show that the existing complementarity between LHC searches and direct detection experiments is specially relevant to disentangle the couplings of the Z' boson to SM particles. It is gratifying to see how, not only different experimental strategies, but also phenomenological and fundamental theoretical input can be combined into a single framework to shed some light into the possible properties of the so far elusive nature of dark matter.

On the other hand, one can study the DM phenomenology from the point of view of a theoretically motivated model that could afford to solve other pathological problems that arise in the SM. SUSY is one candidate that fulfills the above requirements, it can account for the DM particle while solves different issues such as the hierarchy problem. However the minimal phenomenologically viable realization of it, the MSSM, is nowadays in tension with the results from Run 1 of the LHC. In particular in order to achieve a mass of the SM Higgs boson, $m_h \simeq 125$ GeV requires a tune of the parameters within the MSSM. One can consider different extensions of this minimal model in which new contributions to the Higgs mass appear at tree level. Moreover these new extensions provide different prediction on the DM and collider phenomenology. In Part II we study two extensions of the MSSM Higgs sector of the superpotential that are allowed by gauge invariance, the singlet extension, dubbed NMSSM extended with a singlet RH neutrino superfield, and the triplet extension with $Y = 0$, named the TMSSM. Both of them present a DM phenomenology that is directly connected with their LHC signatures.

In Chapter 5 we have investigated exotic collider signatures of the Next-to-Minimal Supersymmetric Standard Model with a right-handed neutrino and sneutrino. This is a construction in which an extra singlet superfield, N, is included in the NMSSM in order to account for RH neutrino and sneutrino states. After electroweak symmetry-breaking takes place, a Majorana mass term is generated for the RH neutrinos which is of the order of the Higgs expectation value and implies an electroweak scale see-saw mechanism, with a small Yukawa coupling $y_N \sim 10^{-6}$, for neutrino mass generation. Such a small neutrino Yukawa leads to a tiny mixing between right and left-handed fields. It is for this reason that the RH neutrino, when produced at the LHC, can be long-lived and give rise to displaced vertices.

We have incorporated the recent constraints on the masses of supersymmetric particles, as well as on low-energy observables. We also impose the presence of a Higgs boson with a mass of approximately 125.5 GeV and consider the existing results on the reduced signal strengths for its decays into Standard Model particles, which place a bound on its invisible and non-standard decays. We study the effect of these constraints on the parameter space of the model.

In the first part of this Chapter we have investigated the production and late decay of RH neutrinos. We show that, due to the small neutrino Yukawa, the RH neutrino can decay in the inner detector of ATLAS or CMS, giving rise to a displaced vertex. This can be observed through the decay products, which involve two leptons ($2\ell + \not{E}_T$) or a lepton with two jets (ℓjj). For a representative number of benchmark points we have simulated the production of RH neutrinos in the current LHC configuration (with a center of mass energy of 8 TeV and an integrated luminosity of $\mathcal{L} = 20$ fb^{-1}), and a future one (13 TeV and $\mathcal{L} = 100$ fb^{-1}), defining a number of basic cuts to single out the signal. We have found that some points of the parameter space can already be probed with the current LHC data, and others can become accessible in the future upgrade. We

have constructed the two-lepton ($m_{\ell\ell}$) and two-jets one lepton ($m_{\ell jj}$) invariant mass distributions for the different benchmark points, showing that the end-point in $m_{\ell\ell}$ and the peak in $m_{\ell jj}$ can give valuable complementary information on the mass of the RH neutrino that can help distinguishing this scenario from models with R-parity violation.

In the second part of this Chapter we have considered the possibility that the stau is the NLSP. We have shown that the stau decay can also be suppressed by the small Yukawa couplings in certain regions of the parameter space. We have simulated the production of staus in the current and future LHC configuration for two benchmark points. The results suggest that some points in the parameter space can be within the reach of the future LHC configuration.

In Chapter 6 we have considered the Higgs phenomenology of the $Y = 0$ triplet extension of the MSSM, dubbed TMSSM, in which the new coupling between the triplet and the MSSM Higgses can alleviate the little hierarchy problem and modify the chargino and neutralino sector.

We have first accurately determined the couplings and pole masses of the stops, charginos, neutralinos and lightest CP-even Higgs h. Then, we have tackled the subtle effects of the Triplino in the $h \to \gamma\gamma$ and $h \to Z\gamma$ loop-induced processes. We have shown that the additional Triplino component in the chargino sector provides a maximal enhancement of 60% in the $R_{\gamma\gamma}$ signal strength, which is slightly larger than previously estimated (i.e. $R_{\gamma\gamma} \lesssim 1.45$) [103]. An enhancement up to 40% can be achieved in the $R_{Z\gamma}$ signal strength, which we find to be highly correlated with the diphoton channel, even though it is always smaller than $R_{\gamma\gamma}$. The parameter region leading to the largest $R_{\gamma\gamma}$ and $R_{Z\gamma}$ is characterized by $\tan\beta \lesssim 2$ and $\mu \sim \mu_\Sigma \sim M_2 \sim 250\,\text{GeV}$, and in particular by light charginos close to the LEP bound. The enhancement in the TMSSM is significantly larger than the one achievable in the MSSM ($\sim 20\%$ for $R_{\gamma\gamma}$) for the same chargino lower mass bound [396]. The measurements of these processes are likely to improve in the next years. LHC is indeed expected to probe the SM prediction of $\Gamma(h \to Z\gamma)$ once $\mathcal{O}(100\ \text{fb}^{-1})$ data is collected [403], and to measure the $g_{h\gamma\gamma}$ effective coupling within a 10% accuracy after a high luminosity 3000 fb^{-1} run [404]. With these further data the Higgs diphoton signal strength will plausibly converge to the SM value. In such a case, sizeable deviations in $h \to Z\gamma$ would not be compatible with the TMSSM. On the contrary, if data will still exhibit a positive deviation from the SM, there would be a clear indication of physics beyond the SM. The above predictions and the tight correlation between $R_{\gamma\gamma}$ and $R_{Z\gamma}$ could be thus crucial to rule out or provide hints for the scenario considered here.

Besides the Higgs decays, we have investigated the DM phenomenology in the TMSSM, focusing on the interplay of the neutralino and chargino sectors enlarged by the triplet components. Similarly to the MSSM, the LSP is a viable DM candidate in the Higgs or Z pole region, and in the so-called well-tempered regime. The Higgs and Z pole regions are characterized by a Bino DM and are poorly sensitive to the Triplino, as the Higgs-Higgsino-Bino is the only relevant coupling. However, the well-tempered neutralino, where the LSP achieves the correct relic density via coannihilation with the lightest chargino, presents a new feature. Indeed the Triplino component of the LSP can substitute the Wino in the well-tempered neutralino and can solve the problem of having $M_1 \sim M_2$ from grand unified model perspective. Indeed the requirement of DM comes at the expenses of satisfying the LUX exclusion limit for SI elastic cross-section on nuclei. The dominant contribution is due to Higgs exchange, which imposes a lower bound on μ. Interestingly

we found that this has an impact for the $R_{\gamma\gamma}$ and $R_{Z\gamma}$ enhancements: the Higgs-chargino coupling is reduced as well suppressing the signal strengths to at most 20%. Notice that these values are once again larger than the ones provided by the MSSM with DM constraints [396], when the Higgs production is SM-like.

The scenario considered here nicely illustrates the complementarity of DM direct searches with LHC. For instance the next generation of direct detection experiments, such as XENON1T, will probe a consistent portion of the neutralino TMSSM parameter space. Moreover it will be capable of constraining the Higgs invisible decay branching ratio up to 1%, in a time scale comparable to the LHC one. In general the TMSSM is less constrained by current LHC bounds on simplified models or supersymmetric searches. Indeed the presence of the Triplino can modify the couplings and the decay modes. This has been already observed for stops in the TMSSM [405] even though a precise estimate of their current mass bound is still missing. On the other hand no study exists for the chargino and neutralino mass bounds. Although we have checked that the present constraints [391, 392] do not apply to our analysis ballpark, a dedicated investigation would be required in order to accurately determine the allowed parameter region. Present data should primarily affect the chargino parameter region with light lightest-neutralino and with small $h \to Z\gamma$ and $h \to \gamma\gamma$ enhancements. With more LHC data strongest bounds are expected, in particular for the DM mass close to the Z or h resonance. On the other hand, in order to probe the coannihilation region (where the spectrum is compressed), ILC data and analyses similar to that proposed in ref. [406] would be crucial.

It is the aim of this Thesis to study different collider aspects of DM models so in a future we can discriminate among them. Specific experiments such as direct and indirect detection ones are specialised in the search of DM, however collider experiments that are designed for different purposes can also help in the identification of the DM nature. In fact, several efforts are taken to improve searches in every different kind of experiments so the searches could be complementaries. We expect in the near future that experiments will corner the dark matter parameter space (or even find it) so we could have some information about it. If this happens the collider information about its properties will be crucial to extract all the relevant information of the DM nature, such as mass, couplings and so on. We are living exciting times with upgraded experiments and maybe future experiments that for sure will reveal us more about the face Nature has.

7.2. Castellano

En esta Tesis hemos estudiado diferentes perspectivas desde las cuales se puede estudiar el problema de la MO. Como sabemos, aproximadamente el 27% del contenido del Universo y el 85% del contenido total de materia es MO, sin embargo la naturaleza de ésta es aún desconocida. La propuesta más favorecida es el hecho de que la MO esté compuesta de partículas que interaccionan débilmente con el contenido del ME, la conocida materia oscura WIMP. Si tenemos en cuenta esto un número indeterminado de posibilidades aparecen bajo diferentes modelos que extienden el ME para cobijar un sector oscuro. Por una parte, uno puede escoger un escenario simple donde el sector de MO y el de ME están acoplados a través de una partícula que asume el papel de mediador. Esta clase de construcciones usualmente se les llama portales. En la Parte I hemos mostrado dos

construcciones basadas en la naturaleza del mediador, ya sea un bosón escalar o un bosón vectorial.

En el Capítulo 3 exploramos el modelo extensión de singlete que es la más simple extensión del sector escalar del ME. Este modelo predice un déficit universal en los acoplos del bosón de Higgs a fermiones del ME y bosones de gauge causado por la mezcla entre los dos estados escalares neutros. En los años venideros, el LHC explorará las propiedades del bosón de Higgs centrándose en posibles desviaciones de las predicciones del ME [401]. En particular, después de su mejora para alta luminosidad, se espera que el LHC acumule cerca de 3000 fb^{-1} a 14 TeV [402]. Esto permitirá medir los acoplos $\gamma\gamma$, WW, ZZ, $b\bar{b}$, y $\tau^+\tau^-$ con una precisión del 2 – 8% de error [401, 402].

Alternativamente, una reducción de la anchura invisible del Higgs implicaría la reducción de las desintegraciones visibles del Higgs, pudiendo ser interpretado como un déficit en los acoplos. La producción directa y posterior detección de este nuevo Higgs podría ciertamente arrojar luz en este punto. Dado que la sección eficaz relevante depende de la masa y de la mezcla del estado de Higgs extra, hemos aplicado los límites experimentales actuales sobre estos dos parámetros. Respecto a los límites provenientes de los EWPO, hemos mejorado análisis previos usando todo el conjunto de observables electrodébiles en lugar de los parámetros oblícuos (S, T), dado que estos últimos solo son presentan una descripción fiable de los efectos del Higgs pesado en la región $m_H \sim m_h$.

Para ilustrar la detección de la producción directa del Higgs pesado, hemos elegido dos puntos de referencia compatibles con los límites actuales, en particular, con los datos del Higgs provenientes del LHC y de los EWPO. Hemos estudiado la producción resonante de pares de bosones de Higgs en el canal de desintegración $hh \to b\bar{b}\,WW \to b\bar{b}\ell^+\nu\ell^-\bar{\nu}$. El principal ruido de la señal es el proceso $t\bar{t}$ dileptónico. Además de aplicar una selección de cortes básicos, hemos aplicado cortes a la variable M_{T2} a los sistemas $2\ell + \not{E}_{\mathrm{T}}$ o $2b + 2\ell + \not{E}_{\mathrm{T}}$ para optimizar la significancia de la señal. Usando solamente el canal dileptónico, una significancia de $\sim 3\sigma$ para 3000 fb^{-1} puede ser alcanzada para el LHC funcionando a 14 TeV para una masa del Higgs pesado de $m_H = 400$ GeV si la mezcla es cercana al valor del límite actual y $\mathrm{BR}(H \to hh) \approx 1$. Una fracción de desintegración menos o un ángulo de mezcla más pequeño requeriría combinar varios canales de desintegración de pares de bosones de Higgs. La complementariedad entre los canales $H \to hh$ y $H \to ZZ$ es analizada para cualquier valor de $\mathrm{BR}(H \to hh)$.

También hemos comprobado que es posible extender el modelo incluyendo un candidato a MO. Con ello la próxima generación de experimentos de detección directa serán capaces de probar una región grande del espacio de parámetros del modelo.

En el Capítulo 4, hemos llevado a cabo un estudio de las características fenomenológicas del sector oculto en escenarios con portales de Stückelberg con bosones Z' que surgen como acciones efectivas a baja energía en ciertas compactificaciones de tipo II en cuerdas con branas intersecantes. Para nuestros propósitos, la propiedad crucial de estas construcciones es la extensión del grupo gauge del ME con varios bosones gauge abelianos ("anómalos") que adquieren masa y pueden mezclarse con bosones análogos del sector oculto.

Muchas propiedades fenomenológicamente interesantes de dichas construcciones están determinadas por las cargas del espectro del ME bajo los $U(1)$ extra del sector visible junto con un puñado de parámetros de mezcla (a, b, c, d). Las posibilidades de elección de dichas cargas es escaso debido a la necesaria identificación de estas simetrías con las simetrías globales aproximadas del ME. Nos hemos centrado en una estructura gauge en particular, los *modelos de Madrid* que surgen

en una gran cantidad de modelos con branas intersecantes. Otras configuraciones son también posibles, y pueden ser estudiadas análogamente. Creemos, sin embargo, que nuestro análisis cubre una porción significativa de todo el panorama de modelos semirealistas de branas.

Una vez que los bosones de los $U(1)$ extra visibles se mezclan con aquellos de los sectores ocultos, el bosón Z' más ligero en masa genera una interacción entre la MO y los fermiones del ME. Una característica remarcable de estos modelos es la aparición natural de patrones de violación de isospín en las interacciones de la MO, contrastando con otros portales simples considerados en la literatura. Hemos explorado las perspectivas para las cantidades f_n/f_p y a_n/a_p en seis puntos de referencia del espacio de parámetros en estas construcciones, incorporando límites provenientes del LHC y de LUX mostrando que en general los valores de estas fracciones tienden a estar dominados por la contribución de los neutrones. Así pues materiales con más sensibilidad a interacciones con neutrones son los más apropiados para estudiar estos escenarios.

De manera genérica, esta construcción nos provee de acoplos que violan isospin tanto en las interacciones que son independientes del espín como en las que son dependientes. Usando nuestra propia simulación del experimento LUX, hemos llevado a cabo una prueba de las regiones excluidas en cada punto usando el método de máximo hueco. Esto nos ha ayudado a analizar de manera consistente un escenario general con interacciones independientes y dependientes del espín (contribuciones del protón y del neutrón) así como en casos generales de violación de isospín en los acoplos de MO. Respecto al LHC, hemos calculado para cada punto del espacio de parámetros la sección eficaz de producción de un bosón Z' multiplicado por su fracción de desintegración de cada desintegración. Con esto, hemos incluido las búsquedas de resonancias en dos leptones (e^+e^- y $\mu^+\mu^-$) y dos jets del experimento ATLAS. De manera remarcable, todas las regiones que son válidas experimentalmente presentan una sección eficaz a neutrones mucho mayor que la de protones para las interacciones independientes del espín mientras que para el caso de las interacciones dependientes del espín el escenario está menos acotado.

Lo que se ha encontrado en este trabajo abre la puerta a escenarios genéricos en los cuales las señales en los experimentos de detección directa puedan estar dominados por los neutrones. Además, hemos mostrado que la complementariedad existente entre las búsquedas del LHC y los experimentos de detección directa de MO es especialmente relevante para desenmarañar los acoplos del bosón Z' a partículas del ME. Es gratificante ver cómo, no solo los resultados experimentales, sino las consecuencias fenomenólogicas y teóricas del modelo pueden ser combinadas en un solo marco para poder arrojar algo de luz sobre las posibles propiedades de la tan elusiva materia oscura.

Por otro lado, uno puede estudiar la fenomenología de la MO desde el punto de vista de un modelo motivado desde la teoría pudiendo resolver ciertos problemas patológicos que adolece el ME. Supersimetría (SUSY) es un candidato que reúne los requerimientos anteriores, puede contener la partícula de MO mientras que resuelve diferentes problemas como el problema de las jerarquías. Sin embargo, la versión fenomenológica viable de esto, el MSSM, está en tensión con los datos actuales provenientes del primer Run del LHC. En particular para poder alcanzar la masa del bosón de Higgs, $m_h \simeq 125$ GeV, éste requiere un afinamiento de los parámetros dentro del MSSM. Entonces se pueden considerar diferentes extensiones de este modelo minimal en las cuales aparecen nuevas contribuciones a la masa del Higgs a nivel árbol. Además, las nuevas extensiones proveen

predicciones diferentes en lo que a fenomenología de MO y colisionadores se refiere. En la Parte II estudiamos dos extensiones del sector de Higgs del MSSM en el superpotencial permitidas por invariancia gauge, la extensión singlete, nombrada NMSSM que a su vez extendemos con un supercampo neutrino dextrógiro, y la extensión triplete con hipercarga cero $Y = 0$, comúnmente llamada TMSSM. Ambas presentan una fenomenología de MO altamente ligada a las señales en el LHC

En el Capítulo 5 investigamos señales exóticas en colisionadores dentro de NMSSM con neutrinos y sneutrinos dextrógiros. Ésta es una construcción en la cual un extra supercampo singlete es añadido, N, al NMSSM para poder tener estados de neutrinos y sneutrinos dextrógiros. Después de que la ruptura de la simetría electrodébil tiene lugar, un término de masa Majorana se genera para los neutrinos dextrógiros que es del orden del valor esperado en el vacío del Higgs lo que implica un mecanismo de *see-saw* a escala electrodébil, con un acoplo Yukawa $y_N \sim 10^{-6}$ para la generación de masa de los neutrinos. Tal acoplo Yukawa pequeño hace que exista una pequeña mezcla entre los campos levógiros y dextrógiros. Por esta razón, el neutrino dextrógiro, una vez producido en el LHC, puede tener un tiempo de desintegración largo dando a su vez vértices desplazados.

Hemos incorporado cotas experimentales a las masas de las partículas supersimétricas al igual que a observables de baja energía. Además imponemos la presencia de un bosón de Higgs de aproximadamente una masa de 125.5 GeV y consideramos los resultados existentes de las señales del Higgs en las diferentes desintegraciones en partículas del ME ya que determinan una cota en desintegraciones no estándar o invisibles. También estudiamos el efecto de dichos límites al espacio de parámetros del modelo.

En la primera parte de este Capítulo hemos investigado la producción y posterior desintegración de neutrinos dextrógiros. Mostramos que, debido al pequeño acoplo Yukawa del neutrino, el neutrino dextrógiro puede desintegrarse en el detector interno de ATLAS o CMS, dando lugar a vértices desplazados. Esto puede ser observado a través de sus productos de desintegración, que involucran dos leptones ($2\ell + \not{E}_T$) o un leptón y dos jets (ℓjj). Hemos simulado la producción de neutrinos dextrógiros para un número representativo de puntos de referencia para la pasada configuración del LHC (con una energía de centro de masas de 8 TeV y una luminosidad integrada de $\mathcal{L} = 20$ fb^{-1}) y la actual para el estado de alta luminosidad (13 TeV and $\mathcal{L} = 100$ fb^{-1}) definiendo un número básico de cortes para aislar la señal. Hemos encontrado que algunos puntos del espacio de parámetros pueden ser ya probados con la configuración pasada del LHC y otro serán accesibles en el futuro cercano. Hemos construido además la distribución de la masa invariante de dos leptones ($m_{\ell\ell}$) y de dos jets y un leptón ($m_{\ell jj}$) para los diferentes puntos de referencia, mostrando que el punto final en la distribución de $m_{\ell\ell}$ y el pico en $m_{\ell jj}$ pueden dar información complementaria de la masa del neutrino dextrógiro ayudando con esto a distinguir este modelo de aquellos que presentan violación de la paridad R.

En la segunda parte de este Capítulo hemos considerado la posibilidad de que el stau es la partícula supersimétrica siguiente a la más ligera. En este caso hemos mostrado que la desintegración del stau está también suprimida por el pequeño acoplo Yukawa en ciertas regiones del espacio de parámetros. Para ello hemos simulado la producción de staus en la antigua configuración del LHC y en la actual para dos puntos de referencia. Los resultados sugieren que algunos puntos del espacio de parámetros pueden ser alcanzados en la futura configuración del LHC.

En el Capítulo 6 hemos considerado la fenomenología del Higgs de la extensión con un triplete

de hipercarga nula, $Y = 0$, del MSSM, llamado TMSSM, en el cual el nuevo acoplo entre el triplete y los Higgses del MSSM puede aliviar el pequeño problema de las jerarquías y además se modifican los sectores de charginos y neutralinos.

Primero se han determinado los acoplos y masas de los stops, charginos, neutralinos y del Higgs más ligero que es par bajo CP, h. Después se ha investigado los efectos del Triplino en los procesos inducidos por *loops* $h \to \gamma\gamma$ y $h \to Z\gamma$. Hemos demostrado que la componente adicional del Triplino en el sector de los charginos provee un aumento del 60% en la señal $R_{\gamma\gamma}$ que es un poco mayor que la estimada anteriormente (i.e. $R_{\gamma\gamma} \lesssim 1.45$) [103]. Para la señal $R_{Z\gamma}$ el factor de aumento puede llegar hasta el 40%, y se encuentra que está muy correlacionado con el canal de difotones, aunque siempre este factor es más pequeño que para $R_{\gamma\gamma}$. La región de parámetros que produce la mayor señal $R_{\gamma\gamma}$ y $R_{Z\gamma}$ viene dada por $\tan\beta \lesssim 2$ y $\mu \sim \mu_\Sigma \sim M_2 \sim 250\,\text{GeV}$, y en particular por charginos ligeros cercanos al límite de LEP. El aumento de dichas señales en el TMSSM es significativamente mayor que el que se puede conseguir en el MSSM ($\sim 20\%$ en $R_{\gamma\gamma}$) para el misma masa mínima del chargino [396]. Las medidas de estos procesos mejorarán en los siguientes años. De hecho se espera que el LHC pruebe la predicción de la desintegración $\Gamma(h \to Z\gamma)$ dentro del ME una vez que se hayan recogidos del orden de $\mathcal{O}(100\ \text{fb}^{-1})$ [403], y por tanto medir el acoplo efectivo $g_{h\gamma\gamma}$ con una precisión del 10% una vez que se alcance una luminosidad de 3000 fb^{-1} [404]. Con esa cantidad de datos futuros posiblemente la señal difotónica del Higgs puede converger a su valor dentro del ME, en cuyo caso si se observan desviaciones significativas en el canal $h \to Z\gamma$ sabemos que no son compatibles con el TMSSM. Sin embargo, si los datos exhiben una desviación positiva con respecto a lo esperado en el ME, habrá una indicación clara de física más allá del ME. Las predicciones anteriores junto con $R_{\gamma\gamma}$ y $R_{Z\gamma}$ podrían ser cruciales para descartar o bien proveer pistas del escenario aquí considerado.

Además de las desintegraciones del Higgs, hemos investigado la fenomenología de MO en el TMSSM, centrándonos en las repercusiones que juegan las componentes del triplete. De manera similar a lo que ocurre en el MSSM, la partícula más ligera es un candidato viable a MO en los polos del Higgs y del bosón Z y en el llamado régimen bien temperado. En las regiones del polo del Z y del Higgs están caracterizadas por una MO del tipo Bino y es insensible a la componente Triplino, dado que el único acoplo relevante es el siguiente: Higgs-Higgsino-Bino. No obstante, el neutralino bien temperado, donde la partícula más ligera es capaz de conseguir la densidad reliquia mediante la coaniquilación con el chargino más ligero, presenta un nuevo atractivo. Ciertamente, la componente Triplino de la partícula más ligera puede sustituir a la componente Wino del neutralino bien temperado y además puede resolver el problema de $M_1 \sim M_2$ que habría si consideramos modelos de gran unificación. Así pues el requerimiento para ser MO viene de la mano del límite de exclusión que impone el experimento LUX en la sección eficaz con núcleos independiente del spin. La contribución más importante es debido al intercambio del Higgs lo que impone un valor mínimo al parámetro μ. Esto tiene un gran impacto en las señales $R_{\gamma\gamma}$ y $R_{Z\gamma}$ el acoplo Higgs-chargino se ve reducido con lo que también se ver reducida la señal llegando a ser cómo máximo un 20%. Es importante notar que estos valores siguen siendo mayores que los que provienen del MSSM cuando se le aplican los límites de MO [396], es decir, cuando el la producción del Higgs es como la del ME.

El escenario aquí considerado ilustra de manera elegante la complementariedad de las búsquedas directas de MO con el LHC. Por ejemplo la próxima generación de experimentos de detección directa, como XENON1T, serán capaces de probar una región consistente del espacio de parámetros

del neutralino en el TMSSM. Además será capaz de poner cotas a la fracción de desintegración invisible del Higgs hasta un 1%, en una escala de tiempos comparable a la del LHC. En general el TMSSM está menos limitado por las presentes cotas del LHC de búsquedas supersimétricas. De hecho, la presencia del Triplino puede modificar los acoplos y los modos de desintegración. Esto ya ha sido observado en el caso de los stops en el TMSSM [405] incluso aunque todavía no hay una precisa estimación de sus actuales límites en la masa. Los datos actuales deberían afectar prioritariamente a la región de parámetros del chargino con un neutralino ligero y con pequeños desviaciones de $h \to Z\gamma$ y $h \to \gamma\gamma$. Con más datos se esperan límites más severos, en particular para masas de MO cercanas a las resonancias del Z o del Higgs. Por otro lado, para probar la región de coaniquilación, dado que el espectro de masas está comprimido, los datos provenientes del ILC y los análisis similares a los propuestos en Ref. [406] serán cruciales.

Es por tanto la razón de esta Tesis estudiar diferentes señales en colisionadores de modelos de MO, de tal manera que en el futuro podamos discriminar entre todos ellos. Experimentos específicos como detección directa e indirecta están especializados en búsqueda de MO, sin embargo los experimentos basados en colisionadores diseñados para otros propósitos pueden a su vez ayudar en la identificación de la naturaleza de la MO. De hecho, se están tomando muchos esfuerzos para mejorar las búsquedas en toda clase de experimentos para que todas las diferentes búsquedas puedan ser complementarias. Esperamos que en un futuro cercano los experimentos cerquen el espacio de parámetros de la MO (o incluso la encuentren) obteniendo así información sobre ella. Si esto ocurre la información proveniente de los colisionadores acerca de sus propiedades será crucial para extraer información relevante acerca de la naturaleza de la MO, como por ejemplo su masa, acoplos, etc. Vivimos tiempos emocionantes con experimentos mejorados y quizás con futuros experimentos que de manera segura arrojarán luz acerca de cómo es la Naturaleza.

Bibliography

[1] D. G. Cerdeño, V. Martín-Lozano, and O. Seto, *Displaced vertices and long-lived charged particles in the NMSSM with right-handed sneutrinos*, *JHEP* **05** (2014) 035, [arXiv:1311.7260].

[2] C. Arina, V. Martín-Lozano, and G. Nardini, *Dark matter versus $h \to \gamma\gamma$ and $h \to \gamma Z$ with supersymmetric triplets*, *JHEP* **08** (2014) 015, [arXiv:1403.6434].

[3] V. Martín-Lozano, J. M. Moreno, and C. B. Park, *Resonant Higgs boson pair production in the $hh \to b\bar{b}\, WW \to b\bar{b}\ell^+\nu\ell^-\overline{\nu}$ decay channel*, *JHEP* **08** (2015) 004, [arXiv:1501.03799].

[4] V. Martín-Lozano, M. Peiró, and P. Soler, *Isospin violating dark matter in Stückelberg portal scenarios*, *JHEP* **04** (2015) 175, [arXiv:1503.01780].

[5] L. E. Ibáñez and V. Martín-Lozano, *A Megaxion at 750 GeV as a First Hint of Low Scale String Theory*, arXiv:1512.08777.

[6] V. De Romeri, J. S. Kim, V. Martín-Lozano, K. Rolbiecki, and R. R. de Austri, *Confronting dark matter with the diphoton excess from a parent resonance decay*, *Eur. Phys. J.* **C76** (2016), no. 5 262, [arXiv:1603.04479].

[7] C. Arina, M. Chala, V. Martin-Lozano, and G. Nardini, *Confronting SUSY models with LHC data via electroweakino production*, arXiv:1610.03822.

[8] **ATLAS Collaboration** Collaboration, G. Aad et al., *Observation of a new particle in the search for the Standard Model Higgs boson with the ATLAS detector at the LHC*, *Phys.Lett.* **B716** (2012) 1–29, [arXiv:1207.7214].

[9] **CMS Collaboration** Collaboration, S. Chatrchyan et al., *Observation of a new boson at a mass of 125 GeV with the CMS experiment at the LHC*, *Phys.Lett.* **B716** (2012) 30–61, [arXiv:1207.7235].

[10] **Gfitter Group** Collaboration, M. Baak et al., *The global electroweak fit at NNLO and prospects for the LHC and ILC*, *Eur.Phys.J.* **C74** (2014), no. 9 3046, [arXiv:1407.3792].

[11] **ATLAS, CMS** Collaboration, G. Aad et al., *Combined Measurement of the Higgs Boson Mass in pp Collisions at $\sqrt{s} = 7$ and 8 TeV with the ATLAS and CMS Experiments*, *Phys. Rev. Lett.* **114** (2015) 191803, [arXiv:1503.07589].

[12] **ATLAS Collaboration** Collaboration, G. Aad et al., *Measurement of the Higgs boson mass from the $H \to \gamma\gamma$ and $H \to ZZ^* \to 4\ell$ channels with the ATLAS detector using 25 fb^{-1} of pp collision data*, *Phys.Rev.* **D90** (2014) 052004, [arXiv:1406.3827].

[13] **CMS** Collaboration, V. Khachatryan et al., *Precise determination of the mass of the Higgs boson and tests of compatibility of its couplings with the standard model predictions using proton collisions at 7 and 8 TeV*, *Eur. Phys. J.* **C75** (2015), no. 5 212, [arXiv:1412.8662].

[14] **ATLAS** Collaboration, T. A. collaboration, *Combined measurements of the Higgs boson production and decay rates in $H \to ZZ^* \to 4\ell$ and $H \to \gamma\gamma$ final states using pp collision data at $\sqrt{s} = 13$ TeV in the ATLAS experiment*, .

[15] **CMS** Collaboration, C. Collaboration, *Updated measurements of Higgs boson production in the diphoton decay channel at $\sqrt{s} = 13$ TeV in pp collisions at CMS.*, .

[16] **CMS** Collaboration, C. Collaboration, *Measurements of properties of the Higgs boson and search for an additional resonance in the four-lepton final state at sqrt(s) = 13 TeV*, .

[17] J. Elias-Miro, J. R. Espinosa, G. F. Giudice, G. Isidori, A. Riotto, and A. Strumia, *Higgs mass implications on the stability of the electroweak vacuum*, *Phys. Lett.* **B709** (2012) 222–228, [arXiv:1112.3022].

[18] G. Degrassi, S. Di Vita, J. Elias-Miro, J. R. Espinosa, G. F. Giudice, G. Isidori, and A. Strumia, *Higgs mass and vacuum stability in the Standard Model at NNLO*, *JHEP* **08** (2012) 098, [arXiv:1205.6497].

[19] D. Buttazzo, G. Degrassi, P. P. Giardino, G. F. Giudice, F. Sala, A. Salvio, and A. Strumia, *Investigating the near-criticality of the Higgs boson*, *JHEP* **12** (2013) 089, [arXiv:1307.3536].

[20] D. G. Cerdeno, *WIMPs: A brief bestiary*, in *Axions, WIMPs and WISPs. Proceedings, 4th Patras Workshop, PATRAS08, Hamburg, Germany, June 18-21, 2008*, pp. 9–12, 2009.

[21] S. Weinberg, *Baryon and Lepton Nonconserving Processes*, *Phys. Rev. Lett.* **43** (1979) 1566–1570.

[22] P. Minkowski, *$\mu \to e\gamma$ at a Rate of One Out of 10^9 Muon Decays?*, *Phys. Lett.* **B67** (1977) 421–428.

[23] T. Yanagida, *HORIZONTAL SYMMETRY AND MASSES OF NEUTRINOS*, *Conf. Proc.* **C7902131** (1979) 95–99.

[24] M. Gell-Mann, P. Ramond, and R. Slansky, *Complex Spinors and Unified Theories*, *Conf. Proc.* **C790927** (1979) 315–321, [arXiv:1306.4669].

[25] R. N. Mohapatra and G. Senjanovic, *Neutrino Mass and Spontaneous Parity Violation*, *Phys.Rev.Lett.* **44** (1980) 912.

[26] B. Patt and F. Wilczek, *Higgs-field portal into hidden sectors*, hep-ph/0605188.

[27] D. Feldman, Z. Liu, and P. Nath, *The Stueckelberg Z-prime Extension with Kinetic Mixing and Milli-Charged Dark Matter From the Hidden Sector*, *Phys.Rev.* **D75** (2007) 115001, [hep-ph/0702123].

[28] A. Falkowski, J. Juknevich, and J. Shelton, *Dark Matter Through the Neutrino Portal*, arXiv:0908.1790.

[29] B. Batell, M. Pospelov, and A. Ritz, *Exploring Portals to a Hidden Sector Through Fixed Targets*, *Phys.Rev.* **D80** (2009) 095024, [arXiv:0906.5614].

[30] P. Crivelli, A. Belov, U. Gendotti, S. Gninenko, and A. Rubbia, *Positronium Portal into Hidden Sector: A new Experiment to Search for Mirror Dark Matter*, *JINST* **5** (2010) P08001, [arXiv:1005.4802].

[31] X. Chu, T. Hambye, and M. H. Tytgat, *The Four Basic Ways of Creating Dark Matter Through a Portal*, *JCAP* **1205** (2012) 034, [arXiv:1112.0493].

[32] R. Essig, J. A. Jaros, W. Wester, P. H. Adrian, S. Andreas, et al., *Working Group Report: New Light Weakly Coupled Particles*, arXiv:1311.0029.

[33] W.-Z. Feng, G. Shiu, P. Soler, and F. Ye, *Building a Stückelberg portal*, *JHEP* **1405** (2014) 065, [arXiv:1401.5890].

[34] W.-Z. Feng, G. Shiu, P. Soler, and F. Ye, *Probing Hidden Sectors with Stückelberg U(1) Gauge Fields*, *Phys.Rev.Lett.* **113** (2014) 061802, [arXiv:1401.5880].

[35] R. Foot and S. Vagnozzi, *Dissipative hidden sector dark matter*, *Phys.Rev.* **D91** (2015), no. 2 023512, [arXiv:1409.7174].

[36] Y. Bai and J. Berger, *Lepton Portal Dark Matter*, *JHEP* **1408** (2014) 153, [arXiv:1402.6696].

[37] S. Baek, P. Ko, and W.-I. Park, *Hidden sector monopole, vector dark matter and dark radiation with Higgs portal*, *JCAP* **1410** (2014), no. 10 067, [arXiv:1311.1035].

[38] K. Blum, M. Cliche, C. Csaki, and S. J. Lee, *WIMP Dark Matter through the Dilaton Portal*, arXiv:1410.1873.

[39] J. F. Cherry, A. Friedland, and I. M. Shoemaker, *Neutrino Portal Dark Matter: From Dwarf Galaxies to IceCube*, arXiv:1411.1071.

[40] G. Arcadi, Y. Mambrini, and F. Richard, *Z-portal dark matter*, arXiv:1411.2985.

[41] L. Bian, T. Li, J. Shu, and X.-C. Wang, *Two component dark matter with multi-Higgs portals*, arXiv:1412.5443.

[42] A. Djouadi, O. Lebedev, Y. Mambrini, and J. Quevillon, *Implications of LHC searches for Higgs–portal dark matter*, *Phys.Lett.* **B709** (2012) 65–69, [arXiv:1112.3299].

[43] A. Djouadi, A. Falkowski, Y. Mambrini, and J. Quevillon, *Direct Detection of Higgs-Portal Dark Matter at the LHC*, *Eur.Phys.J.* **C73** (2013), no. 6 2455, [arXiv:1205.3169].

[44] M. Escudero, A. Berlin, D. Hooper, and M.-X. Lin, *Toward (Finally!) Ruling Out Z and Higgs Mediated Dark Matter Models*, arXiv:1609.09079.

[45] Y. G. Kim, K. Y. Lee, and S. Shin, *Singlet fermionic dark matter*, *JHEP* **0805** (2008) 100, [arXiv:0803.2932].

[46] L. Lopez-Honorez, T. Schwetz, and J. Zupan, *Higgs portal, fermionic dark matter, and a Standard Model like Higgs at 125 GeV*, *Phys.Lett.* **B716** (2012) 179–185, [arXiv:1203.2064].

[47] S. Baek, P. Ko, W.-I. Park, and E. Senaha, *Vacuum structure and stability of a singlet fermion dark matter model with a singlet scalar messenger*, *JHEP* **1211** (2012) 116, [arXiv:1209.4163].

[48] M. Fairbairn and R. Hogan, *Singlet Fermionic Dark Matter and the Electroweak Phase Transition*, *JHEP* **1309** (2013) 022, [arXiv:1305.3452].

[49] P. Langacker, *The Physics of Heavy Z' Gauge Bosons*, *Rev.Mod.Phys.* **81** (2009) 1199–1228, [arXiv:0801.1345].

[50] E. Dudas, Y. Mambrini, S. Pokorski, and A. Romagnoni, *(In)visible Z-prime and dark matter*, *JHEP* **0908** (2009) 014, [arXiv:0904.1745].

[51] S. Cassel, D. Ghilencea, and G. Ross, *Electroweak and Dark Matter Constraints on a Z-prime in Models with a Hidden Valley*, *Nucl.Phys.* **B827** (2010) 256–280, [arXiv:0903.1118].

[52] M. T. Frandsen, F. Kahlhoefer, S. Sarkar, and K. Schmidt-Hoberg, *Direct detection of dark matter in models with a light Z'*, *JHEP* **1109** (2011) 128, [arXiv:1107.2118].

[53] V. Barger, D. Marfatia, and A. Peterson, *LHC and dark matter signals of Z' bosons*, *Phys.Rev.* **D87** (2013), no. 1 015026, [arXiv:1206.6649].

[54] G. Arcadi, Y. Mambrini, M. H. G. Tytgat, and B. Zaldivar, *Invisible Z' and dark matter: LHC vs LUX constraints*, *JHEP* **1403** (2014) 134, [arXiv:1401.0221].

[55] A. Alves, S. Profumo, and F. S. Queiroz, *The dark $Z^{'}$ portal: direct, indirect and collider searches*, *JHEP* **1404** (2014) 063, [arXiv:1312.5281].

[56] A. Alves, A. Berlin, S. Profumo, and F. S. Queiroz, *Dark Matter Complementarity and the Z' Portal*, arXiv:1501.03490.

[57] D. Lopez-Val and T. Robens, *Delta r and the W-boson mass in the Singlet Extension of the Standard Model*, *Phys.Rev.* **D90** (2014) 114018, [arXiv:1406.1043].

[58] T. Robens and T. Stefaniak, *Status of the Higgs Singlet Extension of the Standard Model after LHC Run 1*, arXiv:1501.02234.

[59] A. Falkowski, C. Gross, and O. Lebedev, *A second Higgs from the Higgs portal*, *JHEP* **05** (2015) 057, [arXiv:1502.01361].

[60] B. Cooper, N. Konstantinidis, L. Lambourne, and D. Wardrope, *Boosted $hh \to b\bar{b}b\bar{b}$: a new topology in searches for TeV-scale resonances at the LHC*, *Phys.Rev.* **D88** (2013) 114005, [arXiv:1307.0407].

[61] D. E. Ferreira de Lima, A. Papaefstathiou, and M. Spannowsky, *Standard model Higgs boson pair production in the ($b\bar{b}$)($b\bar{b}$) final state*, *JHEP* **1408** (2014) 030, [arXiv:1404.7139].

[62] N. Chen, C. Du, Y. Fang, and L.-C. Lü, *LHC Searches for The Heavy Higgs Boson via Two B Jets plus Diphoton*, *Phys.Rev.* **D89** (2014), no. 11 115006, [arXiv:1312.7212].

[63] V. Barger, L. L. Everett, C. Jackson, A. Peterson, and G. Shaughnessy, *New physics in resonant production of Higgs boson pairs*, *Phys.Rev.Lett.* **114** (2015) 011801, [arXiv:1408.0003].

[64] V. Barger, L. L. Everett, C. B. Jackson, A. D. Peterson, and G. Shaughnessy, *Measuring the 2HDM Scalar Potential at LHC14*, *Phys.Rev.* **D90** (2014) 095006, [arXiv:1408.2525].

[65] J. M. No and M. Ramsey-Musolf, *Probing the Higgs Portal at the LHC Through Resonant di-Higgs Production*, arXiv:1310.6035.

[66] L. E. Ibanez and A. M. Uranga, *String theory and particle physics: An introduction to string phenomenology*, .

[67] **Super-Kamiokande** Collaboration, C. Regis et al., *Search for Proton Decay via $p- > \mu^+ K^0$ in Super-Kamiokande I, II, and III*, *Phys. Rev.* **D86** (2012) 012006, [arXiv:1205.6538].

[68] H. Goldberg, *Constraint on the Photino Mass from Cosmology*, *Phys. Rev. Lett.* **50** (1983) 1419. [Erratum: Phys. Rev. Lett.103,099905(2009)].

[69] J. R. Ellis, J. S. Hagelin, D. V. Nanopoulos, and M. Srednicki, *Search for Supersymmetry at the anti-p p Collider*, *Phys. Lett.* **B127** (1983) 233–241.

[70] J. R. Ellis, J. S. Hagelin, D. V. Nanopoulos, K. A. Olive, and M. Srednicki, *Supersymmetric Relics from the Big Bang*, *Nucl. Phys.* **B238** (1984) 453–476.

[71] L. M. Krauss, *New Constraints on Ino Masses from Cosmology. 1. Supersymmetric Inos*, *Nucl. Phys.* **B227** (1983) 556–569.

[72] L. E. Ibanez, *The Scalar Neutrinos as the Lightest Supersymmetric Particles and Cosmology*, *Phys. Lett.* **B137** (1984) 160–164.

[73] J. S. Hagelin, G. L. Kane, and S. Raby, *Perhaps Scalar Neutrinos Are the Lightest Supersymmetric Partners*, *Nucl. Phys.* **B241** (1984) 638–652.

[74] G. Jungman, M. Kamionkowski, and K. Griest, *Supersymmetric dark matter*, *Phys. Rept.* **267** (1996) 195–373, [hep-ph/9506380].

[75] D. G. Cerdeno, C. Hugonie, D. E. Lopez-Fogliani, C. Munoz, and A. M. Teixeira, *Theoretical predictions for the direct detection of neutralino dark matter in the NMSSM*, *JHEP* **12** (2004) 048, [hep-ph/0408102].

[76] D. G. Cerdeno, E. Gabrielli, D. E. Lopez-Fogliani, C. Munoz, and A. M. Teixeira, *Phenomenological viability of neutralino dark matter in the NMSSM*, *JCAP* **0706** (2007) 008, [hep-ph/0701271].

[77] C. Hugonie, G. Belanger, and A. Pukhov, *Dark matter in the constrained NMSSM*, *JCAP* **0711** (2007) 009, [arXiv:0707.0628].

[78] A. Djouadi, U. Ellwanger, and A. M. Teixeira, *Phenomenology of the constrained NMSSM*, *JHEP* **04** (2009) 031, [arXiv:0811.2699].

[79] T. Falk, K. A. Olive, and M. Srednicki, *Heavy sneutrinos as dark matter*, *Phys. Lett.* **B339** (1994) 248–251, [hep-ph/9409270].

[80] K. Inoue, A. Kakuto, H. Komatsu, and S. Takeshita, *Low-Energy Parameters and Particle Masses in a Supersymmetric Grand Unified Model*, *Prog. Theor. Phys.* **67** (1982) 1889.

[81] R. A. Flores and M. Sher, *Higgs Masses in the Standard, Multi-Higgs and Supersymmetric Models*, *Annals Phys.* **148** (1983) 95.

[82] A. Arbey, M. Battaglia, A. Djouadi, F. Mahmoudi, and J. Quevillon, *Implications of a 125 GeV Higgs for supersymmetric models*, *Phys.Lett.* **B708** (2012) 162–169, [arXiv:1112.3028].

[83] M. Carena, S. Gori, N. R. Shah, and C. E. Wagner, *A 125 GeV SM-like Higgs in the MSSM and the $\gamma\gamma$ rate*, *JHEP* **1203** (2012) 014, [arXiv:1112.3336].

[84] Z. Kang, T. Li, J. Li, and Y. Liu, *A Rediatively Light Stop Saves the Best Global Fit for Higgs Boson Mass and Decays*, arXiv:1208.2673.

[85] J. Fan and M. Reece, *A New Look at Higgs Constraints on Stops*, arXiv:1401.7671.

[86] H. P. Nilles, M. Srednicki, and D. Wyler, *Weak Interaction Breakdown Induced by Supergravity*, *Phys. Lett.* **B120** (1983) 346.

[87] J. R. Ellis, J. F. Gunion, H. E. Haber, L. Roszkowski, and F. Zwirner, *Higgs Bosons in a Nonminimal Supersymmetric Model*, *Phys. Rev.* **D39** (1989) 844.

[88] M. Drees, *Supersymmetric Models with Extended Higgs Sector*, *Int. J. Mod. Phys.* **A4** (1989) 3635.

[89] J. E. Kim and H. P. Nilles, *The mu Problem and the Strong CP Problem*, *Phys. Lett.* **B138** (1984) 150.

[90] U. Ellwanger, C. Hugonie, and A. M. Teixeira, *The Next-to-Minimal Supersymmetric Standard Model*, *Phys.Rept.* **496** (2010) 1–77, [arXiv:0910.1785].

[91] F. Franke and H. Fraas, *Neutralinos and Higgs bosons in the next-to-minimal supersymmetric standard model*, *Int. J. Mod. Phys.* **A12** (1997) 479–534, [hep-ph/9512366].

[92] A. Djouadi et al., *Benchmark scenarios for the NMSSM*, *JHEP* **07** (2008) 002, [arXiv:0801.4321].

[93] B. Garbrecht, C. Pallis, and A. Pilaftsis, *Anatomy of F(D)-Term Hybrid Inflation*, *JHEP* **12** (2006) 038, [hep-ph/0605264].

[94] D. G. Cerdeno, C. Munoz, and O. Seto, *Right-handed sneutrino as thermal dark matter*, *Phys. Rev.* **D79** (2009) 023510, [arXiv:0807.3029].

[95] F. Deppisch and A. Pilaftsis, *Thermal Right-Handed Sneutrino Dark Matter in the F(D)-Term Model of Hybrid Inflation*, *JHEP* **10** (2008) 080, [arXiv:0808.0490].

[96] D. G. Cerdeno and O. Seto, *Right-handed sneutrino dark matter in the NMSSM*, *JCAP* **0908** (2009) 032, [arXiv:0903.4677].

[97] D. G. Cerdeno, J.-H. Huh, M. Peiro, and O. Seto, *Very light right-handed sneutrino dark matter in the NMSSM*, *JCAP* **1111** (2011) 027, [arXiv:1108.0978].

[98] D. G. Cerdeño, M. Peiró, and S. Robles, *Low-mass right-handed sneutrino dark matter: SuperCDMS and LUX constraints and the Galactic Centre gamma-ray excess*, *JCAP* **1408** (2014) 005, [arXiv:1404.2572].

[99] D. G. Cerdeno, M. Peiro, and S. Robles, *Fits to the Fermi-LAT GeV excess with RH sneutrino dark matter: implications for direct and indirect dark matter searches and the LHC*, *Phys. Rev.* **D91** (2015), no. 12 123530, [arXiv:1501.01296].

[100] D. G. Cerdeno, M. Peiro, and S. Robles, *Enhanced lines and box-shaped features in the gamma-ray spectrum from annihilating dark matter in the NMSSM*, *JCAP* **1604** (2016), no. 04 011, [arXiv:1507.08974].

[101] J. Espinosa and M. Quiros, *Higgs triplets in the supersymmetric standard model*, *Nucl.Phys.* **B384** (1992) 113–146.

[102] S. Di Chiara and K. Hsieh, *Triplet Extended Supersymmetric Standard Model*, *Phys.Rev.* **D78** (2008) 055016, [arXiv:0805.2623].

[103] A. Delgado, G. Nardini, and M. Quiros, *Large diphoton Higgs rates from supersymmetric triplets*, *Phys.Rev.* **D86** (2012) 115010, [arXiv:1207.6596].

[104] A. Delgado, G. Nardini, and M. Quiros, *A Light Supersymmetric Higgs Sector Hidden by a Standard Model-like Higgs*, *JHEP* **1307** (2013) 054, [arXiv:1303.0800].

[105] N. Arkani-Hamed, A. Delgado, and G. Giudice, *The Well-tempered neutralino*, *Nucl.Phys.* **B741** (2006) 108–130, [hep-ph/0601041].

[106] F. Zwicky, *Die Rotwerschiebung von extragalaktischen Nebeln*, *Helv. Phys. Acta* **6** (1930) 110–127.

[107] V. Rubin, J. Ford, and W. Kent, *Rotation of the Andromeda Nebula from a Spectroscopic Survey of Emission Regions*, *Astrophys. J* **159** (1970) 379.

[108] M. W. Goodman and E. Witten, *Detectability of Certain Dark Matter Candidates*, *Phys. Rev.* **D31** (1985) 3059.

[109] A. van Albada, J. Bahcall, K. Begeman, and R. Sancisi, *The Distribution of Dark Matter in the Spiral Galaxy NGC.3198*, *Astrophys. J* **295** (1985) 305.

[110] K. Begeman, A. Broeils, and R. Sanders, *Extended rotation curves of spiral galaxies: Dark haloes and modified dynamics*, *Mon. Not. Roy. Astron. Soc* **249** (1991) 523.

[111] D. Clowe, M. Bradac, A. H. Gonzalez, M. Markevitch, S. W. Randall, C. Jones, and D. Zaritsky, *A direct empirical proof of the existence of dark matter*, *Astrophys. J.* **648** (2006) L109–L113, [astro-ph/0608407].

[112] J. Bekenstein and M. Milgrom, *Does the missing mass problem signal the breakdown of Newtonian gravity?*, *Astrophys. J.* **286** (1984) 7–14.

[113] F. Zwicky, *On the masses of nebulae and clusters of nebulae*, *Astrophys. J.* **86** (1937) 217.

[114] A. N. Taylor, S. Dye, T. J. Broadhurst, N. Benitez, and E. van Kampen, *Gravitational lens magnification and the mass of abell 1689*, *Astrophys. J.* **501** (1998) 539, [astro-ph/9801158].

[115] D. Clowe, A. Gonzalez, and M. Markevitch, *Weak lensing mass reconstruction of the interacting cluster 1E0657-558: Direct evidence for the existence of dark matter*, *Astrophys. J.* **604** (2004) 596–603, [astro-ph/0312273].

[116] J. Hughes and Y. Tanaka, *The X-Ray Spectrum of Abell 665*, *Astrophys. J.* **62** (1992) 398.

[117] *http://www.esa.int/spaceinimages/Images/2013/03/Planck_CMB*, .

[118] **Planck** Collaboration, P. A. R. Ade et al., *Planck 2013 results. XVI. Cosmological parameters*, *Astron. Astrophys.* **571** (2014) A16, [arXiv:1303.5076].

[119] A. Dar, *Dark matter and big bang nucleosynthesis*, *Astrophys. J.* **449** (1995) 550, [astro-ph/9504082]. [,21(1995)].

[120] A. A. Klypin, A. V. Kravtsov, O. Valenzuela, and F. Prada, *Where are the missing Galactic satellites?*, *Astrophys. J.* **522** (1999) 82–92, [astro-ph/9901240].

[121] M. R. Lovell, C. S. Frenk, V. R. Eke, A. Jenkins, L. Gao, and T. Theuns, *The properties of warm dark matter haloes*, *Mon. Not. Roy. Astron. Soc.* **439** (2014) 300–317, [arXiv:1308.1399].

[122] **SuperCDMS** Collaboration, R. Agnese et al., *New Results from the Search for Low-Mass Weakly Interacting Massive Particles with the CDMS Low Ionization Threshold Experiment*, *Phys. Rev. Lett.* **116** (2016), no. 7 071301, [arXiv:1509.02448].

[123] **SuperCDMS** Collaboration, R. Agnese et al., *Search for Low-Mass Weakly Interacting Massive Particles with SuperCDMS*, *Phys. Rev. Lett.* **112** (2014), no. 24 241302, [arXiv:1402.7137].

[124] **CRESST** Collaboration, G. Angloher et al., *Results on light dark matter particles with a low-threshold CRESST-II detector*, *Eur. Phys. J.* **C76** (2016), no. 1 25, [arXiv:1509.01515].

[125] D. S. Akerib et al., *Results from a search for dark matter in LUX with 332 live days of exposure*, arXiv:1608.07648.

[126] **PandaX-II** Collaboration, A. Tan et al., *Dark Matter Results from First 98.7-day Data of PandaX-II Experiment*, *Phys. Rev. Lett.* **117** (2016) 121303, [arXiv:1607.07400].

[127] **XENON1T** Collaboration, E. Aprile, *The XENON1T Dark Matter Search Experiment*, *Springer Proc. Phys.* **148** (2013) 93–96, [arXiv:1206.6288].

[128] **LZ** Collaboration, D. S. Akerib et al., *LUX-ZEPLIN (LZ) Conceptual Design Report*, arXiv:1509.02910.

[129] **SuperCDMS** Collaboration, R. Agnese et al., *Projected Sensitivity of the SuperCDMS SNOLAB experiment*, *Submitted to: Phys. Rev. D* (2016) [arXiv:1610.00006].

[130] J. Billard, L. Strigari, and E. Figueroa-Feliciano, *Implication of neutrino backgrounds on the reach of next generation dark matter direct detection experiments*, *Phys. Rev.* **D89** (2014), no. 2 023524, [arXiv:1307.5458].

[131] D. G. Cerdeno and A. M. Green, *Direct detection of WIMPs*, arXiv:1002.1912.

[132] J. L. Feng, J. Kumar, D. Marfatia, and D. Sanford, *Isospin-Violating Dark Matter*, *Phys.Lett.* **B703** (2011) 124–127, [arXiv:1102.4331].

[133] X. Gao, Z. Kang, and T. Li, *Origins of the Isospin Violation of Dark Matter Interactions*, *JCAP* **1301** (2013) 021, [arXiv:1107.3529].

[134] G. Bélanger, A. Goudelis, J.-C. Park, and A. Pukhov, *Isospin-violating dark matter from a double portal*, *JCAP* **1402** (2014) 020, [arXiv:1311.0022].

[135] K. Hamaguchi, S. P. Liew, T. Moroi, and Y. Yamamoto, *Isospin-Violating Dark Matter with Colored Mediators*, *JHEP* **1405** (2014) 086, [arXiv:1403.0324].

[136] **Fermi-LAT** Collaboration, M. Ackermann et al., *Searching for Dark Matter Annihilation from Milky Way Dwarf Spheroidal Galaxies with Six Years of Fermi Large Area Telescope Data*, *Phys. Rev. Lett.* **115** (2015), no. 23 231301, [arXiv:1503.02641].

[137] **Fermi-LAT** Collaboration, M. Ackermann et al., *Search for gamma-ray spectral lines with the Fermi large area telescope and dark matter implications*, *Phys. Rev.* **D88** (2013) 082002, [arXiv:1305.5597].

[138] **AMS 01** Collaboration, M. Aguilar et al., *Cosmic-ray positron fraction measurement from 1 to 30-GeV with AMS-01*, *Phys. Lett.* **B646** (2007) 145–154, [astro-ph/0703154].

[139] **PAMELA** Collaboration, O. Adriani et al., *An anomalous positron abundance in cosmic rays with energies 1.5-100 GeV*, *Nature* **458** (2009) 607–609, [arXiv:0810.4995].

[140] **AMS** Collaboration, M. Aguilar et al., *First Result from the Alpha Magnetic Spectrometer on the International Space Station: Precision Measurement of the Positron Fraction in Primary Cosmic Rays of 0.5–350 GeV*, *Phys. Rev. Lett.* **110** (2013) 141102.

[141] D. Hooper, P. Blasi, and P. D. Serpico, *Pulsars as the Sources of High Energy Cosmic Ray Positrons*, *JCAP* **0901** (2009) 025, [arXiv:0810.1527].

[142] G. Bertone, M. Cirelli, A. Strumia, and M. Taoso, *Gamma-ray and radio tests of the e+e- excess from DM annihilations*, *JCAP* **0903** (2009) 009, [arXiv:0811.3744].

[143] S. Galli, F. Iocco, G. Bertone, and A. Melchiorri, *CMB constraints on Dark Matter models with large annihilation cross-section*, *Phys. Rev.* **D80** (2009) 023505, [arXiv:0905.0003].

[144] T. R. Slatyer, N. Padmanabhan, and D. P. Finkbeiner, *CMB Constraints on WIMP Annihilation: Energy Absorption During the Recombination Epoch*, *Phys. Rev.* **D80** (2009) 043526, [arXiv:0906.1197].

[145] **Fermi-LAT** Collaboration, M. Ackermann et al., *Measurement of separate cosmic-ray electron and positron spectra with the Fermi Large Area Telescope*, *Phys. Rev. Lett.* **108** (2012) 011103, [arXiv:1109.0521].

[146] **IceCube** Collaboration, M. G. Aartsen et al., *Search for dark matter annihilations in the Sun with the 79-string IceCube detector*, *Phys. Rev. Lett.* **110** (2013), no. 13 131302, [arXiv:1212.4097].

[147] **ANTARES** Collaboration, S. Adrian-Martinez et al., *First results on dark matter annihilation in the Sun using the ANTARES neutrino telescope*, *JCAP* **1311** (2013) 032, [arXiv:1302.6516].

[148] **ATLAS** Collaboration, G. Aad et al., *Search for new phenomena in final states with an energetic jet and large missing transverse momentum in pp collisions at $\sqrt{s}$ =8 TeV with the ATLAS detector*, *Eur. Phys. J.* **C75** (2015), no. 7 299, [arXiv:1502.01518]. [Erratum: Eur. Phys. J.C75,no.9,408(2015)].

[149] **CMS** Collaboration, V. Khachatryan et al., *Search for dark matter, extra dimensions, and unparticles in monojet events in proton–proton collisions at $\sqrt{s} = 8$ TeV*, *Eur. Phys. J.* **C75** (2015), no. 5 235, [arXiv:1408.3583].

[150] **ATLAS** Collaboration, G. Aad et al., *Search for new phenomena in events with a photon and missing transverse momentum in pp collisions at $\sqrt{s} = 8$ TeV with the ATLAS detector*, *Phys. Rev.* **D91** (2015), no. 1 012008, [arXiv:1411.1559]. [Erratum: Phys. Rev.D92,no.5,059903(2015)].

[151] **CMS** Collaboration, V. Khachatryan et al., *Search for new phenomena in monophoton final states in proton-proton collisions at $\sqrt{s} = 8$ TeV*, *Phys. Lett.* **B755** (2016) 102–124, [arXiv:1410.8812].

[152] **ATLAS** Collaboration, G. Aad et al., *Search for new particles in events with one lepton and missing transverse momentum in pp collisions at $\sqrt{s} = 8$ TeV with the ATLAS detector*, *JHEP* **09** (2014) 037, [arXiv:1407.7494].

[153] **ATLAS** Collaboration, G. Aad et al., *Search for Dark Matter in Events with Missing Transverse Momentum and a Higgs Boson Decaying to Two Photons in pp Collisions at $\sqrt{s} = 8$ TeV with the ATLAS Detector*, *Phys. Rev. Lett.* **115** (2015), no. 13 131801, [arXiv:1506.01081].

[154] **ATLAS** Collaboration, G. Aad et al., *Search for dark matter produced in association with a Higgs boson decaying to two bottom quarks in pp collisions at $\sqrt{s} = 8$ TeV with the ATLAS detector*, *Phys. Rev.* **D93** (2016), no. 7 072007, [arXiv:1510.06218].

[155] *Search for Dark Matter in association with a Higgs boson decaying to b-quarks in pp collisions at $\sqrt{s} = 13$ TeV with the ATLAS detector*, Tech. Rep. ATLAS-CONF-2016-019, CERN, Geneva, Mar, 2016.

[156] *Search for dark matter produced in association with a hadronically decaying vector boson in pp collisions at $\sqrt{s} = 13$ TeV with the ATLAS detector at the LHC*, Tech. Rep. ATLAS-CONF-2015-080, CERN, Geneva, Dec, 2015.

[157] **CMS** Collaboration, V. Khachatryan et al., *Search for physics beyond the standard model in final states with a lepton and missing transverse energy in proton-proton collisions at sqrt(s) = 8 TeV*, *Phys. Rev.* **D91** (2015), no. 9 092005, [arXiv:1408.2745].

[158] **CMS Collaboration** Collaboration, *Search for dark matter production in association with jets, or hadronically decaying W or Z boson at $\sqrt{s} = 13$ TeV*, Tech. Rep. CMS-PAS-EXO-16-013, CERN, Geneva, 2016.

[159] **CMS Collaboration** Collaboration, *Search for Dark Matter produced in association with bottom quarks*, Tech. Rep. CMS-PAS-B2G-15-007, CERN, Geneva, 2016.

[160] D. Abercrombie et al., *Dark Matter Benchmark Models for Early LHC Run-2 Searches: Report of the ATLAS/CMS Dark Matter Forum*, arXiv:1507.00966.

[161] O. Buchmueller, M. J. Dolan, and C. McCabe, *Beyond Effective Field Theory for Dark Matter Searches at the LHC*, *JHEP* **01** (2014) 025, [arXiv:1308.6799].

[162] G. Busoni et al., *Recommendations on presenting LHC searches for missing transverse energy signals using simplified s-channel models of dark matter*, arXiv:1603.04156.

[163] A. De Simone and T. Jacques, *Simplified models vs. effective field theory approaches in dark matter searches*, *Eur. Phys. J.* **C76** (2016), no. 7 367, [arXiv:1603.08002].

[164] C. Englert, M. McCullough, and M. Spannowsky, *S-Channel Dark Matter Simplified Models and Unitarity*, arXiv:1604.07975.

[165] A. Hill and J. van der Bij, *Strongly interacting singlet-doublet Higgs model*, *Phys.Rev.* **D36** (1987) 3463–3473.

[166] M. Veltman and F. Yndurain, *Radiative corrections to W W scattering*, *Nucl.Phys.* **B325** (1989) 1.

[167] T. Binoth and J. van der Bij, *Influence of strongly coupled, hidden scalars on Higgs signals*, *Z.Phys.* **C75** (1997) 17–25, [hep-ph/9608245].

[168] R. Schabinger and J. D. Wells, *A Minimal spontaneously broken hidden sector and its impact on Higgs boson physics at the large hadron collider*, *Phys.Rev.* **D72** (2005) 093007, [hep-ph/0509209].

[169] G. Bhattacharyya, G. C. Branco, and S. Nandi, *Universal Doublet-Singlet Higgs Couplings and phenomenology at the CERN Large Hadron Collider*, *Phys.Rev.* **D77** (2008) 117701, [arXiv:0712.2693].

[170] M. Bowen, Y. Cui, and J. D. Wells, *Narrow trans-TeV Higgs bosons and $H \to hh$ decays: Two LHC search paths for a hidden sector Higgs boson*, *JHEP* **0703** (2007) 036, [hep-ph/0701035].

[171] V. Barger, P. Langacker, M. McCaskey, M. J. Ramsey-Musolf, and G. Shaughnessy, *LHC Phenomenology of an Extended Standard Model with a Real Scalar Singlet*, *Phys.Rev.* **D77** (2008) 035005, [arXiv:0706.4311].

[172] V. Barger, P. Langacker, M. McCaskey, M. Ramsey-Musolf, and G. Shaughnessy, *Complex Singlet Extension of the Standard Model*, *Phys.Rev.* **D79** (2009) 015018, [arXiv:0811.0393].

[173] S. Dawson and W. Yan, *Hiding the Higgs Boson with Multiple Scalars*, *Phys.Rev.* **D79** (2009) 095002, [arXiv:0904.2005].

[174] S. Bock, R. Lafaye, T. Plehn, M. Rauch, D. Zerwas, et al., *Measuring Hidden Higgs and Strongly-Interacting Higgs Scenarios*, *Phys.Lett.* **B694** (2010) 44–53, [arXiv:1007.2645].

[175] S. Baek, P. Ko, and W.-I. Park, *Search for the Higgs portal to a singlet fermionic dark matter at the LHC*, *JHEP* **1202** (2012) 047, [arXiv:1112.1847].

[176] P. J. Fox, D. Tucker-Smith, and N. Weiner, *Higgs friends and counterfeits at hadron colliders*, *JHEP* **1106** (2011) 127, [arXiv:1104.5450].

[177] C. Englert, T. Plehn, D. Zerwas, and P. M. Zerwas, *Exploring the Higgs portal*, *Phys.Lett.* **B703** (2011) 298–305, [arXiv:1106.3097].

[178] C. Englert, J. Jaeckel, E. Re, and M. Spannowsky, *Evasive Higgs Maneuvers at the LHC*, *Phys.Rev.* **D85** (2012) 035008, [arXiv:1111.1719].

[179] B. Batell, S. Gori, and L.-T. Wang, *Exploring the Higgs Portal with 10/fb at the LHC*, *JHEP* **1206** (2012) 172, [arXiv:1112.5180].

[180] C. Englert, T. Plehn, M. Rauch, D. Zerwas, and P. M. Zerwas, *LHC: Standard Higgs and Hidden Higgs*, *Phys.Lett.* **B707** (2012) 512–516, [arXiv:1112.3007].

[181] R. S. Gupta and J. D. Wells, *Higgs boson search significance deformations due to mixed-in scalars*, *Phys.Lett.* **B710** (2012) 154–158, [arXiv:1110.0824].

[182] D. Bertolini and M. McCullough, *The Social Higgs*, *JHEP* **1212** (2012) 118, [arXiv:1207.4209].

[183] M. J. Dolan, C. Englert, and M. Spannowsky, *New Physics in LHC Higgs boson pair production*, *Phys.Rev.* **D87** (2013), no. 5 055002, [arXiv:1210.8166].

[184] B. Batell, D. McKeen, and M. Pospelov, *Singlet Neighbors of the Higgs Boson*, *JHEP* **1210** (2012) 104, [arXiv:1207.6252].

[185] G. M. Pruna and T. Robens, *The Higgs Singlet extension parameter space in the light of the LHC discovery*, *Phys.Rev.* **D88** (2013) 115012, [arXiv:1303.1150].

[186] **LHC Higgs Cross Section Working Group** Collaboration, S. Heinemeyer et al., *Handbook of LHC Higgs Cross Sections: 3. Higgs Properties*, arXiv:1307.1347.

[187] **ALEPH Collaboration, DELPHI Collaboration, L3 Collaboration, OPAL Collaboration, SLD Collaboration, LEP Electroweak Working Group, SLD Electroweak Group, SLD Heavy Flavour Group** Collaboration, S. Schael et al., *Precision electroweak measurements on the Z resonance*, *Phys.Rept.* **427** (2006) 257–454, [hep-ex/0509008].

[188] **ALEPH Collaboration, DELPHI Collaboration, L3 Collaboration, OPAL Collaboration, LEP Electroweak Working Group** Collaboration, S. Schael et al., *Electroweak Measurements in Electron-Positron Collisions at W-Boson-Pair Energies at LEP*, arXiv:1302.3415.

[189] D. Y. Bardin, M. S. Bilenky, G. Mitselmakher, G. Mitselmakher, T. Riemann, et al., *A Realistic Approach to the Standard Z Peak*, *Z.Phys.* **C44** (1989) 493.

[190] D. Y. Bardin, M. S. Bilenky, A. Chizhov, A. Sazonov, A. Sazonov, et al., *Analytic approach to the complete set of QED corrections to fermion pair production in e+ e- annihilation*, *Nucl.Phys.* **B351** (1991) 1–48, [hep-ph/9801208].

[191] D. Y. Bardin, M. S. Bilenky, A. Sazonov, Y. Sedykh, Y. Sedykh, et al., *QED corrections with partial angular integration to fermion pair production in e+ e- annihilation*, *Phys.Lett.* **B255** (1991) 290–296, [hep-ph/9801209].

[192] D. Y. Bardin, M. S. Bilenky, A. Chizhov, O. Fedorenko, S. N. Ganguli, et al., *ZFITTER: An Analytical program for fermion pair production in e+ e- annihilation*, hep-ph/9412201.

[193] D. Y. Bardin, P. Christova, M. Jack, L. Kalinovskaya, A. Olchevski, et al., *ZFITTER v.6.21: A Semianalytical program for fermion pair production in e+ e- annihilation*, *Comput.Phys.Commun.* **133** (2001) 229–395, [hep-ph/9908433].

[194] A. Arbuzov, *Light pair corrections to electron positron annihilation at LEP / SLC*, hep-ph/9907500.

[195] A. Arbuzov, M. Awramik, M. Czakon, A. Freitas, M. Grunewald, et al., *ZFITTER: A Semi-analytical program for fermion pair production in e+ e- annihilation, from version 6.21 to version 6.42*, *Comput.Phys.Commun.* **174** (2006) 728–758, [hep-ph/0507146].

[196] ZFITTER support group, ZFITTER 6.43, June, 2008. http://zfitter.desy.de.

[197] B. W. Lee, C. Quigg, and H. Thacker, *Weak Interactions at Very High-Energies: The Role of the Higgs Boson Mass*, *Phys.Rev.* **D16** (1977) 1519.

[198] **ATLAS Collaboration** Collaboration, *Search for a high-mass Higgs boson in the $H \to WW \to l\nu l\nu$ decay channel with the ATLAS detector using 21 fb^{-1} of proton-proton collision data*, . http://cds.cern.ch/record/1562879.

[199] **ATLAS Collaboration** Collaboration, *Measurements of the properties of the Higgs-like boson in the four lepton decay channel with the ATLAS detector using 25 fb^{-1} of proton-proton collision data*, . http://cds.cern.ch/record/1523699.

[200] **CMS Collaboration** Collaboration, C. Collaboration, *Search for a standard model like Higgs boson in the decay channel H to ZZ to l+l- q qbar at CMS*, . http://cds.cern.ch/record/1564157.

[201] **CMS Collaboration** Collaboration, *Properties of the Higgs-like boson in the decay H to ZZ to 4l in pp collisions at sqrt s =7 and 8 TeV*, . http://cds.cern.ch/record/1523767.

[202] **CMS Collaboration** Collaboration, *Update on the search for the standard model Higgs boson in pp collisions at the LHC decaying to W + W in the fully leptonic final state*, .

[203] A. Belyaev, N. D. Christensen, and A. Pukhov, *CalcHEP 3.4 for collider physics within and beyond the Standard Model*, *Comput.Phys.Commun.* **184** (2013) 1729–1769, [arXiv:1207.6082].

[204] G. Belanger, F. Boudjema, P. Brun, A. Pukhov, S. Rosier-Lees, et al., *Indirect search for dark matter with micrOMEGAs2.4*, *Comput.Phys.Commun.* **182** (2011) 842–856, [arXiv:1004.1092].

[205] T. Li and Y.-F. Zhou, *Strongly first order phase transition in the singlet fermionic dark matter model after LUX*, *JHEP* **1407** (2014) 006, [arXiv:1402.3087].

[206] **LUX Collaboration** Collaboration, D. Akerib et al., *First results from the LUX dark matter experiment at the Sanford Underground Research Facility*, *Phys.Rev.Lett.* **112** (2014) 091303, [arXiv:1310.8214].

[207] T. A. collaboration, *A search for resonant Higgs-pair production in the $b\bar{b}b\bar{b}$ final state in pp collisions at $\sqrt{s} = 8$ TeV*, . http://cds.cern.ch/record/1666518.

[208] **CMS Collaboration** Collaboration, C. Collaboration, *Search for di-Higgs resonances decaying to 4 bottom quarks*, . http://cds.cern.ch/record/1748425/files/.

[209] **ATLAS Collaboration** Collaboration, G. Aad et al., *Search For Higgs Boson Pair Production in the $\gamma\gamma b\bar{b}$ Final State using pp Collision Data at $\sqrt{s} = 8$ TeV from the ATLAS Detector*, arXiv:1406.5053.

[210] **CMS Collaboration** Collaboration, C. Collaboration, *Search for the resonant production of two Higgs bosons in the final state with two photons and two bottom quarks*, . http://inspirehep.net/record/1292910/files/.

[211] **LHC Higgs Cross Section Working Group** Collaboration, S. Dittmaier et al., *Handbook of LHC Higgs Cross Sections: 1. Inclusive Observables*, arXiv:1101.0593.

[212] T. Sjostrand, S. Mrenna, and P. Z. Skands, *PYTHIA 6.4 Physics and Manual*, *JHEP* **0605** (2006) 026, [hep-ph/0603175].

[213] H.-L. Lai, M. Guzzi, J. Huston, Z. Li, P. M. Nadolsky, et al., *New parton distributions for collider physics*, *Phys.Rev.* **D82** (2010) 074024, [arXiv:1007.2241].

[214] **DELPHES 3** Collaboration, J. de Favereau et al., *DELPHES 3, A modular framework for fast simulation of a generic collider experiment*, *JHEP* **1402** (2014) 057, [arXiv:1307.6346].

[215] M. Cacciari, G. P. Salam, and G. Soyez, *FastJet User Manual*, *Eur.Phys.J.* **C72** (2012) 1896, [arXiv:1111.6097].

[216] M. Cacciari, G. P. Salam, and G. Soyez, *The Anti-k(t) jet clustering algorithm*, *JHEP* **0804** (2008) 063, [arXiv:0802.1189].

[217] **ATLAS Collaboration** Collaboration, *Measurement of the Mistag Rate with 5 fb^{-1} of Data Collected by the ATLAS Detector*, . http://cds.cern.ch/record/1435194.

[218] M. El-Kacimi and R. Lafaye, *Simulation of neutral Higgs pairs production processes in PYTHIA using HPAIR matrix elements*, .

[219] S. Dawson, S. Dittmaier, and M. Spira, *Neutral Higgs boson pair production at hadron colliders: QCD corrections*, *Phys.Rev.* **D58** (1998) 115012, [hep-ph/9805244].

[220] M. Czakon and A. Mitov, *Top++: A Program for the Calculation of the Top-Pair Cross-Section at Hadron Colliders*, *Comput.Phys.Commun.* **185** (2014) 2930, [arXiv:1112.5675].

[221] C. Lester and D. Summers, *Measuring masses of semiinvisibly decaying particles pair produced at hadron colliders*, *Phys.Lett.* **B463** (1999) 99–103, [hep-ph/9906349].

[222] A. Barr, C. Lester, and P. Stephens, *m(T2): The Truth behind the glamour*, *J.Phys.* **G29** (2003) 2343–2363, [hep-ph/0304226].

[223] W. S. Cho, K. Choi, Y. G. Kim, and C. B. Park, *Measuring the top quark mass with m(T2) at the LHC*, *Phys.Rev.* **D78** (2008) 034019, [arXiv:0804.2185].

[224] **CDF Collaboration** Collaboration, T. Aaltonen et al., *Top Quark Mass Measurement using m_{T2} in the Dilepton Channel at CDF*, *Phys.Rev.* **D81** (2010) 031102, [arXiv:0911.2956].

[225] **ATLAS Collaboration** Collaboration, *Top quark mass measurement in the eμ channel using the mT2 variable at ATLAS*, .

[226] **CMS Collaboration** Collaboration, S. Chatrchyan et al., *Measurement of masses in the $t\bar{t}$ system by kinematic endpoints in pp collisions at $\sqrt{s}$ = 7 TeV*, *Eur.Phys.J.* **C73** (2013) 2494, [arXiv:1304.5783].

[227] K. Choi, S. Choi, J. S. Lee, and C. B. Park, *Reconstructing the Higgs boson in dileptonic W decays at hadron collider*, *Phys.Rev.* **D80** (2009) 073010, [arXiv:0908.0079].

[228] K. Choi, J. S. Lee, and C. B. Park, *Measuring the Higgs boson mass with transverse mass variables*, *Phys.Rev.* **D82** (2010) 113017, [arXiv:1008.2690].

[229] H.-C. Cheng and Z. Han, *Minimal Kinematic Constraints and M_{T2}* , *JHEP* **0812** (2008) 063, [arXiv:0810.5178].

[230] W. S. Cho, K. Choi, Y. G. Kim, and C. B. Park, *M_{T2}-assisted on-shell reconstruction of missing momenta and its application to spin measurement at the LHC*, *Phys.Rev.* **D79** (2009) 031701, [arXiv:0810.4853].

[231] C. B. Park, *Reconstructing the heavy resonance at hadron colliders*, *Phys.Rev.* **D84** (2011) 096001, [arXiv:1106.6087].

[232] J. M. Butterworth, A. R. Davison, M. Rubin, and G. P. Salam, *Jet substructure as a new Higgs search channel at the LHC*, *Phys.Rev.Lett.* **100** (2008) 242001, [arXiv:0802.2470].

[233] A. Papaefstathiou, L. L. Yang, and J. Zurita, *Higgs boson pair production at the LHC in the $b\bar{b}W^+W^-$ channel*, *Phys.Rev.* **D87** (2013) 011301, [arXiv:1209.1489].

[234] C. G. Lester, *The stransverse mass, MT2, in special cases*, *JHEP* **1105** (2011) 076, [arXiv:1103.5682].

[235] A. J. Barr, B. Gripaios, and C. G. Lester, *Measuring the Higgs boson mass in dileptonic W-boson decays at hadron colliders*, *JHEP* **0907** (2009) 072, [arXiv:0902.4864].

[236] C. Lester and A. Barr, *MTGEN: Mass scale measurements in pair-production at colliders*, *JHEP* **0712** (2007) 102, [arXiv:0708.1028].

[237] W. S. Cho, K. Choi, Y. G. Kim, and C. B. Park, *Gluino Stransverse Mass*, *Phys.Rev.Lett.* **100** (2008) 171801, [arXiv:0709.0288].

[238] W. S. Cho, K. Choi, Y. G. Kim, and C. B. Park, *Measuring superparticle masses at hadron collider using the transverse mass kink*, *JHEP* **0802** (2008) 035, [arXiv:0711.4526].

[239] **CMS** Collaboration, S. Chatrchyan et al., *Search for a standard-model-like Higgs boson with a mass in the range 145 to 1000 GeV at the LHC*, *Eur.Phys.J.* **C73** (2013) 2469, [arXiv:1304.0213].

[240] **CMS Collaboration** Collaboration, G. Bayatian et al., *CMS technical design report, volume II: Physics performance*, *J.Phys.* **G34** (2007) 995–1579. http://cds.cern.ch/record/942733/files/lhcc-2006-021.pdf.

[241] **ATLAS Collaboration** Collaboration, N. Rompotis, *Beyond Standard Model Higgs boson physics with ATLAS*, .

[242] R. Blumenhagen, M. Cvetic, P. Langacker, and G. Shiu, *Toward realistic intersecting D-brane models*, *Ann.Rev.Nucl.Part.Sci.* **55** (2005) 71–139, [hep-th/0502005].

[243] R. Blumenhagen, B. Kors, D. Lust, and S. Stieberger, *Four-dimensional String Compactifications with D-Branes, Orientifolds and Fluxes*, *Phys.Rept.* **445** (2007) 1–193, [hep-th/0610327].

[244] F. Marchesano, *Progress in D-brane model building*, *Fortsch.Phys.* **55** (2007) 491–518, [hep-th/0702094].

[245] Z. Kakushadze, G. Shiu, S. H. Tye, and Y. Vtorov-Karevsky, *A Review of three family grand unified string models*, *Int.J.Mod.Phys.* **A13** (1998) 2551–2598, [hep-th/9710149].

[246] G. Cleaver, M. Cvetic, J. Espinosa, L. Everett, P. Langacker, et al., *Physics implications of flat directions in free fermionic superstring models 1. Mass spectrum and couplings*, *Phys.Rev.* **D59** (1999) 055005, [hep-ph/9807479].

[247] B. Holdom, *Two U(1)'s and Epsilon Charge Shifts*, *Phys.Lett.* **B166** (1986) 196.

[248] D. Lust and S. Stieberger, *Gauge threshold corrections in intersecting brane world models*, *Fortsch.Phys.* **55** (2007) 427–465, [hep-th/0302221].

[249] S. Abel and B. Schofield, *Brane anti-brane kinetic mixing, millicharged particles and SUSY breaking*, *Nucl.Phys.* **B685** (2004) 150–170, [hep-th/0311051].

[250] S. A. Abel, J. Jaeckel, V. V. Khoze, and A. Ringwald, *Illuminating the Hidden Sector of String Theory by Shining Light through a Magnetic Field*, *Phys.Lett.* **B666** (2008) 66–70, [hep-ph/0608248].

[251] S. Abel, M. Goodsell, J. Jaeckel, V. Khoze, and A. Ringwald, *Kinetic Mixing of the Photon with Hidden U(1)s in String Phenomenology*, *JHEP* **0807** (2008) 124, [arXiv:0803.1449].

[252] M. Goodsell, J. Jaeckel, J. Redondo, and A. Ringwald, *Naturally Light Hidden Photons in LARGE Volume String Compactifications*, *JHEP* **0911** (2009) 027, [arXiv:0909.0515].

[253] M. Cicoli, M. Goodsell, J. Jaeckel, and A. Ringwald, *Testing String Vacua in the Lab: From a Hidden CMB to Dark Forces in Flux Compactifications*, *JHEP* **1107** (2011) 114, [arXiv:1103.3705].

[254] F. Gmeiner and G. Honecker, *Complete Gauge Threshold Corrections for Intersecting Fractional D6-Branes: The Z6 and Z6' Standard Models*, *Nucl.Phys.* **B829** (2010) 225–297, [arXiv:0910.0843].

[255] G. Honecker, *Kaehler metrics and gauge kinetic functions for intersecting D6-branes on toroidal orbifolds - The complete perturbative story*, *Fortsch.Phys.* **60** (2012) 243–326, [arXiv:1109.3192].

[256] B. Kors and P. Nath, *A Stueckelberg extension of the standard model*, *Phys.Lett.* **B586** (2004) 366–372, [hep-ph/0402047].

[257] R. Dermisek, H. Verlinde, and L.-T. Wang, *Hypercharged Anomaly Mediation*, *Phys.Rev.Lett.* **100** (2008) 131804, [arXiv:0711.3211].

[258] H. Verlinde, L.-T. Wang, M. Wijnholt, and I. Yavin, *A Higher Form (of) Mediation*, *JHEP* **0802** (2008) 082, [arXiv:0711.3214].

[259] G. Shiu, P. Soler, and F. Ye, *Millicharged Dark Matter in Quantum Gravity and String Theory*, *Phys.Rev.Lett.* **110** (2013), no. 24 241304, [arXiv:1302.5471].

[260] D. Ghilencea, L. Ibanez, N. Irges, and F. Quevedo, *TeV scale Z-prime bosons from D-branes*, *JHEP* **0208** (2002) 016, [hep-ph/0205083].

[261] R. Blumenhagen, M. Cvetic, and T. Weigand, *Spacetime instanton corrections in 4D string vacua: The Seesaw mechanism for D-Brane models*, *Nucl.Phys.* **B771** (2007) 113–142, [hep-th/0609191].

[262] L. Ibanez and A. Uranga, *Neutrino Majorana Masses from String Theory Instanton Effects*, *JHEP* **0703** (2007) 052, [hep-th/0609213].

[263] B. Florea, S. Kachru, J. McGreevy, and N. Saulina, *Stringy Instantons and Quiver Gauge Theories*, *JHEP* **0705** (2007) 024, [hep-th/0610003].

[264] L. E. Ibanez, F. Marchesano, and R. Rabadan, *Getting just the standard model at intersecting branes*, *JHEP* **0111** (2001) 002, [hep-th/0105155].

[265] E. J. Chun, J.-C. Park, and S. Scopel, *Dark matter and a new gauge boson through kinetic mixing*, *JHEP* **1102** (2011) 100, [arXiv:1011.3300].

[266] A. Drozd, B. Grzadkowski, J. F. Gunion, and Y. Jiang, *Extending two-Higgs-doublet models by a singlet scalar field - the Case for Dark Matter*, *JHEP* **1411** (2014) 105, [arXiv:1408.2106].

[267] D. Cremades, L. Ibanez, and F. Marchesano, *Yukawa couplings in intersecting D-brane models*, *JHEP* **0307** (2003) 038, [hep-th/0302105].

[268] G. Belanger, F. Boudjema, A. Pukhov, and A. Semenov, *micrOMEGAs3: A program for calculating dark matter observables*, *Comput.Phys.Commun.* **185** (2014) 960–985, [arXiv:1305.0237].

[269] P. Klos, J. Menéndez, D. Gazit, and A. Schwenk, *Large-scale nuclear structure calculations for spin-dependent WIMP scattering with chiral effective field theory currents*, *Phys.Rev.* **D88** (2013), no. 8 083516, [arXiv:1304.7684].

[270] **ATLAS** Collaboration, G. Aad et al., *Search for high-mass dilepton resonances in pp collisions at $\sqrt{s} = 8$ TeV with the ATLAS detector*, *Phys.Rev.* **D90** (2014), no. 5 052005, [arXiv:1405.4123].

[271] **CDF Collaboration** Collaboration, T. Aaltonen et al., *Search for new particles decaying into dijets in proton-antiproton collisions at s**(1/2) = 1.96-TeV*, *Phys.Rev.* **D79** (2009) 112002, [arXiv:0812.4036].

[272] **ATLAS** Collaboration, G. Aad et al., *Search for New Physics in the Dijet Mass Distribution using 1 fb^{-1} of pp Collision Data at $\sqrt{s} = 7$ TeV collected by the ATLAS Detector*, *Phys.Lett.* **B708** (2012) 37–54, [arXiv:1108.6311].

[273] **CMS** Collaboration, G. Aad et al., *The CMS Collaboration, Search for Narrow Resonances using the Dijet Mass Spectrum with 19.6 fb^{-1} of pp Collisions at $\sqrt{s} = 8$ TeV, CMS-PAS-EXO-12-059 (2013)*, .

[274] M. S. Carena, A. Daleo, B. A. Dobrescu, and T. M. Tait, *Z' gauge bosons at the Tevatron*, *Phys.Rev.* **D70** (2004) 093009, [hep-ph/0408098].

[275] M. Chala, F. Kahlhoefer, M. McCullough, G. Nardini, and K. Schmidt-Hoberg, *Constraining Dark Sectors with Monojets and Dijets*, *JHEP* **07** (2015) 089, [arXiv:1503.05916].

[276] P. Fayet, *U-boson production in e+ e- annihilations, psi and Upsilon decays, and Light Dark Matter*, *Phys.Rev.* **D75** (2007) 115017, [hep-ph/0702176].

[277] T. Teubner, K. Hagiwara, R. Liao, A. Martin, and D. Nomura, *Update of g-2 of the Muon and Delta Alpha*, *Chin.Phys.* **C34** (2010) 728–734, [arXiv:1001.5401].

[278] S. Yellin, *Finding an upper limit in the presence of unknown background*, *Phys.Rev.* **D66** (2002) 032005, [physics/0203002].

[279] **XENON100 Collaboration** Collaboration, E. Aprile et al., *Likelihood Approach to the First Dark Matter Results from XENON100*, *Phys.Rev.* **D84** (2011) 052003, [arXiv:1103.0303].

[280] **LUX Collaboration** Collaboration, D. Akerib et al., *The Large Underground Xenon (LUX) Experiment*, *Nucl.Instrum.Meth.* **A704** (2013) 111–126, [arXiv:1211.3788].

[281] D. Cerdeno, M. Fornasa, J. Huh, and M. Peiro, *Nuclear uncertainties in the spin-dependent structure functions for direct dark matter detection*, *Phys.Rev.* **D87** (2013) 023512, [arXiv:1208.6426].

[282] E. Accomando, A. Belyaev, L. Fedeli, S. F. King, and C. Shepherd-Themistocleous, *Z' physics with early LHC data*, *Phys.Rev.* **D83** (2011) 075012, [arXiv:1010.6058].

[283] N. Arkani-Hamed, L. J. Hall, H. Murayama, D. Tucker-Smith, and N. Weiner, *Small neutrino masses from supersymmetry breaking*, *Phys. Rev.* **D64** (2001) 115011, [hep-ph/0006312].

[284] D. Hooper, J. March-Russell, and S. M. West, *Asymmetric sneutrino dark matter and the Omega(b) / Omega(DM) puzzle*, *Phys. Lett.* **B605** (2005) 228–236, [hep-ph/0410114].

[285] C. Arina and N. Fornengo, *Sneutrino cold dark matter, a new analysis: Relic abundance and detection rates*, *JHEP* **11** (2007) 029, [arXiv:0709.4477].

[286] C. Arina, *Sneutrino cold dark matter in extended MSSM models*, in *Proceedings, 43rd Rencontres de Moriond on Electroweak Interactions and Unified Theories: La Thuile, Italy, March 1-8, 2008*, 2008. arXiv:0805.1991.

[287] G. Belanger, M. Kakizaki, E. K. Park, S. Kraml, and A. Pukhov, *Light mixed sneutrinos as thermal dark matter*, *JCAP* **1011** (2010) 017, [arXiv:1008.0580].

[288] B. Dumont, G. Belanger, S. Fichet, S. Kraml, and T. Schwetz, *Mixed sneutrino dark matter in light of the 2011 XENON and LHC results*, *JCAP* **1209** (2012) 013, [arXiv:1206.1521].

[289] **CMS** Collaboration, S. Chatrchyan et al., *Observation of a new boson at a mass of 125 GeV with the CMS experiment at the LHC*, *Phys. Lett.* **B716** (2012) 30–61, [arXiv:1207.7235].

[290] U. Ellwanger, *Higgs Bosons in the Next-to-Minimal Supersymmetric Standard Model at the LHC*, *Eur. Phys. J.* **C71** (2011) 1782, [arXiv:1108.0157].

[291] L. J. Hall, D. Pinner, and J. T. Ruderman, *A Natural SUSY Higgs Near 126 GeV*, *JHEP* **04** (2012) 131, [arXiv:1112.2703].

[292] U. Ellwanger, *A Higgs boson near 125 GeV with enhanced di-photon signal in the NMSSM*, *JHEP* **03** (2012) 044, [arXiv:1112.3548].

[293] J. F. Gunion, Y. Jiang, and S. Kraml, *The Constrained NMSSM and Higgs near 125 GeV*, *Phys. Lett.* **B710** (2012) 454–459, [arXiv:1201.0982].

[294] A. Arvanitaki and G. Villadoro, *A Non Standard Model Higgs at the LHC as a Sign of Naturalness*, *JHEP* **02** (2012) 144, [arXiv:1112.4835].

[295] S. F. King, M. Muhlleitner, and R. Nevzorov, *NMSSM Higgs Benchmarks Near 125 GeV*, *Nucl. Phys.* **B860** (2012) 207–244, [arXiv:1201.2671].

[296] Z. Kang, J. Li, and T. Li, *On Naturalness of the MSSM and NMSSM*, *JHEP* **11** (2012) 024, [arXiv:1201.5305].

[297] J.-J. Cao, Z.-X. Heng, J. M. Yang, Y.-M. Zhang, and J.-Y. Zhu, *A SM-like Higgs near 125 GeV in low energy SUSY: a comparative study for MSSM and NMSSM*, *JHEP* **03** (2012) 086, [arXiv:1202.5821].

[298] U. Ellwanger and C. Hugonie, *Higgs bosons near 125 GeV in the NMSSM with constraints at the GUT scale*, *Adv.High Energy Phys.* **2012** (2012) 625389, [arXiv:1203.5048].

[299] R. Benbrik, M. Gomez Bock, S. Heinemeyer, O. Stal, G. Weiglein, and L. Zeune, *Confronting the MSSM and the NMSSM with the Discovery of a Signal in the two Photon Channel at the LHC*, *Eur. Phys. J.* **C72** (2012) 2171, [arXiv:1207.1096].

[300] J. F. Gunion, Y. Jiang, and S. Kraml, *Could two NMSSM Higgs bosons be present near 125 GeV?*, *Phys. Rev.* **D86** (2012) 071702, [arXiv:1207.1545].

[301] J. Cao, Z. Heng, J. M. Yang, and J. Zhu, *Status of low energy SUSY models confronted with the LHC 125 GeV Higgs data*, *JHEP* **10** (2012) 079, [arXiv:1207.3698].

[302] G. Belanger, U. Ellwanger, J. F. Gunion, Y. Jiang, S. Kraml, and J. H. Schwarz, *Higgs Bosons at 98 and 125 GeV at LEP and the LHC*, *JHEP* **01** (2013) 069, [arXiv:1210.1976].

[303] K. Kowalska, S. Munir, L. Roszkowski, E. M. Sessolo, S. Trojanowski, and Y.-L. S. Tsai, *Constrained next-to-minimal supersymmetric standard model with a 126 GeV Higgs boson: A global analysis*, *Phys. Rev.* **D87** (2013) 115010, [arXiv:1211.1693].

[304] S. F. King, M. Mühlleitner, R. Nevzorov, and K. Walz, *Natural NMSSM Higgs Bosons*, *Nucl. Phys.* **B870** (2013) 323–352, [arXiv:1211.5074].

[305] **CMS Collaboration** Collaboration, *Combination of standard model Higgs boson searches and measurements of the properties of the new boson with a mass near 125 GeV*, .

[306] **ATLAS Collaboration** Collaboration, *Measurements of the properties of the Higgs-like boson in the two photon decay channel with the ATLAS detector using 25* fb^{-1} *of proton-proton collision data*, .

[307] **ATLAS Collaboration** Collaboration, *Measurements of the properties of the Higgs-like boson in the* $WW^{(*)} \to \ell\nu\ell\nu$ *decay channel with the ATLAS detector using 25* fb^{-1} *of proton-proton collision data*, .

[308] **ATLAS Collaboration** Collaboration, *Combined measurements of the mass and signal strength of the Higgs-like boson with the ATLAS detector using up to 25* fb^{-1} *of proton-proton collision data*, .

[309] **ATLAS Collaboration** Collaboration, *Search for invisible decays of a Higgs boson produced in association with a Z boson in ATLAS*, .

[310] J. R. Espinosa, M. Muhlleitner, C. Grojean, and M. Trott, *Probing for Invisible Higgs Decays with Global Fits*, *JHEP* **1209** (2012) 126, [arXiv:1205.6790].

[311] G. Belanger, B. Dumont, U. Ellwanger, J. Gunion, and S. Kraml, *Status of invisible Higgs decays*, *Phys.Lett.* **B723** (2013) 340–347, [arXiv:1302.5694].

[312] A. Falkowski, F. Riva, and A. Urbano, *Higgs at last*, *JHEP* **11** (2013) 111, [arXiv:1303.1812].

[313] P. P. Giardino, K. Kannike, I. Masina, M. Raidal, and A. Strumia, *The universal Higgs fit*, *JHEP* **05** (2014) 046, [arXiv:1303.3570].

[314] J. Ellis and T. You, *Updated Global Analysis of Higgs Couplings*, *JHEP* **1306** (2013) 103, [arXiv:1303.3879].

[315] A. Djouadi and G. Moreau, *The couplings of the Higgs boson and its CP properties from fits of the signal strengths and their ratios at the 7+8 TeV LHC*, *Eur. Phys. J.* **C73** (2013), no. 9 2512, [arXiv:1303.6591].

[316] G. Belanger, B. Dumont, U. Ellwanger, J. F. Gunion, and S. Kraml, *Global fit to Higgs signal strengths and couplings and implications for extended Higgs sectors*, *Phys. Rev.* **D88** (2013) 075008, [arXiv:1306.2941].

[317] U. Ellwanger, J. F. Gunion, and C. Hugonie, *NMHDECAY: A Fortran code for the Higgs masses, couplings and decay widths in the NMSSM*, *JHEP* **02** (2005) 066, [hep-ph/0406215].

[318] U. Ellwanger and C. Hugonie, *NMHDECAY 2.0: An Updated program for sparticle masses, Higgs masses, couplings and decay widths in the NMSSM*, *Comput. Phys. Commun.* **175** (2006) 290–303, [hep-ph/0508022].

[319] U. Ellwanger and C. Hugonie, *NMSPEC: A Fortran code for the sparticle and Higgs masses in the NMSSM with GUT scale boundary conditions*, *Comput. Phys. Commun.* **177** (2007) 399–407, [hep-ph/0612134].

[320] Y. Kanehata, T. Kobayashi, Y. Konishi, O. Seto, and T. Shimomura, *Constraints from Unrealistic Vacua in the Next-to-Minimal Supersymmetric Standard Model*, *Prog. Theor. Phys.* **126** (2011) 1051–1076, [arXiv:1103.5109].

[321] **LHCb** Collaboration, R. Aaij et al., *Measurement of the $B_s^0 \to \mu^+\mu^-$ branching fraction and search for $B^0 \to \mu^+\mu^-$ decays at the LHCb experiment*, *Phys. Rev. Lett.* **111** (2013) 101805, [arXiv:1307.5024].

[322] **CMS** Collaboration, S. Chatrchyan et al., *Measurement of the B(s) to mu+ mu- branching fraction and search for B0 to mu+ mu- with the CMS Experiment*, *Phys. Rev. Lett.* **111** (2013) 101804, [arXiv:1307.5025].

[323] M. Ciuchini, G. Degrassi, P. Gambino, and G. F. Giudice, *Next-to-leading QCD corrections to B —¿ X(s) gamma in supersymmetry*, *Nucl. Phys.* **B534** (1998) 3–20, [hep-ph/9806308].

[324] G. D'Ambrosio, G. F. Giudice, G. Isidori, and A. Strumia, *Minimal flavor violation: An Effective field theory approach*, *Nucl. Phys.* **B645** (2002) 155–187, [hep-ph/0207036].

[325] M. Misiak et al., *Estimate of $\mathcal{B}(\bar{B} \to X_s\gamma)$ at $O(\alpha_s^2)$*, *Phys. Rev. Lett.* **98** (2007) 022002, [hep-ph/0609232].

[326] M. Misiak and M. Steinhauser, *NNLO QCD corrections to the anti-B —¿ X(s) gamma matrix elements using interpolation in m(c)*, *Nucl. Phys.* **B764** (2007) 62–82, [hep-ph/0609241].

[327] **Heavy Flavor Averaging Group** Collaboration, Y. Amhis et al., *Averages of B-Hadron, C-Hadron, and tau-lepton properties as of early 2012*, arXiv:1207.1158.

[328] **BaBar** Collaboration, J. P. Lees et al., *Evidence of $B^+ \to \tau^+\nu$ decays with hadronic B tags*, *Phys. Rev.* **D88** (2013), no. 3 031102, [arXiv:1207.0698].

[329] **Muon g-2** Collaboration, G. W. Bennett et al., *Final Report of the Muon E821 Anomalous Magnetic Moment Measurement at BNL*, *Phys. Rev.* **D73** (2006) 072003, [hep-ex/0602035].

[330] F. Jegerlehner and A. Nyffeler, *The Muon g-2*, *Phys. Rept.* **477** (2009) 1–110, [arXiv:0902.3360].

[331] **New (g-2)** Collaboration, F. Gray, *Measuring the muon's anomalous magnetic moment to 0.14 ppm*, *J. Phys. Conf. Ser.* **312** (2011) 102006, [arXiv:1009.0799].

[332] M. Davier, A. Hoecker, B. Malaescu, and Z. Zhang, *Reevaluation of the Hadronic Contributions to the Muon g-2 and to alpha(MZ)*, *Eur. Phys. J.* **C71** (2011) 1515, [arXiv:1010.4180]. [Erratum: Eur. Phys. J.C72,1874(2012)].

[333] K. Hagiwara, R. Liao, A. D. Martin, D. Nomura, and T. Teubner, *$(g-2)_\mu$ and $\alpha(M_Z^2)$ re-evaluated using new precise data*, *J. Phys.* **G38** (2011) 085003, [arXiv:1105.3149].

[334] **OPAL, DELPHI, LEP Working Group for Higgs boson searches, ALEPH, L3** Collaboration, R. Barate et al., *Search for the standard model Higgs boson at LEP*, *Phys. Lett.* **B565** (2003) 61–75, [hep-ex/0306033].

[335] **DELPHI, OPAL, ALEPH, LEP Working Group for Higgs Boson Searches, L3** Collaboration, S. Schael et al., *Search for neutral MSSM Higgs bosons at LEP*, *Eur. Phys. J.* **C47** (2006) 547–587, [hep-ex/0602042].

[336] M. Drees, *A Supersymmetric Explanation of the Excess of Higgs–Like Events at the LHC and at LEP*, *Phys. Rev.* **D86** (2012) 115018, [arXiv:1210.6507].

[337] **XENON100** Collaboration, E. Aprile et al., *Dark Matter Results from 225 Live Days of XENON100 Data*, *Phys.Rev.Lett.* **109** (2012) 181301, [arXiv:1207.5988].

[338] **ATLAS** Collaboration, G. Aad et al., *Search for a light Higgs boson decaying to long-lived weakly-interacting particles in proton-proton collisions at $\sqrt{s} = 7$ TeV with the ATLAS detector*, *Phys. Rev. Lett.* **108** (2012) 251801, [arXiv:1203.1303].

[339] **ATLAS** Collaboration, G. Aad et al., *Search for displaced muonic lepton jets from light Higgs boson decay in proton-proton collisions at $\sqrt{s} = 7$ TeV with the ATLAS detector*, *Phys. Lett.* **B721** (2013) 32–50, [arXiv:1210.0435].

[340] **ATLAS** Collaboration, G. Aad et al., *Search for long-lived, heavy particles in final states with a muon and multi-track displaced vertex in proton-proton collisions at $\sqrt{s} = 7$ TeV with the ATLAS detector*, *Phys. Lett.* **B719** (2013) 280–298, [arXiv:1210.7451].

[341] **CMS** Collaboration, S. Chatrchyan et al., *Search in leptonic channels for heavy resonances decaying to long-lived neutral particles*, *JHEP* **02** (2013) 085, [arXiv:1211.2472].

[342] S. Bobrovskyi, J. Hajer, and S. Rydbeck, *Long-lived higgsinos as probes of gravitino dark matter at the LHC*, *JHEP* **02** (2013) 133, [arXiv:1211.5584].

[343] **CMS Collaboration** Collaboration, G. L. e. a. Bayatian, *CMS Physics: Technical Design Report Volume 1: Detector Performance and Software*, . There is an error on cover due to a technical problem for some items.

[344] **ATLAS** Collaboration, G. Aad et al., *Expected Performance of the ATLAS Experiment - Detector, Trigger and Physics*, arXiv:0901.0512.

[345] A. Bartl, M. Hirsch, A. Vicente, S. Liebler, and W. Porod, *LHC phenomenology of the mu nu SSM*, *JHEP* **05** (2009) 120, [arXiv:0903.3596].

[346] F. E. Paige, *Determining SUSY particle masses at LHC*, *eConf* **C960625** (1996) SUP114, [hep-ph/9609373]. [,710(1996)].

[347] M. M. Nojiri and Y. Yamada, *Neutralino decays at the CERN LHC*, *Phys. Rev.* **D60** (1999) 015006, [hep-ph/9902201].

[348] B. K. Gjelsten, D. J. Miller, and P. Osland, *Measurement of SUSY masses via cascade decays for SPS 1a*, *JHEP* **12** (2004) 003, [hep-ph/0410303].

[349] **CMS** Collaboration, S. Bhattacharya, *Efficiency measurement of b-tagging algorithms developed by the CMS experiment*, arXiv:1110.4569.

[350] **ATLAS Collaboration** Collaboration, *Search for supersymmetry in events with four or more leptons in 21 fb^{-1} of pp collisions at $\sqrt{s} = 8$ TeV with the ATLAS detector*, .

[351] **CMS Collaboration** Collaboration, *Search for RPV SUSY in the four-lepton final state*, .

[352] R. Barbier et al., *R-parity violating supersymmetry*, *Phys. Rept.* **420** (2005) 1–202, [hep-ph/0406039].

[353] L. M. Carpenter, D. E. Kaplan, and E.-J. Rhee, *Reduced fine-tuning in supersymmetry with R-parity violation*, *Phys. Rev. Lett.* **99** (2007) 211801, [hep-ph/0607204].

[354] H. K. Dreiner and G. G. Ross, *R-parity violation at hadron colliders*, *Nucl. Phys.* **B365** (1991) 597–613.

[355] P. W. Graham, D. E. Kaplan, S. Rajendran, and P. Saraswat, *Displaced Supersymmetry*, *JHEP* **07** (2012) 149, [arXiv:1204.6038].

[356] *A search for heavy long-lived sleptons using 16 fb^{-1} of pp collisions at $\sqrt{s} = 8$ TeV with the ATLAS detector*, .

[357] C. Arina and M. E. Cabrera, *Multi-lepton signatures at LHC from sneutrino dark matter*, *JHEP* **04** (2014) 100, [arXiv:1311.6549].

[358] **Particle Data Group** Collaboration, J. Beringer et al., *Review of Particle Physics (RPP)*, *Phys.Rev.* **D86** (2012) 010001.

[359] **ATLAS** Collaboration, G. Aad et al., *Search for third generation scalar leptoquarks in pp collisions at sqrt(s) = 7 TeV with the ATLAS detector*, *JHEP* **1306** (2013) 033, [arXiv:1303.0526].

[360] **CMS** Collaboration, S. Chatrchyan et al., *Search for top-squark pair production in the single-lepton final state in pp collisions at $\sqrt{s} = 8$ TeV*, tech. rep., 2013.

[361] **CMS** Collaboration, S. Chatrchyan et al., *Search for gluino mediated bottom- and top-squark production in multijet final states in pp collisions at 8 TeV*, *Phys.Lett.* **B725** (2013) 243–270, [arXiv:1305.2390].

[362] **ATLAS** Collaboration, "Gluino-mediated stop production." https://atlas.web.cern.ch/Atlas/GROUPS/PHYSICS/CombinedSummaryPlots/SUSY/index.html#ATLAS_SUSY_Gtt, 2013.

[363] R. Franceschini and R. Torre, *RPV stops bump off the background*, *Eur.Phys.J.* **C73** (2013) 2422, [arXiv:1212.3622].

[364] B. Fuks and G. Nardini, "Light stops." work in preparation.

[365] M. Papucci, J. T. Ruderman, and A. Weiler, *Natural SUSY Endures*, *JHEP* **1209** (2012) 035, [arXiv:1110.6926].

[366] J. Espinosa and M. Quiros, *Upper bounds on the lightest Higgs boson mass in general supersymmetric Standard Models*, *Phys.Lett.* **B302** (1993) 51–58, [hep-ph/9212305].

[367] P. Bandyopadhyay, K. Huitu, and A. Sabanci, *Status of $Y = 0$ Triplet Higgs with supersymmetry in the light of ~ 125 GeV Higgs discovery*, arXiv:1306.4530.

[368] F. Staub, *From Superpotential to Model Files for FeynArts and CalcHep/CompHep*, *Comput.Phys.Commun.* **181** (2010) 1077–1086, [arXiv:0909.2863].

[369] F. Staub, *Automatic Calculation of supersymmetric Renormalization Group Equations and Self Energies*, *Comput.Phys.Commun.* **182** (2011) 808–833, [arXiv:1002.0840].

[370] W. Porod, *SPheno, a program for calculating supersymmetric spectra, SUSY particle decays and SUSY particle production at e+ e- colliders*, *Comput.Phys.Commun.* **153** (2003) 275–315, [hep-ph/0301101].

[371] W. Porod and F. Staub, *SPheno 3.1: Extensions including flavour, CP-phases and models beyond the MSSM*, *Comput.Phys.Commun.* **183** (2012) 2458–2469, [arXiv:1104.1573].

[372] B. Allanach, A. Djouadi, J. Kneur, W. Porod, and P. Slavich, *Precise determination of the neutral Higgs boson masses in the MSSM*, *JHEP* **0409** (2004) 044, [hep-ph/0406166].

[373] **ATLAS** Collaboration, G. Aad et al., *Search for Invisible Decays of a Higgs Boson Produced in Association with a Z Boson in ATLAS*, arXiv:1402.3244.

[374] **CMS** Collaboration, CMS, *Search for invisible Higgs produced in association with a Z boson*, tech. rep., 2013.

[375] A. Djouadi, *The Anatomy of electro-weak symmetry breaking. II. The Higgs bosons in the minimal supersymmetric model*, *Phys.Rept.* **459** (2008) 1–241, [hep-ph/0503173].

[376] **ATLAS** Collaboration, *Search for the Standard Model Higgs boson in the $H \to Z\gamma$ decay mode with pp collisions at $\sqrt{s} = 7$ and 8 TeV*, tech. rep., 2013.

[377] **CMS** Collaboration, S. Chatrchyan et al., *Search for a Higgs boson decaying into a Z and a photon in pp collisions at $\sqrt{s} = 7$ and 8 TeV*, *Phys.Lett.* **B726** (2013) 587–609, [arXiv:1307.5515].

[378] R. Cahn, M. S. Chanowitz, and N. Fleishon, *Higgs Particle Production by $Z \to H\gamma$*, *Phys.Lett.* **B82** (1979) 113.

[379] L. Bergstrom and G. Hulth, *Induced Higgs Couplings to Neutral Bosons in e^+e^- Collisions*, *Nucl.Phys.* **B259** (1985) 137.

[380] A. Djouadi, V. Driesen, W. Hollik, and A. Kraft, *The Higgs photon - Z boson coupling revisited*, *Eur.Phys.J.* **C1** (1998) 163–175, [hep-ph/9701342].

[381] **ATLAS Collaboration** Collaboration, *Combined coupling measurements of the Higgs-like boson with the ATLAS detector using up to 25 fb^{-1} of proton-proton collision data*, . http://cds.cern.ch/record/1528170.

[382] F. Boudjema, G. Drieu La Rochelle, and S. Kulkarni, *One-loop corrections, uncertainties and approximations in neutralino annihilations: Examples*, *Phys.Rev.* **D84** (2011) 116001, [arXiv:1108.4291].

[383] P. Junnarkar and A. Walker-Loud, *The Scalar Strange Content of the Nucleon from Lattice QCD*, *Phys.Rev.* **D87** (2013) 114510, [arXiv:1301.1114].

[384] R. Koch, *A New Determination of the pi N Sigma Term Using Hyperbolic Dispersion Relations in the (nu**2, t) Plane*, *Z. Phys.* **C15** (1982) 161–168.

[385] J. Gasser, H. Leutwyler, and M. E. Sainio, *Form-factor of the sigma term*, *Phys. Lett.* **B253** (1991) 260–264.

[386] A. Bottino, F. Donato, N. Fornengo, and S. Scopel, *Implications for relic neutralinos of the theoretical uncertainties in the neutralino nucleon cross-section*, *Astropart. Phys.* **13** (2000) 215–225, [hep-ph/9909228].

[387] M. M. Pavan, I. I. Strakovsky, R. L. Workman, and R. A. Arndt, *The pion nucleon Sigma term is definitely large: Results from a GWU analysis of pi N scattering data*, *PiN Newslett.* **16** (2002) 110–115, [hep-ph/0111066].

[388] R. R. de Austri and C. P. d. l. Heros, *Impact of nucleon matrix element uncertainties on the interpretation of direct and indirect dark matter search results*, arXiv:1307.6668.

[389] J. Lee, M. Carena, J. Ellis, A. Pilaftsis, and C. Wagner, *CPsuperH2.3: an Updated Tool for Phenomenology in the MSSM with Explicit CP Violation*, *Comput.Phys.Commun.* **184** (2013) 1220–1233, [arXiv:1208.2212].

[390] F. Feroz, M. Hobson, and M. Bridges, *MultiNest: an efficient and robust Bayesian inference tool for cosmology and particle physics*, *Mon.Not.Roy.Astron.Soc.* **398** (2009) 1601–1614, [arXiv:0809.3437].

[391] **ATLAS** Collaboration, G. Aad et al., *Search for direct production of charginos and neutralinos in events with three leptons and missing transverse momentum in* $\sqrt{s} = 8TeV$ *pp collisions with the ATLAS detector*, *JHEP* **04** (2014) 169, [arXiv:1402.7029].

[392] **CMS** Collaboration, V. Khachatryan et al., *Searches for electroweak production of charginos, neutralinos, and sleptons decaying to leptons and W, Z, and Higgs bosons in pp collisions at 8 TeV*, *Eur. Phys. J.* **C74** (2014), no. 9 3036, [arXiv:1405.7570].

[393] **LHCb** Collaboration, R. Aaij et al., *First Evidence for the Decay* $B_s^0 \to \mu^+\mu^-$, *Phys.Rev.Lett.* **110** (2013) 021801, [arXiv:1211.2674].

[394] **COUPP** Collaboration, E. Behnke et al., *First Dark Matter Search Results from a 4-kg* CF_3I *Bubble Chamber Operated in a Deep Underground Site*, *Phys.Rev.* **D86** (2012) 052001, [arXiv:1204.3094].

[395] **XENON100** Collaboration, E. Aprile et al., *Limits on spin-dependent WIMP-nucleon cross sections from 225 live days of XENON100 data*, *Phys.Rev.Lett.* **111** (2013) 021301, [arXiv:1301.6620].

[396] J. A. Casas, J. M. Moreno, K. Rolbiecki, and B. Zaldivar, *Implications of light charginos for Higgs observables, LHC searches and dark matter*, arXiv:1305.3274.

[397] B. Batell, S. Jung, and C. E. Wagner, *Very Light Charginos and Higgs Decays*, *JHEP* **1312** (2013) 075, [arXiv:1309.2297].

[398] M. Cirelli, N. Fornengo, and A. Strumia, *Minimal dark matter*, *Nucl.Phys.* **B753** (2006) 178–194, [hep-ph/0512090].

[399] C. Arina, G. Bertone, and H. Silverwood, *Complementarity of direct and indirect Dark Matter detection experiments*, *Phys.Rev.* **D88** (2013) 013002, [arXiv:1304.5119].

[400] M. Farina, M. Kadastik, D. Pappadopulo, J. Pata, M. Raidal, et al., *Implications of XENON100 and LHC results for Dark Matter models*, *Nucl.Phys.* **B853** (2011) 607–624, [arXiv:1104.3572].

[401] S. Dawson, A. Gritsan, H. Logan, J. Qian, C. Tully, et al., *Higgs Working Group Report of the Snowmass 2013 Community Planning Study*, arXiv:1310.8361.

[402] M. E. Peskin, *Estimation of LHC and ILC Capabilities for Precision Higgs Boson Coupling Measurements*, arXiv:1312.4974.

[403] J. M. Campbell, R. K. Ellis, W. T. Giele, and C. Williams, *Finding the Higgs boson in decays to $Z\gamma$ using the matrix element method at Next-to-Leading Order*, *Phys.Rev.* **D87** (2013), no. 7 073005, [arXiv:1301.7086].

[404] M. E. Peskin, *Comparison of LHC and ILC Capabilities for Higgs Boson Coupling Measurements*, arXiv:1207.2516.

[405] J. de Blas, A. Delgado, B. Ostdiek, and M. Quirós, *Indirect effects of supersymmetric triplets in stop decays*, *JHEP* **1401** (2014) 177, [arXiv:1311.3654].

[406] S. Porto, G. A. Moortgat-Pick, and K. Rolbiecki, *Towards discrimination of MSSM and NMSSM scenarios at colliders*, in *International Workshop on Future Linear Colliders (LCWS13) Tokyo, Japan, November 11-15, 2013*, 2014. arXiv:1404.1053.